

**The E&L Magmatic Ni-Cu-(PGE) Deposit, Northwestern British Columbia:
Preliminary Sulfide Petrology, Platinum-Group Element Mineralogy and
Lead Isotope Systematics**

By

Eric Douglas James Vandenburg

A THESIS SUBMITTED IN PARTIAL FULFILLMENT OF THE REQUIREMENTS FOR
THE DEGREE OF

BACHELOR OF SCIENCE

in

THE FACULTY OF SCIENCE

(Honours Geological Sciences)

This thesis conforms to the required standard

Supervisor

THE UNIVERSITY OF BRITISH COLUMBIA

(Vancouver)

April, 2020

©Eric Douglas James Vandenburg, 2020

Abstract

The olivine gabbro-hosted E&L magmatic Ni-Cu-(PGE) sulfide deposit is located in the Jurassic Eskay Rift back-arc basin within the Stikine Terrane of northwestern British Columbia and is one of only two known high-grade magmatic Ni-Cu-(PGE) massive sulfide deposits in the Canadian Cordillera. The E&L intrusion is hosted in the 180.7 Ma Nickel Mountain Gabbro Complex and by Upper Hazelton Group pyritic black shales and mudstones. The petrology of sulfide and platinum group minerals and the lead (Pb) isotopic compositions of ore minerals were investigated to provide constraints on mineralization mechanisms and the source of metals in the deposit. The textures of pyrrhotite-pentlandite-chalcopyrite-magnetite are typical of magmatic ore deposits and platinum group minerals are predominantly tellurides and bismuthotellurides. Unusual sieve-textured magnetite in the semi-net-textured sulfides of the Lower Chamber and “pseudo-cuneiform” magnetite in the massive sulfides of the Lower Discovery Zone are interpreted to be the result of disequilibrium-induced resorption. The Pb isotopic compositions of sulfide minerals analyzed directly in thin section by laser ablation-inductively coupled plasma-mass spectrometry (LA-ICP-MS) are variable with many of the results overlapping within analytical uncertainty. Some of the higher temperature sulfides (e.g., pyrrhotite) have relatively unradiogenic Pb isotope compositions, whereas lower temperature minerals (e.g., chalcopyrite) have compositions indicating the effects of crustal contaminant and of secondary hydrothermal alteration. Isotope mixing models suggest that variable degrees of contamination occurred at depth of a mantle-derived magma by the Triassic-Jurassic island-arc basement of Stikinia and at shallower depths by Upper Hazelton Group strata. The similarities in Pb isotopic ratios between E&L sulfides and sulfides from other deposit types in the region highlight the relative isotopic homogeneity of the Stikinia crust during the Early-Middle Jurassic. Combined, trace element and Pb isotopic geochemical variations from the E&L intrusion and deposit are consistent with post-collisional decompression melting of a metasomatized mantle source during the transtensional development of the Eskay Rift, with no genetic relationship to the Nickel Mountain Gabbro Complex. Given the inferred ascent path of the parent magmas along areas of high structural permeability and the lack of upper age constraints on mineralization, there may be a close tectonic relationship between mineralization at the E&L deposit and the nearby Eskay Creek and Anyox volcanogenic massive sulfide (VMS) deposits.

Table of Contents

Title Page	i
Abstract.....	ii
Table of Contents	iii
List of Figures.....	vi
List of Tables	viii
List of Abbreviations	ix
Acknowledgements	xi
1. Introduction.....	1
2. Background	3
2.1. Regional Geology	3
2.2. Local Surface Geology	5
2.3. Orebody Geology	9
2.4. Exploration History	13
2.5. Previous Studies of the E&L Ni-Cu (PGE) Deposit	15
3. Samples and Analytical Methods	17
3.1. Samples.....	17
3.2. Petrography.....	17
3.3. Scanning Electron Microscopy.....	19
3.4. Laser Ablation ICP-MS of Sulfides	19
3.4.1. <i>General Overview</i>	19
3.4.2. <i>Test Analyses and Calibration</i>	20
3.4.3. <i>Data Reduction</i>	22
4. Results	26
4.1. Petrography and Scanning Electron Microscopy	26
4.1.1. <i>Spatsizi Formation Pyritic Mudstone</i>	26
4.1.2. <i>Upper Chamber</i>	28
4.1.3. <i>Lower Chamber</i>	32

4.1.4. <i>Massive Sulfides: The Lower Discovery Zone and Northeast Zone</i>	36
4.2. Trace and Platinum Group Mineral Mineralogy	44
4.3. LA-ICP-MS Pb Isotope Analysis of Sulfide Minerals	44
4.3.1. <i>Lower Discovery Zone</i>	49
4.3.2. <i>Northeast Zone</i>	53
4.3.3. <i>Upper Chamber</i>	53
4.3.4. <i>Lower Chamber</i>	54
4.3.5. <i>Hazelton Group</i>	54
5. Discussion.....	58
5.1. Insights from Sulfide Petrology.....	58
5.1.1. <i>Deformation within the Massive Sulfide Orebodies</i>	58
5.1.2. <i>Distribution of Trace Mineralogy in the Lower Discovery Zone</i>	60
5.1.3. <i>Origin of the Peculiar Magnetite Textures</i>	64
5.2. Insights from Pb Isotopic Analysis of Sulfide Minerals.....	69
5.2.1. <i>Source of Mineralization and Effect of Crustal Assimilation on the Isotopic Signatures of Sulfides</i>	69
5.2.2. <i>Crystallization History of Sulfides and Potential Influence on Isotopic Compositions</i>	76
5.2.3. <i>Stratigraphic Variations in Pb Isotopic Compositions in the Lower Discovery Zone Orebody</i>	79
5.3. Synthesis.....	81
5.3.1. <i>Relationship Between the E&L Deposit and Other Deposits Within the Eskay Rift and the Surrounding Golden Triangle</i>	81
5.3.2. <i>Petrogenetic Constraints on Mineralization, the Host E&L Intrusion, and the Nickel Mountain Gabbro Complex</i>	83
5.3.3. <i>Comparisons with Other Magmatic Ni-Cu (PGE) Deposits and Implications for Prospectivity in Former Back-arc and Transtensional Settings</i>	91
6. Conclusions.....	96
6.1. Recommendations for Future Work	98
Bibliography	101

Appendices.....111

Appendix A: Sample Scans, Thin Section Scans, Photomicrographs, and Thin Section Descriptions112

Appendix B: Backscattered Electron Photomicrographs and EDS Spectra of Select Platinum Group and Trace Minerals154

Appendix C: Supplementary Information for LA-ICP-MS Analysis of Sulfides166

List of Figures

Figure 2.1. Regional geologic setting of the E&L Deposit.....	4
Figure 2.2. Geologic Map of the Garibaldi Claim	7
Figure 2.3. Field photography from Nickel Mountain during the 2018 and 2019 field seasons	8
Figure 2.4. Geologic cross-sections of the E&L deposit	12
Figure 3.1. $^{208}\text{Pb}/^{206}\text{Pb}$ of the glass references NIST SRM 610, NIST SRM 612 and BCR2-G, and the polymetal sulfide pellet MASS-1 measured in this study	24
Figure 3.2. $^{207}\text{Pb}/^{206}\text{Pb}$ of the glass references NIST SRM 610, NIST SRM 612 and BCR2-G, and the polymetal sulfide pellet MASS-1 measured in this study	25
Figure 4.1. Photomicrographs and backscattered electron (BSE) images of 19-EV-46-01 pyritic mudstone from the Spatsizi Formation.....	27
Figure 4.2. Ternary diagram for the classification of mafic rocks on the basis of modal mineralogy of gabbro samples from the Upper and Lower Chambers	29
Figure 4.3. Photomicrographs of representative textures and mineralogy within the Upper Chamber	30
Figure 4.4. Photomicrographs of representative textures and mineralogy within the Lower Chamber	34
Figure 4.5. Photomicrographs of representative textures and mineralogy within the Lower Discovery Zone.....	39
Figure 4.6. Photomicrographs of representative textures and mineralogy within the Northeast Zone.....	40
Figure 4.7. Backscattered electron images of non-PGM trace minerals associated with E&L base metal sulfides	45
Figure 4.8. Backscattered electron images of PGM trace minerals associated with E&L base metal sulfides	46
Figure 4.9. Analysis of E&L platinum group mineralogy	48
Figure 4.10. Concentration of Pb (ppm) vs. 2RSE % on $^{208}\text{Pb}/^{206}\text{Pb}$ determined by split-stream LA-ICP-MS	50
Figure 4.11. Diagram of $^{208}\text{Pb}/^{206}\text{Pb}$ vs. $^{207}\text{Pb}/^{206}\text{Pb}$ determined by LA-ICP-MS for sulfide minerals from the E&L deposit.....	56
Figure 4.12. Diagram of $^{208}\text{Pb}/^{206}\text{Pb}$ vs. $^{207}\text{Pb}/^{206}\text{Pb}$ determined by LA-ICP-MS for sulfide minerals from the E&L deposit sorted by zone	57

Figure 5.1. Schematic diagram of the Lower Discovery Zone illustrating variations in the trace mineralogy with stratigraphic position in the sulfide orebody.....	61
Figure 5.2. Stratigraphic variations in Au, Ag, Zn, and IPGE (Os, Rh, Ru, Ir) concentrations within the Lower Discovery Zone for borehole EL-19-48	62
Figure 5.3. Stratigraphic variations in Au, Ag, Zn, and IPGE (Os, Rh, Ru, Ir) concentrations within the Lower Discovery Zone for borehole EL-19-53	63
Figure 5.4. Schematic diagram illustrating the potential origin of the “pseudo-cuneiform” magnetite in the Lower Discovery Zone.....	66
Figure 5.5. Plot of $^{208}\text{Pb}/^{206}\text{Pb}$ vs. $^{207}\text{Pb}/^{206}\text{Pb}$ comparing the LA-ICP-MS isotopic compositions of E&L sulfides with age-corrected fields for back-arc basin basalts, the Wrangellia large igneous province, Pacific Ocean MORB, and island arc basalts	70
Figure 5.6. Plot of $^{208}\text{Pb}/^{206}\text{Pb}$ vs. $^{207}\text{Pb}/^{206}\text{Pb}$ comparing the LA-IC-MS isotopic compositions of E&L sulfides with the plumbotectonics growth curves of Zartman and Haines (1988) and potential reservoirs that could produce the observed isotopic ratios in sulfides	71
Figure 5.7. Plot of $^{208}\text{Pb}/^{206}\text{Pb}$ vs. $^{207}\text{Pb}/^{206}\text{Pb}$ showing petrogenetic processes and mixing arrays between end members	75
Figure 5.8. Diagram of $^{208}\text{Pb}/^{206}\text{Pb}$ vs. $^{207}\text{Pb}/^{206}\text{Pb}$ for sulfides from the Lower Discovery Zone	78
Figure 5.9. Stratigraphic variations in modal percentage-corrected average $^{208}\text{Pb}/^{206}\text{Pb}$ and $^{207}\text{Pb}/^{206}\text{Pb}$ for borehole EL-19-53.....	80
Figure 5.10. Plot of $^{208}\text{Pb}/^{206}\text{Pb}$ vs. $^{207}\text{Pb}/^{206}\text{Pb}$ comparing the isotopic compositions of E&L sulfides with nearby deposits in the Golden Triangle.....	82
Figure 5.11. Extended primitive mantle-normalized trace element patterns and chondrite-normalized REE patterns for the average concentrations of E&L intrusion, Nickel Mountain Gabbro and Group 1 and 2 Hazelton Group basalts	84
Figure 5.12. Trace element diagrams illustrating the geochemical variations in the E&L intrusion, Nickel Mountain Gabbro and Group 1 and 2 Hazelton Group basalts.....	85
Figure 5.13. Schematic E-W cross-section illustrating the geodynamic setting of the Stikinia microplate ca. 190 Ma.....	88
Figure 5.14. Schematic NE-SW cross-section illustrating the proposed post-subduction geodynamic setting of accreted inboard terranes and the Eskay Rift at ca. 180-175 Ma.	89
Figure 5.15. Schematic cross section through a hypothesized E&L magmatic plumbing system hosted in a sinistral-shear transtensional setting.....	90

List of Tables

Table 2.1. Exploration history of the E&L deposit.....	14
Table 3.1. Summary of samples analyzed in this study	18
Table 3.2. Laser and ICP-MS setup	21
Table 4.1. Comparisons of the Lower Discovery Zone and the Northeast Zone.....	37
Table 4.2. Mineralogy of the E&L base metal sulfides	47
Table 4.3. Summary of LA-ICP-MS Pb isotopic compositions of sulfide minerals from the E&L deposit	51
Table 5.1. Summary of end-members used in E&L mixing modelling.....	73
Table 5.2. Comparison of the E&L deposit with selected Ni-Cu (PGE) deposits hosted in convergent margin and collisional environments	93

List of Abbreviations

Minerals		Abbr.	Description
Abbr.	Description		
Ag-Pn	Ag-pentlandite	Tapl	telargpalite
Alt	altaite	Te	native tellurium
Amph	amphibole (uralite)	Tlc	talc
Cal	calcite	T-Pn	tarnished pentlandite (violarite)
Ccp	chalcopyrite	Ttm	titanomagnetite
Co-Pn	cobaltpentlandite	Vio	violarite
Cpx	clinopyroxene	Geochemistry and Analytics	
Elec	electrum	AFC	assimilation-fractional crystallization
Ep	epidote	BABB	back-arc basin basalts
Gal	galena	BSE	backscattered electron
Hs	hessite	cm	centimeter
Mer	merenskyite	DM	depleted mantle
Mich	michenerite	EDS	energy-dispersive X-ray spectroscopy
Mon	moncheite	EM-I	enriched mantle-I
Mt	magnetite	EM-II	enriched mantle-II
Ol	olivine	Fo	forsterite number
Pd-mel	Pd-melonite	HSE	highly siderophile elements
PGM	platinum group mineral	HSFE	high field strength elements
Plag	plagioclase	HREE	heavy rare-earth elements
Pn	pentlandite	HR-SF-ICP- MS	high resolution-sector field- inductively coupled plasma- mass spectrometer
Pn (F)	flame pentlandite	Hz	hertz
Po	pyrrhotite	IAB	island arc basalts
Pt-mer	Pt-merenskyite	IPGE	iridium platinum group elements
Py	pyrite	iss	intermediate solid-solution sulfide
Qtz	quartz	J	joule
Rh-mon	Rh-moncheite	km	kilometer
Sb-Spy	Sb-sperrylite		
Ser	sericite		
Sph	sphalerite		
Spy	sperrylite		
Srp	serpentine		
Sul	sulfide minerals		

Abbr.	Description
LA-ICP-MS	laser ablation-inductively coupled plasma-mass spectrometer
LC	lower crust
LREE	light rare earth elements
m	meter
Ma	million years, million years ago
mm	millimeter
MORB	mid-ocean ridge basalt
mss	monosulfide solid-solution
nm	nanometer
OIB	ocean island basalts
OR	orogene
oxygen fugacity	fO_2
PGE	platinum-group elements
PMORB	Pacific Ocean MORB
PPL	plane-polarized light
ppm	parts per million
Quad	quadrupole
REE	rare earth elements
(2)RSE	relative standard error
s	seconds
SEM	scanning electron microscope
SSB	sample standard bracketing
TE	trace element
ID-TIMS	isotope dilution-thermal ionization mass spectrometry
XPL	cross-polarized light
UC	upper crust
μ	$^{238}\text{U}/^{204}\text{Pb}$

Abbr.	Description
μm	micrometer or micron
ω	$^{232}\text{Th}/^{204}\text{Pb}$
Reference materials and institutes	
NIST	National Institute of Standards and Technology, USA
SRM	standard reference material
USGS	United States Geological Survey
E&L deposit, Eskay Camp, and North American Cordillera	
BC	British Columbia
CCT	Cache Creek Terrane
CPC	Coast Plutonic Complex
EC	Eskay Creek
HG	Hazelton Group
KSM	Kerr-Sulphurets-Mitchell
LC	Lower Chamber
LDZ	Lower Discovery Zone
NCVP	Northern Cordilleran Volcanic Province
NEZ	Northeast Zone
NMGC	Nickel Mountain Gabbro Complex
QN	Quesnellia
ST	Stikinia
UC	Upper Chamber
WR	Wrangellia
General abbreviations	
VMS	volcanogenic massive sulfide
VTEM	Versatile Time Domain Electromagnetics

Acknowledgements

First and foremost, I thank my supervisor, Dr. James S. Scoates, for his guidance, support, and feedback during the course of this thesis. It was truly an honour to conduct this project under his supervision. Thanks also to Dr. Dominique Weis for her advice on experimental design of the LA-ICP-MS analyses, and to Dr. Kenneth A. Hickey for his discussions regarding the solid-state deformation of sulfide minerals. I am also very grateful to Dr. Marghaleray Amini for her invaluable assistance and guidance with the LA-ICP-MS analyses and data processing, and to Jenni Lai and Lan Kato for their assistance with SEM analysis.

I express my deepest gratitude to Garibaldi Resources Corporation, especially Steve Regoci and Jeremy Hanson, for the funding, access to samples, and approval necessary to conduct this project. This thesis would not exist if it were not for their support. I would also like to acknowledge all of the staff and coworkers up at the Garibaldi camp during the summer of 2019 for their impeccable work and for a great field season. Insight provided throughout the course of this project by Dr. Peter C. Lightfoot is also greatly appreciated. I also thank Russell Ashton (UWO) for his correspondence, words of wisdom, and sharing in the burden of trying to figure out how this fascinating deposit formed.

To my friends, most notably Dylan Spence, Lars Gibbard, Connor Lyons, Sydney Kaoira Hampson, Andrea Sanlorenzo, Adam Faridz, and Abigail Fraser: thanks for all the adventures and for making the past few years the most enjoyable so far. To my parents and brother: thanks for all your support in helping me to achieve my dreams and for never ceasing to believe in me. Last, but certainly not least, to my girlfriend Esther Sentoso: thank you for everything – your understanding, your companionship, and for staying with me through thick and thin.

This project was funded by Garibaldi Resources Corporation, with additional funds provided by a SEG Canada Foundation Student Research Grant to Eric Vandenburg in 2019.

1. Introduction

Exploration for magmatic Ni-Cu (PGE) deposits has been focused within the boundaries of Archean to Paleoproterozoic cratons and within the Mesoproterozoic to Phanerozoic large igneous provinces adjacent to these cratons (Arndt *et al.*, 2006; Barnes *et al.*, 2016). While many major deposits are hosted in these intraplate settings, whether they be komatiite associated (Kambalda, Mount Keith, Raglan, Dundonald), intraplate-rifting related (Noril'sk-Talnakh, Pechenga, Duluth, Eagle, Voisey's Bay), or bolide impact related (Sudbury), there has been a significant deficit in research and exploration for deposits in convergent margin settings, particularly with respect to former back-arc basins (Naldrett, 2004; Manor, 2014). Despite the association of PGE mineralization with Alaskan-type ultramafic complexes in convergent settings (Turnagain, Tulameen), their prospectivity for significant high-grade base metal sulfide mineralization remains low compared to the typical conduit and chonolith-hosted styles of magmatic sulfide mineralization (Nixon *et al.*, 1997; Ripley, 2010). However, significant deposits have been found within former convergent margin settings, including Aguablanca, Spain; Kalatongke and Huangshandong, China; and Kotalahti, Finland (Manor, 2014). Within the Canadian Cordillera, only two significant deposits of magmatic massive Ni-Cu (PGE) mineralization have been discovered: Giant Mascot, near Hope, British Columbia (Manor, 2014) and E&L, located north of Stewart, British Columbia near Eskay Creek.

Isotopic geochemistry represents a valuable tool in studying the age, evolution and sources (magmas, fluids, metals) of ore deposits (Champion & Huston, 2016; Eglinton, 2018). The development of in situ analytical techniques for the measurement of isotopic ratios, most importantly laser ablation-inductively coupled plasma-mass spectrometry (LA-ICP-MS), has allowed for relatively rapid, time and cost-effective, and spatially precise analyses of geologic

materials (Darling *et al.*, 2012; Ver Hoeve *et al.*, 2018). For sulfides, LA-ICP-MS analysis enables the ability to resolve sub-grain scale variations in Pb isotopic ratios and it is possible to simultaneously measure trace element and isotopic compositions (Darling *et al.*, 2012). The Pb isotope system is one of the most powerful isotope systems in the geochemical toolkit for constraining igneous processes, including crustal contamination, source characterization and magma mixing (Weis, 2016b). The product of three decay schemes, this isotope system is unique with three radiogenic isotopes (^{238}U decays to ^{206}Pb , ^{235}U decays to ^{207}Pb and ^{232}Th decays to ^{208}Pb) and one stable isotope, ^{204}Pb (Weis, 2016b; Halla, 2018). The product of decay chains. U and Th are lithophile elements, whereas Pb behaves as a chalcophile element within the crust (Weis, 2016a). As a result, Pb will partition into an immiscible sulfide melt rather than remain in the silicate magma during the genesis of a Ni-Cu-PGE deposit (Darling *et al.*, 2012). The sulfide minerals will record isotopic ratios close to their initial values at crystallization, providing important insights into their source composition.

This study focuses on the sulfide and silicate petrology, platinum group mineralogy, and lead isotope systematics of Ni-Cu-PGE mineralization associated with the E&L intrusion of the Nickel Mountain Gabbro Complex, located within the former back-arc setting of the Eskay mining camp in northwestern British Columbia. No historical mining activity has taken place at the deposit and its characteristics remain relatively poorly understood owing to the early stage in the exploration timeline and the lack of adequate scientific research. The focus of this thesis is to highlight the petrogenetic processes of the ore system, to constrain its source, and to provide insight into the possibility for future Ni-Cu-PGE exploration targets in former back-arc transtensional settings in the Canadian Cordillera and around the world.

2. Background

2.1. Regional Geology

The E&L Nickel Mountain property is located within the Eskay Camp in the Intermontane Belt of the Canadian Cordillera (Fig. 2.1.) (Colpron *et al.*, 2007). The deposit lies within the northern portion of the Stikinia Terrane, which forms a northwest-trending belt extending from the southern Yukon to south-central British Columbia that is composed of late Paleozoic to early Mesozoic island arc volcanics and related intrusions (Gabrielse *et al.*, 1991; Ash *et al.*, 1995). A broad region of uplift formed during the accretion of Stikinia known as the Stikine Arch and is responsible for much of the topography within the region. The dominant rocks of Stikinia in the Eskay Camp consist of the Upper Paleozoic Stikine assemblage, the Upper Triassic Stuhini Group, and Lower to Middle Jurassic Hazelton Group and their associated calc-alkaline to alkaline intrusions (Ash *et al.*, 1995).

The Stikine assemblage, deposited from the Devonian to the Permian, consists of tholeiitic to calc-alkaline, mafic to bimodal flows, and volcanoclastic rocks interbedded with carbonate, minor shale, and chert (Logan *et al.*, 2000, Alldrick *et al.*, 2004). The Stikine assemblage is unconformably overlain by the Stuhini Group, which consists of Lower to Middle Triassic sediments and Upper Triassic submarine basalt-andesite flows and volcanic breccias. An angular unconformity separates the Stuhini and Hazelton Groups, where the character of the volcanic rocks transitions from subaqueous to subaerial. The basal Jack Formation is composed of sandstones, polymict conglomerates, siltstones, and shales, as well as a minor volcanoclastic component (Nelson, *et al.*, 2018). Overlying the Jack Formation is the Betty Creek Formation, which consists of andesitic to dacitic volcanic rocks and sedimentary rocks. Above this is the Eddontenajon Formation, which consists of mafic to felsic flows and volcanoclastic rocks. This is

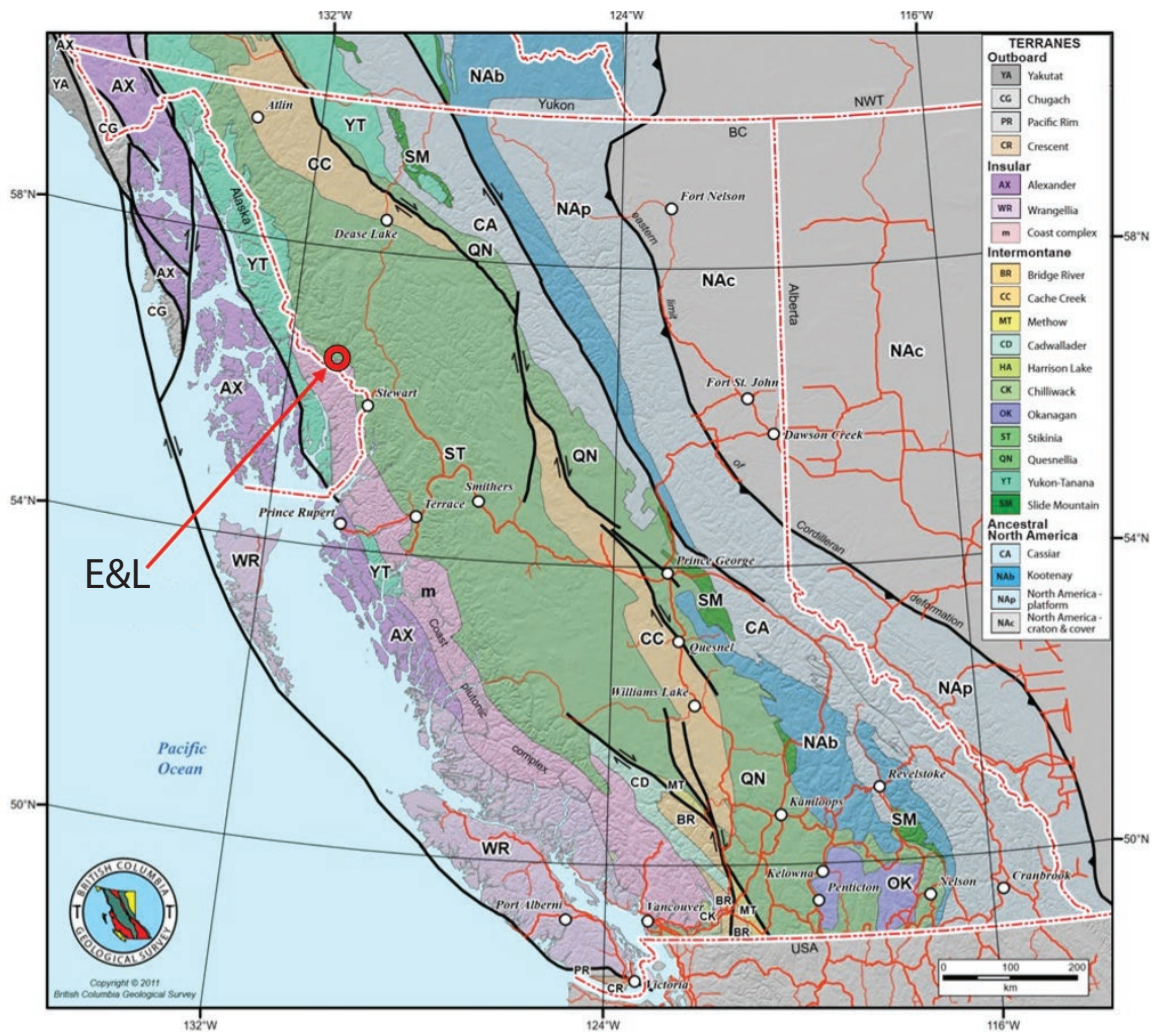


Figure 2.1. Regional geologic setting of the E&L Deposit. Based on Nelson & Kyba (2014).

in turn overlain by the clastic sediments and limestones of the Spatsizi Formation. The uppermost formation of the Hazelton Group is the Iskut River Formation, which consists of sedimentary rocks and bimodal volcanic rocks associated with the opening of the Eskay Rift system (Nelson, *et al.*, 2018).

The intrusions of the Texas Creek and Brucejack suites are cogenetic and coeval with the volcanic rocks of the Lower Hazelton Group and are interspersed throughout the region. The mid-Jurassic to mid-Cretaceous Bowser Basin is located south of the Stikine Arch and records marine and non-marine clastic sedimentation during the amalgamation of the Intermontane Terranes (Logan *et al.*, 2000). Peak metamorphism of prehnite-pumpellyite to lower greenschist facies was attained during the mid-Cretaceous, likely coeval with the formation of the Skeena fold-and-thrust belt (Alldrick *et al.*, 2004).

2.2. Local Surface Geology

The E&L deposit is located on the southwestern flank of Nickel Mountain, 18 km southwest of the Eskay Creek Mine, with the orebody outcropping at elevations between 1842-1892 m above sea level (Fig. 2.2.). Located on the side of the E&L glacier, recent glacial retreat has allowed for a better understanding of the surficial geology of the deposit. The local geology consists of northeast-trending, gently northwest-dipping mudstones and siltstones the Iskut River Formation (Toarcian age). Volcanic rocks of the Betty Creek Formation are present at the base of the mountain (Hancock, 1990). These sedimentary rocks are intruded by four 100 m-wide plugs and one 800 m-wide stock assigned to the Nickel Mountain Gabbro Complex. The Nickel Mountain Gabbro Complex consists of Fe-Ti oxide-bearing equigranular gabbro with minor

local norite, exhibiting greenschist facies metamorphism, propylitic, and potassic alteration (Russell Ashton, pers. comm., July 18, 2019). Plagioclase has been variably sericitized and minor replacement of mafic minerals by chlorite is common. Within the Nickel Mountain Gabbro Complex is a small intrusion known as the E&L intrusion, which consists of orbicular, stellate, and variable-textured Fe-Ti oxide-bearing olivine melagabbros, gabbro-norites, and gabbros collectively referred to as “taxitic,” along with minor wehrlite (Russell Ashton, pers. comm., July 18, 2019; Peter Lightfoot, pers. comm., June 11, 2019). The rocks of the E&L intrusion host disseminated and net-textured sulfides (pyrrhotite + pentlandite + chalcopyrite + magnetite) and are therefore believed to be the source of the massive sulfide deposit (Peter Lightfoot, pers. comm., June 11, 2019). Outcrops of massive and semi-massive sulfide are found within hornfelsed and altered sedimentary rocks at the contacts with taxites. The E&L intrusion has been subjected to the same alteration as the Nickel Mountain Gabbro Complex.

The transtensional structures of the Eskay Rift, which transects the property, is considered to have played a role in the intrusion of the parent magmas of E&L and the Nickel Mountain Gabbro Complex, likely triggering decompression melting and creating the accommodation space required for intrusion (Peter Lightfoot, pers. comm., June 11, 2019). Both intrusions predate regional deformation and are cross-cut by post-tectonic mafic and lamprophyre dikes. North-northwest of the mountain, the Iskut River Formation is truncated by the Jurassic Lehto Porphyry pluton, which consists of variably altered, alkali feldspar-megacrystic monzonite (Hancock, 1990). Deformation in the region is dated at ~110 Ma and is expressed by shortening along a northeast axis, a weak penetrative axial cleavage within sedimentary rocks, and block faulting within volcanic units (Alldrick *et al.*, 1987; Hancock, 1990). To the south of the mountain, the Cone Glacier volcano (part of the Iskut-Unuk River

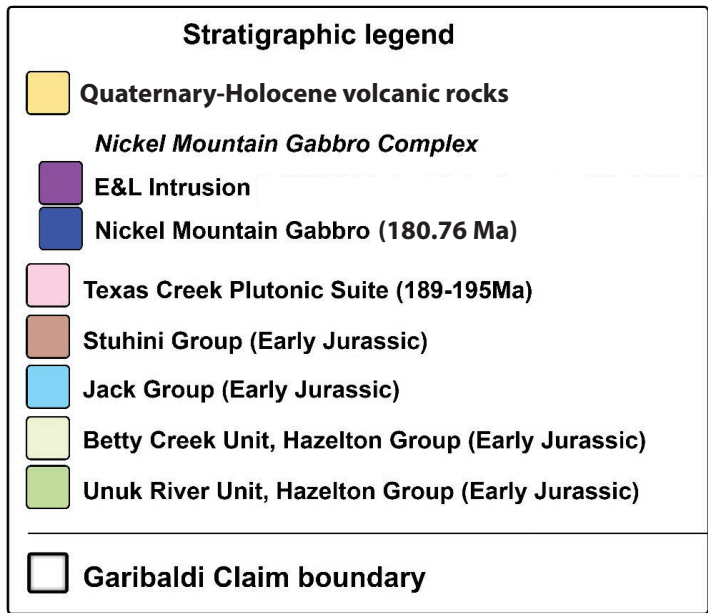
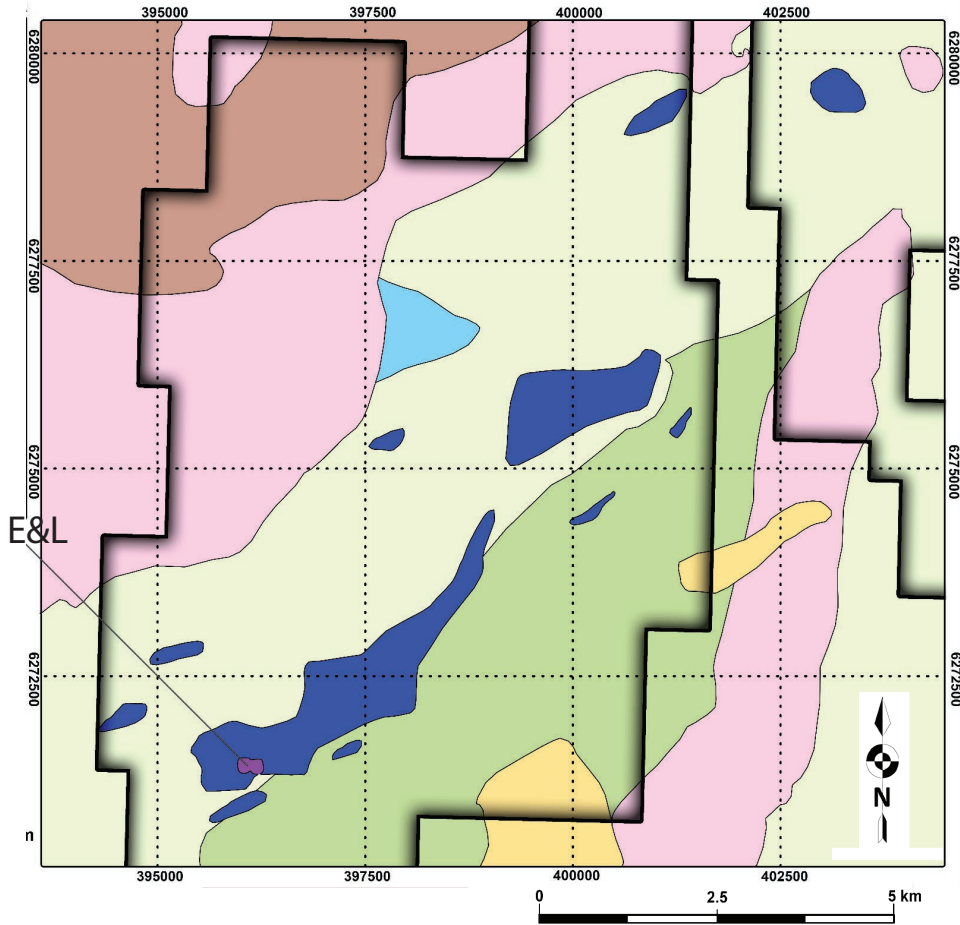


Figure 2.2. Geologic map of the Garibaldi Nickel Mountain Claim. Modified from Lightfoot *et al.* (2019).

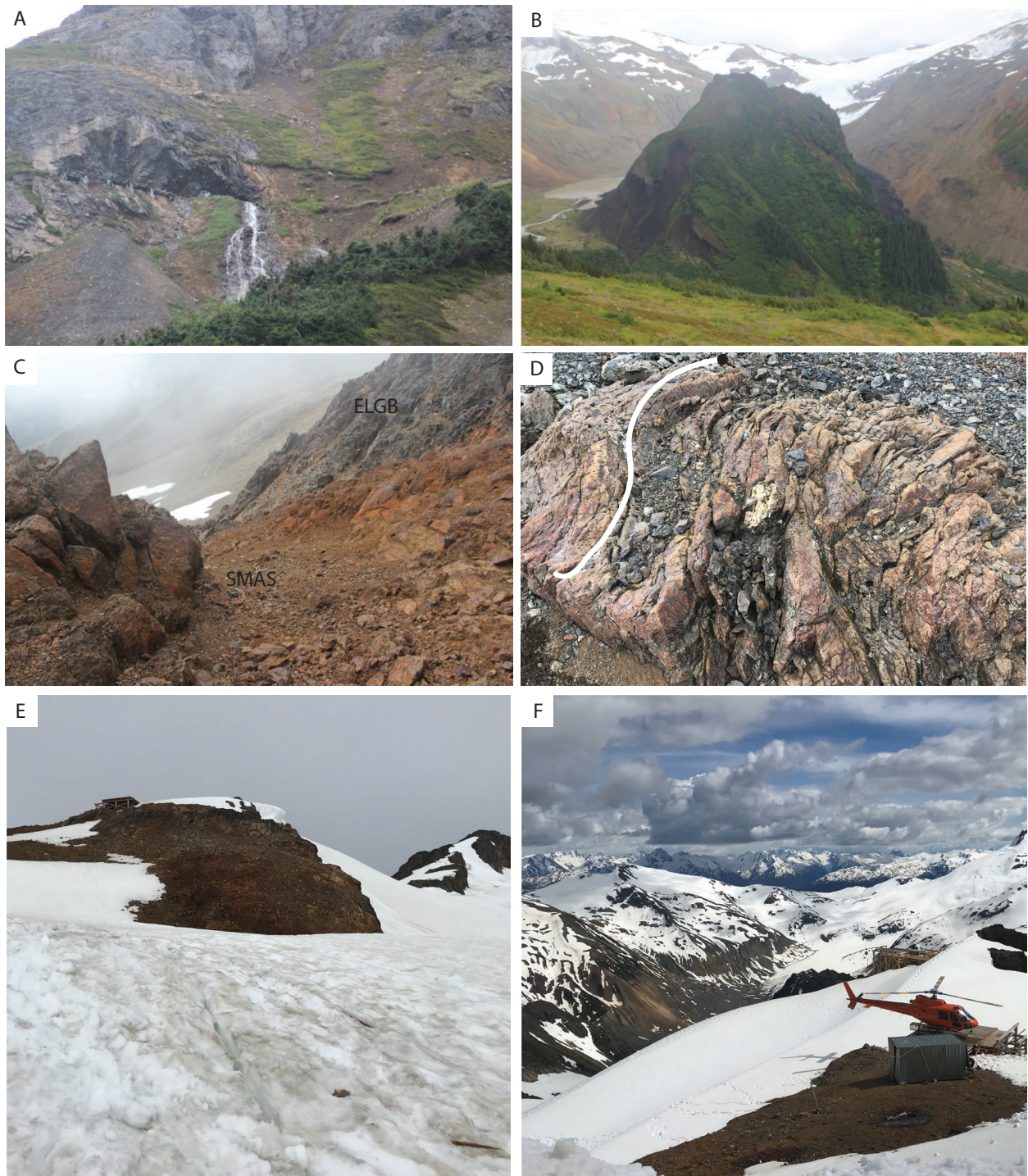


Figure 2.3. Field photography from Nickel Mountain during the 2018 and 2019 field seasons. A) The old Sumitomo mining adit and spoil dump at 1500 m elevation above sea level (masl); tunneling of the adit stopped short of reaching massive sulfide. B) The Quaternary Cone Glacier volcano from the southern flank of Nickel Mountain. C) Contact in the Gully Zone between gossanous semi-massive sulfide (SMAS) and unmineralized to sparsely mineralized E&L Gabbro (ELGB). D) Diabase dyke on a ridge near Anomaly C, to the west of the toe of Copper King glacier. Note that the interior of the dike is folded, however the contacts are not. E) View of the Crevasse Zone mineralization from the E&L glacier. F) View from the top of the ridge at Nickel Mountain, highlighting the glaciated topography of the locality. Photographs A), B) and C) courtesy of Peter Lightfoot.

cones) records Quaternary-Holocene subglacial and subaerial volcanism in the form of plagioclase- and olivine-phyric basalt flows. This volcanism is associated with the Northern Cordillera Volcanic Province and likely exploited the long-lived structural weaknesses close to the E&L intrusion (Fig. 2.3. B) (Hauksdóttir *et al.*, 1994; Nelson, 2017).

The two intrusions are mineralogically and geochemically distinct (Russell Ashton, pers. comm., July 18, 2019). The E&L gabbros contain olivine of FO_{78-84} , indicating that the parent magma was likely a high-magnesium tholeiitic magma (Peter Lightfoot, pers. comm., June 11, 2019). Olivine is also strongly depleted in Ni and Co, consistent with the partitioning of these elements into a sulfide melt (Peter Lightfoot, pers. comm., June 11, 2019). The Nickel Mountain Gabbro Complex and E&L intrusions may reflect separate pulses of magma, rather than differentiates. Major element geochemistry suggests different differentiation trends for the E&L and Nickel Mountain Gabbro Complex intrusions (Peter Lightfoot, pers. comm., June 11, 2019). Primitive mantle-normalized trace element plots suggest different sources for the two intrusions. The E&L intrusion has trace element concentrations that are closer to primitive mantle values than the Nickel Mountain Gabbro Complex intrusion, suggesting that the latter represents a more evolved magma. Both series exhibit decoupled LILE-HSFE patterns and the Nb-Ta troughs characteristic of subduction zone-derived magmas (Peter Lightfoot, pers. comm., June 11, 2019).

2.3. Orebody Geology

The E&L deposit consists of four different styles of sulfide mineralization: disseminated (blebby), semi-net to net-textured, semi-massive, and massive sulfide. There are four main

massive sulfide orebodies currently known: the Northeast Zone, the Northwest Zone, the Upper and Lower Discovery Zones and the Crevasse Zone (Fig. 2.4.).

Disseminated sulfide mineralization is associated with taxitic and orbicular olivine gabbros that define the Upper Chamber above the Northeast, Discovery and Crevasse Zones. This style of mineralization is characterized by 1-25 vol% irregular blebby to locally interstitial sulfides (typically Po>Ccp>Pn). Higher modal percentages of sulfides are typically associated with larger, better-developed orbicules and higher modal percentages of olivine (Russell Ashton, pers. comm., July 18, 2019). Chalcopyrite is typically at the top of the blebs, with pentlandite and pyrrhotite at the bottom, providing a useful geopetal indicator. Minor platinum group minerals can be found within these sulfides (Russell Ashton, pers. comm., July 18, 2019). Disseminated sulfides (albeit rare) also occur within mixed zones between the E&L gabbro and sedimentary rocks, likely reflecting the in-situ scavenging of sulfur from the country sediments to produce sulfide droplets (Russell Ashton, pers. comm., July 18, 2019). With the exception of the orbicular-textured silicates, the style of sulfide mineralization is remarkably similar to the disseminated sulfides found within the Talnakh taxites at Noril'sk (Peter Lightfoot, pers. comm., June 11, 2019).

Semi-net to net-textured sulfide mineralization is mostly found within the Lower Chamber, which is located below all currently known massive sulfide orebodies and is separated by a mudstone interval. This mineralization style is characterized by a semi-continuous to continuous matrix of sulfides (typically >5 modal %) containing a framework of olivine oikocrysts with minor plagioclase chadacrysts (Barnes *et al.*, 2018).

Semi-massive sulfide mineralization occurs along the fringes of the massive sulfide orebodies. Most silicate inclusions within this style of mineralization consist of recrystallized

country rock, rather than gabbro. Some of the hanging wall contacts with the massive sulfide orebodies consist of semi-massive sulfides with gabbro inclusions. The modal percentage of sulfide ranges between 20 and 90% (Barnes *et al.*, 2018). Some of this semi-massive sulfide appears to have formed by the infiltration of sulfide melt into cracks in the country rock.

Massive sulfide mineralization exhibits a wide range of compositions and textures and is defined by a modal percentage of greater than 90% sulfide. As noted above, the massive sulfide mineralization makes up four main orebodies, with two minor surficial orebodies. The main sulfide minerals in massive sulfide intervals are pyrrhotite, chalcopyrite, and pentlandite. Magnetite is also present and locally is a major phase. Pyrrhotite is the most abundant mineral within the massive sulfides. The abundance of chalcopyrite and pentlandite is variable, with some intervals having more chalcopyrite than pentlandite and vice versa. Some supergene and hypogene alteration have occurred, as evidenced by the replacement of pentlandite by violarite (Hancock, 1990; Russell Ashton, pers. comm., July 18, 2019). The main textures within the massive sulfide intervals are regular and strained loop textures, as well as “leopard print” massive sulfide. Some intervals exhibit deformation in the form of remobilized chalcopyrite. The orebodies exhibit typical fractionation patterns, with Cu-, Pt-, Pd- and Au- rich upper portions. PGM comprise <1 modal % of the massive sulfide, and most of these PGM are tellurides. Minor electrum, sphalerite, gold, vein-controlled calcite, and pyrite are also found within the orebodies.

The Lower Discovery Zone is currently the largest of the massive sulfide orebodies and is believed to follow the taxite-mudstone contact. Within this zone, Ir-platinum group elements concentrations increase towards the middle of the interval, with high concentrations associated with magnetite (Peter Lightfoot, pers. comm., June 11, 2019; Russell Ashton, pers. comm., July

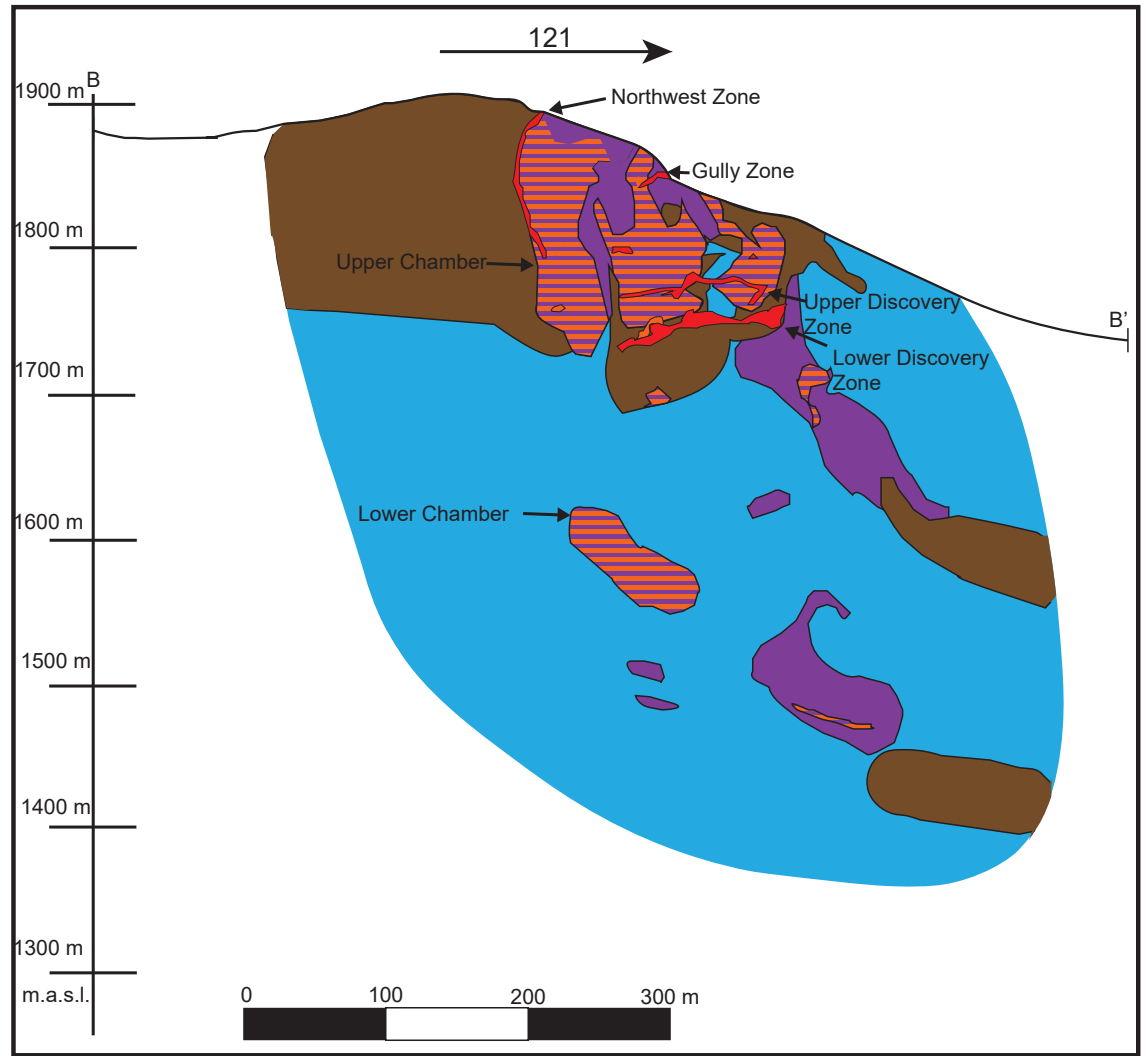
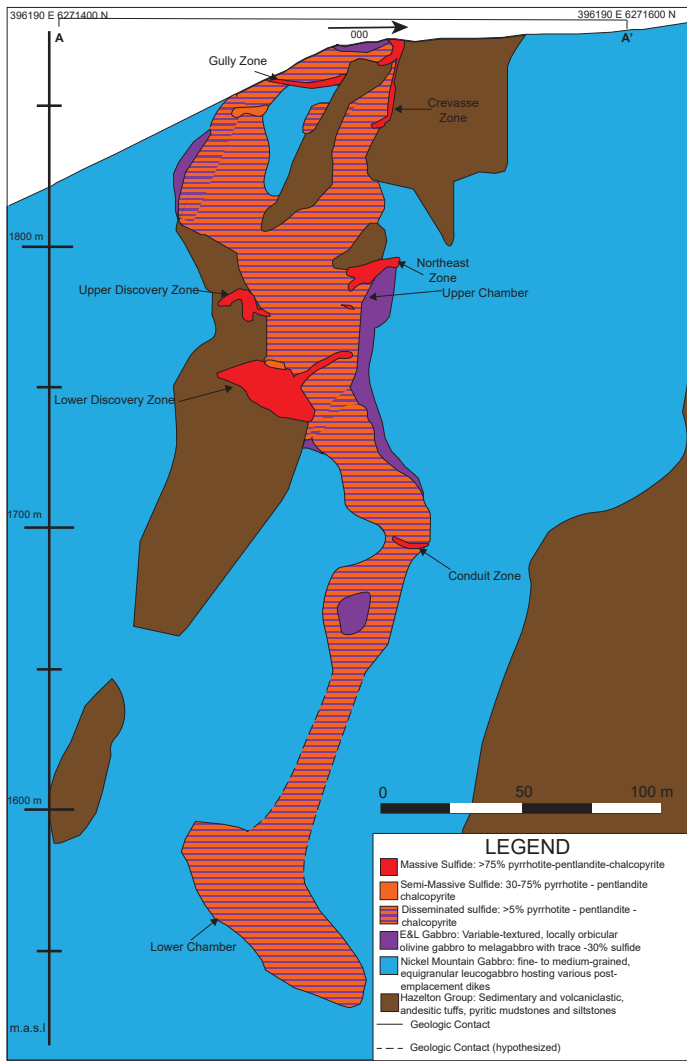


Figure 2.4. Geologic cross-sections of the E&L deposit (modified and redrawn from Garibaldi Resources Corporation, 2020).

18, 2019). Most pentlandite within this zone is granular, with a very low percentage of flame pentlandite. Magnetite shows strong resorption patterns.

A substyle of massive sulfide mineralization is described by Ashton (pers. comm.) as “contact massive sulfide.” This substyle is present in the Northeast Zone orebody. It is similar to regular massive sulfide in terms of major sulfide, oxide and PGM mineralogy, but has less resorbed magnetite, violarite alteration and more flame pentlandite (Russell Ashton, pers. comm., July 18, 2019).

2.4. Exploration History

Nickel-copper sulfide mineralization on Nickel Mountain was first discovered in 1958 by prospectors Ed and Lela Freeze while working on the property for the BIK syndicate (Silver Standard Mines Limited, Kerr-Addison Gold Mines Limited and McIntyre – Porcupine Mines Limited). From 1965-1966, Silver Standard followed up on this discovery with an exploration program comprised of geological mapping, geochemical sampling, hand trenching, and X-ray drilling totaling 487 m over 12 holes (Hedley, 1965).

In 1970, Silver Standard optioned the property to Sumitomo. Sumitomo subsequently launched an extensive exploration program from 1970-1971, including the construction of a 450 m-long exploration adit (Fig. 2.3. A) at 390 m below the surficial mineralized zones and underground drilling of 11 diamond drill holes totaling 2,240 m.

Following the work by Sumitomo, the property was mostly dormant. From 1986 to 2011, a wide range of exploration work was completed (Table 2.1.). The most significant activity during this period was by Lexington Resources Ltd. in 1990 and consisted of sampling,

Table 2.1. Exploration history of the E&L deposit.

Date	Activity	Owner
1958	Nickel-copper sulfide showings first discovered by Ed and Lela Freeze	
1965-1966	Surface exploration and drilling	Silver Standard Mines Limited
1966	Construction of Snippaker Creek Airstrip	
1967	Construction of tote road from airstrip to future location of adit	
1970	E&L property optioned to Sumitomo, construction of the adit	Sumitomo
1970-1971	Diamond drilling	
1972-1986	Property lays dormant	
1986-1987	Ground magnetometer, airborne magnetic and VLF electromagnetic surveys conducted by Western Geophysical Aero Data Ltd.	
1987	PGE analysis of trench samples	Silver Standard Mines Limited
1989	Fieldwork conducted by the BCGS (Hancock)	
1990	Fieldwork, drilling, geophysical surveys	Lexington Resources Limited
1991-2015	Property lays dormant	Silver Standard Mines Limited
2016	E&L and surrounding claims optioned to Garibaldi Resources Corporation, surface exploration	Garibaldi Resources Corporation
2016	DeCoors Mining options surrounding property to Garibaldi	
2017-Present	Exploration, drilling, geophysics of E&L and surrounding claims	

geophysical surveys and the diamond drilling of a 135 m-deep hole. The property was dormant again from 1991-2016, until Garibaldi Resources Corporation optioned the property.

In 2016 Garibaldi Resources launched an exploration program consisting of prospecting on the E&L property and channel sampling of the surficial massive sulfide outcrops. In 2017, a VTEM survey was completed, along with 3678.5 m of diamond drilling over 14 holes. Diamond drilling, mapping, geophysics, and sampling continued over the course of the 2018 and 2019 field seasons.

2.5. Previous Studies of the E&L Ni-Cu (PGE) Deposit

Unlike the nearby Eskay Creek deposit, few studies have been conducted on the E&L deposit since its discovery in 1958 and, as a result, the geological history and characteristics of deposit are poorly understood. Due to the inherent nature of the early stage exploration program, the structure of the deposit and the extent of mineralization have not been fully constrained. Sharp (1965) and Cabri (1966) completed the first scientific studies of E&L. The first major study was completed in 1990 by Kirk D. Hancock of the British Columbia Geological Survey and it consisted of petrography, structural analysis, and surficial mapping of the deposit. Hancock proposed an emplacement age of mineralization ranging from the mid-Jurassic to mid-Cretaceous and concluded that there was no link between the E&L intrusion and the nearby Coast Plutonic Suite.

No further scientific research was conducted on the deposit until 2017, when Garibaldi hired Dr. Peter Lightfoot as their technical advisor. Since then, Lightfoot has conducted significant research on the petrology, structure and geochemistry of the rocks that make up the

E&L deposit. Lightfoot (pers. comm., June 11, 2019) proposed that the E&L intrusion and related Nickel Mountain Gabbro Complex are associated with the Eskay Rift back-arc basin, and that transtension during the Jurassic generated the magmas that gave rise to the deposit. Since 2017, geochronology samples have been sent to Dr. Kevin Chamberlain at the University of Wyoming for U-Pb dating of zircon and baddeleyite within the E&L and Nickel Mountain gabbros. Previous work by Chamberlain (unpublished data) established a U-Pb age of 186.0 ± 2 Ma for the Nickel Mountain gabbro, which is consistent with the surrounding Hazelton Group strata (187.1 ± 1.9 Ma for the surrounding Betty Creek Formation rocks) (Cutts *et al.*, 2015). To date, no other radiogenic isotope research has been conducted on the deposit. Follow-up work by Dr. Chamberlain in 2020 established a Zircon CA-TIMS U-Pb age of 180.71 ± 0.37 Ma (Chamberlain, unpublished data).

At present, Russell Ashton is conducting an M.Sc. thesis at the University of Western Ontario on the genesis, petrography and major, minor and trace element geochemistry of the E&L deposit.

3. Samples and Analytical Methods

3.1. Samples

The samples analyzed in this study were collected during Garibaldi Resources Corporation's 2019 drilling program in the summer of 2019. Drill core from boreholes EL-18-24 and EL-18-30 from the 2018 drilling season and EL-19-46, EL-19-48, EL-19-53, and EL-19-54 from the 2019 drilling season were sampled using a diamond-bladed rock saw. The lithology, borehole ID, and depth intervals of 20 representative samples from the E&L deposit are indicated in Table 3.1. A total of 11 massive and semi-massive sulfide samples from the Lower Discovery Zone orebody were collected to examine if any chemical and isotopic heterogeneities exist within the main orebody. Two massive sulfide samples collected from the Northeast Zone orebody to compare isotopic ratios to those from the Lower Discovery Zone. Three melagabbro and two orbicular/taxitic gabbro samples were collected to examine the isotopic and chemical composition of sulfides within the Lower and Upper Chambers, respectively. In addition, one pyritic mudstone sample was collected from the Hazelton Group to examine the potential influence of crustal contamination on Pb isotopic ratios.

3.2. Petrography

Polished thin sections for 20 samples were prepared at Vancouver Petrographics Ltd. For petrographic analysis of samples, a Nikon Eclipse E600 POL polarizing microscope was utilized, with a Rebel EOS T21 camera mounted on the microscope for taking photomicrographs. An Epson Perfection 4490 PHOTO scanner was used to make scans of silicate thin sections in normal and cross-polarized transmitted light.

Table 3.1. Summary of samples analyzed in this study.

Sample Number	Lithology	Mineralization¹	Borehole	From (m)	To (m)
19-EV-24-01	Massive sulfide	M	EL-18-24	188.8	188.85
19-EV-24-02	Massive sulfide	M	EL-18-24	190.64	190.69
19-EV-30-01	Massive sulfide	M	EL-18-30	76.4	76.45
19-EV-30-02	Massive sulfide	M	EL-18-30	78.5	78.55
19-EV-46-01	Pyritic mudstone	-	EL-19-46	230.85	230.9
19-EV-48-01	Cpx-bearing semi-massive sulfide	S	EL-19-48	118.24	118.29
19-EV-48-02	Massive sulfide	M	EL-19-48	118.77	118.83
19-EV-48-03	Massive sulfide	M	EL-19-48	120	120.05
19-EV-48-04	Orbicular olivine gabbro	D	EL-19-48	106.34	106.39
19-EV-53-01	Orbicular olivine gabbro	D	EL-19-53	117.42	117.47
19-EV-53-02	Cpx-bearing massive sulfide	M	EL-19-53	132.12	132.17
19-EV-53-03	Magnetite-rich massive sulfide	Mmt	EL-19-53	133.56	133.61
19-EV-53-04	Massive sulfide	M	EL-19-53	142.85	142.9
19-EV-53-05	Massive sulfide	M	EL-19-53	144.75	144.8
19-EV-53-06	Massive sulfide	M	EL-19-53	146.83	146.88
19-EV-53-07	Massive sulfide	M	EL-19-53	148.5	148.55
19-EV-53-08	Orbicular olivine gabbro	D	EL-19-53	84.37	84.42
19-EV-54-01	Olivine melagabbro	D	EL-19-54	302.23	302.28
19-EV-54-02	Olivine melagabbro	SN-N	EL-19-54	310.19	310.24
19-EV-54-03	Olivine melagabbro	SN	EL-19-54	319.98	320.03

¹Abbreviations: D-disseminated sulfide, M-massive sulfide, S-semi-massive sulfide, Mmt- magnetite-rich massive sulfide, SN-semi-net textured sulfide, N-net-textured sulfide.

3.3. Scanning Electron Microscopy

The analysis of 15 carbon-coated thin sections was conducted at the Electron Microbeam and X-ray Diffraction Facility at the University of British Columbia (UBC) using a Philips XL30 electron microscope equipped with a Bruker Quantax 200 energy dispersion X-ray microanalysis system and an XFlash 6010 SDD detector. This technique was used to identify suitable areas for laser ablation analysis, image areas on the micrometer scale, and to aid in the identification of small sulfide mineral and platinum group mineral identification. EDS quantitative data was collected in order to plot PGM compositions on ternary diagrams.

3.4. Laser Ablation ICP-MS Analysis of Sulfides

3.4.1. General Overview

Trace element concentrations and lead isotope ratios of sulfide minerals (pyrrhotite, pentlandite, chalcopyrite, pyrite) were determined directly in thin section by LA-ICP-MS at the Pacific Centre for Isotopic and Geochemical Research (PCIGR), University of British Columbia (Vancouver, Canada). The analyses were conducted using a RESOLUTION M-50-LR (Applied Spectra) ArF excimer laser (Coherent COMPex Pro 110, 193 nm) connected to a split stream setup comprised of an Agilent 7700x quadrupole ICP-MS and a Nu Instruments Attom (Nu Instruments, Ltd.) single collector high-resolution sector field ICP-MS (HR-SF-ICP-MS). Trace element analyses were carried out on the 7700x, whereas Pb isotopes were measured using the Attom.

Spots of 89 μm diameter were ablated for 40 s at a repetition rate of 8 Hz, with an energy

density of $\sim 2 \text{ J/cm}^2$ on the sample. This was preceded by a short pre-ablation to remove surface contaminants and followed by 30 s washout time for background correction. Ablation was carried out under a He atmosphere where Ar served as the carrier gas and was admixed with N_2 for signal enhancement. The mass spectrometer was tuned for maximum sensitivity, low oxides, and mass bias. Oxides were monitored by ThO/Th and were consistently below 0.3%. Mass bias was monitored by U over Th and kept at $95\% <^{238}\text{U}/^{232}\text{U} < 105\%$. Laser ablation instrumentation, operating conditions and quantification methods are summarized in Table 3.2.

3.4.2. Test Analyses and Calibration

Analysis by laser ablation requires sample-standard bracketing using reference materials with a known composition to calibrate and calculate the concentrations or isotopic compositions of the unknown sample. The calibration standard should ideally match the concentration levels and matrix of the unknown samples and also needs to be homogeneous at the micron scale to yield high levels of accuracy. For the analysis of silicates, there are a number of synthetic and natural standards available, including NIST series standards and USGS reference glasses. Sulfides, however, can be problematic as they tend to melt during ablation and therefore do not ablate reproducibly (e.g., Fourny et al., 2020). The choice of an internal standard can also be challenging. For example, pyrite provides the choice of Fe and S to be used as internal standards, both of which are strongly interfered during ICP-MS analysis. There is no clear consensus with regards to an internationally certified sulfide reference material. The Canyon Diablo meteorite can be used as a standard, although it is more common to use powdered sulfide pellets, such as USGS MASS-1. The issues with this standard, however, include the fact that it does not ablate well, its relatively poor reproducibility, and its tendency to sputter during ablation. Recent

Table 3.2. Laser and ICP-MS setup.

Laser Ablation System			
Laser system	Resonetics RESolution M-50-LR Class I		
Ablation cell	Laurin 2-volume cell		
Laser wavelength	193 nm (Coherent COMPex Pro 110 ArF excimer laser source)		
Attenuation Factor	12%T		
Pulse duration	4 ns		
Carrier gas flow	He (0.8 L/min)		
ICP-MS parameters (Pb isotopes)			
Model	Nu Instruments Attom HR-ICP-MS		
RF power	1300 W		
Gas flows:			
Cooling gas	13 L/min		
Auxiliary gas	0.9 L/min		
Argon nebulizer	1.20L/min		
Instrument resolution	300		
ThO/Th ratio	< 0.6%		
ICP-MS parameters (trace elements)			
Model	Agilent 7700x quadrupole ICP-MS		
RF power	1350 W		
Gas flows:			
Cooling gas	13L/min		
Auxillary gas	1L/min		
Argon nebulizer	1.20L/min		
ThO ⁺ /Th ⁺	< 0.3%		
²³⁸ U/ ²³² Th ratio	95%-105%		
Data acquisition parameters - spot analysis			
Laser spot size	34 μm		
Laser energy density at sample	2J/m ²		
Repetition rate	8 Hz		
Fluence	2J/cm ²		
Acquisition mode	Time resolved		
Mass sweep time	200 μs (Pb isotope ratios)		
Analysis time	70 s: 30 s gas blank, 40 s of ablation		
Quantification			
Calibration standards:	NIST	SRM610	glass
1) Pb isotope ratios	NIST	SRM610	glass
2) Trace elements	Igor Pro™ Iolite extension (Paton <i>et al.</i> , 2011)		
Data processing			

studies suggest the use of nanopowder pellets that show improved ablation characteristics (Garbe-Schönberg and Müller, 2014). Hence, the standard FeS-1 with values from UQAC (Savard *et al.*, 2018) was used here as a quality control monitor for the trace element analyses.

During the analyses conducted for this study, the measured Pb isotope ratios were well-matched to the values for reference materials, however, the accuracy of the trace element concentrations was not satisfactory. With the exception of GSE-1G, carryover and cross-contamination were determined not to be significant. Before the analysis of the planned spots, testing on untargeted areas was conducted. This testing revealed that ^{56}Fe and ^{57}Fe were not suitable internal standard elements (e.g., interference with $^{10}\text{Ar}^{16}\text{O}$) and that NIST 610, NIST 612, and BCR2-G were not ideal primary calibration materials as they did not yield an accurate value for GSE-1G, which has a concentration level closest to the unknowns. Accurate values were obtained for the reference materials themselves (with the exception of GSE-1G) when using ^{29}Si as the internal standard (and also ^{57}Fe), however, confidence in the accuracy of the results for the unknowns required an accurate value for GSE-1G to be achieved. As a result, further testing was conducted using the FeS-1 material proposed by UQAC.

3.4.3. Data Reduction

Calibration was carried out by standard-sample bracketing using the synthetic silicate glass NIST SRM 610 as the external standard and ^{56}Fe as the internal standard for trace element analyses using values obtained from default values for pyrrhotite, chalcopyrite, pentlandite, pyrite, and violarite. For the analysis of Pb isotopes, ^{208}Pb was used as the internal standard. BCR2-G, NIST SRM 612, MASS-1, and FeS-1 were analyzed to assess the accuracy of the analyses. Data reduction was performed using the Iolite v.3 extension for Igor Pro (Paton *et al.*,

2011). Rather than using the default exponential fit functions in the original package DRS for single-detector analyses, the data reduction scheme (DRS) used for Pb analysis (Pb_Faraday_JCAF) was modified by applying linear normalization to a standard (e.g., Crowe *et al.*, 2003; Souders and Sylvester, 2010; Pietruszka and Neymark, 2017). To correct for mass bias, the DRS was applied to the raw baseline-subtracted masses. The DRS utilized the manual reduction method described by Fourny (2018), Cho (2019). and Fourny *et al.* (2020).

Reference materials (BCR2-G, NIST SRM612, MASS-1) and bracketing standard (NIST SRM610) were measured every two to three samples (Figs. 3.1. and 3.2.). BCR2-G and NIST SRM612 were used as secondary standards to assess accuracy. The average measured value of BCR2-G was $^{208}\text{Pb}/^{206}\text{Pb} = 2.07 \pm 0.04$ and $^{207}\text{Pb}/^{206}\text{Pb} = 0.833 \pm 0.02$ ($n = 74$), which are within 0.2% of the recommended reference values of $^{208}\text{Pb}/^{206}\text{Pb} = 2.066$ and $^{207}\text{Pb}/^{206}\text{Pb} = 0.833$ (Jochum and Enzweiler, 2014). The average measured value of NIST SRM612 was $^{208}\text{Pb}/^{206}\text{Pb} = 2.16 \pm 0.02$ and $^{207}\text{Pb}/^{206}\text{Pb} = 0.908 \pm 0.006$ ($n = 74$), which is within 0.2% of the recommended reference values of $^{208}\text{Pb}/^{206}\text{Pb} = 2.1647$ and $^{207}\text{Pb}/^{206}\text{Pb} = 0.9073$ (Jochum and Enzweiler, 2014). MASS-1 was analyzed to examine the effect of sulfide matrices on the accuracy of the analyses. The average measured value was $^{208}\text{Pb}/^{206}\text{Pb} = 2.04 \pm 0.06$ and $^{207}\text{Pb}/^{206}\text{Pb} = 0.828 \pm 0.01$ ($n = 74$), which are within 7% of the accepted reference values of $^{208}\text{Pb}/^{206}\text{Pb} = 1.939$ and $^{207}\text{Pb}/^{206}\text{Pb} = 0.778$ (Souders and Sylvester, 2010). The relatively low accuracy of the MASS-1 analyses and the systematic difference between observed and true values is likely due to the need to polish the MASS-1 standard prior to ablation following heavy use, which was not performed.

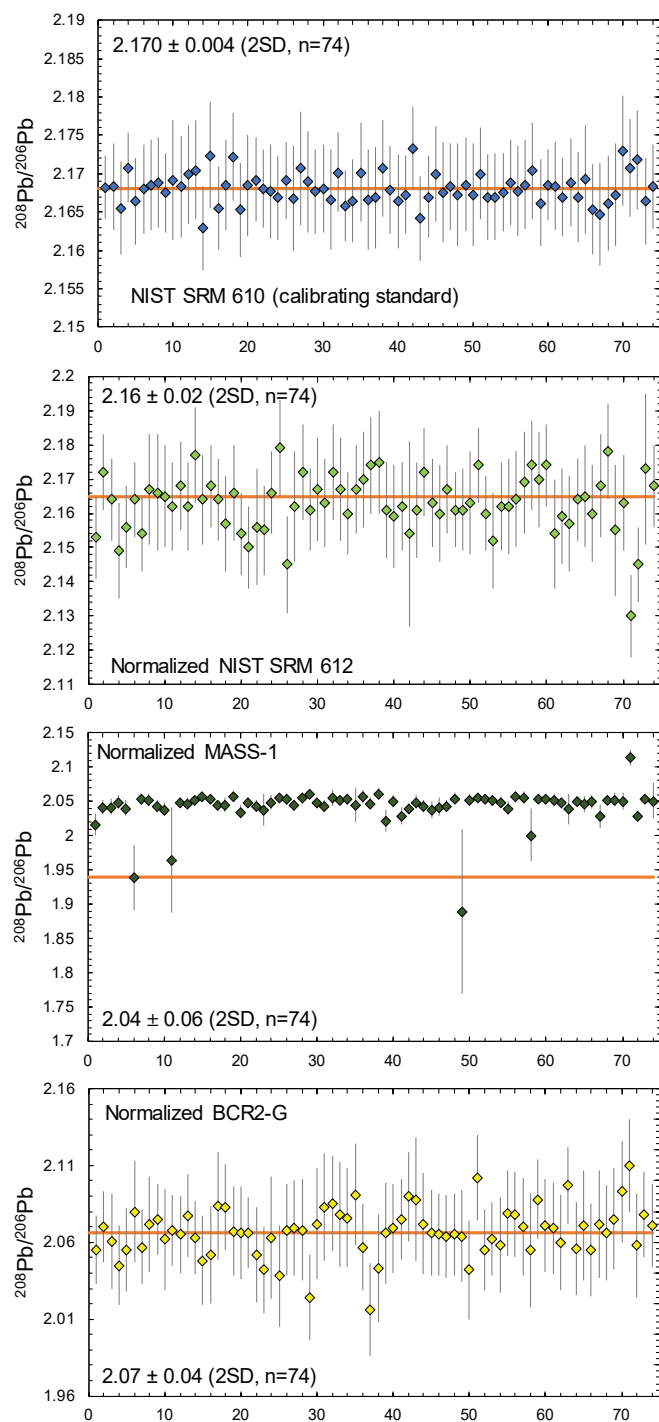


Figure 3.1. $^{208}\text{Pb}/^{206}\text{Pb}$ of the glass references NIST SRM 610, NIST SRM 612 and BCR2-G, and the polymetal sulfide pellet MASS-1 measured in this study. The Pb isotope ratios of NIST SRM 610 are as measured, whereas the Pb isotope ratios of NIST SRM 612, BCR2-G, and MASS-1 have been normalized using the recommended values for NIST SRM 610 (Jochum and Enzweiler, 2014). Orange lines indicate the recommended values for NIST SRM 610 (Jochum and Enzweiler, 2014), NIST SRM 612 (Jochum and Enzweiler, 2014), BCR2-G (Jochum and Enzweiler, 2014), and MASS-1 (Souders and Sylvester, 2010). The numbers represent the average values of analyses with their reproducibility (2SD, n = number of analyses). Error bars are 2SE. Note that the vertical scale is different on each diagram.

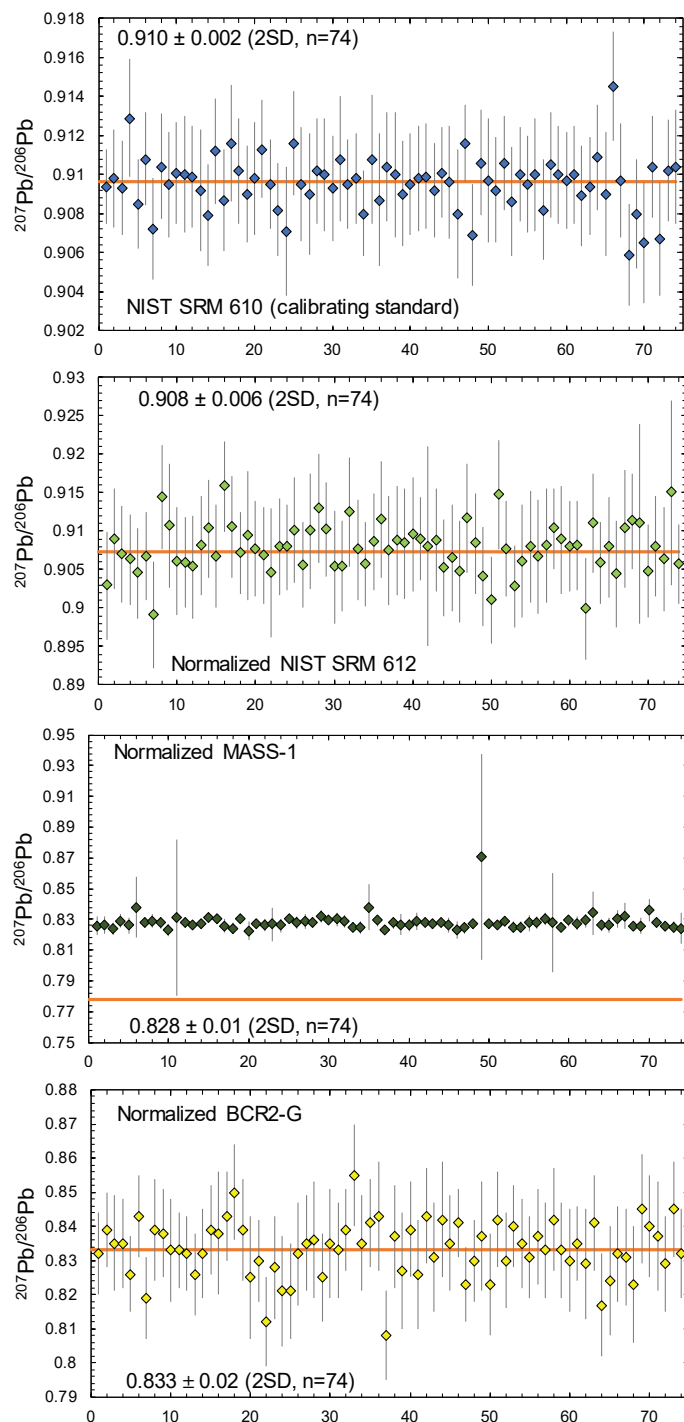


Figure 3.2. $^{207}\text{Pb}/^{206}\text{Pb}$ of the glass references NIST SRM 610, NIST SRM 612 and BCR2-G, and the polymetal sulfide pellet MASS-1 measured in this study. The Pb isotope ratios of NIST SRM 610 are as measured, whereas the Pb isotope ratios of NIST SRM 612, BCR2-G, and MASS-1 have been normalized using the recommended values for NIST SRM 610 (Jochum and Enzweiler, 2014). Orange lines indicate the recommended values for NIST SRM 610 (Jochum and Enzweiler, 2014), NIST SRM 612 (Jochum and Enzweiler, 2014), BCR2-G (Jochum and Enzweiler, 2014), and MASS-1 (Souders and Sylvester, 2010). The numbers represent the average values of analyses with their reproducibility (2SD, n = number of analyses). Error bars are 2SE. Note that the vertical scale is different on each diagram.

4. Results

4.1. Petrography and Scanning Electron Microscopy

4.1.1. Spatsizi Formation (Hazelton Group) Pyritic Mudstone

The pyritic mudstone sample 19-EV-46-01 from borehole EL-19-46 consists of predominantly mud-sized particles with a minor rounded fine sand to silt-sized particle component. The fine sand to silt-sized particles appear to be composed mainly of quartz and feldspar clasts, with some clasts exhibiting the diagnostic polysynthetic twinning of plagioclase feldspar (Fig. 4.1. C). The sample contains 20 vol% subhedral-euhedral pyrite, which is interpreted to be diagenetic in nature (Fig. 4.1. A). The more pyrite-rich horizons define the fine bedding within the lithology when coupled with the changes in the proportion of mud-sized sediments. Energy dispersion spectra (EDS) analysis of these pyrite grains reveals that they are essentially homogeneous in composition. Alteration within the sample consists of <0.5 mm stepped veins of quartz, pyrite and chalcopyrite that cross-cut the bedding within the sample (Fig. 4.1. B). Minor hematite alteration also occurs locally. Secondary pyrite can be distinguished from primary diagenetic pyrite by its massive, anhedral habit, and cross-cutting behavior. No macro- or microfossils were found within the sample. However, nearby fossil beds within the same lithostratigraphic package on Nickel Mountain have yielded late Toarcian biostratigraphic ages from ammonites. On the basis of stratigraphy, this pyritic mudstone lithology is likely attributed to the Spatsizi Formation of the Hazelton Group (Nelson *et al.*, 2018).

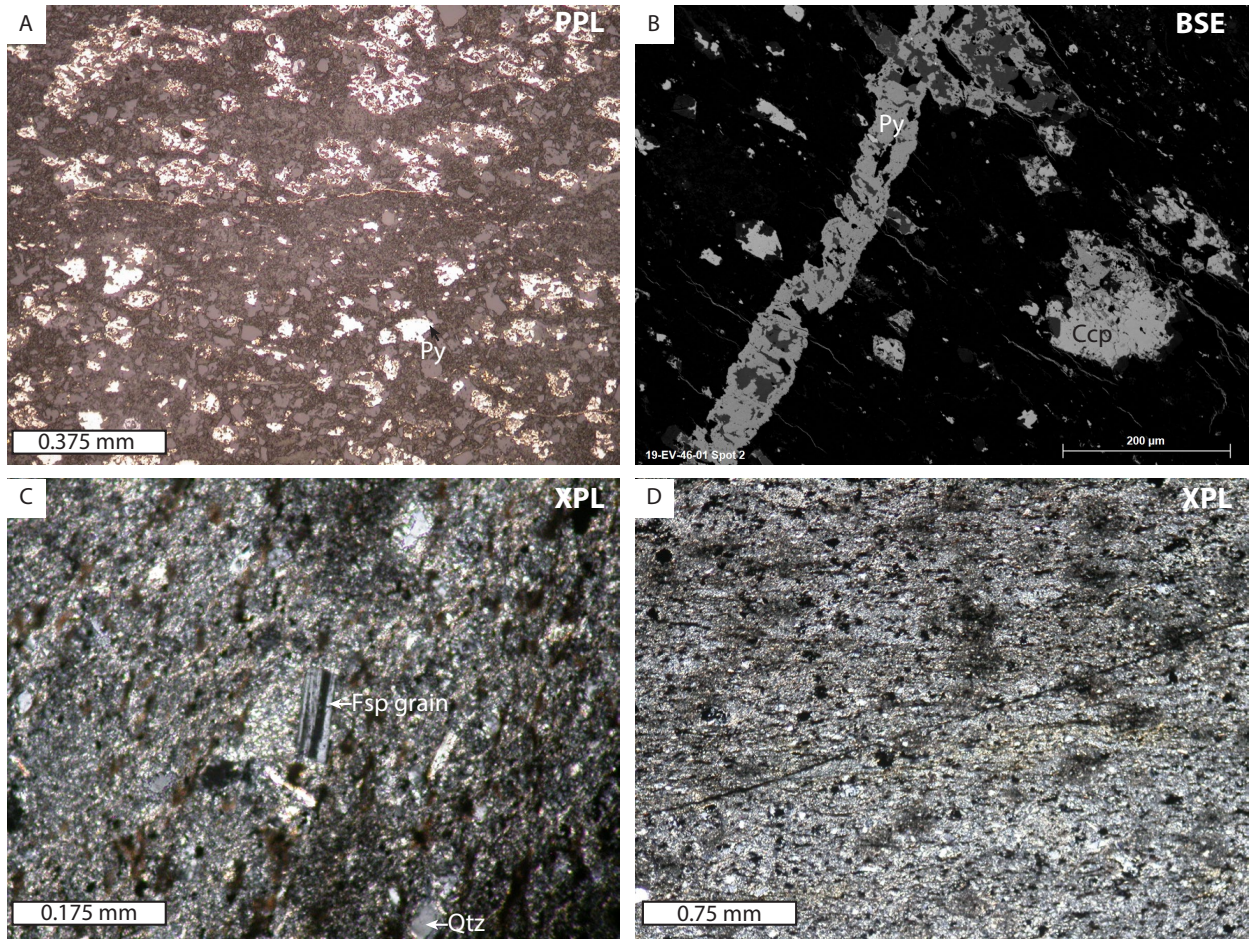


Figure 4.1. Photomicrographs and backscattered electron (BSE) images of 19-EV-46-01 pyritic mudstone from the Spatsizi Formation. A) photomicrograph of primary pyrite. B) BSE image of a vein containing secondary pyrite and chalcopyrite. C) photomicrograph of an individual feldspar clast displaying characteristic polysynthetic twinning. D) Photomicrograph showing the typical clastic texture of the mudstone. Abbreviations: Py = pyrite, Ccp = chalcopyrite, Qtz = quartz.

4.1.2 Upper Chamber

Lithologies within the Upper Chamber consist of variably altered, fine- to coarse-grained, inequigranular, orbicular olivine gabbros with variable abundances of blebby disseminated sulfide mineralization (Fig. 4.2.).

The non-sulfide portion of the Upper Chamber sample consists of olivine, plagioclase, and clinopyroxene \pm titanomagnetite. Olivine is present as fine- to medium-grained, subhedral to euhedral, equant crystals, locally replaced to variable degrees by talc, serpentine, and secondary magnetite. Where completely altered, olivine does not retain its relict shape, and instead forms anhedral masses. Clinopyroxene is present as fine- to coarse-grained, anhedral to subhedral, interstitial crystals. In 19-EV-53-08, single pyroxene crystals comprise up to 5-10 vol% of the thin section. Although it is the most alteration-resistant silicate phase within the upper chamber, clinopyroxene is locally altered and pseudomorphed by uralite and minor chlorite (Fig. 4.3. C, E). Fine- to medium-grained, anhedral to euhedral plagioclase occurs in a variety of shapes, including bladed laths and tabular crystals. Plagioclase commonly displays polysynthetic twinning and exhibits variable degrees of sericite, chlorite, and epidote alteration (Fig. 4.3. E). Titanomagnetite is present as a minor primary phase, occurring as medium-grained, anhedral-subhedral crystal exhibiting ilmenite exsolution lamellae (oxyexsolved) (Fig. 4.3. G). A wide range of silicate textures is exhibited within Upper Chamber samples. Zones with high proportions of mafic minerals commonly display an orthocumulate to mesocumulate texture, with olivine chadacrysts enclosed by clinopyroxene oikocrysts (Fig. 4.3. A). These areas are interpreted to be the cores of orbicules. Other areas exhibit a more typical poikilitic texture, with subhedral-euhedral plagioclase laths enclosed by clinopyroxene oikocrysts (Fig. 4.3. B). Other areas exhibit a hypidiomorphic texture, with relatively equigranular grain size distributions.

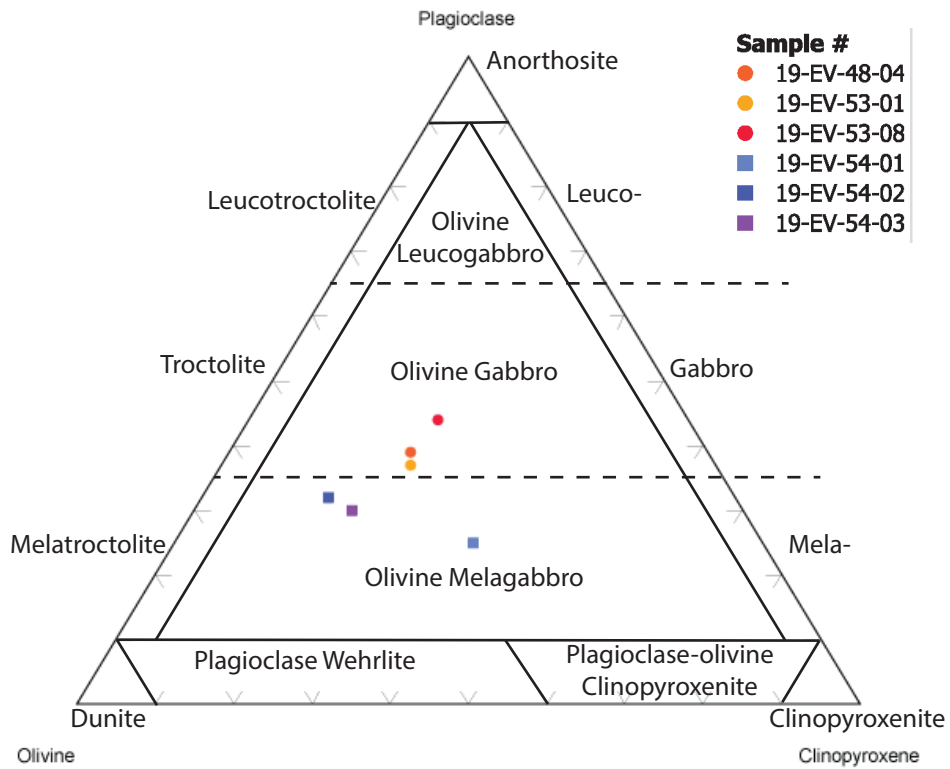


Figure 4.2. Ternary diagram for the classification of mafic rocks on the basis of modal mineralogy of gabbro samples from the Upper and Lower Chambers. Circles denote Upper Chamber samples and squares denote Lower Chamber samples.

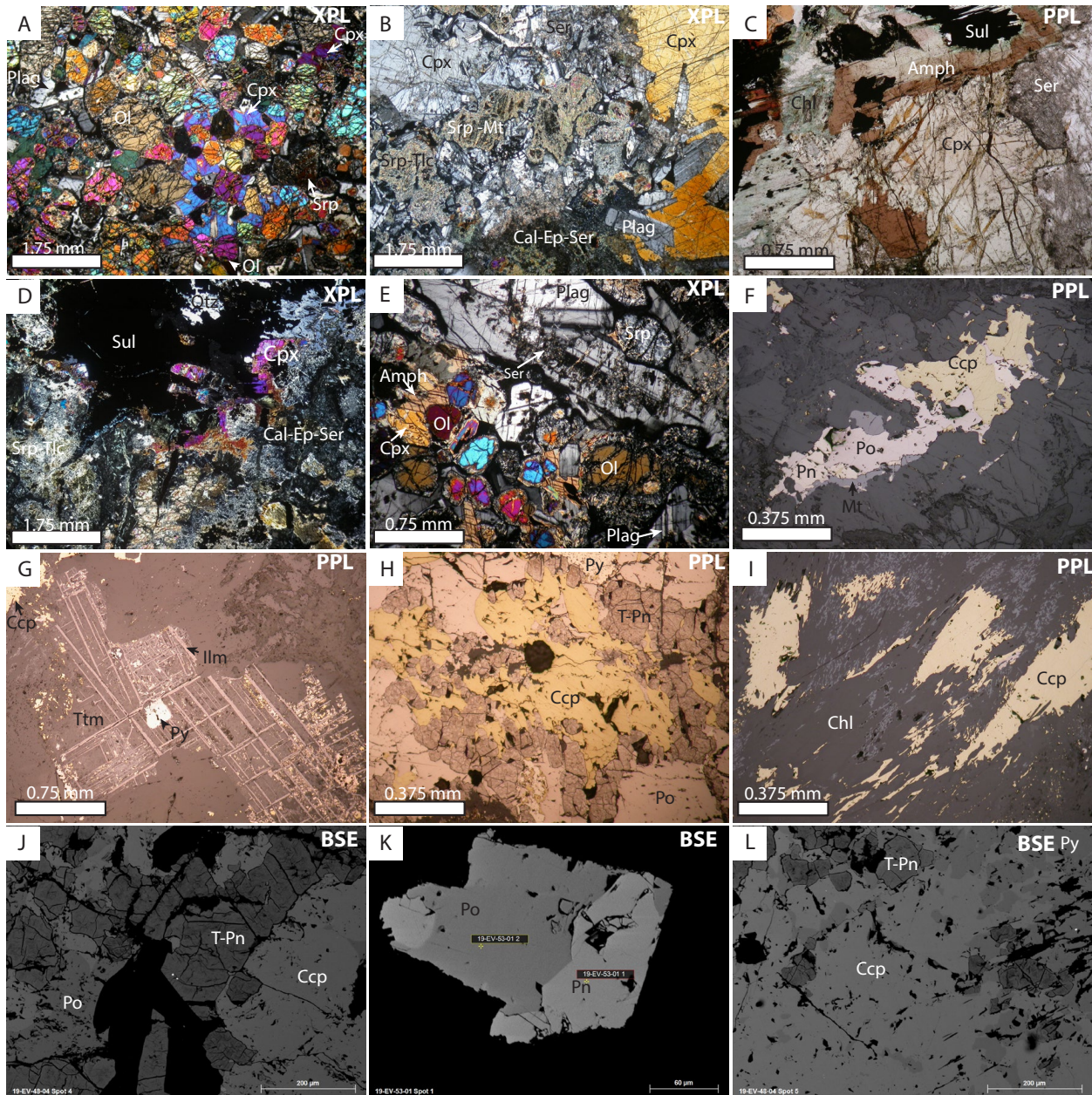


Figure 4.3. Photomicrographs of representative textures and mineralogy within the Upper Chamber. A) Mesocumulate texture of mafic minerals found towards the centre of an orbicule (19-EV-53-01). B) Coarse-grained poikilitic clinopyroxene enclosing plagioclase chadacrysts (19-EV-53-08). C) Uralitization of clinopyroxene (19-EV-53-08). D) Margin of a globular sulfide displaying the range of alteration present within the Upper Chamber; only olivine enclosed within sulfides is unaltered (19-EV-48-04). E) Clinopyroxene oikocrysts enclosing olivine and plagioclase partially altered to uralite (note their relict shapes) (19-EV-53-01). F) Sulfide bleb (19-EV-53-01). G) Titanomagnetite grain displaying ilmenite exsolution lamellae, with internal alteration-associated pyrite and chalcopyrite (19-EV-53-08). H) Altered sulfide bleb, illustrating grain relationships between tarnished pentlandite, pyrite, chalcopyrite, and pentlandite (19-EV-48-04). I) Remobilized chalcopyrite within chlorite (19-EV-53-08). J) Tarnished pentlandite (violarite) (19-EV-48-04). K) Sulfide bleb (19-EV-53-01). L) Grain relationships in altered sulfide bleb (19-EV-48-04). Abbreviations: Cpx = clinopyroxene, Ol = olivine, Plag = plagioclase, Sul = sulfide, Qtz = quartz, Ser = sericite, Ep = epidote, Cal = calcite, Amph = amphibole (uralite), Srp = serpentine, Mt = magnetite, Tlc = talc, Po = pyrrhotite, Pn = pentlandite, Ccp = chalcopyrite, Py = pyrite, T-Pn = tarnished pentlandite (violarite), Ttm = titanomagnetite.

Based on grain relationships, olivine likely crystallized first, with clinopyroxene and plagioclase likely growing simultaneously.

Sulfide mineralization within the Upper Chamber consists of 1-50 vol% interstitial blebby disseminated to globular disseminated sulfide that occurs between grains and orbicules. Blebs range in size from 0.2 mm to 40 mm and they exhibit a range of morphologies along a continuum from ameboid-shaped blebs within interstices between silicate minerals to subrounded globules (Fig. 4.3. F, K, L). In 19-EV-48-04, some blebs are connected and almost completely enclose orbicules. Some of these globules display geopetal structures, as evidenced by the differentiation of globules into chalcopyrite-rich tops and pyrrhotite-rich bottoms in the 19-EV-53-01 hand sample. Sulfide mineralogy in the Upper Chamber consists of pyrrhotite, chalcopyrite, and pentlandite, with secondary pyrite. Pyrrhotite is the predominant sulfide mineral, exceeding 50 vol% of the total sulfide mineralization and occurs as anhedral to euhedral grains less than 4 mm in size. Chalcopyrite comprises less than 35 vol% of the mineralization, occurring as <2 mm anhedral, amoeboid-shaped grains, and stringers. Pentlandite only occurs within the less altered samples, making up less than 12 vol% of the mineralization and is present as <0.5 mm, subhedral grains on the boundaries between chalcopyrite and pyrrhotite. Secondary pyrite is found within altered samples as 0.5-3 mm anhedral-euhedral grains that typically occur along the fringes of sulfide blebs. Pyrite comprises up to 16 vol% of sulfide mineralization in altered samples (19-EV-48-04 and 19-EV-53-08). Violarite pseudomorphs after pentlandite are also associated with pyrite and occur along bleb fringes and cracks. This alteration phase likely formed as the result of the infiltration of oxidizing (supergene) fluids (Fig. 4.3. H, J). Primary magnetite also occurs within blebs as small <0.7 mm subhedral-euhedral grains, displaying varying degrees of resorption.

In more altered samples, a significant amount of sulfide remobilization has occurred, as evidenced by the presence of finely disseminated (<0.5 mm) sulfides comprised of subequal proportions of chalcopyrite and pyrite within secondary minerals such as chlorite and serpentinized olivine (Fig. 4.3. H, I). These disseminations have jagged shapes, likely owing to the habits of the secondary minerals that fill the interstices. Some titanomagnetite grains contain considerable amounts of these disseminated sulfides and likely reflect metamorphic infiltration.

4.1.3 Lower Chamber

Samples from the Lower Chamber consist of medium-grained, inequigranular, locally orthocumulate-textured olivine melagabbros with 5-20 vol% disseminated to net-textured sulfides.

The primary mineralogy of the olivine melagabbros consists of olivine, clinopyroxene, and plagioclase. Olivine makes up 34-44 vol% and is present as very fine- to medium-grained (0.3-2 mm), subhedral to euhedral, equant crystals, exhibiting 15-70 vol% alteration to serpentine, magnetite, and talc. Clinopyroxene comprises 11-20 vol% and is present as very fine- to medium-grained (0.25-2 mm), anhedral-subhedral, locally poikilitic crystals, with minor alteration to uralite. Plagioclase comprises 23-26 vol% and is present as very fine- to medium-grained (0.1-1.5 mm), subhedral to euhedral crystals in a number of shapes, including laths, semi-stellate and bladed forms. Plagioclase exhibits polysynthetic twinning and is 20-90 vol% altered to sericite. The Lower Chamber olivine melagabbros are dominated by orthocumulate textures, with clinopyroxene oikocrysts enclosing olivine and plagioclase chadacrysts (Fig. 4.4. A). Some regions display subophitic to intergranular textures where plagioclase crystals are larger, and in contact with one another, and clinopyroxene fills the voids (Fig. 4.4. C). As

observed in 19-EV-54-03, some plagioclase-rich zones also take on a semi-stellate appearance, characterized by <1 mm radial aggregates of plagioclase laths with interstitial clinopyroxene (Fig. 4.4. D). These textures are typically consistent with magma mingling, similar to those observed within the Noril'sk-Talnakh deposits (Lightfoot and Evans-Lamswood, 2015).

Secondary alteration phases within the silicate component of the olivine melagabbros consists of calcite-sericite-epidote assemblages and chlorite after plagioclase, serpentine, magnetite and talc after olivine, and chlorite, uralite, and biotite after clinopyroxene. Alteration within the Lower Chamber is very patchy with little to no zonation; many nearly pristine, unaltered domains are adjacent to highly altered domains. The most altered sample, 19-EV-54-01, does show progressive zonation of alteration within a portion of the thin section. The degree to which the relict igneous texture is preserved also varies within alteration zones; some zones contain nearly flawless pseudomorphs of the original minerals, whereas other zones have been transformed into a fine-grained aggregate of secondary minerals.

Mineralization within the Lower Chamber consists of 5-20 vol% disseminated to net-textured sulfides that occur within the interstices of the silicate minerals. Where disseminated, blebs are less than 1.5 mm (Fig. 4.4. E, G). In 19-EV-54-02, the sulfides locally form an interconnected network between silicate minerals, characteristic of semi-net to net-textured mineralization (Fig. 4.4. B, H). The main phases comprising the mineralization are pyrrhotite, pentlandite, chalcopyrite, and magnetite. Pyrrhotite is the dominant sulfide phase, ranging in modal abundance from 4 to 15 vol% within samples. Individual crystals have an anhedral shape, likely owing to the shape of the interstices that the sulfides occupy, and are typically less than 0.8 mm in size. No deformation twinning is observed within the Lower Chamber pyrrhotites. Given the relatively small size of the blebs, the lack of twinning could be due to the minimal

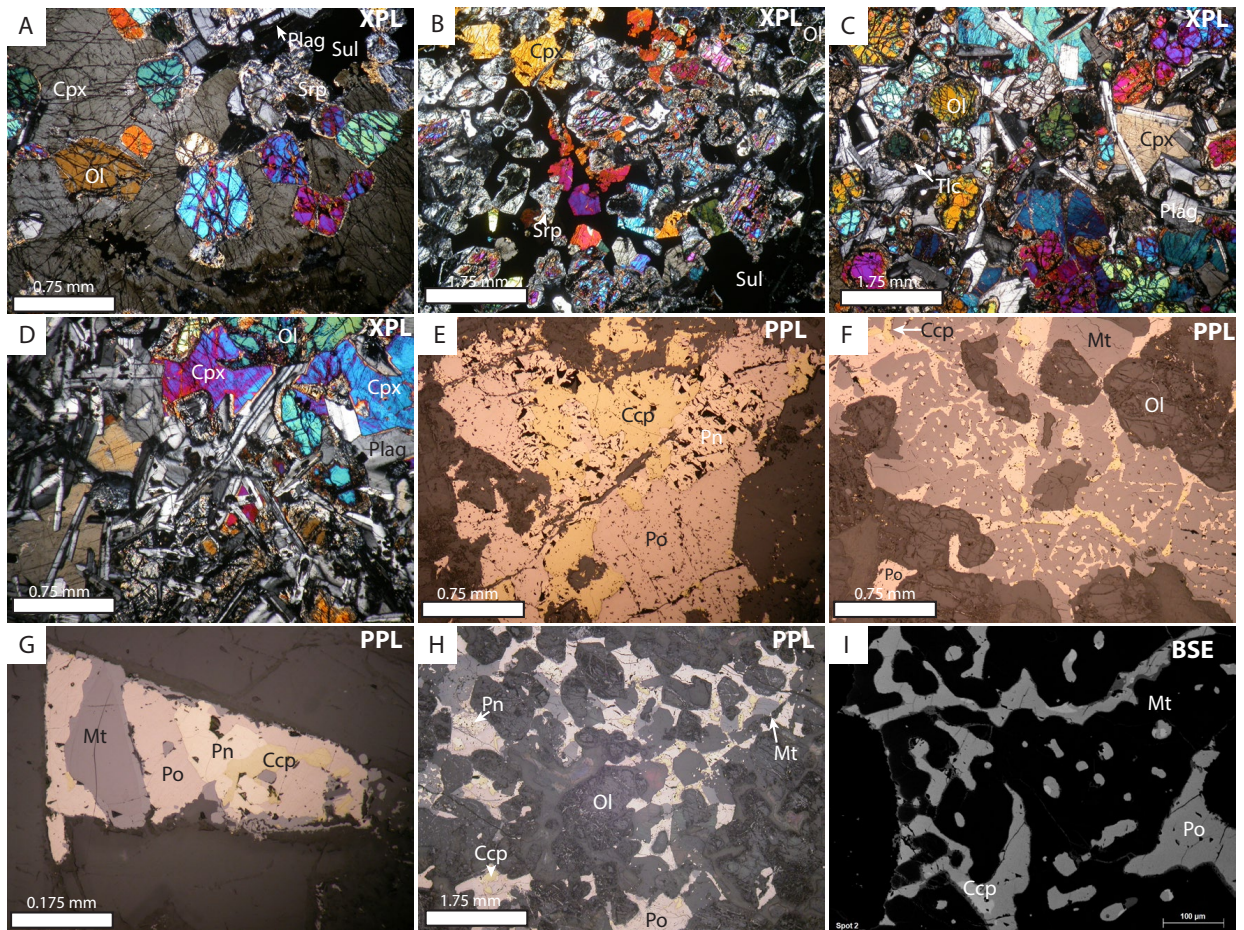


Figure 4.4. Photomicrographs of representative textures and mineralogy within the Lower Chamber. A) Locally orthocumulate texture of 19-EV-54-01 with olivine chadacrysts enclosed by clinopyroxene oikocrysts. B) Semi-net-textured sulfides illustrating grain relationships between silicate phases (19-EV-54-02). C) Typical silicate grain relationships in sulfide-poor region of sample (19-EV-54-03). D) Semi-stellate plagioclase texture (19-EV-54-03). E) Sulfide grain relationships in disseminated sulfide bleb (19-EV-54-01). F) Sieve-textured magnetite in semi-net-textured sulfides (19-EV-54-02). G) Interstitial sulfide, illustrating sulfide and oxide grain relationships. H) Locally net-textured sulfides, illustrating sulfide grain relationships (19-EV-54-02). I) Backscattered electron image of sieve-textured magnetite (19-EV-54-02). Abbreviations: Cpx = clinopyroxene, Ol = olivine, Plag = plagioclase, Srp = serpentine, Tlc = talc, Sul = sulfide, Mt = magnetite, Po = pyrrhotite, Pn = pentlandite, Ccp = chalcopyrite.

impact of strain on blebs during deformation. Chalcopyrite comprises 1-2 vol% of the samples, occurring along pyrrhotite grain boundaries, as exsolutions within pyrrhotite, and with pentlandite proximal to magnetite. The grains are anhedral in shape and are typically less than 1 mm in size. Pentlandite comprises 0.5-3 vol% of the mineralogy within the samples, occurring in association with chalcopyrite. Individual grains are less than 1 mm and exhibit little to no internal fractures, in contrast to their counterparts within other mineralized zones. Pentlandite grains also exhibit minimal alteration to violarite within the Lower Chamber sulfides. The net-textured sulfides within the Lower Chamber lack well-developed dihedral angles that typically characterize this mineralization style within other deposits. Whether this is due to deformation or simply the physical conditions during crystallization is unclear. A minor amount of sulfide remobilization has occurred within this zone, as evidenced by the presence of small disseminations of chalcopyrite within fractures in olivine and alteration products. Given the well-developed, euhedral shapes of olivine and clinopyroxene crystals completely surrounded by sulfides, the silicate minerals in the Lower Chamber likely crystallized earlier than the sulfide minerals, with the sulfide melt likely percolating through the void spaces between individual crystals.

One of the most interesting features of the Lower Chamber net-textured sulfides is the presence of “sieve-textured” magnetites (Fig. 4.4. F, I). Primary magnetite comprises 1-6 vol% of the lower chamber lithologies, typically occurring along the contacts between sulfide and silicate minerals. Individual crystals are subhedral, typically less than 0.8 mm in size and exhibit no signs of deformation; unlike magnetite within the Lower Discovery Zone, there is no evidence for shattering of individual grains within the Lower Chamber. This is likely due to deposit-scale stress field variations and the resultant differences in the degree of deformation

experienced between zones. What is most notable about Lower Chamber magnetite, however, is the presence of <0.2 mm wide pits within grains that have been infilled by sulfides, giving them an appearance akin to that of “swiss cheese”. In some areas, these pits have coalesced to form a network of sulfide blobs within crystals. These textures are most pronounced within 19-EV-54-02, where magnetite comprises the largest modal percentage of any Lower Chamber sample. On the basis of its similarity in appearance to the disequilibrium sieve textures exhibited by clinopyroxene and plagioclase crystals in volcanic rocks (Cox *et al.*, 1979), the term “sieve-textured” magnetite is used to describe this occurrence. Although a similar magnetite texture can be observed on a limited scale within the Lower Discovery Zone massive sulfides, the Lower Chamber provides the most widespread and pronounced examples of this texture.

4.1.4 Massive Sulfides: The Lower Discovery and Northeast Zones

Samples from the Lower Discovery and Northeast Zones display a wide range of lithologies, including clinopyroxene-bearing semi-massive and massive sulfides, magnetite-rich massive sulfides, and normal massive sulfides. Similar to the other Ni-Cu-PGE deposits, massive sulfide mineralization is dominated by a pyrrhotite-chalcopyrite-pentlandite-magnetite mineral assemblage and provides the best indicators into the interrelationships between sulfide mineral phases (Naldrett, 2004). The key differences between mineralization in the Lower Discovery Zone and Northeast Zone are outlined in Table 4.1.; Northeast Zone mineralization tends to be more heavily deformed in comparison to its Lower Discovery Zone counterparts. This deformation is manifested by the folded loops seen in 19-EV-30-01 (Fig. 4.6. C).

Table 4.1. Comparisons of the Lower Discovery Zone and the Northeast Zone.

	Lower Discovery Zone	Northeast Zone
Magnetite	More resorbed	Less resorbed
Violarite	Violarite alteration common	Little-no violarite alteration
Flame Pentlandite	Less common	More common
Pyrrhotite	Deformation twinned	Fractured

In all samples, the silicate and sulfide-oxide phases are hosted by or proximal to pyrrhotite. Pyrrhotite predominantly occurs as <1 cm, beige, anhedral grains that surround pentlandite, chalcopyrite, magnetite, and clinopyroxene. Minor occurrences of pyrrhotite in chalcopyrite-rich domains as <1 mm, anhedral blebs are also present in many of the more chalcopyrite-rich samples. The modal percentages in samples from the Lower Discovery Zone and Northeast Zone range from 35 vol% in magnetite-rich massive sulfides to 77 vol% in the most pyrrhotite-rich massive sulfide intervals. In cross-polarized reflected light, monoclinic and hexagonal exsolutions are visible as parallel to irregular bands and patches. In some samples, this banding displays textures akin to crenulation cleavage or folding in deformed rocks (Fig. 4.5. F). In others, most notably 19-EV-53-06, pyrrhotite displays narrow lensoidal and spindle-shaped composite lamellae, containing thin monoclinic-hexagonal exsolutions (Fig. 4.5. E). These composite lamellae typically cross-cut regions of un-twinned pyrrhotite and are oriented in more than one principal direction (Fig. 4.5. B; Fig. 4.6. A). In some cases, the more spindle-shaped composite lamellae are oriented parallel to the direction of flame pentlandite lensoids, which suggests that the processes that formed these structures were coeval with low-temperature exsolution. As will be discussed in section 5.1.1., what is considered deformation twinning may actually be lamellar exsolution, and they potentially share similar origins within Ni-Cu-PGE deposits. Thus, the terms “deformation twinning” and “exsolutions” will be used interchangeably in reference to pyrrhotite.

Pentlandite occurs in two forms within the Lower Discovery Zone and Northeast Zone orebodies: granular, consisting of <4 mm, light cream, subhedral to euhedral crystals with irregular fractures, occurring as individual grains, granular veinlets, and disseminated aggregates; and flame exsolutions, consisting of <0.2 mm, light cream, anhedral exsolutions

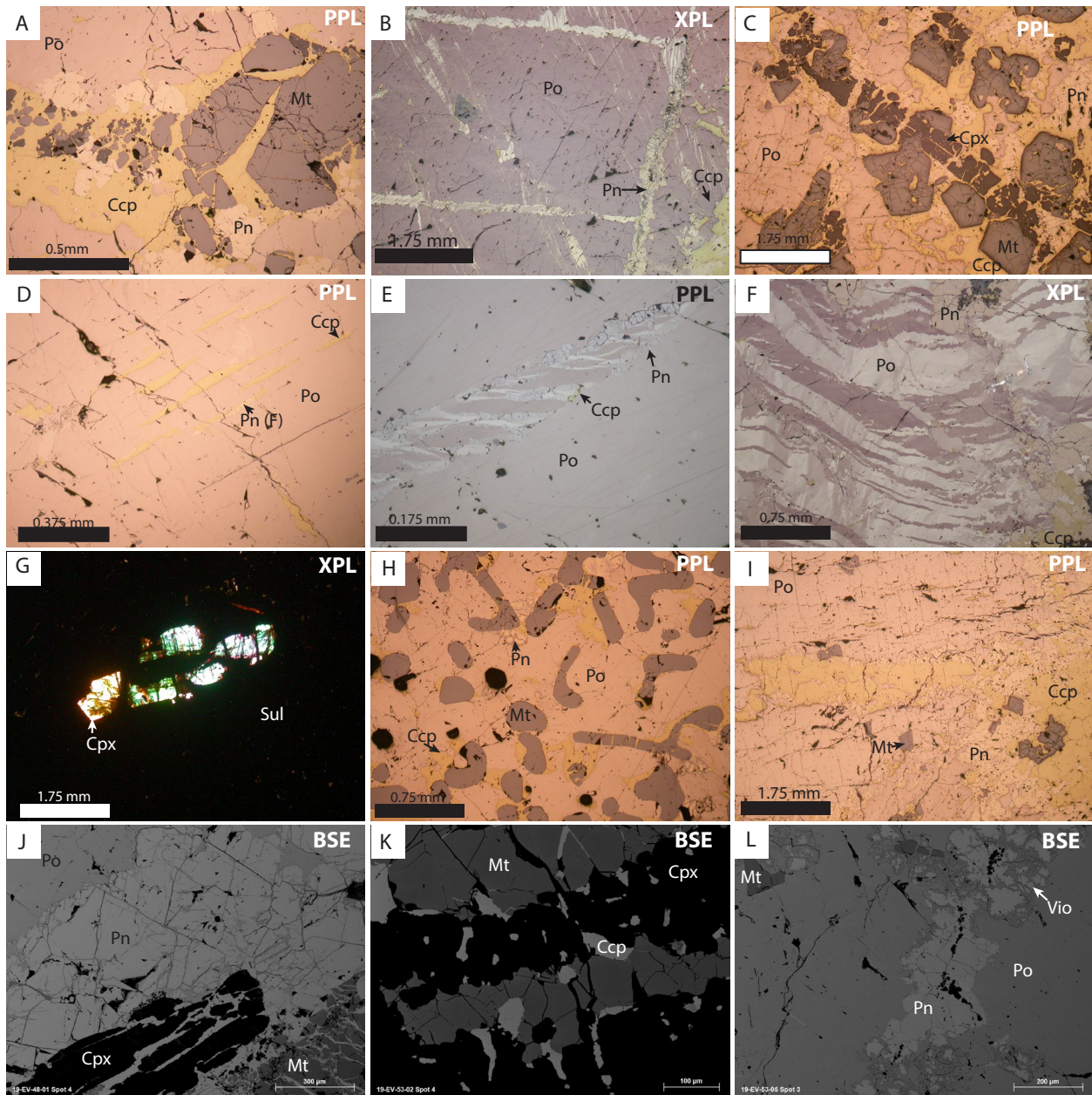


Figure 4.5. Photomicrographs of representative textures and mineralogy within the Lower Discovery Zone. A) broken magnetite displaced by remobilized chalcopyrite (19-EV-48-02). B) Two-directional pyrrhotite twinning, with composite lamellae forming a rectangular shape (19-EV-53-06). C) Silicate, oxide, and sulfide phase relationships in semi-massive sulfide, including skeletal nature of clinopyroxene phenocrysts (19-EV-48-01). D) Lination defined by “wispy” chalcopyrite (19-EV-53-05). E) Spindle-shaped composite lamellae of pyrrhotite enclosed by lensoidal flame pentlandite (19-EV-53-02). F) Wavy “crenulation” deformation twinning of pyrrhotite (19-EV-24-01). G) Skeletal clinopyroxene phenocryst in transmitted light (19-EV-48-02). H) Pseudo-cuneiform texture of magnetite with infilling of cracks by chalcopyrite (19-EV-53-03). I) Sulfide grain relationships on edge of loop (19-EV-53-07). J) Backscattered electron image of granular pentlandite and shattered magnetite in semi-massive sulfide (19-EV-48-01). K) Oxide and sulfide minerals infilling skeletal clinopyroxene (19-EV-53-02). L) Granular pentlandite with violarite alteration (19-EV-53-06). Abbreviations: Cpx = clinopyroxene, Sul = sulfide, Mt = magnetite, Po = pyrrhotite, Pn = pentlandite, Ccp = chalcopyrite, Pn (F) = flame pentlandite, Vio = violarite.

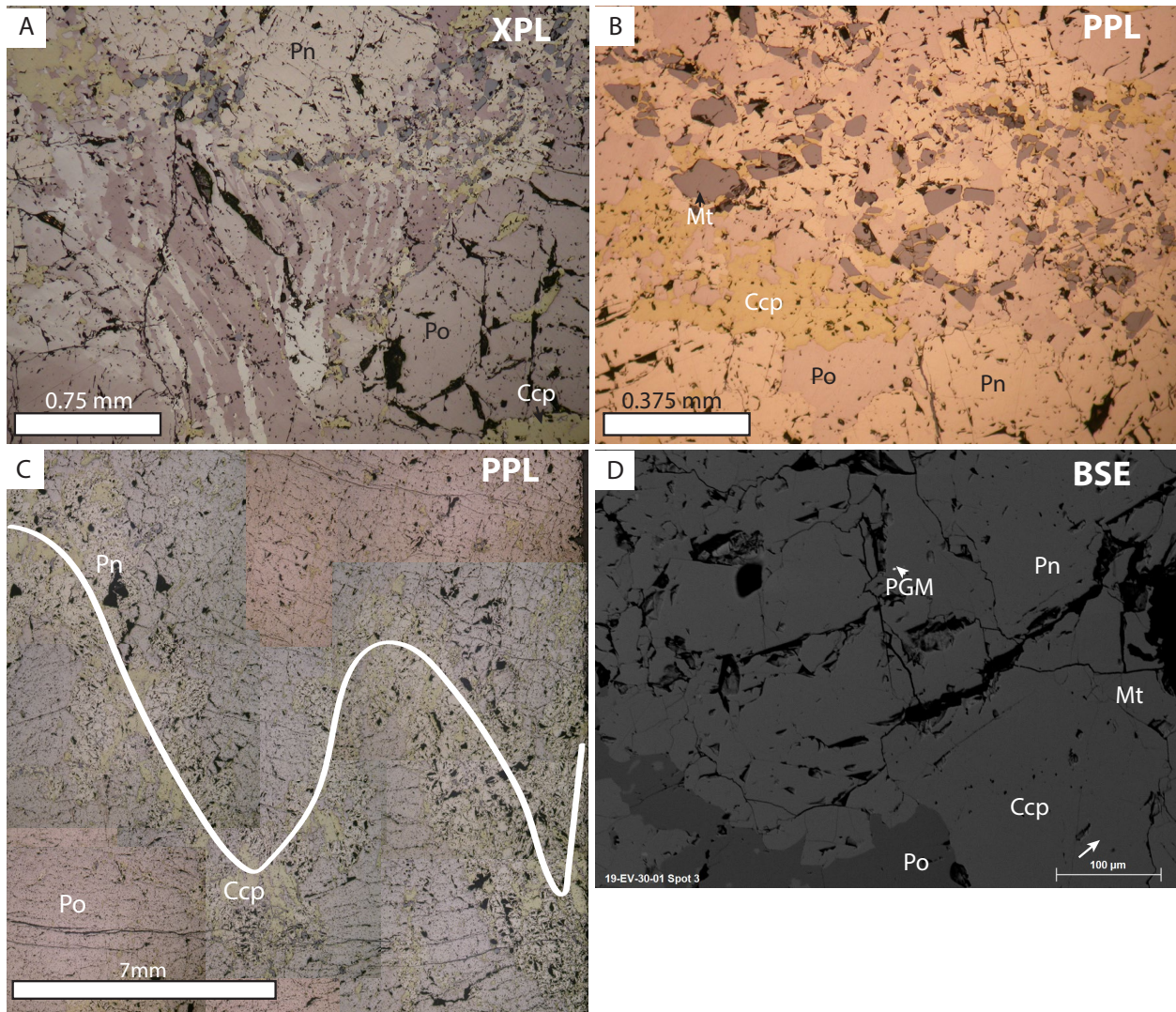


Figure 4.6. Photomicrographs of representative textures and mineralogy within the Northeast Zone. A) Deformation twinning in pyrrhotite grains adjacent to undeformed pyrrhotite grains (19-EV-30-02). B) Broken magnetites with unaltered pentlandite (19-EV-30-02). C) Stitched photomicrograph of folded loop texture comprised of granular pentlandite and chalcopyrite (19-EV-30-01). D) Backscattered electron image of granular pentlandite (19-EV-30-01). Abbreviations: Mt = magnetite, Po = pyrrhotite, Pn = pentlandite, Ccp = chalcopyrite, PGM = platinum group mineral.

from pyrrhotite. Pentlandite comprises 8-30 vol% of the samples, with flame pentlandite comprising no greater than 2 vol%. Fractures and grain boundaries are commonly altered to purple-tinged violarite, which replaces up to 20 vol% of the primary pentlandite (Fig. 4.5. L). In its granular form, pentlandite occurs along grain boundaries of pyrrhotite, as granular veins, or within loop structures in association with chalcopyrite (Fig. 4.5. I; Fig. 4.6. D). In some cases, chalcopyrite has infilled larger fractures and embayments within its structure. On the other hand, Flame pentlandite occurs exclusively as exsolutions within pyrrhotite, occurring along cleavage faces and fracture planes. Flame pentlandite displays little to no alteration to violarite, unlike its granular counterpart. Some of the composite pyrrhotite lamellae contain flame pentlandite exsolutions oriented parallel to the direction of twinning.

Chalcopyrite comprises 8-29 vol% of the samples from the Lower Discovery Zone and Northeast Zone and is present as <0.8 mm brassy yellow, anhedral veinlets, and disseminated blebs within pyrrhotite and as infill between fractured granular pentlandite, magnetite, and pyrrhotite. In many samples, chalcopyrite and granular pentlandite form loops that partially enclose pyrrhotite grains, with chalcopyrite commonly partially enclosed by pentlandite coronas and containing small blebs of pyrrhotite. In the more deformed areas, such as in 19-EV-53-05, chalcopyrite is present as lineations along pyrrhotite cleavage planes, suggesting that chalcopyrite was remobilized by plastic deformation processes subsequent to the primary crystallization of the sulfide melt (Fig. 4.5. D). It is also possible that these lineations represent exsolution from pyrrhotite. Evidence for post-crystallization remobilization of chalcopyrite is evident in many of the hand samples, such as 19-EV-53-04, where chalcopyrite infills fractures perpendicular to the direction of partially sheared loops.

Magnetite displays a wide range of textures within the Lower Discovery Zone and Northeast Zone, comprising 0.5 vol% of the mineralogy in the least magnetite-rich samples and up to 36 vol% in the magnetite-rich massive sulfide sample 19-EV-53-03. It is present as <2 mm, grey, subhedral to very locally euhedral, resorbed and brittle fractured crystals (Fig. 4.6. B). The larger crystals are commonly the most fractured and resorbed; many smaller crystals display a lower degree of resorption and exhibit a more euhedral shape. In some samples, such as 19-EV-48-01, the larger magnetite crystals are broken into <0.4 mm fragments, although they have not been significantly remobilized, with infilling of the cracks by chalcopyrite. In these samples, the original crystal shape has essentially been retained. In other samples, such as 19-EV-48-02 and 19-EV-53-06, the fractured portions of magnetite are associated with remobilized chalcopyrite, forming “fragment tails” adjacent to the original grain, as well as chalcopyrite veins containing substantial amounts of magnetite fragments (Fig. 4.5. A). In most samples, many of the magnetite crystals are sub-rounded to rounded, owing to the degree of resorption experienced in the sulfide melt during crystallization. The most interesting textures are found within the magnetite-rich massive sulfide lithology from sample 19-EV-53-03. In this lithology, many of the magnetite crystals take on a “cuneiform” appearance, owing to their morphological similarities with the intergrowths of alkali feldspar and quartz found within pegmatitic granites. Hence, the term “pseudo-cuneiform magnetite” will be used to describe magnetite exhibiting this morphology; no paragenetic process is implicated in the name and possible reasons for the formation of this texture will be discussed below in section 5.3. These pseudo-cuneiform magnetites are typically less than 1.5 mm in size, display ameboid and “arrow” shapes, and a small degree of fracturing is locally present (Fig. 4.5. H). The occurrence of fracturing with sharp edges, infilled by chalcopyrite, suggests that brittle deformation of magnetite was not syn-

crystallization, but rather occurred subsequent to crystallization and resorption of magnetite. In some samples, such as 19-EV-24-01, many small magnetite crystals take on a linear shape; this is likely due to late-stage crystallization of magnetite veins.

Skeletal clinopyroxene “phenocrysts” are present within the upper portions of the Lower Discovery Zone orebody, as evidenced by its occurrence in samples 19-EV-48-01 and 19-EV-53-02 (Fig. 4.5. C, G, J, K). These skeletal clinopyroxenes are typically 1-5 mm in size, exhibit variable degrees of twinning, and typically form elongate chains and pitted and zoned equant crystals, comprising up to 15 vol% of the mineralogy of some samples. These clinopyroxenes were likely scavenged from the overlying silicate melt. The semi-massive sulfides that host these crystals are atypical, as they do not represent emulsion at the silicate-sulfide interface.

Minor alteration phases are present in some samples (e.g. 19-EV-24-02). The main alteration phase in the massive sulfides is calcite, which typically occurs within 0.1-0.7 mm-wide irregular veins. Quartz is also a major component within some veins.

Macroscopic and microscopic textures within the massive sulfide ores provide evidence for the occurrence of post-emplacement deformation of the orebodies. As mentioned previously, the majority of the magnetites in the Lower Discovery Zone and Northeast Zone have been fractured and infilled with chalcopyrite, most likely owing to brittle deformation of magnetite accompanied by plastic deformation of chalcopyrite. In some regions, chalcopyrite appears to have been “filter pressed” between pyrrhotite grains and has remobilized magnetite fragments. Deformation of the orebodies also likely accounts for the unusual deformation twinning of pyrrhotite observed in Lower Discovery Zone and Northeast Zone samples. In many of the hand samples, deformation of the loop textures can be directly observed, such as in 19-EV-53-05.

4.2. Trace and Platinum Group Mineral Mineralogy

The most common trace minerals within the E&L deposit are sphalerite and electrum, which are likely associated with late-stage crystallization of the sulfide orebodies. Electrum has an average composition of $\text{Ag}_{0.35}\text{Au}_{0.65}$ ($n = 11$). The majority of the platinum group minerals identified are tellurides or bismuthotellurides, predominantly merenskyite (PdTe_2), moncheite (PtTe_2), and melonite (NiTe_2) (Table 4.2.; Fig 4.9. A, B). The majority of the PGM occur as within-grain exsolutions in sulfides and the largest proportion are associated with pentlandite (Fig 4.9. C, D). Merenskyite and moncheite are the most common PGM within the E&L deposit. There are three main compositional varieties of merenskyite: Pt-rich, Ni-rich, and near-stoichiometric merenskyite (Fig 4.9. A). Moncheite also has three varieties: Pd-rich, unusually Ni-rich, and stoichiometric moncheite. Non-palladian and palladian melonite are also present and become increasingly abundant towards the bottom of the Lower Discovery Zone orebody. Sperrylite is also relatively common and a significant proportion of the grains analyzed exhibit an unusually Sb-rich composition. Despite being rare, IPGMs such as Rh-telluride increase in abundance towards the middle of the sulfide orebodies. Other uncommon PGMs include michenerite, vincentite, and telargpalite (Table 4.2.). Semimetal minerals, such as hessite and altaite, are also found within the deposit; the vast majority of these minerals are tellurides (Table 4.2.). Scanning electron photomicrographs and EDS spectra for trace minerals are provided in Appendix B.

4.3. LA-ICP-MS Pb Isotope Analysis of Sulfide Minerals

A total of 15 samples were analyzed for Pb isotopes by LA-ICP-MS (Table 4.3.). Lead concentrations within magmatic sulfide minerals are variable with pyrrhotite typically containing

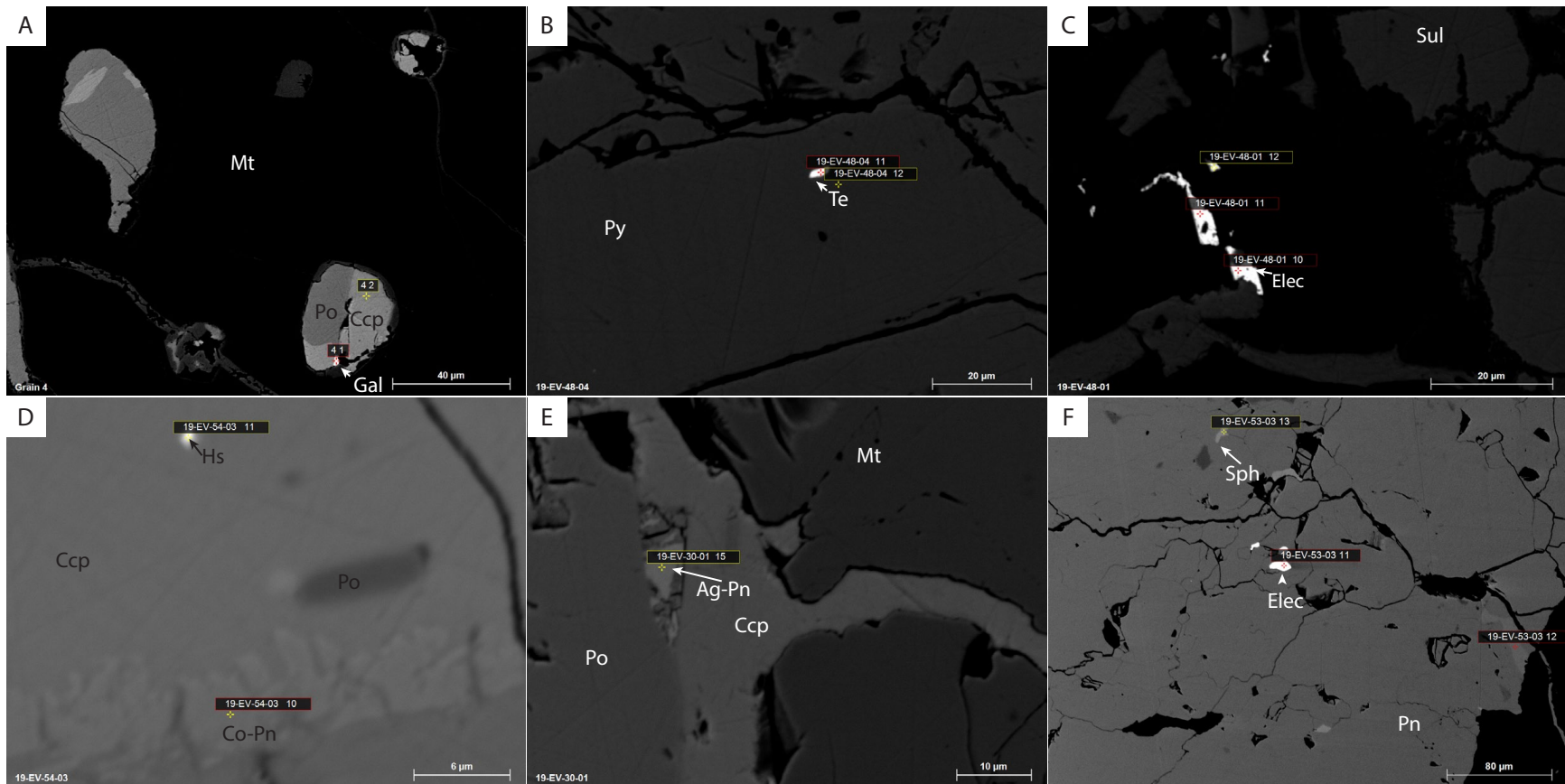


Figure 4.7. Backscattered electron images of non-PGM trace minerals associated with E&L base metal sulfides. A) Galena on grain boundary of pyrrhotite within magnetite sieve (19-EV-54-02). B) Native tellurium exsolved within pyrite (19-EV-48-04). C) Electrum on edge of sulfide grains (19-EV-48-01). D) Cobaltpentlandite on boundary of chalcopyrite grain and exsolution of hessite within chalcopyrite grain (19-EV-54-03). E) Ag-pentlandite exsolution on grain boundary between chalcopyrite and pyrrhotite (19-EV-30-01). F) Electrum and sphalerite within pentlandite (19-EV-53-03). Abbreviations: Mt = magnetite, Po = pyrrhotite, Pn = pentlandite, Ccp = chalcopyrite, Py = pyrite, Sul = sulfide, Gal = galena, Te = native tellurium, Elec = electrum, Co-pn = cobaltpentlandite, Hs = hessite, Ag-Pn = Ag-pentlandite, Sph = sphalerite.

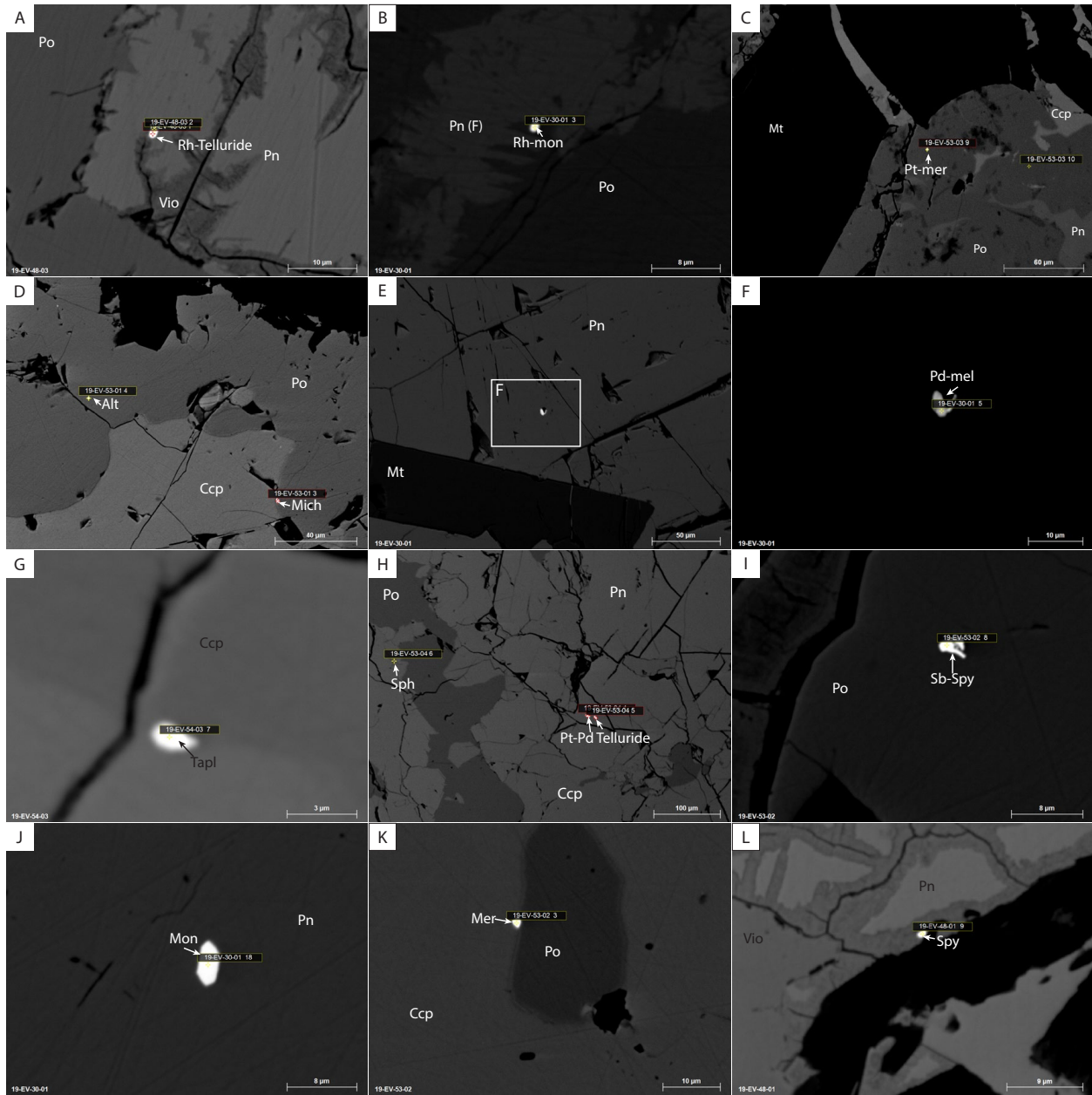


Figure 4.8. Backscattered electron images of PGM trace minerals associated with E&L base metal sulfides. A) Rhodium telluride exsolution within granular pentlandite (19-EV-48-03). B) Rhodiniferous moncheite exsolution within flame pentlandite (19-EV-30-01). C) Pt-merenskyite exsolution within pyrrhotite (19-EV-53-03). D) Altaite exsolution within pyrrhotite grain and michenerite at pyrrhotite-chalcopyrite grain boundary. E) Pd-melonite exsolution within pentlandite (19-EV-30-01). F) Detailed view of E), illustrating the anhedral shape of Pd-melonite (19-EV-30-01). G) Telargpalite exsolution within chalcopyrite (19-EV-54-03). H) Pt-Pd telluride along pentlandite fracture (19-EV-53-04). I) Sb-sperrylite exsolution within pyrrhotite (19-EV-53-02). J) Euhedral moncheite within pentlandite (19-EV-30-01). K) Merenskyite on grain boundary between pyrrhotite and chalcopyrite (19-EV-53-02). L) Sperrylite on edge of pentlandite grain (19-EV-48-01). Abbreviations: Mt = magnetite, Po = pyrrhotite, Pn = pentlandite, Ccp = chalcopyrite, Vio = violarite, Pn (F) = flame pentlandite, Rh-mon = Rh-moncheite, Pt-mer = Pt-merenskyite, Alt = altaite, Mich = michenerite, Pd-mel = Pd-melonite, Tapl = telargpalite, Sph = sphalerite, Sb-spy = Sb-sperrylite, Mon = moncheite, Mer = merenskyite, Spy = sperrylite.

Table 4.2. Mineralogy of the E&L base metal sulfides.

Mineral ¹	Formula	Description	Zone	Photographic Evidence
<u>Major ore minerals</u>				
Pyrrhotite	Fe _{1-x} S	Most abundant sulfide mineral in all zones, massive	All	Figs. 4.3.- 4.8.
Pentlandite	(Fe,Ni) ₉ S ₈	Primary Ni ore mineral; occurs as massive, blocky grains and flame exsolutions in Po	All	Figs. 4.3.- 4.8.
Chalcopyrite	CuFeS ₂	Massive and infilling fractures	All	Figs. 4.3.- 4.8.
Magnetite	Fe ₃ O ₄	Subhedral-euhedral grains, locally fractured and exhibiting varying degrees of resorption	All	Figs. 4.3.- 4.8.
<u>Minor and trace ore minerals</u>				
Pyrite	FeS ₂	Product of alteration; euhedral cubic to anhedral shape	Upper Chamber	Fig. 4.3. (G, H), 4.7. (B)
Argentopentlandite	Ag(Fe,Ni) ₈ S ₈	Exsolution lamellae and inclusions within Ccp	Northeast	Fig. 4.7. (E)
Cobaltpentlandite	(Fe,Ni,Co) ₉ S ₈	Flames in Po	Lower Chamber	Fig. 4.7. (D)
Violarite	FeNi ₂ S ₄	Product of late-stage alteration; occurs along cracks and grain boundaries in Pn	All	Figs. 4.3. (H, J, L), 4.5. (L), 4.8. (A, L)
Electrum	Au _{0.2-0.8} Ag _{0.2-0.8}	Common in upper portions of massive sulfide intervals; inclusions (<30 μm) in Ccp, or Pn, and at sulfide-sulfide and sulfide-silicate interfaces	All	Fig. 4.7. (C, F)
Ilmenite	FeTiO ₃	Occurs as oxyexsolved lamellae within Mt	Upper Chamber, Lower Chamber	Fig. 4.3. (G)
<u>Pb, Zn Sulfides</u>				
Galena	PbS	Rare; in fractures in blebs, at sulfide-silicate interfaces or as inclusions in Ccp and Po	Discovery, Lower Chamber	Fig. 4.7. (A)
Sphalerite	(Zn,Cd,Mn)S	Anhedral; in Ccp and Pn	All	Figs. 4.7. (F), 4.8. (H)
<u>Te-bearing</u>				
Native Tellurium	Te	Rare; inclusions in Py and Po	Discovery, Upper Chamber	Fig. 4.7. (B)
<u>Platinum group minerals</u>				
Merenskyite	(Pd,Ni,Pt)(Te,Bi) ₂	Most common PGM (<12 μm); associated with Po, Pn and Ccp; inclusions or occur at sulfide-sulfide interfaces	All	Fig. 4.8. (C, K)
Moncheite	(Pt,Pd)(Te,Bi) ₂	Second most common PGM (<10 μm); inclusions in Po, Pn and Ccp or occur at sulfide-sulfide and sulfide-oxide interfaces	All	Fig. 4.8. (B, J)
Michenerite	PdBiTe	Rare; occurs as inclusions within Po and at sulfide-sulfide interfaces	Upper Chamber, Lower Chamber	Fig. 4.8. (D)
Rhodium Telluride	?	Rare; occurs as inclusions within Pn and Po	Discovery	Fig. 4.8. (A)
Vincentite	(Pd,Pt) ₃ (As,Sb,Te)	Rare; found at sulfide-sulfide interfaces	Discovery, Lower Chamber	-
Sperrylite	PtAs ₂	Common; found as regular and Sb and Te-rich forms; occurs as inclusions within Po, Pn and Ccp and at sulfide-sulfide interfaces	Discovery, Northeast	Fig. 4.8. (I, L)
Palladoan Melonite	(Pd,Ni)(Te,Bi) ₂	Rare; occurs as inclusions within Pn	Lower Chamber, Discovery, Northeast	Fig. 4.8. (E, F)
Telargpalite	(Pd,Ag) ₃ (Te,Bi)	Rare; occurs as inclusions within Ccp	Lower Chamber	Fig. 4.8. (G)
<u>Other tellurides</u>				
Altaite	PbTe	Rare; occurs as inclusions within Po	Upper Chamber, Discovery	Fig. 4.8. (D)
Hessite	Ag ₂ Te	Common; occurs as inclusions within Po and Ccp	Lower Chamber	Fig. 4.7. (D)

¹Bold minerals denote the most common minerals in their respective groups.

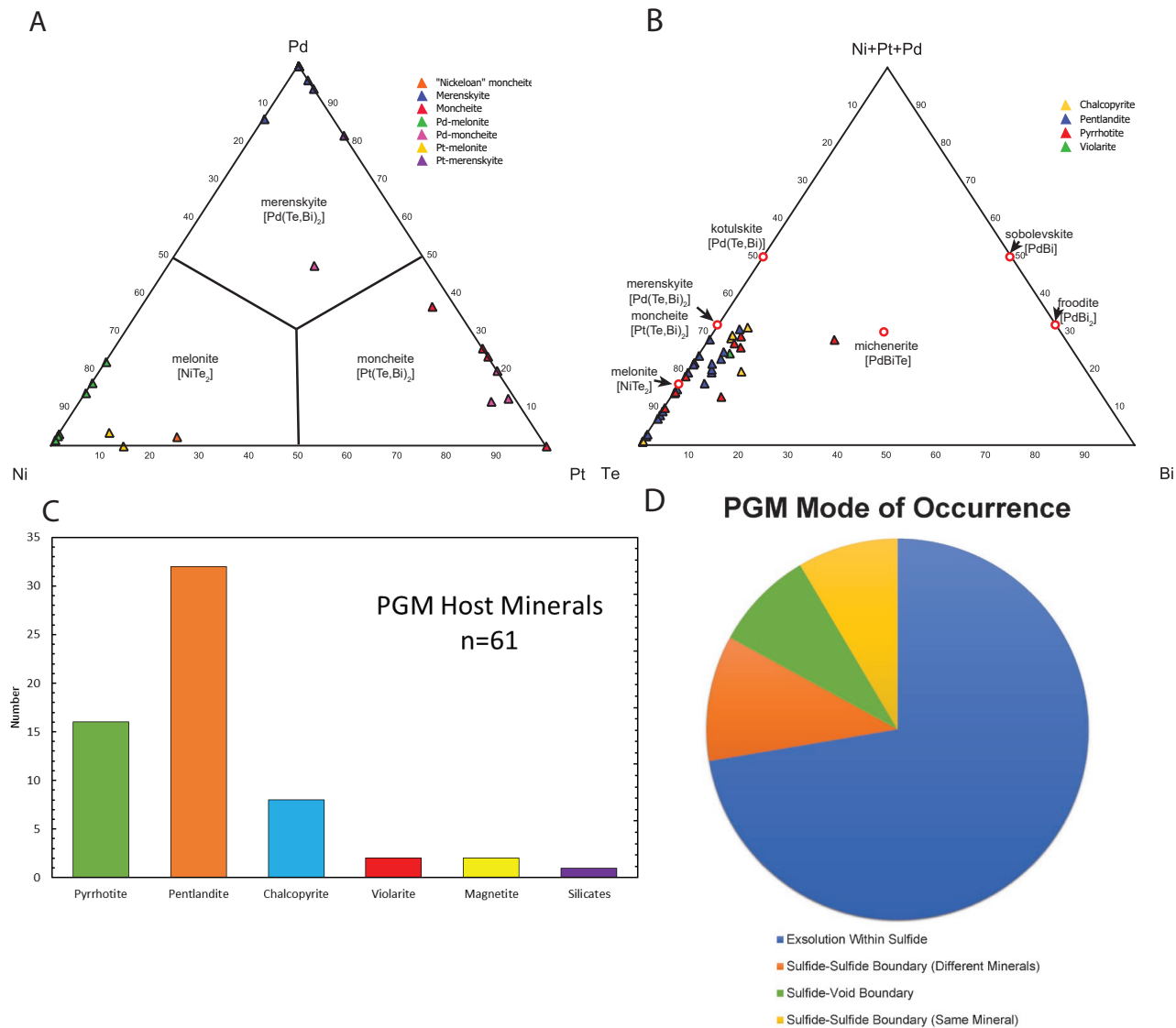


Figure 4.9. Analysis of E&L platinum group mineralogy. A) Ternary plot showing the distribution of EDS-derived compositions of telluride and bismuthotelluride minerals for the merenskyite, moncheite, and melonite end-members, with the binary joins indicating solid-solution series between minerals. B) Ni+Pt+Pd-Te-Bi ternary plot for EDS-derived compositions of platinum group minerals in E&L ores. C) Histogram showing that the most common PGM host is pentlandite. D) Pie chart showing that the most common mode of occurrence for PGM is exsolution within sulfide grains.

the lowest Pb concentrations (average = 22.8 ppm) and chalcopyrite on average with the highest Pb concentrations (average = 83 ppm). Pyrite contains the highest average Pb concentrations (100 ppm) of all of the minerals analyzed. Average uncertainties on $^{208}\text{Pb}/^{206}\text{Pb}$ are 3.9% 2RSE for sulfide minerals (Fig. 4.10.). On average, chalcopyrite has the lowest isotope ratio standard errors of any mineral due to its higher Pb concentrations (i.e., more analyte). There are no significant correlations between specific mineralized zone and Pb concentrations. Moreover, there are no significant correlations between Pb concentrations and isotopic compositions, which indicates U and Th concentrations in the majority of sulfides are very low. This eliminates the need for the age-correction of isotopic ratios and thus the isotopic compositions of the sulfides can be accepted as initial values. Photomicrographs of analyzed materials and locations of spot analyses are provided in Appendix C.

4.3.1. Lower Discovery Zone

The Pb concentrations and isotopic compositions of magmatic sulfide minerals were analyzed in eight samples from the Lower Discovery Zone of the E&L deposit. The Pb isotopic compositions are distributed along an elongate trend, with an average composition of $^{207}\text{Pb}/^{206}\text{Pb} = 0.843 \pm 0.027$ and $^{208}\text{Pb}/^{206}\text{Pb} = 2.076 \pm 0.064$ ($n = 45$) (Fig. 4.12. A, D). Chalcopyrite has lowest average analytical uncertainty of the sulfides from the Lower Discovery Zone (1.87% 2RSE on $^{208}\text{Pb}/^{206}\text{Pb}$), forming a relatively homogeneous cluster with an average composition of $^{207}\text{Pb}/^{206}\text{Pb} = 0.830 \pm 0.011$ and $^{208}\text{Pb}/^{206}\text{Pb} = 2.041 \pm 0.015$ ($n = 14$) (Fig. 4.11. A). The isotopic compositions of pentlandite (both flame and granular) have a larger distribution, with $^{207}\text{Pb}/^{206}\text{Pb} = 0.840 \pm 0.011$ and $^{208}\text{Pb}/^{206}\text{Pb} = 2.091 \pm 0.085$ ($n = 11$; 4.36% 2RSE on $^{208}\text{Pb}/^{206}\text{Pb}$) (Fig. 4.11. B). Flame pentlandite is associated with a significantly lower average analytical uncertainty

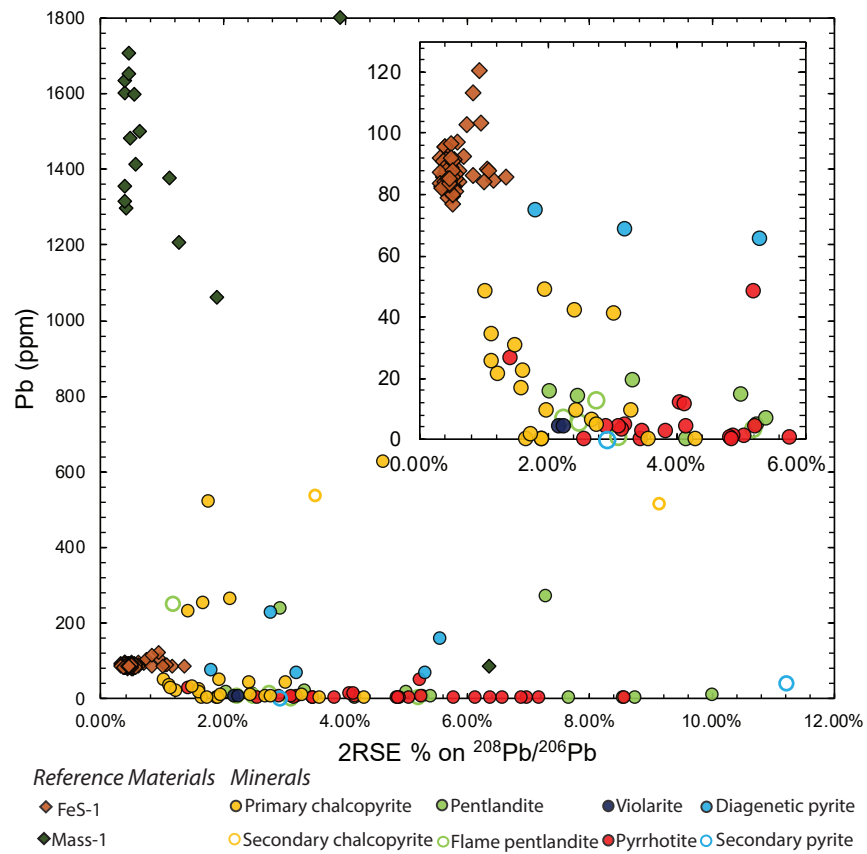


Figure 4.10. Concentration of Pb (ppm) vs. 2RSE % on $^{208}\text{Pb}/^{206}\text{Pb}$ determined by split-stream LA-ICP-MS. The rectangle in the lower left shows the area expanded in the inset plot that focuses on sulfide analyses from the E&L deposit. Precision generally increases with higher Pb concentration.

Table 4.3. Summary of LA-ICP-MS Pb isotopic compositions of sulfide minerals from the E&L deposit.

Zone ¹	Sample	Spot Name	Mineral ²	²⁰⁸ Pb/ ²⁰⁶ Pb	2SE	²⁰⁷ Pb/ ²⁰⁶ Pb	2SE	U (ppm)	Th (ppm)	Pb (ppm)
NEZ	19-EV-30-01	EV301Ccp1	Ccp	1.998	0.086	0.816	0.035	<dl	<dl	<dl
		EV301Ccp2	Ccp	2.029	0.034	0.822	0.014	<dl	15.8	250.5
		EV301Po2	Po	2.046	0.099	0.867	0.054	<dl	4.7	30.55
NEZ	19-EV-30-02	EV302Ccp1	Ccp	2.018	0.03	0.83	0.018	<dl	91	520
		EV302Ccp2	Ccp	2.055	0.036	0.842	0.016	<dl	<dl	5.415
		EV302Pn1	Pn (G)	2.2	0.16	0.857	0.063	<dl	<dl	270.5
		EV302Pnf1	Pn (F)	2.054	0.051	0.852	0.023	<dl	<dl	0.6995
HG	19-EV-46-01	EV302Po1	Po	1.747	0.085	0.84	0.035	<dl	<dl	<dl
		EV46Ccp1	Ccp (S)	2.3	0.21	0.87	0.054	49	150	515
		EV46Ccp2	Ccp (S)	2.031	0.071	0.841	0.033	<dl	<dl	534.5
		EV46Py1	Py (D)	1.98	0.11	0.811	0.042	<dl	<dl	159
		EV46Py2	Py (D)	2.013	0.056	0.829	0.032	<dl	<dl	227
		EV46Py3	Py (D)	2.07	0.11	0.84	0.029	<dl	<dl	65.7
		EV46Py4	Py (D)	2.036	0.037	0.828	0.018	0.766	1.46	75
LDZ	19-EV-48-01	EV46Py5	Py (D)	2.001	0.064	0.816	0.02	15.6	24.4	68.45
		Ev481Ccp1	Ccp	2	0.066	0.829	0.034	<dl	<dl	9.585
		EV481Ccp2	Ccp	2.047	0.034	0.834	0.018	<dl	<dl	<dl
		EV481Pn1	Pn (G)	2.29	0.2	0.911	0.095	<dl	<dl	48.35
		EV481Po1	Po	2.05	0.085	0.857	0.036	<dl	<dl	48.75
		Ev481Po2	Po	2.094	0.067	0.876	0.038	<dl	<dl	6.245
		LDZ	19-EV-48-03	EV483Po1	Po	2.22	0.19	0.907	0.086	<dl
LDZ	19-EV-48-03	EV483Po2	Po	2.11	0.11	0.866	0.055	<dl	<dl	34.55
		UC	19-EV-48-04	EV484Ccp1	Ccp	2.077	0.063	0.851	0.03	<dl
UC	19-EV-48-04	EV484Ccp2	Ccp	2.079	0.041	0.839	0.02	<dl	<dl	9.435
		EV484Po1	Po	2.119	0.086	0.867	0.032	<dl	<dl	<dl
		EV484Py1	Py (S)	2.158	0.063	0.85	0.034	<dl	<dl	<dl
		Ev484Py2	Py (S)	2.14	0.24	0.823	0.046	<dl	<dl	7.7
		EV484Vio1	Vio	2.071	0.045	0.838	0.018	<dl	<dl	11.8
		EV484Vio2	Vio	2.084	0.047	0.848	0.021	<dl	<dl	11.75
		UC	19-EV-53-01	EV531Ccp2	Ccp	2.012	0.072	0.819	0.035	<dl
UC	19-EV-53-01	EV531Pn1	Pn	2.2	0.22	0.865	0.069	<dl	<dl	<dl
		EV531Pn2	Pn	2.34	0.2	0.93	0.1	<dl	<dl	38.55
		EV531Po1	Po	2.037	0.084	0.823	0.048	<dl	<dl	4.4
		EV531Po2	Po	1.95	0.14	0.843	0.077	<dl	<dl	3.995
		LDZ	19-EV-53-02	EV532Ccp1	Ccp	2.04	0.021	0.833	0.011	<dl
LDZ	19-EV-53-02	EV532Ccp2	Ccp	2.053	0.04	0.843	0.02	<dl	<dl	<dl
		EV532Pn1	Pn (G)	2.09	0.11	0.837	0.042	<dl	<dl	4.555
		EV532Po1	Po	2.032	0.064	0.84	0.023	<dl	<dl	<dl
		EV532Po2	Po	2.07	0.072	0.845	0.028	<dl	<dl	22.55
		LDZ	19-EV-53-03	EV533Ccp1	Ccp	2.049	0.055	0.846	0.025	<dl
LDZ	19-EV-53-03	EV533Ccp2	Ccp	2.037	0.05	0.817	0.021	<dl	<dl	1.57
		EV533Po1	Po	2.15	0.15	0.866	0.071	<dl	<dl	25.4
		EV533Po2	Po	2.037	0.029	0.841	0.013	<dl	<dl	7.24

Zone ¹	Sample	Spot Name	Mineral ²	²⁰⁸ Pb/ ²⁰⁶ Pb	2SE	²⁰⁷ Pb/ ²⁰⁶ Pb	2SE	U (ppm)	Th (ppm)	Pb (ppm)
LDZ	19-EV-53-04	EV534Ccp1	Ccp	2.045	0.023	0.8257	0.0087	<dl	<dl	12.8
		EV534Ccp2	Ccp	2.047	0.025	0.828	0.012	<dl	34	249.5
		EV534Pn2	Pn (G)	2.04	0.11	0.837	0.044	<dl	<dl	3.345
		EV534Pnf1	Pn (F)	2.11	0.047	0.866	0.032	<dl	<dl	0.951
		EV534Pnf2	Pn (F)	2.066	0.057	0.832	0.028	<dl	<dl	<dl
		EV534Po1	Po	2.08	0.12	0.876	0.072	<dl	<dl	4.755
		EV534Po3	Po	2.12	0.13	0.804	0.067	<dl	<dl	6.6
		EV534Po4	Po	2.089	0.065	0.86	0.03	<dl	<dl	0.3715
LDZ	19-EV-53-05	EV535Ccp1	Ccp	2.05	0.039	0.84	0.021	<dl	<dl	14.185
		EV535Ccp2	Ccp	2.02	0.056	0.805	0.021	<dl	<dl	19.4
		EV535Ccp3	Ccp	2.04	0.039	0.842	0.018	<dl	<dl	14.45
		EV535Pnf1	Pn (F)	2.053	0.024	0.834	0.012	<dl	<dl	4.48
		EV535Po1	Po	1.98	0.1	0.826	0.049	<dl	<dl	4.515
		EV535Po2	Po	2.13	0.14	0.878	0.073	<dl	<dl	0.78
LDZ	19-EV-53-06	EV536Ccp1	Ccp	2.045	0.033	0.829	0.013	<dl	<dl	48.35
		EV536Ccp2	Ccp	2.059	0.033	0.823	0.017	<dl	<dl	3.285
		EV536Pn1	Pn (G)	1.96	0.15	0.794	0.068	<dl	<dl	2.6
		EV536Pn2	Pn (G)	2.023	0.05	0.843	0.026	<dl	<dl	0.4115
		EV536Pnf1	Pn (F)	2.12	0.11	0.835	0.046	<dl	<dl	26.45
		EV536Po1	Po	2.05	0.1	0.81	0.059	<dl	<dl	0.3905
		EV536Po2	Po	2.062	0.06	0.854	0.028	<dl	<dl	0.389
		EV536Po3	Po	2.035	0.078	0.824	0.034	<dl	<dl	4.1
LDZ	19-EV-53-07	EV537Ccp1	Ccp	2.058	0.036	0.821	0.015	<dl	<dl	0.995
		EV537Ccp2	Ccp	2.033	0.023	0.835	0.014	<dl	<dl	0.4635
		EV537Pn1	Pn (G)	2.073	0.069	0.809	0.022	<dl	<dl	1.22
		EV537Pn2	Pn (G)	2.2	0.11	0.877	0.049	<dl	<dl	4.04
		EV537Pnf1	Pn (F)	2.068	0.064	0.81	0.026	<dl	<dl	2.545
		EV537Po1	Po	2.18	0.15	0.886	0.073	<dl	<dl	0.4725
		EV537Po2	Po	2.2	0.14	0.884	0.066	<dl	<dl	0.452
		LC	19-EV-54-02	EV542Ccp1	Ccp	2.042	0.029	0.823	0.015	<dl
		EV542Ccp2	Ccp	2.056	0.05	0.844	0.025	<dl	<dl	42.2
		EV542Pn2	Pn	2.042	0.06	0.844	0.023	<dl	117	625
		EV542Po2	Po	2.1	0.11	0.873	0.045	16	67	263
LC	19-EV-54-03	EV543Ccp1	Ccp	2.052	0.095	0.802	0.031	<dl	57	235.5
		EV543Ccp2	Ccp	2.069	0.044	0.821	0.019	<dl	<dl	<dl
		EV543Pn1	Pn	2.163	0.09	0.822	0.033	<dl	<dl	15.8
		EV543Pn2	Pn	2.057	0.042	0.82	0.017	<dl	<dl	4.365
		EV543Po1	Po	2.053	0.071	0.825	0.033	<dl	<dl	<dl
		EV543Po2	Po	2.073	0.053	0.835	0.022	<dl	<dl	<dl

All reported values are measured ratios. 2SE is 2×standard error for each analysis. <dl denotes below detection limit.

¹Abbreviations: HG – Hazelton Group, LDZ – Lower Discovery Zone, LC – Lower Chamber, NEZ – Northeast Zone, UC – Upper Chamber. ²Abbreviations: (S) – denotes secondary mineralization, Ccp – chalcopyrite, Pn (G) – granular pentlandite, Pn – pentlandite, Pn (F) – flame pentlandite, Po – pyrrhotite, Py – diagenetic pyrite (unless denoted with (S)), Vio – Violarite.

(2.89% 2RSE on $^{208}\text{Pb}/^{206}\text{Pb}$) due to its higher Pb concentrations. The isotopic compositions of pyrrhotite show a relatively similar range to that of pentlandite, but with a slightly larger average analytical uncertainty (4.87% 2RSE on $^{208}\text{Pb}/^{206}\text{Pb}$), and an average composition $^{207}\text{Pb}/^{206}\text{Pb} = 0.856 \pm 0.022$ and $^{208}\text{Pb}/^{206}\text{Pb} = 2.094 \pm 0.064$ (n = 18) (Fig 4.11. C).

4.3.2. Northeast Zone

The Pb concentrations and isotopic compositions of pyrrhotite, pentlandite, and chalcopyrite were measured from two samples from the Northeast Zone (Fig 4.12. A, C). The Pb isotopic compositions show the largest variation in $^{208}\text{Pb}/^{206}\text{Pb}$ of the mineralized zones with an average $^{207}\text{Pb}/^{206}\text{Pb} = 0.841 \pm 0.018$ and $^{208}\text{Pb}/^{206}\text{Pb} = 2.018 \pm 0.125$ (n = 8). Approximately half (7/15) of the spots analyzed within the samples have high 2RSE values >9% and thus are not discussed further. Chalcopyrite has an average $^{207}\text{Pb}/^{206}\text{Pb} = 0.828 \pm 0.011$ and $^{208}\text{Pb}/^{206}\text{Pb} = 2.025 \pm 0.024$ (n = 4; 2.30% 2RSE on $^{208}\text{Pb}/^{206}\text{Pb}$).

4.3.3. Upper Chamber

The Pb concentrations and isotopic compositions of pyrrhotite, pentlandite, chalcopyrite, pyrite, and violarite were measured from two samples from the Upper Chamber (Fig 4.12. A, F). Their Pb isotopic compositions define the second largest spread of any zone analyzed, with an average composition of $^{207}\text{Pb}/^{206}\text{Pb} = 0.850 \pm 0.073$ and $^{208}\text{Pb}/^{206}\text{Pb} = 2.105 \pm 0.256$ (n = 12). Chalcopyrite has an average composition of $^{207}\text{Pb}/^{206}\text{Pb} = 0.836 \pm 0.016$ and $^{208}\text{Pb}/^{206}\text{Pb} = 2.056 \pm 0.038$ (n = 3; 2.86% 2RSE on $^{208}\text{Pb}/^{206}\text{Pb}$), and pyrrhotite has an average composition of $^{207}\text{Pb}/^{206}\text{Pb} = 0.844 \pm 0.022$ and $^{208}\text{Pb}/^{206}\text{Pb} = 2.035 \pm 0.084$ (n = 3; 5.12% 2RSE on $^{208}\text{Pb}/^{206}\text{Pb}$).

The compositions of secondary pyrite plot with similar $^{207}\text{Pb}/^{206}\text{Pb}$ to chalcopyrite, but higher $^{208}\text{Pb}/^{206}\text{Pb}$. Pentlandite has higher $^{207}\text{Pb}/^{206}\text{Pb}$ and $^{208}\text{Pb}/^{206}\text{Pb}$ than all other minerals, however, its alteration product, violarite, has similar isotopic ratios to Upper Chamber chalcopyrite.

4.3.4. Lower Chamber

The Pb concentrations and isotopic ratios of pyrrhotite, pentlandite, and chalcopyrite were measured from two samples from the Lower Chamber (Fig. 4.12. A, E). Their Pb isotopic compositions are relatively restricted, with average $^{207}\text{Pb}/^{206}\text{Pb} = 0.831 \pm 0.019$ and $^{208}\text{Pb}/^{206}\text{Pb} = 2.071 \pm 0.037$ ($n = 10$). Lower Chamber chalcopyrite has an average $^{207}\text{Pb}/^{206}\text{Pb} = 0.822 \pm 0.017$ and $^{208}\text{Pb}/^{206}\text{Pb} = 2.055 \pm 0.011$ ($n = 4$; 2.65% 2RSE on $^{208}\text{Pb}/^{206}\text{Pb}$). Pyrrhotite is characterized by higher $^{207}\text{Pb}/^{206}\text{Pb}$ than the other minerals, with an average $^{207}\text{Pb}/^{206}\text{Pb} = 0.822 \pm 0.017$ and $^{208}\text{Pb}/^{206}\text{Pb} = 2.055 \pm 0.011$ ($n = 4$; 2.65% 2RSE on $^{208}\text{Pb}/^{206}\text{Pb}$). The isotopic compositions of pentlandite are variable with average $^{207}\text{Pb}/^{206}\text{Pb} = 0.829 \pm 0.013$ and $^{208}\text{Pb}/^{206}\text{Pb} = 2.087 \pm 0.66$ ($n = 3$; 3.05% 2RSE on $^{208}\text{Pb}/^{206}\text{Pb}$).

4.3.5. Hazelton Group

The Pb concentrations and isotopic compositions of diagenetic pyrite and secondary chalcopyrite were analyzed in one sample (19-EV-46-01) from the surrounding Hazelton Group pyritic mudstones. Their Pb isotopic compositions are somewhat similar to those from the Upper Chamber, with an average $^{207}\text{Pb}/^{206}\text{Pb} = 0.834 \pm 0.020$ and $^{208}\text{Pb}/^{206}\text{Pb} = 2.062 \pm 0.109$ ($n = 7$) (Fig. 4.12. A, B). Diagenetic pyrite is characterized by an average $^{207}\text{Pb}/^{206}\text{Pb} = 0.825 \pm 0.011$ and $^{208}\text{Pb}/^{206}\text{Pb} = 2.020 \pm 0.034$ ($n = 5$), and has an average analytical uncertainty of 3.73%

2RSE on $^{208}\text{Pb}/^{206}\text{Pb}$ (Fig 4.11. D). Secondary chalcopyrite has a variable isotopic composition – there are not enough analyses to report an accurate sample average.

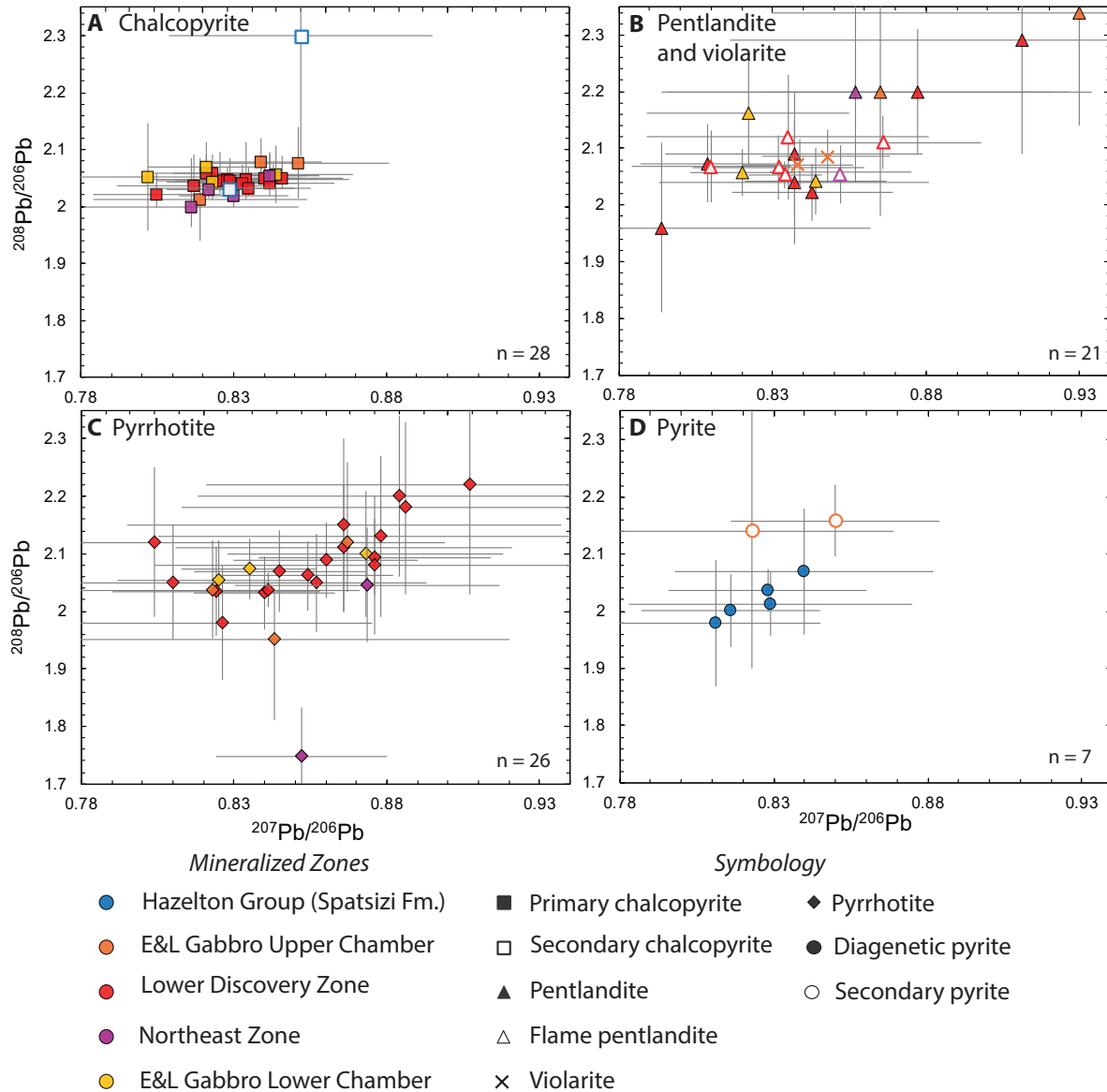


Figure 4.11. Diagram of $^{208}\text{Pb}/^{206}\text{Pb}$ vs. $^{207}\text{Pb}/^{206}\text{Pb}$ determined by LA-ICP-MS for sulfide minerals from the E&L deposit. The number of analyses ($n = xx$) is indicated in each plot and errors are reported as 2SE ($2 \times$ standard error on individual analysis). A) Analyses of primary and secondary chalcopyrite. Note the lower degree of analytical uncertainty on primary chalcopyrite compared to other minerals. B) Analyses of pentlandite, flame pentlandite and violarite. Note the relatively wider range in isotopic compositions and larger analytical uncertainty compared to primary chalcopyrite. C) Analyses of Pyrrhotite. D) Analyses of diagenetic and secondary pyrite.

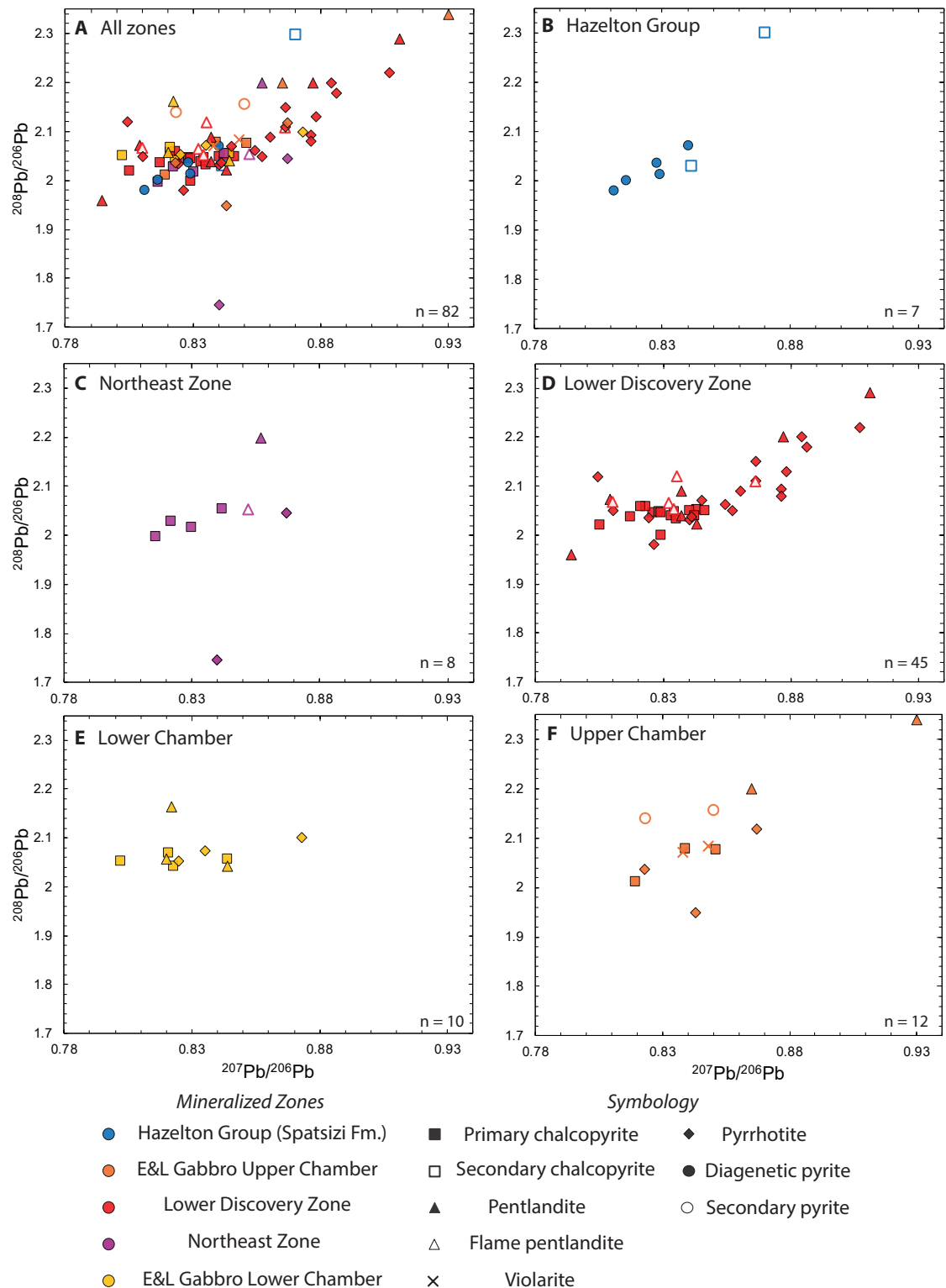


Figure 4.12. Diagram of $^{208}\text{Pb}/^{206}\text{Pb}$ vs. $^{207}\text{Pb}/^{206}\text{Pb}$ determined by LA-ICP-MS for sulfide minerals from the E&L deposit sorted by zone. The number of analyses ($n = xx$) is indicated in each plot. A) Analyses of sulfide minerals from all zones. B) Analyses of diagenetic pyrite and secondary chalcopyrite from the Hazelton Group. C) Analyses of pyrrhotite, pentlandite, and chalcopyrite from the Northeast Zone. D) Analyses of chalcopyrite, pyrrhotite, pentlandite and flame pentlandite from the Lower Discovery Zone. E) Analyses of pyrrhotite, pentlandite and chalcopyrite from the Lower Chamber. F) Analyses of pyrrhotite, pentlandite, violarite, chalcopyrite and secondary pyrite from the Upper Chamber.

5. Discussion

5.1. Insights from Sulfide Petrology

5.1.1. Deformation within the Massive Sulfide Orebodies

The significant amount of deformation twinning within pyrrhotite in the Lower Discovery Zone and Northeast Zone was likely produced at temperatures exceeding 275° C (Marshall and Gilligan, 1987). The region is interpreted to have undergone upper prehnite-pumpellyite to lower greenschist facies metamorphism, thus it is likely that pyrrhotite was also subjected to some degree of ductile deformation. At these temperatures, monoclinic pyrrhotite may have been converted back into monosulfide solid solution (mss), which would also be accompanied by resorption of flame pentlandite (Lightfoot *et al.*, 2017). In some locations, deformation twinning of pyrrhotite has the appearance akin to crenulation cleavage, however, many of these deformation twins in pyrrhotite may be exsolution lamellae. According to Lianxing and Vokes (1996), anisotropic stresses can also play a major role in controlling exsolution and annealing processes in pyrrhotite.

Zones of coarser lamellae may represent a more advanced stage of annealing relative to zones of fine lamellae, with the process proceeding to minimize strain energy. (Lianxing and Vokes, 1996). The composite lamellae may represent an even more advanced stage of annealing within pyrrhotite, where distortion of lamellae occurs. Many of these composite lamellae exhibit slight optical discontinuities, which could be evidence of strain variations within pyrrhotite grains. This suggests that annealing and maturation of lamellae in pyrrhotite could be promoted and accelerated by deformation (Lianxing and Vokes, 1996). The exsolved chalcopyrite “lineations” within pyrrhotite-rich zones of some samples display minor degrees of kink banding similarly oriented to the crenulations in pyrrhotite. Despite their crenulated appearance, the

pyrrhotite deformation twins suggest that the deposit only underwent one major deformation event. However, without studying the crystallographic orientations of pyrrhotite, it is not possible to accurately determine the number of deformation events and the principal stress directions required to produce this twinning.

Flame pentlandite is locally aligned parallel to deformation twinning in pyrrhotite within the orebodies. Evidence for recrystallization of granular pentlandite is scarce and it is likely that the metamorphic grade and time scales were insufficient for this to occur, unlike at other Ni-Cu deposits such as Sudbury (Mukwakwami *et al.*, 2014). The folded loops in 19-EV-30-01 have thick hinges with thinner limbs, which suggests that a passive folding mechanism produced these structures. All of the fold axes within the sample have roughly the same axial trace orientation. While loop textures in massive sulfides can exhibit a folded appearance, the extent to which these loops are folded is unusual and likely implicates post-crystallization deformation.

At the relatively low grade of metamorphism, there was a significant rheological contrast between the different mineral phases within the massive sulfide orebodies. The strain was accommodated by fracturing of magnetite crystals and by solid-state deformation of chalcopyrite. The magnetite fragments were remobilized within chalcopyrite, resulting in the envelopment of larger magnetite grains by fragmental “tails”. Small-scale remobilization of chalcopyrite is also evident in the Upper Chamber (e.g., 19-EV-53-08), where chalcopyrite has been remobilized and surrounded by chlorite. This remobilization process likely occurred on a relatively large scale: Cu-rich sulfide veins have been found in drill core within the host sedimentary rocks proximal to the massive sulfide intervals. A study focused on the structural geology and microscale deformation features of the deposit would be required to properly constrain and characterize the timing, duration, and number of deformation events.

5.1.2. Distribution of Trace Mineralogy in the Lower Discovery Zone

Based on petrographic and SEM investigation of samples from the Lower Discovery Zone, there is a systematic distribution of trace minerals within the Lower Discovery Zone orebody (Fig. 5.2.). The top of the Lower Discovery Zone, just below the sulfide-silicate interface, contains abundant skeletal clinopyroxene crystals (up to 15 vol%). These “phenocrysts” are interpreted to have been scavenged from the overlying silicate melt. Near the top of the Lower Discovery Zone orebody, there is also an unusually magnetite-rich layer, comprising up to 36 vol% in sample 19-EV-53-03. The magnetite content within the ores gradually increases from the bottom of the orebody (reaching on average <2 vol%), before sharply increasing in abundance near the top. The origin of this magnetite layer is discussed below in section 5.1.3. and could be due to cotectic crystallization or settling of magnetite from the silicate melt.

The electrum and sphalerite abundances of the trace mineral assemblage also increase towards the top of the orebody, the former of which is reflected by a progressive increase in the gold, silver, and zinc concentrations up-hole within the Lower Discovery Zone (Fig. 5.3.). This distribution is compatible with the current understanding of sulfide melt crystallization. During fractional crystallization of a sulfide melt, Au, Ag, and Zn will partition into the residual fractionated sulfide liquid or intermediate solid solution (iss), rather than being incorporated into monosulfide solid solution (mss) (Dare *et al.*, 2010; Lightfoot, 2016; Mansur *et al.*, 2019). Zinc is most likely to pair with sulfur to form sphalerite, whereas Au and Ag will pair together to form electrum.

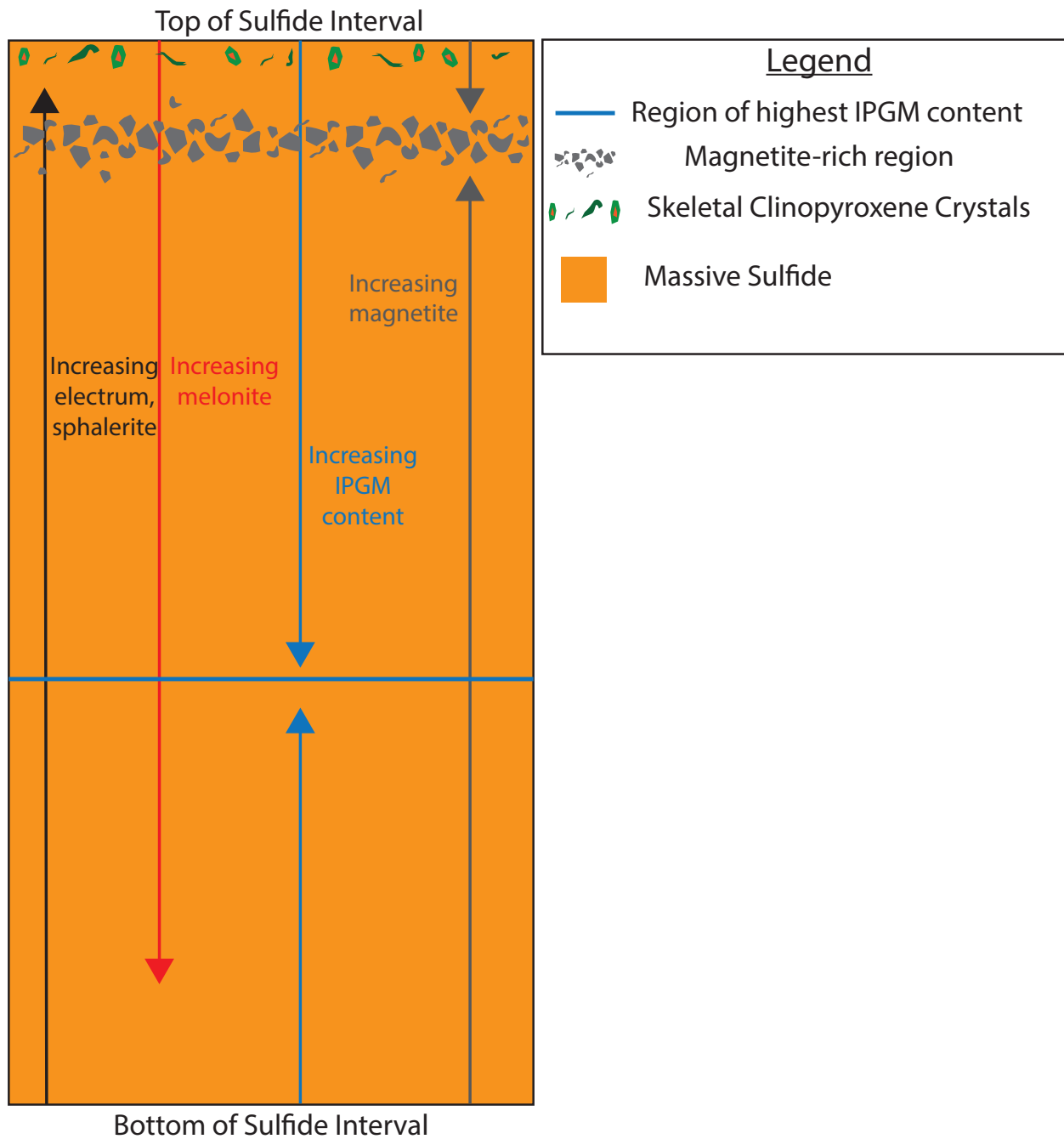


Figure 5.1. Schematic diagram of the Lower Discovery Zone illustrating variations in the trace mineralogy with stratigraphic position in the sulfide orebody. Not to scale.

EL-19-48

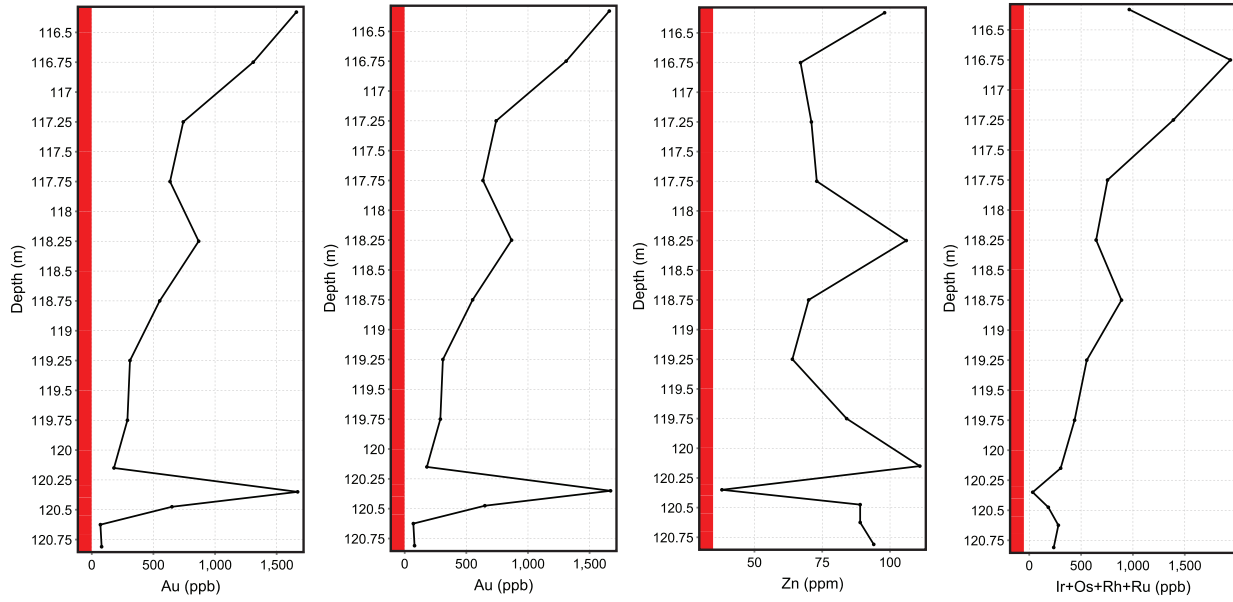


Figure 5.2. Stratigraphic variations in Au, Ag, Zn, and IPGE (Os, Rh, Ru, Ir) concentrations within the Lower Discovery Zone for borehole EL-19-48 (Garibaldi Resources Corporation, unpublished data).

EL-19-53

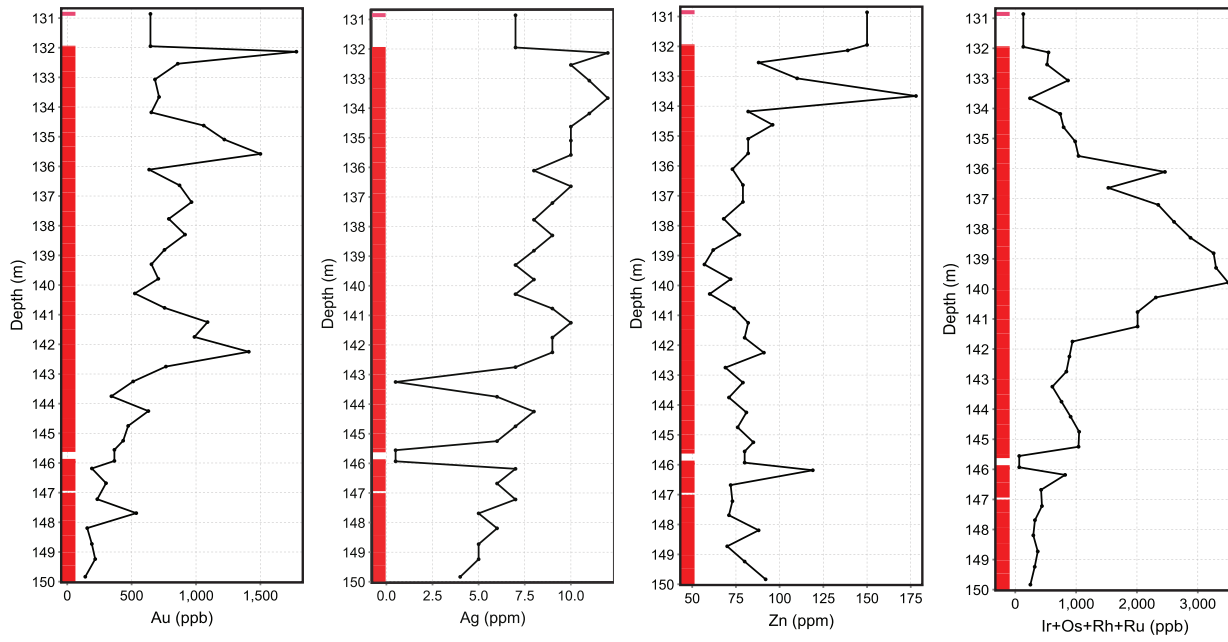


Figure 5.3. Stratigraphic variations in Au, Ag, Zn, and IPGE (Os, Rh, Ru, Ir) concentrations within the Lower Discovery Zone for borehole EL-19-53 (Garibaldi Resources Corporation, unpublished data).

There is no stratigraphic variation in the dominant Pt- and Pd-bearing minerals within the Lower Discovery Zone. Merenskyite, moncheite, and sperrylite are the dominant Pt-platinum group element (PPGE)-bearing minerals throughout the orebody. However, the abundance of Ir-platinum group minerals (IPGM) (i.e., Ru-, Rh-, Ir-, Os-bearing) increases towards the middle of the orebody. The most common IPGM within the Lower Discovery Zone is Rh-telluride, which is most abundant in sample 19-EV-48-03. This trend is reflected in the peak of IPGE concentration towards the middle of the massive sulfide interval and is also consistent with the current understanding of massive sulfide crystallization trends (Fig. 5.3.). Unlike Au, Ag, Pt, and Pd, the IPGE are most compatible in mss (Dare *et al.*, 2010; Mansur *et al.*, 2019). Moreover, within mss, the IPGE will diffuse towards the boundary with iss, thus explaining their highest concentrations within the middle of the orebody (Mansur *et al.*, 2019). Melonite is the one trace mineral that increases in abundance towards the bottom of the orebody. This could be due to the decreasing highly siderophile elements available to pair with Te. However, tellurium is most compatible with iss (Mansur, 2019) and decreases in concentration towards the bottom of the massive sulfide interval, thus the origin of this trend remains unresolved.

5.1.3. Origin of the Peculiar Magnetite Textures

As previously described in sections 4.1.3. and 4.1.4, the sieve-textured magnetites of the Lower Chamber and pseudo-cuneiform magnetite of the Lower Discovery Zone are unlike any previously described textures from a magmatic Ni-Cu-PGE deposit. Although it is common for magnetite to experience a relatively low degree of resorption during the crystallization and differentiation of an immiscible sulfide melt (Prichard *et al.*, 2004), the magnetite textures within the E&L deposit may be indicative of high degrees of resorption under disequilibrium

conditions. The modal percentage of magnetite within some horizons of the massive sulfide orebodies (up to 36 vol%) is unusual for a magmatic sulfide deposit. According to Naldrett (1969), most magmatic ores contain less than 10 vol% magnetite, although closed-system crystallization of a Fe-S-O melt under closed system conditions can produce ores with up to 40 vol% magnetite. Most ore-forming systems do not behave as closed systems, therefore this is an unsuitable explanation for the abundance of magnetite within the upper portion of the Lower Discovery Zone. Under closed-system conditions, magnetite should be evenly distributed throughout the orebody (e.g., Voisey's Bay) (Naldrett *et al.*, 2000), whereas the E&L deposit contains a single magnetite-rich horizon and a low modal abundance throughout the rest of the orebody.

Given the tectonic setting of the Eskay Rift during the Jurassic, the E&L parent magma was likely relatively hydrous, given its arc or back-arc origin (Sinton & Fryer, 1987). The relatively high-temperature, hydrous nature of the E&L parent magma may be manifested by the orbicular textures within the Upper Chamber (Peter Lightfoot, pers. comm., June 10, 2019). Sulfide saturation could have occurred at relatively high oxygen fugacity (fO_2), but still lower than oxygen fugacities equivalent to the quartz-fayalite-magnetite (QFM) buffer, compared to other magmatic sulfide ores. At such an fO_2 , monosulfide solid solution would still be the first solid phase to crystallize out of the sulfide melt, however, the liquid-line-of-descent will reach the mss-magnetite cotectic at a higher temperature compared to other systems (Naldrett, 1969). This would result in a higher modal percentage of magnetite within the massive sulfides, which is the first requirement for generating a magnetite-rich horizon within the Lower Discovery Zone.

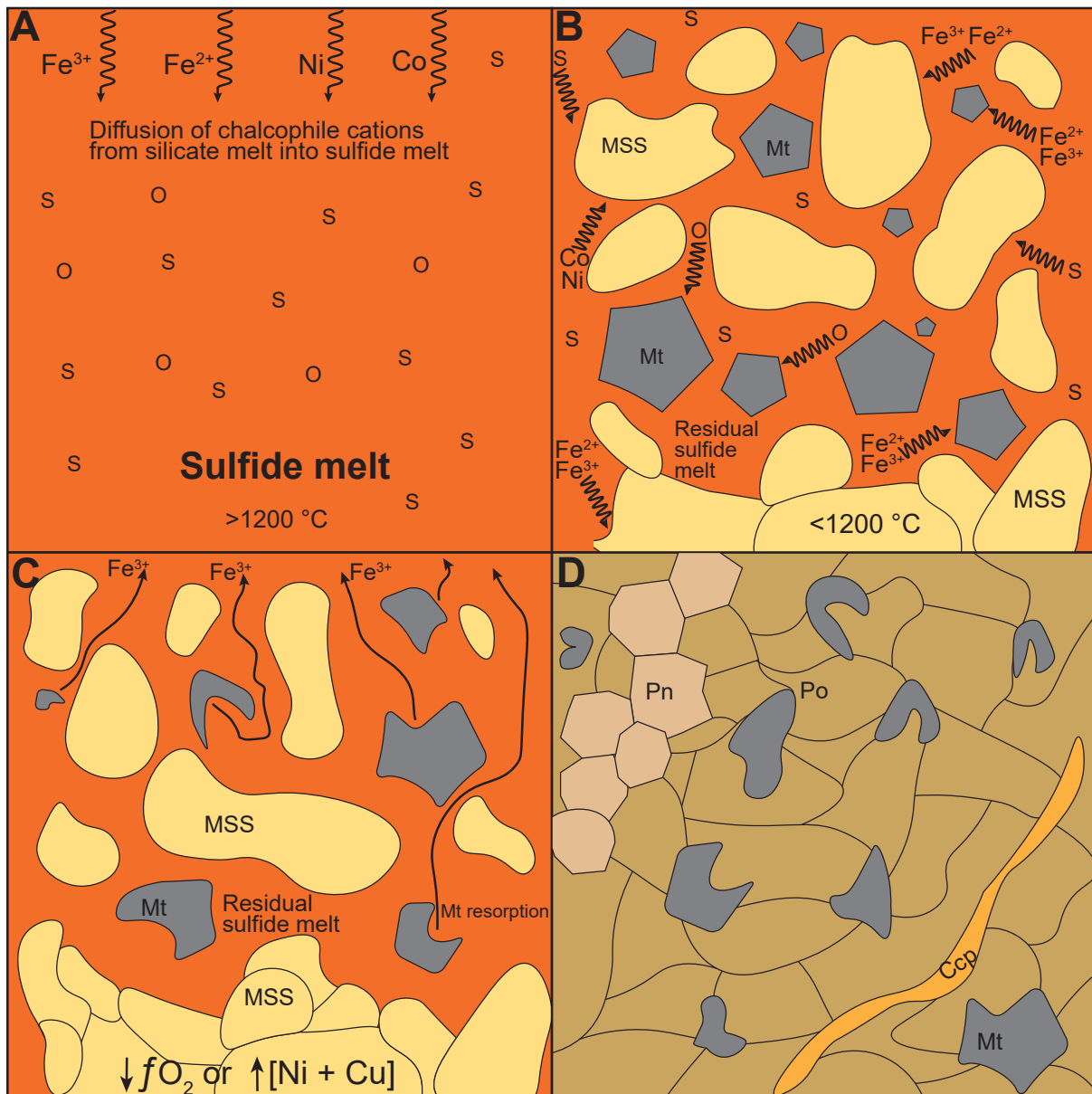


Figure 5.4. Schematic diagram illustrating the potential origin of the “pseudo-cuneiform” magnetite in the Lower Discovery Zone (adapted from Fonseca *et al.*, 2008; Dare *et al.*, 2012; Boutroy *et al.*, 2014). A) Diffusion of chalcophile cations from the overlying silicate melt into the sulfide melt, including Fe^{3+} . B) Cooling of the sulfide melt results in the crystallization of mss and magnetite along a cotectic; some Fe^{3+} from the melt is incorporated in magnetite. C) A shift to disequilibrium conditions triggers the resorption of magnetite back into the melt, potentially causing Fe^{3+} to diffuse back into the silicate melt. D) Fully crystallized pyrrhotite-pentlandite-chalcopyrite massive sulfide with “pseudo-cuneiform” magnetite.

The relatively hydrous nature of the E&L parent magma may also explain the distribution of sulfide textures within the deposit. In the Upper Chamber, the majority of the disseminated sulfides exhibit a rounded to subrounded and ameboidal morphology. The addition of H₂O lowers the liquidus of a silicate melt, but has a negligible impact upon the liquidus of a sulfide melt (Naldrett, 1969). In the Upper Chamber, the spherical sulfide bleb morphology may reflect the formation of sulfide droplets prior to the silicate liquidus being reached and the simultaneous crystallization of sulfide and silicate minerals, similar to the process that gave rise to this texture at Noril'sk-Talnakh (Barnes *et al.*, 2019), and within a Uruguayan mafic dike (Prichard *et al.*, 2004). Conversely, provided that the interpretation of the Lower Chamber as a cumulate pile is correct, the silicate melt in this zone would have reached the liquidus before the sulfide melt, forcing the sulfide to occupy the interstices between silicate grains, forming the observed semi-net to net-textured sulfides (Barnes *et al.*, 2017). The inferred crystallization histories of the two chambers also reconcile the differences in the abundance of magnetite and its textural variations. Magnetite within the Upper Chamber commonly contains oxy-exsolved lamellae of ilmenite within its structure, which suggests that they did not originate from the sulfide melt, as these melts do not contain significant amounts of Ti. The crystallization of mss would have increased the fO_2 of the sulfide melt and caused the diffusion of Fe₂O₃ outwards towards the sulfide-silicate interface. At this interface, Fe₂O₃ would be able to combine with the FeO and TiO₂ in the silicate melt, producing the observed titanomagnetite, as previously inferred for other deposits (Naldrett, 1969; Naldrett *et al.*, 2000; Prichard *et al.*, 2004; Fonseca *et al.*, 2008; Dare *et al.*, 2012). In contrast, the lack of ilmenite lamellae within magnetite from the Lower Discovery Zone magnetites suggests that they originated from the sulfide, rather than the silicate melt. Percolation of sulfide droplets into a cumulate pile provides a reasonable explanation for the

abundance of sieve-textured magnetite within the Lower Chamber. Following the percolation of sulfide droplets from the melt, the cumulates of the Lower Chamber would have allowed for the majority of oxygen to remain within the sulfide droplets during interstitial infilling and crystallize along the mss-magnetite cotectic (Naldrett, 1969). There is, however, a small proportion of titanomagnetite that exists along sulfide-silicate interfaces within the Lower Chamber samples. This is interpreted to be the result of small-scale ferric iron (Fe^{3+}) diffusion into an evolved melt residue. As the rate of sulfide droplet settling exceeds the sulfide-silicate equilibration timescale (Mungall, 2002; Robertson *et al.*, 2015; Barnes and Robertson, 2019), the relative rates of settling within the two chambers likely did not play a significant role in the formation of these minerals.

The last step in producing the magnetite textures within the Lower Discovery Zone and Lower Chamber is disequilibrium-induced resorption. These conditions require the disturbance of the magmatic system (including the sulfide melt) (Fig. 5.4.). This disturbance could be attributed to the introduction of a new, more anhydrous pulse of magma into the E&L magmatic system. This hypothetical magma batch would have had a lower relative $f\text{O}_2$ than previous batches, allowing for easier diffusion of ferric iron (Fe^{3+}) back into the silicate melt from the sulfide melt. This would lower the oxygen content of the sulfide melt, pushing the system off of the mss-pyrrhotite cotectic and back into the mss field. This shift would require magnetite resorption, accounting for the pseudo-cuneiform and sieve-textured magnetites. Alternatively, this resorption could also be triggered by the progressive upgrading of the Ni + Cu content of the sulfide melt. Celmer (1988) and Naldrett (1989) investigated the role of Ni and Cu content on the oxygen content of sulfide melts. In sulfide melts with higher Ni and Cu content, oxygen is less soluble compared to in more Fe-rich melts (Celmer, 1988; Naldrett, 1989; Yoshiki-Gravelsins

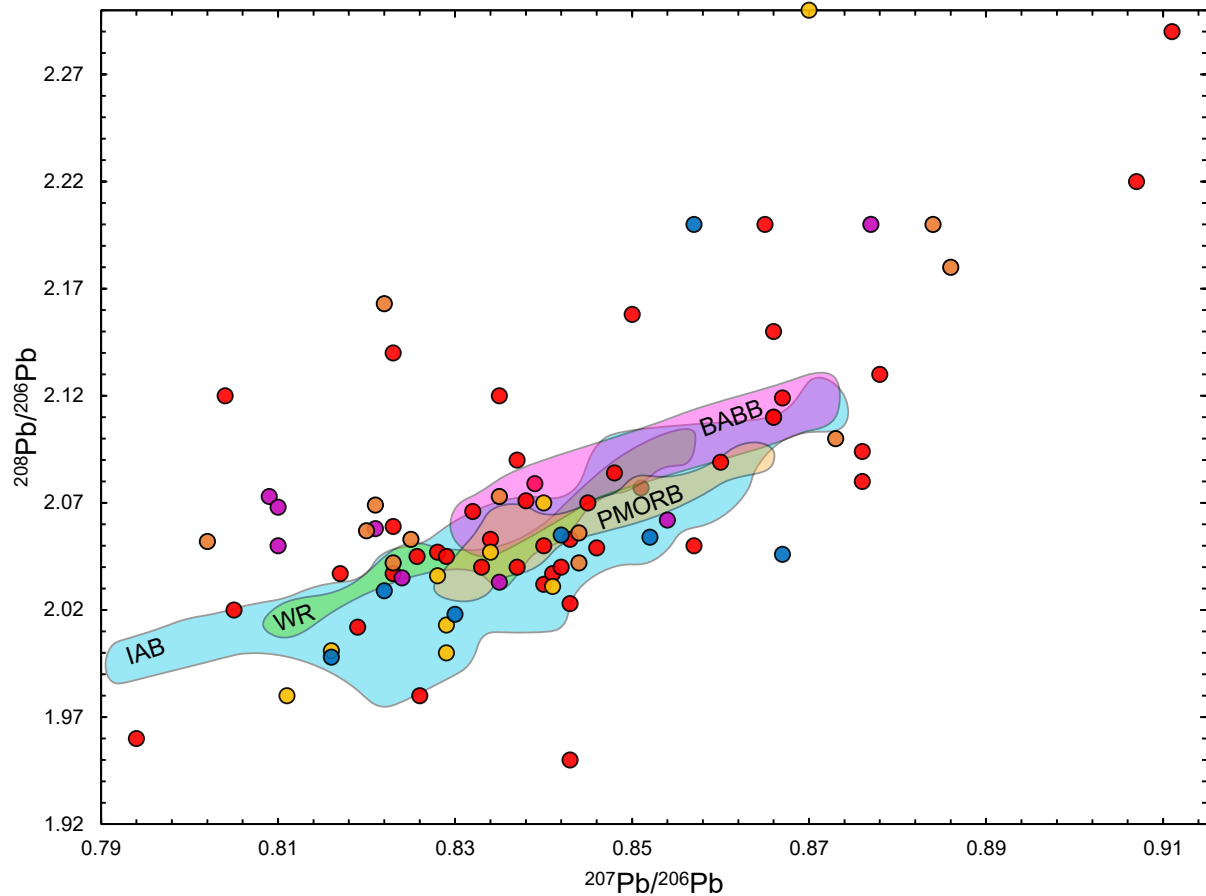
and Toguri, 1993). Thus, upgrading the Ni and Cu content of the Lower Discovery Zone sulfide melt could have resulted in an upward shift of the magnetite-mss cotectic, causing the system to switch back to only crystallizing mss out of the melt. This process could result in the resorption of crystallized magnetite back into the sulfide melt.

5.2. Insights from Pb Isotopic Analysis of Sulfide Minerals

5.2.1. Source of Mineralization and Effect of Crustal Assimilation on the Isotopic Signatures of Sulfides

The relatively large range in Pb isotope ratios determined for sulfide minerals from the E&L intrusion allows for evaluation of the source of mineralization and the potential effect of crustal assimilation during magma transport, emplacement, and crystallization. The isotopic compositions of the sulfide minerals overlap with age-corrected $^{208}\text{Pb}/^{206}\text{Pb}$ - $^{207}\text{Pb}/^{206}\text{Pb}$ fields for island-arc basalts (IAB), Pacific MORB (PMORB) (White *et al.*, 1987; White, 1993), the Wrangellia large igneous province or LIP (WR) (Greene *et al.*, 2009) and back-arc basin basalts (BABB) (Fig. 5.5.). Given the similar isotopic signatures of these fields defined by these relatively young rocks, interpretation of geodynamic setting solely on the basis of $^{208}\text{Pb}/^{206}\text{Pb}$ - $^{207}\text{Pb}/^{206}\text{Pb}$ diagrams is insufficient, however, inferences on source and assimilation can be made.

The measured isotopic ratios of E&L sulfides are compared with a number of potential sources and influencing reservoirs in Figure 5.6. The majority of sulfide analyses plot close to the upper crustal and orogene growth curves of Zartman and Haines (1988) with only a few analyses plotting close to the mantle growth curve or the lower crustal growth curve. This suggests an overwhelmingly crustal source for the Pb within the sulfides, as mantle-sourced Pb is isotopically unradiogenic compared to Pb derived from the upper crust. This crustal influence is



Mineralized Zones

- Hazelton Group (Spatsizi Fm.)
- E&L Gabbro Upper Chamber
- Lower Discovery Zone
- Northeast Zone
- E&L Gabbro Lower Chamber

Figure 5.5. Plot of $^{208}\text{Pb}/^{206}\text{Pb}$ vs. $^{207}\text{Pb}/^{206}\text{Pb}$ comparing the LA-ICP-MS isotopic compositions of E&L sulfides with age-corrected fields for back-arc basin basalts (BABB), the Wrangellia large igneous province (WR), Pacific Ocean MORB (PMORB), and island-arc basalts (IAB). All global values were corrected to an age of 180 Ma assuming $\mu = 7.2$ and $\omega = 18.0$ for BABB, $\mu = 12.7$ and $\omega = 34.3$ for PMORB, and $\mu = 8.3$ and $\omega = 32.37$ for IAB. Data for Wrangellia are from Greene *et al.* (2009), data for BABB and IAB were obtained from the PetDB database (<https://www.earthchem.org/petdb>) and data for PMORB are from White *et al.* (1987) and White (1993). Note that the 2s uncertainty error bars are not shown for the results from this study for clarity.

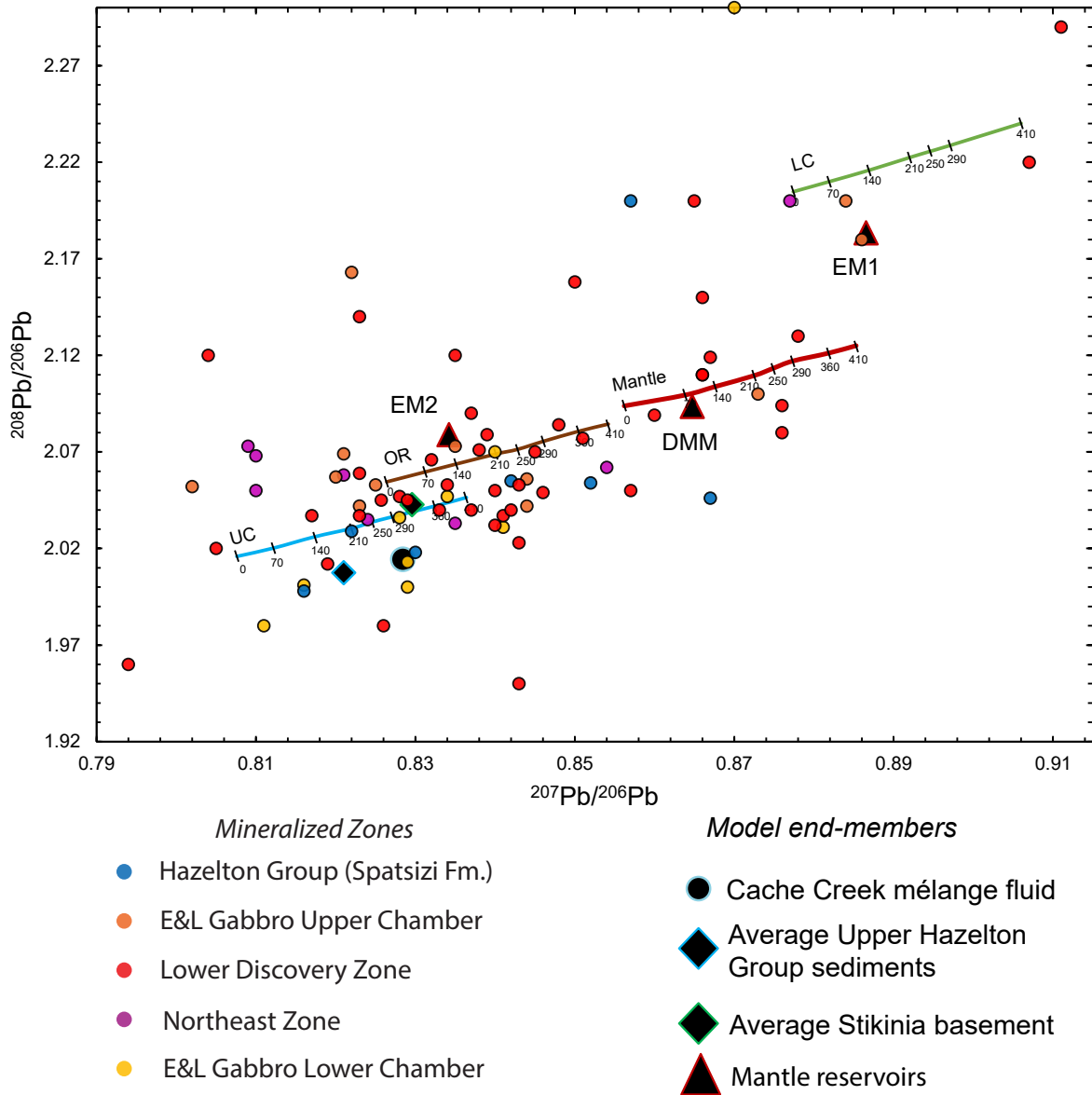


Figure 5.6. Plot of $^{208}\text{Pb}/^{206}\text{Pb}$ vs. $^{207}\text{Pb}/^{206}\text{Pb}$ comparing the LA-IC-MS isotopic compositions of E&L sulfides with the plumbotectonics growth curves of Zartman and Haines (1988) and potential reservoirs that could produce the observed isotopic ratios in sulfides. Growth curves are labelled from 0 Ma (present day) to 410 Ma. Abbreviations: DMM – depleted MORB mantle, EM1 – enriched mantle 1, EM2 – enriched mantle 2, UC – upper crust, OR – Orogene, LC – Lower Crust. DMM and Cache Creek mélange fluid values are corrected to 180 Ma assuming $\mu = 5$ and $\omega = 12.5$ for DMM, and assuming $\mu = 15.5$ and $\omega = 27.3$ for Cache Creek mélange. Values for EM1 and EM2 are present-day values. The average value of Upper Hazelton Group sedimentary rocks is from Garibaldi Resources Corporation (unpublished data). Data sources: DMM (White, 1993; Salters and Stracke, 2004; Jackson and Dasgupta, 2008), EM1 and EM2 (Zindler and Hart, 1986; Workman *et al.*, 2004; Jackson and Dasgupta, 2008), Cache Creek mélange fluid (King *et al.*, 2007), average Stikinia basement (Godwin *et al.*, 1990). Note that the 2 σ uncertainty error bars are not shown for the results from this study for clarity.

also reflected in the number of analyses that plot close to the composition of average Stikinia basement, as inferred by the average isotopic composition of galena from the Iskut-Unuk region of Godwin *et al.* (1990), and to a lesser degree, the composition of average sedimentary rocks of the Upper Hazelton Group. The underlying Stikinia arc basement likely played an important role in controlling the Pb isotopic evolution of this magmatic system. The age of this basement can be constrained to Triassic-Jurassic, as the Pb isotopic compositions of the Paleozoic intrusions in the area (e.g., Forrest Kerr Pluton) have isotopic compositions that are insufficiently radiogenic to explain the observed trends (Childe, 1996) (Fig. 5.10.).

Subduction underneath Stikinia occurred continuously from the Pennsylvanian until the early Toarcian (Marsden and Thorkelson, 1992; Nelson *et al.*, 2013), thus mantle metasomatism likely had a significant influence on the source of this E&L mineralization. King *et al.* (2007) demonstrated that the contribution of mélangé-derived fluids to the Pb isotopic compositions of arc magmas can be significant in some convergent margin settings. During subduction, especially during the Upper Triassic and Lower Jurassic, fluids from the Cache Creek mélangé may have been introduced into the mantle wedge beneath Stikinia, along with fluids resulting from devolatilization of the subducting slab. The composition of this mélangé-derived fluid is inferred from Catalina mélangé fluid isotopic compositions back-corrected to 180 Ma (King *et al.*, 2007) (Fig. 5.6.). Although the potential input of this fluid may have had an influence on source isotopic compositions, its composition plots too close to the compositions of the crustal reservoir for its contribution to be examined given the relative precision of the LA-ICP-MS analyses.

Two-stage binary mixing equations following the method of Langmuir *et al.* (1978) were examined to explore the role of mixing between different mantle and crustal reservoirs in the

Table 5.1. Summary of end-members used in E&L mixing modelling.

End-member	$^{207}\text{Pb}/^{206}\text{Pb}$	$^{208}\text{Pb}/^{206}\text{Pb}$	Pb (ppm)
DMM	0.8647	2.094	0.0232
EM-I	0.8865	2.183	0.144
Melt (98% DMM – 2% EM1)	0.8672	2.104	6.56
Average Stikinia basement	0.8296	2.043	14
Average Upper Hazelton Group sediments	0.821	2.0075	15
Cache Creek mélange fluid	0.8284	2.014	2.67

Data Sources: Pb isotopes – DMM (White, 1993; Salters and Stracke, 2004; Jackson and Dasgupta, 2008), EM1 (Zindler and Hart, 1986; Jackson and Dasgupta, 2008), average Stikinia basement (Godwin *et al.*, 1990), Cache Creek mélange fluid (King *et al.*, 2007); Pb concentrations – DMM (Salters and Stracke, 2004), EM1 (Workman *et al.*, 2004), melt ((Workman *et al.*, 2004), average Stikinia basement and Upper Hazelton Group sediments (Garibaldi Resources Corporation, unpublished data), Cache Creek mélange fluid (King *et al.*, 2007).

genesis of the E&L deposit (Table 5.1.). The first stage involves mixing between mantle reservoirs, in which an EM-1 mantle source ($^{208}\text{Pb}/^{206}\text{Pb} = 2.183$, $^{207}\text{Pb}/^{206}\text{Pb} = 0.8865$, Pb = 0.144 ppm) (Zindler and Hart, 1986; Jackson and Dasgupta, 2008) is mixed to variable degrees with a DMM mantle source ($^{208}\text{Pb}/^{206}\text{Pb} = 2.094$, $^{207}\text{Pb}/^{206}\text{Pb} = 0.8647$, Pb = 0.0232 ppm) (White, 1993; Salters and Stracke, 2004; Jackson and Dasgupta, 2008) to produce the uncontaminated E&L parent magma. The second stage involves mixing between the E&L parent magma with crustal reservoirs. Given that many of the sulfides are characterized by relatively low $^{208}\text{Pb}/^{206}\text{Pb}$ and $^{207}\text{Pb}/^{206}\text{Pb}$, one of these reservoirs must be relatively U-rich and Th-poor. As E&L intrusion was emplaced into pyritic black shales, the average sedimentary rocks of the Upper Hazelton Group ($^{208}\text{Pb}/^{206}\text{Pb} = 2.0075$, $^{207}\text{Pb}/^{206}\text{Pb} = 0.821$, Pb = 15 ppm) is inferred to be one of these reservoirs, as black shales are typically U-rich (Bell, 1978). The other crustal reservoir is the average Stikinia basement ($^{208}\text{Pb}/^{206}\text{Pb} = 2.043$, $^{207}\text{Pb}/^{206}\text{Pb} = 0.8296$, Pb = 14 ppm) (Godwin *et al.*, 1990).

One of the possible two-stage mixing models involves mixing of 98% DMM with 2% EM-1 to produce the E&L parent magma ($^{208}\text{Pb}/^{206}\text{Pb} = 2.104$, $^{207}\text{Pb}/^{206}\text{Pb} = 0.8672$, Pb = 6.56 ppm) (Fig. 5.7.). The stage 2 process is illustrated as mixing lines between the mantle melt composition (red-filled star) with average Stikinia basement and with average Upper Hazelton group, however, crustal assimilation likely involves both crustal end-members. Stage 2 mixing is able to reproduce the range of many of the observed sulfide isotopic compositions, although given the relatively large spread of the results, mixing with other sources cannot be ruled out. The formation of E&L intrusion and deposit may have involved multiple pulses of magma with variable degrees of mixing between mantle reservoirs (e.g., Nicholson and Shirey, 1990), a process that could explain the relatively unradiogenic heterogeneities in the isotopic

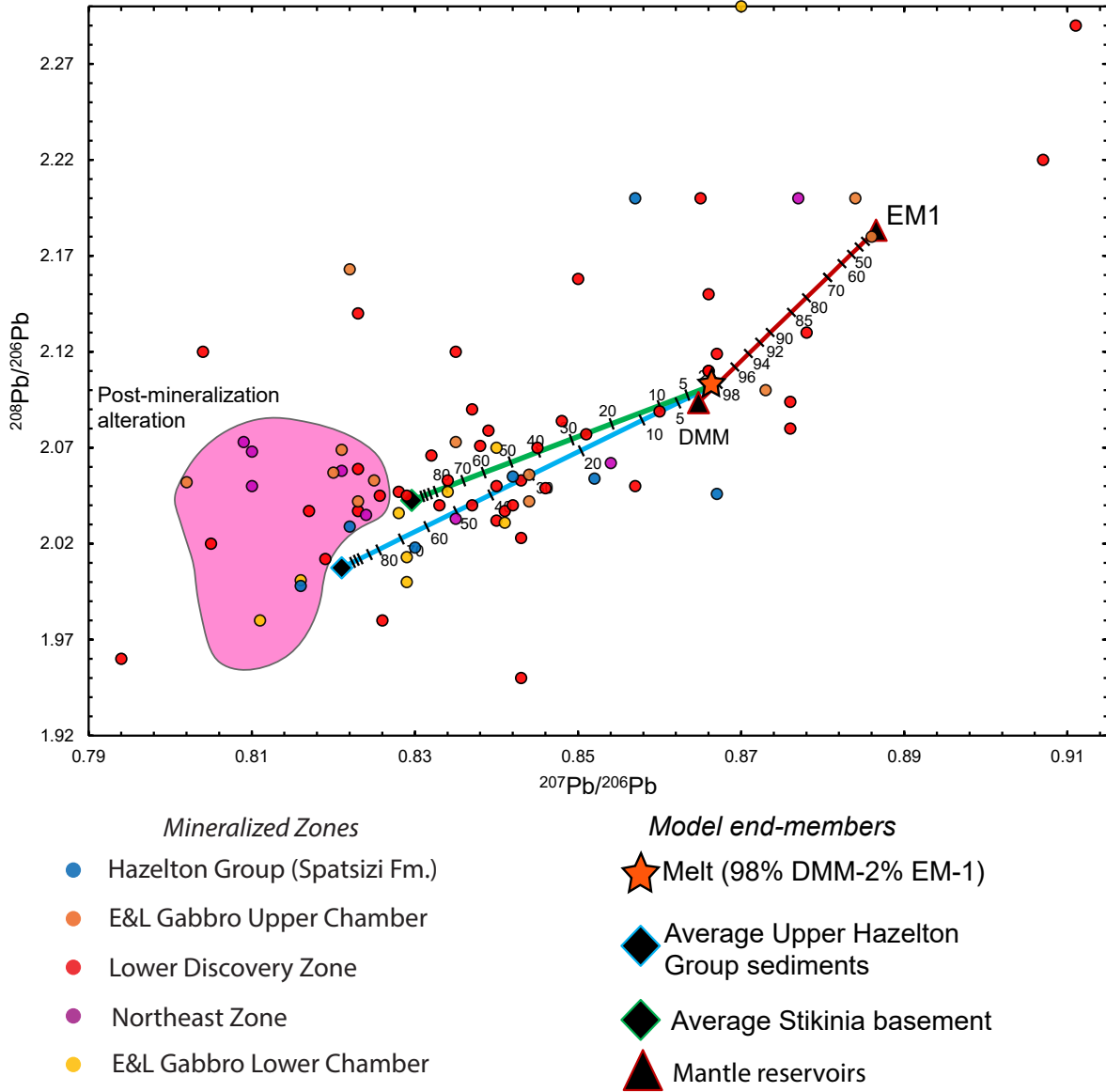


Figure 5.7. Plot of $^{208}\text{Pb}/^{206}\text{Pb}$ vs. $^{207}\text{Pb}/^{206}\text{Pb}$ showing petrogenetic processes and mixing arrays between end members: EM1 and DMM (black triangles with red outline), Melt (98% DMM + 2% EM1) (orange star), average Upper Hazelton Group sedimentary rocks (black diamond with blue outline), and average Stikinia basement (black diamond with green outline). The production of the parental melt is modeled to involve mixing between EM1 and DMM sources (red line). Subsequent contamination of this melt by average Stikinia basement (green line) and average Upper Hazelton Group sedimentary rocks (blue line) could produce many of the observed isotopic compositions recorded in the E&L sulfides. Post-mineralization modification due to hydrothermal and meteoric fluids could produce the relatively radiogenic isotopic compositions of sulfides highlighted within the pink field. Note that other processes may be involved. Numbers along mixing line numbers are percentages. Data sources: DMM (White, 1993; Salters and Stracke, 2004; Jackson and Dasgupta, 2008), EM1 (Zindler and Hart, 1986; Jackson and Dasgupta, 2008), average Stikinia basement (Godwin *et al.*, 1990), average Upper Hazelton Group sedimentary rocks (Garibaldi Resources Corporation, unpublished data). Note that the 2s uncertainty error bars are not shown for the results from this study for clarity.

compositions of some of the sulfides. The E&L parent magmas were likely contaminated by Stikinia island arc basement deeper in the crust, where magmas may have been stored within staging chambers and underwent crustal assimilation and magma mixing, as has been hypothesized for other mafic magmatic systems such as Noril'sk-Talnakh (Wooden *et al.*, 1992), Aguablanca (Tornos *et al.*, 2001), and Skaergaard (Cho, 2019). Crustal contamination by Upper Hazelton Group sediments occurred at higher crustal levels and may have been the trigger of sulfide liquid saturation. Numerous pulses of magma during the formation of the deposit could also explain the differences between the isotopic compositions of the Upper and Lower Chamber sulfides, where isotopic equilibration did not occur due to the relative lack of sulfide-sulfide grain contacts (e.g., Jinchuan, Yang *et al.*, 2007). Post-mineralization modification of the deposit could explain the analyses with lower isotopic ratios, particularly $^{207}\text{Pb}/^{206}\text{Pb}$, compared to those of the crustal reservoirs (Fig. 5.7.). Post-mineralization alteration likely gave rise to the discrepancies between the Pb isotopic compositions of sulfides and feldspars in the Bushveld Complex where the feldspars were closed to Pb addition, while the sulfides remained open (Mathez and Waight, 2007; Ripley and Li, 2007). Thus, for E&L, an influx of U-rich, radiogenic hydrothermal fluid could have changed the Pb isotopic signature of the magmatic sulfides through the addition of radiogenic Pb, a process that may have occurred during regional metamorphism in the Cretaceous (Hancock, 1990).

5.2.2. Crystallization History of Sulfides and Potential Influence on Isotopic Compositions

The observed trend in the isotopic compositions of sulfide minerals from the Lower Discovery Zone can potentially be explained by the crystallization of an immiscible sulfide melt. The majority of the pyrrhotite and granular pentlandite analyses have Pb isotopic compositions

that are relatively less radiogenic than those of flame pentlandite and chalcopyrite (Fig. 5.8.), although most of the analyses just overlap within analytical uncertainty (Fig. 4.10.). Given that granular pentlandite and pyrrhotite are high-temperature exsolutions of mss, there may have been less time for the adjacent country rocks to impart a radiogenic isotopic signature upon these minerals. As a result, the isotopic ratios of these early crystallization products may represent compositions closer to those of the magma source, rather than the country rock. However, as the sulfide melt cooled, the Pb isotopic compositions of sulfide minerals that crystallized out of the immiscible sulfide melt would become increasingly radiogenic, reflecting the isotopic compositions of the country rock rather than of the magma source. Thus, the sulfide minerals that crystallized from iss (chalcopyrite, galena, electrum, etc.), as well as low-temperature flame pentlandite exsolutions from pyrrhotite, would have relatively radiogenic isotopic compositions. A few pyrrhotite analyses have lower, more radiogenic ratios compared to the majority of the analyses of this mineral (Fig. 4.11. C) and could be explained by the exsolution of monoclinic pyrrhotite from the higher temperature hexagonal pyrrhotite, a process that occurs at relatively low temperatures (Naldrett, 2010).

An alternative explanation for the observed trend involves the post-mineralization alteration of the sulfide orebody. Given that Pb is relatively mobile and is concentrated in sulfides, and that sulfide minerals can re-equilibrate at relatively low temperatures, the Pb isotopic compositions of sulfide minerals may record low-temperature processes (e.g., Mathez and Waight, 2003). Cation diffusion typically occurs in chalcopyrite at lower temperatures than in pyrrhotite (Cherniak, 2010). Thus, the minerals that crystallized at lower temperatures may record overprinting by hydrothermal fluids at temperatures below the closure temperature for hexagonal pyrrhotite. Given that Pb is highly soluble in chloride-rich fluids (Seccombe and

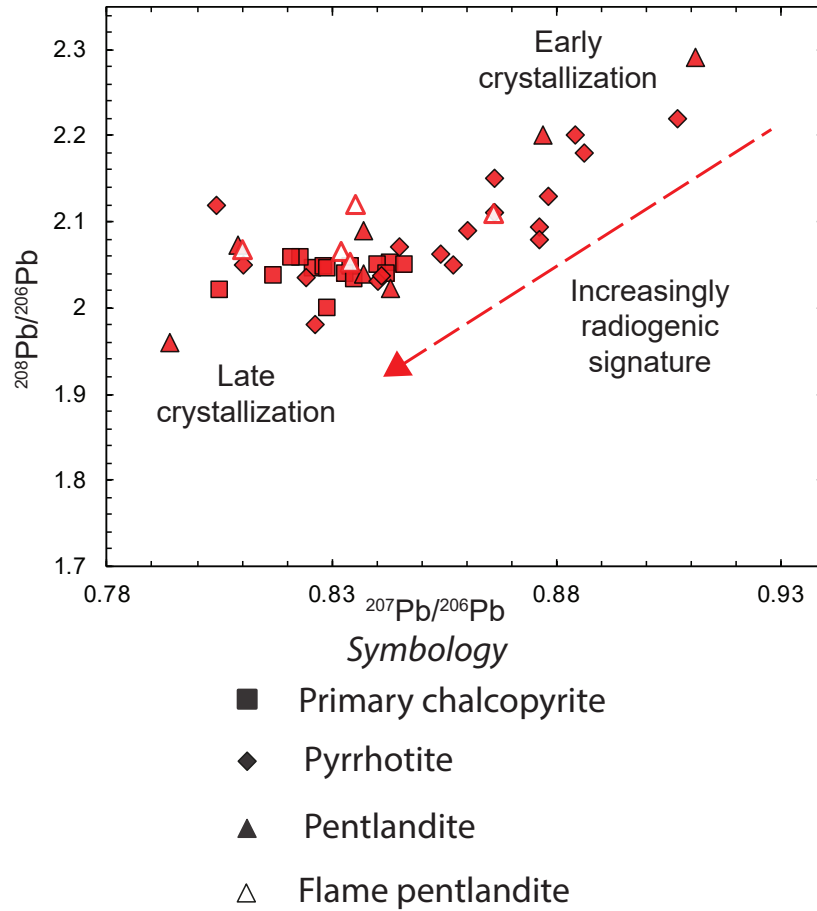


Figure 5.8. Plot of $^{208}\text{Pb}/^{206}\text{Pb}$ vs. $^{207}\text{Pb}/^{206}\text{Pb}$ for sulfides from the Lower Discovery Zone. The sulfides are divided into an “early crystallization” stage with relatively unradiogenic Pb isotopic compositions and a “late crystallization” stage with relatively radiogenic compositions. Note that the 2s uncertainty error bars are not shown for clarity.

Barnes, 1990) and that the Nickel Mountain gabbros, and E&L gabbros to a lesser degree, have undergone potassic alteration, this is a possible scenario.

5.2.3. Stratigraphic Variations in Pb Isotopic Compositions in the Lower Discovery Zone Orebody

The average $^{208}\text{Pb}/^{206}\text{Pb}$ - $^{207}\text{Pb}/^{208}\text{Pb}$ isotopic compositions of massive sulfide samples change through a vertical transect of the Lower Discovery Zone orebody (EL-19-53) (Fig. 5.9). The average Pb isotopic composition for each sample was calculated by taking a weighted average based on its modal mineralogy. From these average values, a number of observations can be made. The upper part of the Lower Discovery Zone orebody is characterized by relatively radiogenic $^{208}\text{Pb}/^{206}\text{Pb}$ and $^{207}\text{Pb}/^{208}\text{Pb}$, which decrease slightly downsection before increasing again near the base of the orebody. The relatively radiogenic isotopic ratios in the top of the massive sulfide interval could be due to fractionation processes within the sulfide orebody, where the residual iss liquid would rise to the top of the interval during crystallization and would have had more time to interact with and diffuse Pb from the adjacent country rocks, similar to the process mentioned in the previous section. The transition to higher $^{208}\text{Pb}/^{206}\text{Pb}$ and $^{207}\text{Pb}/^{208}\text{Pb}$ may reflect the transition from iss to mss, where sulfides would crystallize at higher temperatures and thus diffuse less Pb from the country rocks. The progressive decrease in Pb isotopic ratios towards the bottom of the massive sulfide orebody could have resulted from increasing crustal contributions to the Pb isotopic compositions of the sulfides, owing to the relatively U-rich nature of the pyritic mudstones. The increase in Pb isotopic ratios at the bottom of the orebody could be due to contact with a less radiogenic sedimentary layer (e.g., Darling *et al.*, 2012; McNamara *et al.*, 2017) or due to chilled margin crystallization of a thin layer of sulfide (e.g.,



Figure 5.9. Stratigraphic variations in modal percentage-corrected average $^{208}\text{Pb}/^{206}\text{Pb}$ and $^{207}\text{Pb}/^{206}\text{Pb}$ for borehole EL-19-53. Note that the 2s error bars are not shown for clarity.

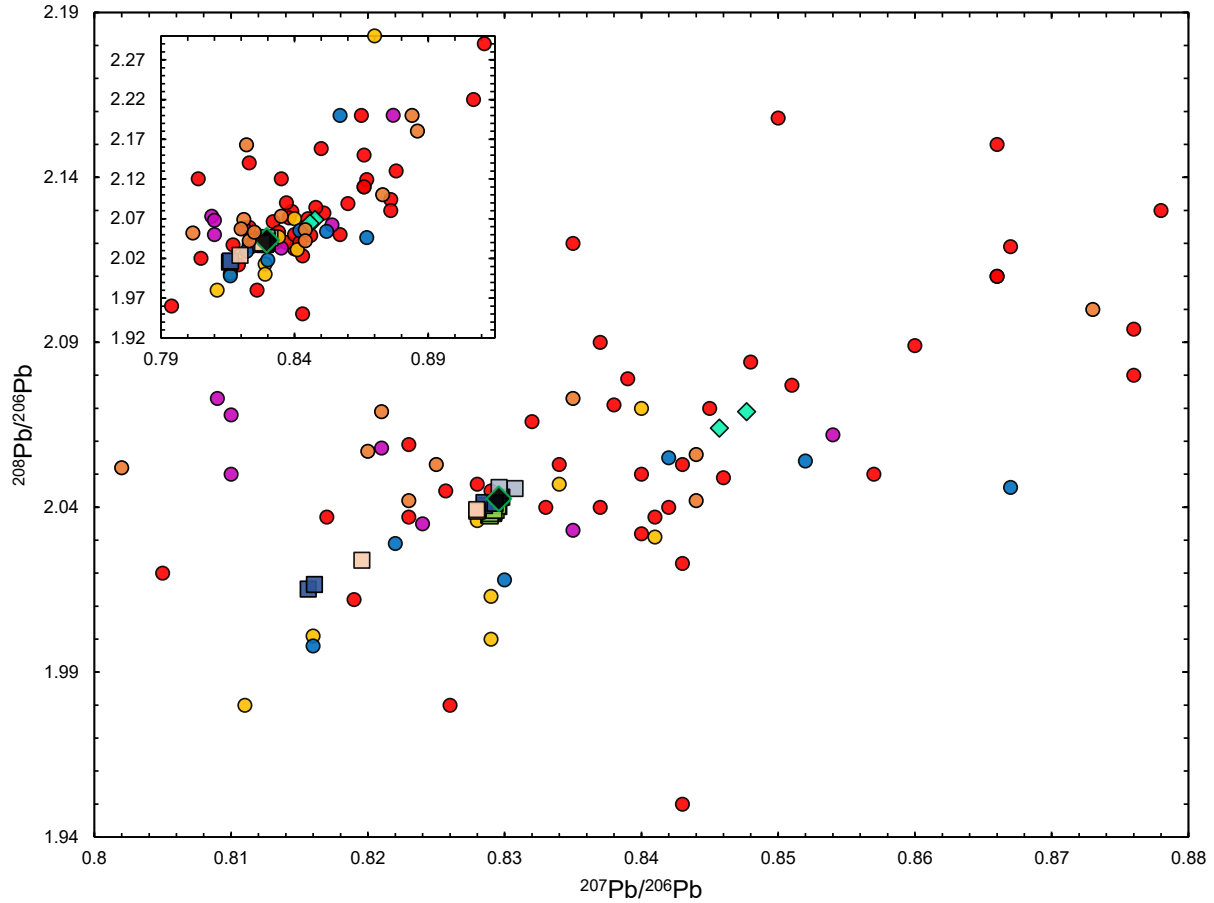
Barnes and Mungall, 2018) that prevented the diffusion of footwall-derived Pb into these sulfide minerals.

5.3. Synthesis

5.3.1. Relationship Between the E&L Deposit and Other Deposits Within the Eskay Rift and the Surrounding Golden Triangle

Given the age constraints on the E&L intrusion from stratigraphy and from the U-Pb zircon age of 180.71 Ma for the Nickel Mountain Gabbro Complex (Chamberlain, unpublished data), which may predate E&L mineralization, the maximum age of the deposit is early-mid Toarcian. If the E&L intrusion represents a separate, distinct pulse of magma, the formation of the deposit could have occurred as late as the Aalenian, based on the tectonomagmatic setting of the Eskay Rift (Gagnon *et al.*, 2012; Barresi *et al.*, 2014). Given that most magmatic Ni-Cu-PGE deposits are formed at or above the stratigraphic level in which they are emplaced (Leshner, 2019b), mineralization is most likely associated with Spatsizi Formation or younger-aged strata belonging to the Upper Hazelton Group. Mineralization in the KSM-Brucejack system (197-193 Ma) (Nelson and Kyba, 2014) and the Bronson corridor (~190 Ma) (Kyba and Nelson, 2015) predates the development of the E&L-Nickel Mountain magmatic system. The possibility of contemporaneous emplacement of the E&L intrusion and mineralization at the nearby Eskay Creek VMS deposit (175 Ma) (Childe, 1996) cannot be ruled out. Further investigation and geochronological studies of the E&L intrusion should be conducted to place robust age constraints on the timing of mineralization.

The Pb isotopic compositions of the KSM-Brucejack system, Bronson corridor, and Eskay Creek deposit are approximately the same ($^{207}\text{Pb}/^{206}\text{Pb} = 0.830$, $^{208}\text{Pb}/^{206}\text{Pb} = 2.04$) and is



- | <i>E&L deposit</i> | <i>Golden Triangle</i> |
|---------------------------------|---------------------------------------|
| ● Hazelton Group (Spatsizi Fm.) | ◆ Iskut-Eskay average galena |
| ● E&L Gabbro Upper Chamber | ■ Eskay Creek (VMS) |
| ● Lower Discovery Zone | ■ Bronson corridor (mesothermal) |
| ● Northeast Zone | ■ KSM-Brucejack (porphyry-epithermal) |
| ● E&L Gabbro Lower Chamber | ◆ Devonian Forrest Kerr Pluton |

Figure 5.10. Plot of $^{208}\text{Pb}/^{206}\text{Pb}$ vs. $^{207}\text{Pb}/^{206}\text{Pb}$ comparing the isotopic compositions of E&L sulfides with nearby deposits in the Golden Triangle. Data sources: average Iskut-Eskay galena (Godwin *et al.*, 1990), Eskay Creek (Childe, 1996), KSM-Brucejack (Godwin *et al.*, 1990), Bronson corridor (Godwin *et al.*, 1990), Forrest Kerr pluton (Childe, 1997). Note that the 2s uncertainty error bars are not shown for the results from this study for clarity.

consistent with the average isotopic composition of galena from the Iskut-Unuk region (Fig. 5.10.) (Godwin *et al.*, 1990). This suggests that the local Stikinian basement had a significant influence on the isotopic compositions of these deposits, imparting upon them the same distinct “flavour” as was imparted upon E&L intrusion and deposit. Exceptions include sulfides from the Snip and Johnny deposits, which could implicate the influence of either post-160 Ma modification and mineralization, or local basement heterogeneities. A significant proportion of the sulfide minerals analyzed by LA-ICP-MS from the E&L deposit show similar Pb isotopic compositions to those from nearby deposits, although with greater spread and variation, which supports the impact of the local Stikinian basement on the isotopic composition of the E&L orebodies. In contrast to the surrounding deposits, where only crustal sources are involved, the trends observed in the magmatic sulfides represent mixing between multiple mantle and crustal geochemical reservoirs and not just a basement signature.

5.3.2. Petrogenetic Constraints on Mineralization, the Host E&L Intrusion, and the Nickel Mountain Gabbro Complex

Trace element for whole rocks from the host E&L intrusion and the Nickel Mountain Gabbro Complex are available (Garibaldi Resources Corporation, unpublished data) and can be used to place additional constraints on the origin of the magmas that formed the E&L deposit. Extended primitive mantle-normalized patterns and chondrite-normalized rare earth element (REE) patterns indicate that there are significant differences between the average compositions of E&L and Nickel Mountain gabbros (Fig. 5.11.). Along with Group 1 and Group 2 Hazelton basalts (Barresi *et al.*, 2015), both intrusive suites are characterized by the prominent negative Nb-Ta anomalies typical of subduction zone-derived magmas (e.g., Elliott, 2004). The Nickel

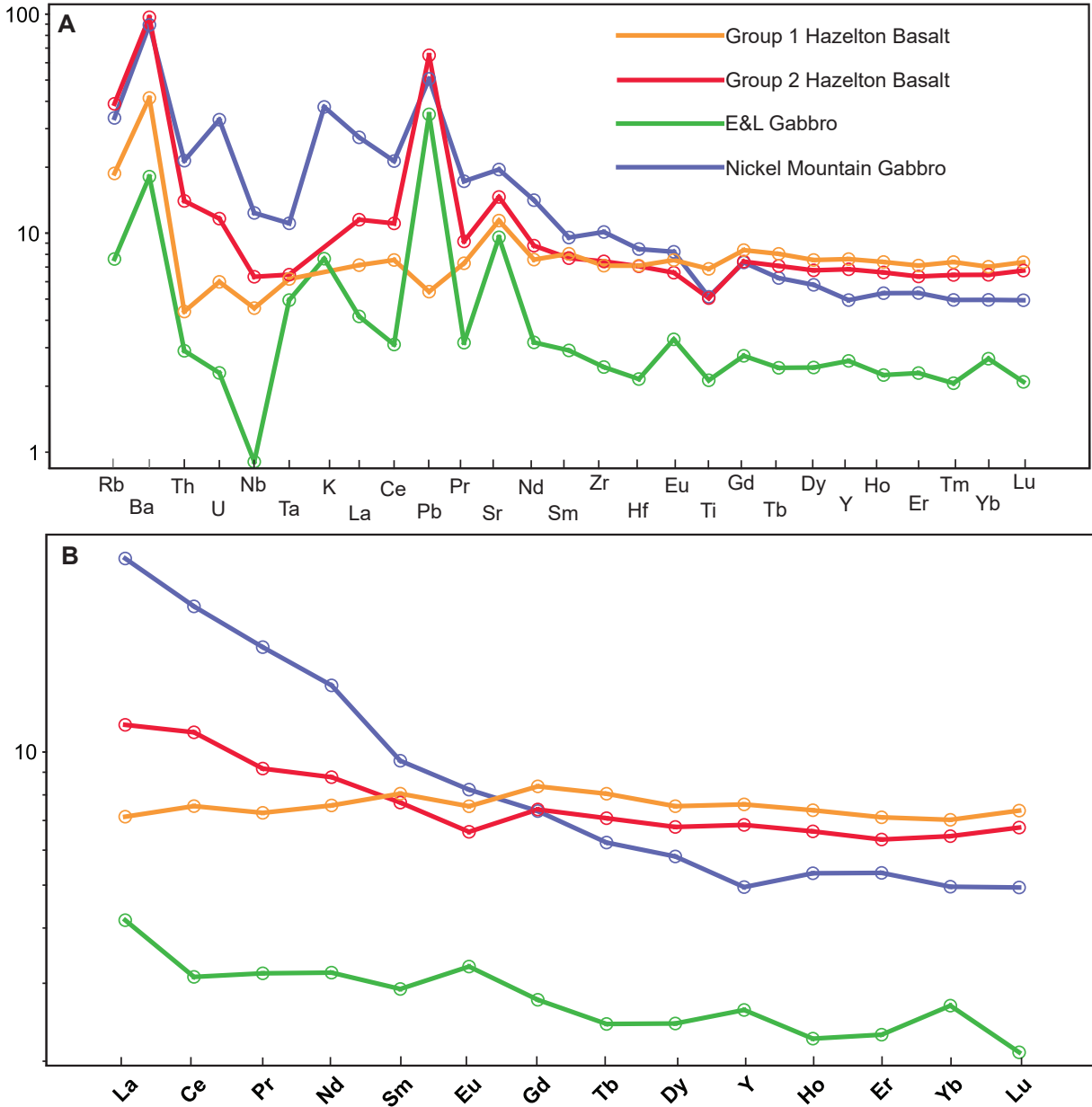


Figure 5.11. Extended primitive mantle-normalized trace element patterns (A) and chondrite-normalized REE patterns (B) for the average concentrations of the E&L intrusion, Nickel Mountain Gabbro Complex (Garibaldi Resources Corporation, unpublished data) and Group 1 and 2 Hazelton Group basalts (Barresi *et al.*, 2015). Normalizing values from Sun and McDonough (1989).

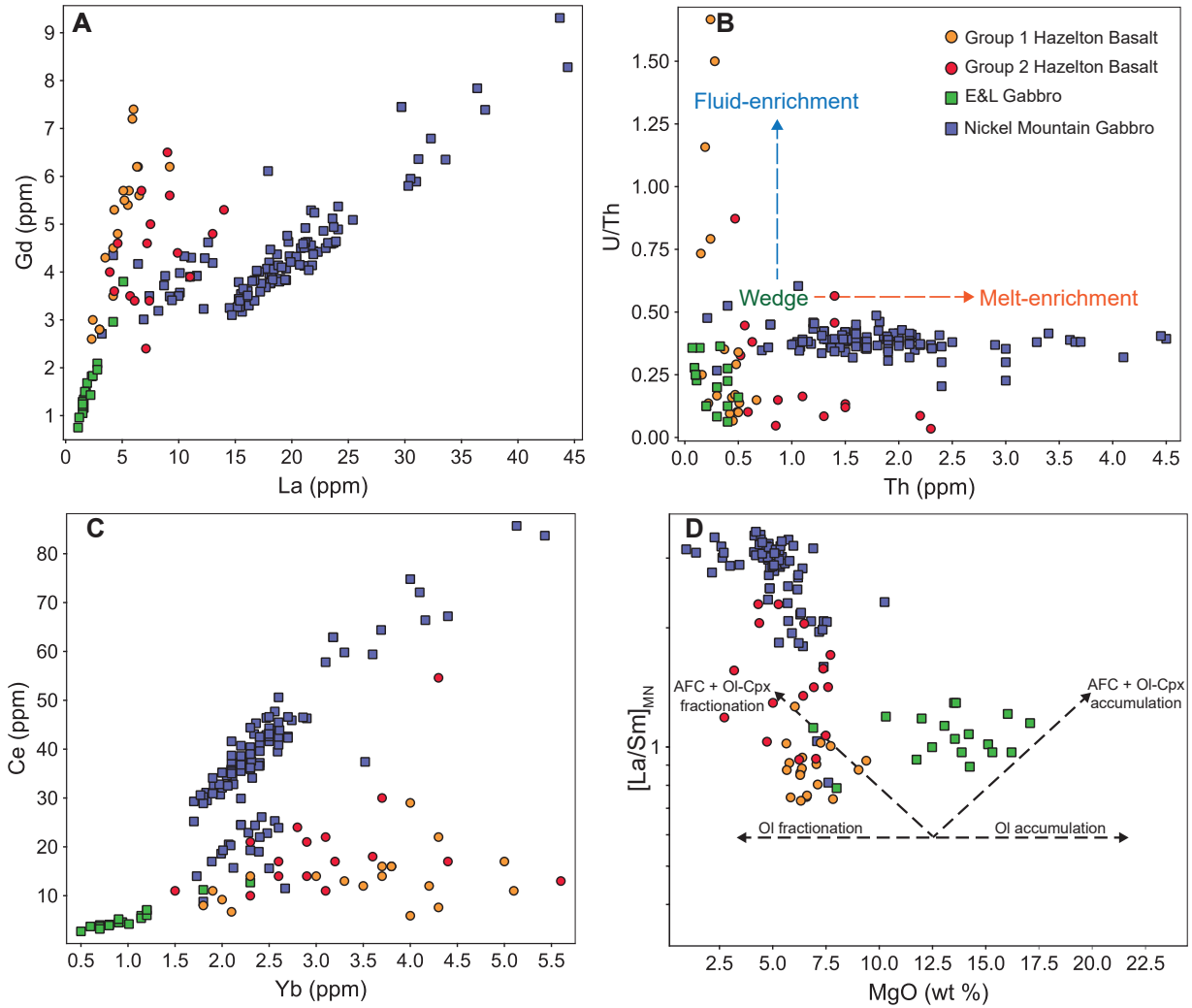


Figure 5.12. Trace element diagrams illustrating the geochemical variations in the E&L intrusion, Nickel Mountain Gabbro Complex (Garibaldi Resources Corporation, unpublished data) and Group 1 and 2 Hazelton Group basalts (Barresi *et al.*, 2015). A) Plot of Gd vs. La showing the different trends defined by rocks for the E&L intrusion and Nickel Mountain Gabbro Complex. B) Plot of U/Th ratios vs. Th (Hawkesworth *et al.*, 1997) illustrating the relative contributions of fluid and melt enhancement in the mantle source. C) Plot of Ce vs. Yb. Fractional crystallization arrays are defined by both increasing Ce and Yb – note the difference between rocks from the E&L intrusion and Nickel Mountain Gabbro Complex. D) Plot of primitive mantle-normalized (Sun and McDonough, 1989) La/Sm ratios vs. MgO (Leshner *et al.*, 2001) illustrating the differences in dominant magmatic processes for the E&L Intrusion and Nickel Mountain Gabbro Complex. Abbreviations: Ol – olivine, Cpx – clinopyroxene.

Mountain gabbros, however, display greater relative enrichments of the large ion lithophile elements (LILE), high field strength elements (HSFE), and REE compared to the E&L gabbros, which are generally more depleted (but less so than MORB). The average trace element profiles for all four units are broadly similar in shape with the E&L intrusion showing a much more pronounced Nb-Ta trough and positive Pb anomaly. For E&L, Nickel Mountain, and Group 2 basalts, the relative enrichment in Pb relative to Ce and Pr are typical for a metasomatized mantle source (Pearce and Peate, 1995), but may also reflect contamination during sample processing. The Nickel Mountain gabbros are strongly enriched in light REE compared to E&L gabbros and Hazelton Group basalts, with a steep light to middle REE profile and lower HREE compared to the flat REE patterns of the basalts. Despite the relative depletion in REE compared to other units, the average chondrite-normalized pattern for the E&L gabbros is more similar to Group 2 Hazelton basalts than it is to Nickel Mountain gabbros, potentially suggesting a common source. The relatively flat REE patterns of the E&L gabbros and the basalts, along with the negative Nb and Ta anomalies, are consistent with a back-arc affinity and melting of spinel peridotite (Dostal *et al.*, 1976) above the garnet-spinel transition.

The low Th concentrations coupled with medium-U/Th for Group 1 basalts and E&L gabbros suggest a metasomatized mantle source for the parent magmas (Hawkesworth *et al.*, 1997) (Fig. 5.12. B). The Nickel Mountain Gabbro Complex may be precluded from solely having such a source, as the higher Th concentrations and low- to medium-U/Th is consistent with a melt-enriched mantle source. This provides a strong argument for there being no genetic or temporal association between the E&L and Nickel Mountain intrusions, which is supported by different trends for each intrusive suite on a plot of Gd vs. La (Fig. 5.12. A). In fact, Group 1 basalts appear to be co-linear with the E&L gabbros, which could suggest either a genetic link, or

at the very least, derivation from the same source. Ratios of Ce/Yb (Fig. 5.12. C) also indicate that there is no genetic relationship between E&L and Nickel Mountain magmas, as they do not lie along the same arrays. Thus, fractional crystallization cannot explain the differences between the two intrusive suites. The observed trends also preclude a link between E&L and Nickel Mountain magmas through variable effects of crustal contamination as demonstrated in a plot of primitive mantle-normalized La/Sm vs. MgO (e.g., Lesher *et al.*, 2001) (Fig. 5.12. D). Some E&L and Nickel Mountain gabbro samples have similar MgO despite having drastically different La/Sm ratios. The mechanism of magma evolution for Nickel Mountain Gabbro Complex was likely dominated by AFC (assimilation-fractional crystallization) processes combined with the fractionation of olivine and clinopyroxene and E&L gabbros appear to have been dominated by AFC processes combined with the accumulation of olivine and clinopyroxene. Although AFC processes were important in the magmatic evolution of both suites, their trace element variations cannot be reconciled with derivation from a common parental magma.

In summary, trace element variations implicate a metasomatized mantle source for the E&L intrusion, suggest a back-arc affinity for the magmatic suite, and preclude a genetic and contemporaneous linkage with the Nickel Mountain Gabbro Complex. The Nickel Mountain Gabbro Complex must predate the emplacement of the E&L intrusion, although at present, no contact between the two intrusions has been recovered. The Pb isotopic and trace element geochemistry can be reconciled with the geologic setting of the Eskay Rift and Stikinia. During the Lower Jurassic, Stikinia was the site of a double subduction zone, with the Hazelton Trough back-arc basin sandwiched between an east- and west-facing arc system (Nelson *et al.*, 2013) (Fig. 5.13.). Subduction, which had persisted since the Mississippian, resulted in the progressive metasomatism of the sub-arc mantle wedge. The metasomatic fluids were likely derived from

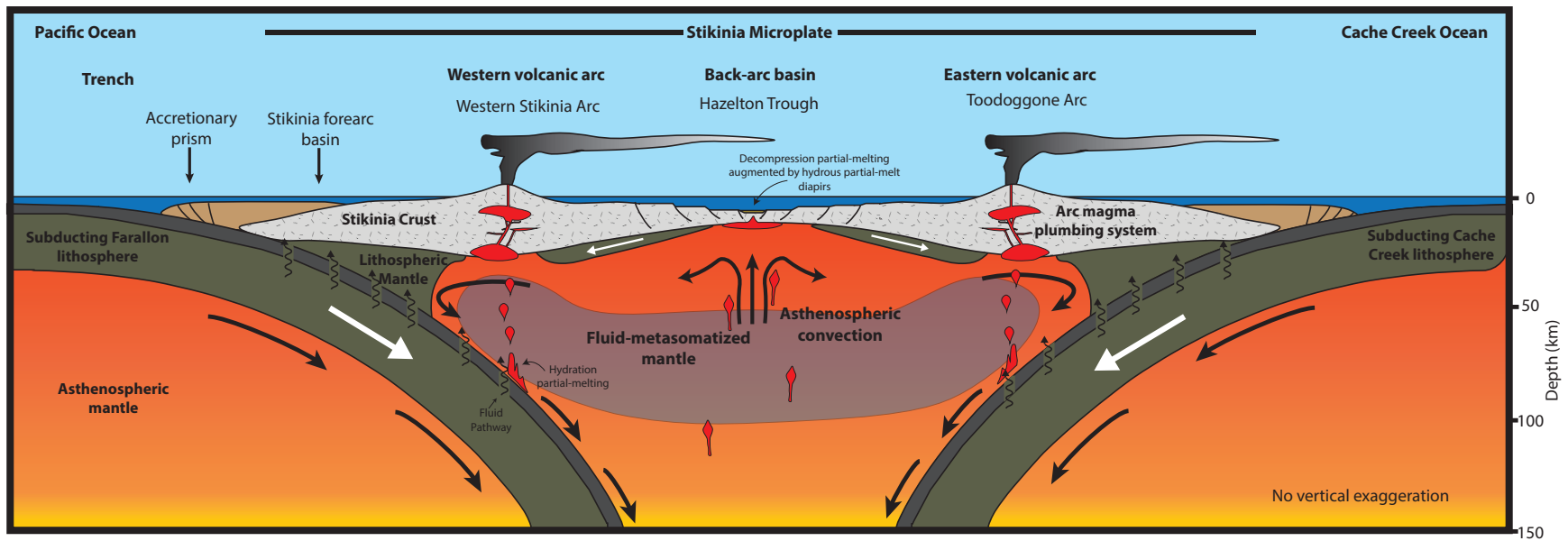


Figure 5.13. Schematic E-W cross-section illustrating the geodynamic setting of the Stikinia microplate ca. 190 Ma (Marsden and Thorkelson, 1992; Stern, 2002; Nelson and Colpron, 2007).

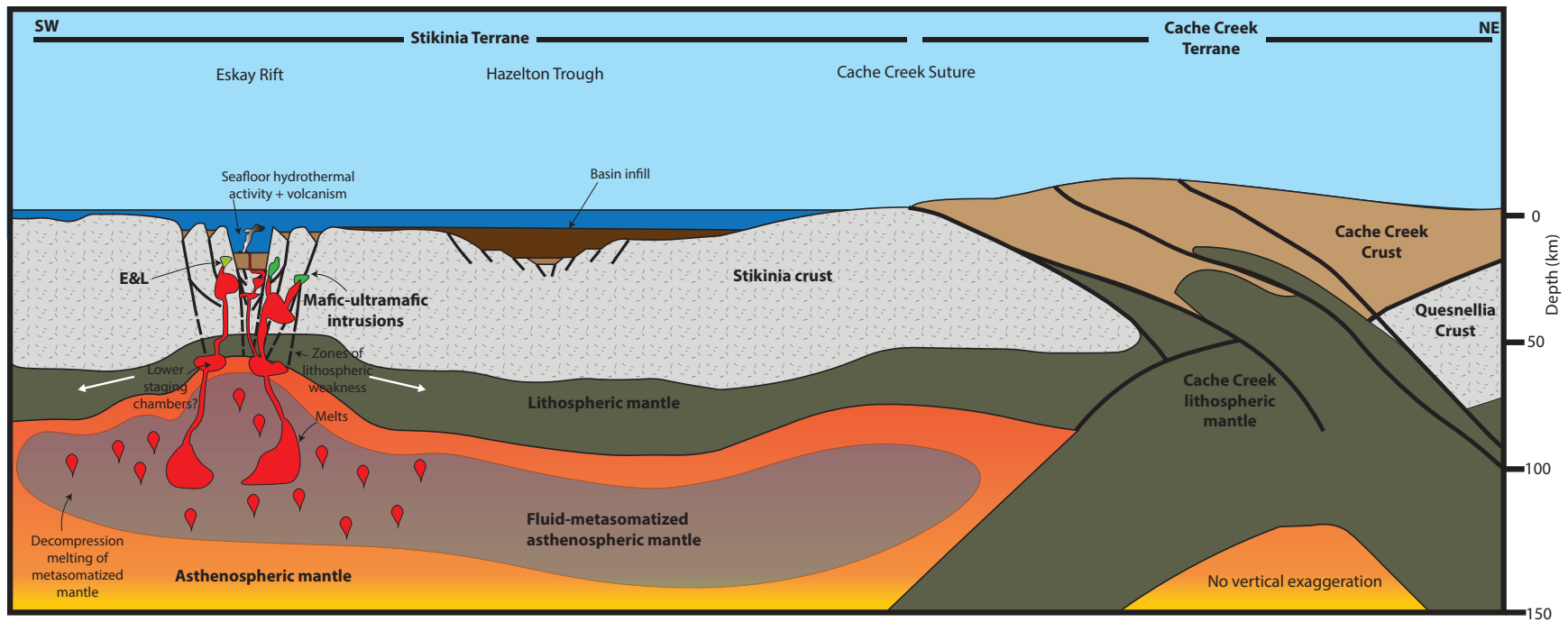


Figure 5.14. Schematic NE-SW cross-section illustrating the proposed post-subduction geodynamic setting of accreted inboard terranes and the Eskay Rift at ca. 180-175 Ma. In this configuration, decompression melting of a metasomatized mantle leads to production of the E&L parental magma (Gagnon *et al.*, 2012; Nelson *et al.*, 2013; Barresi *et al.*, 2015).

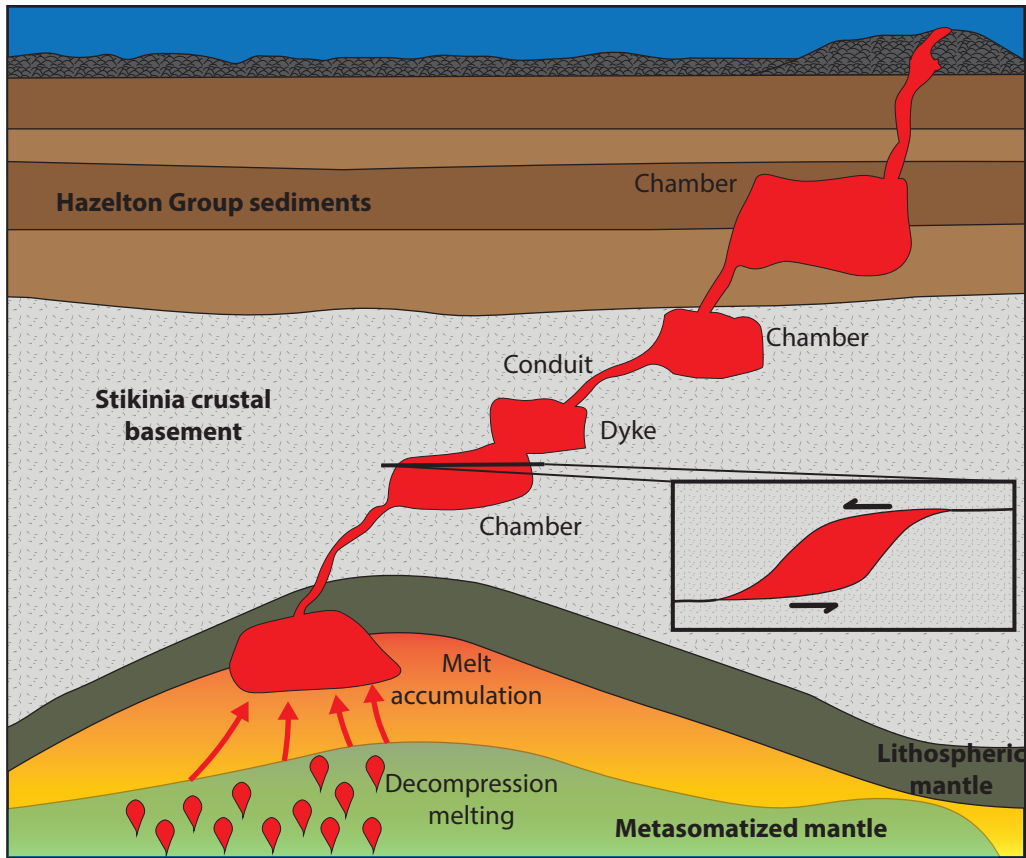


Figure 5.15. Schematic cross section through a hypothesized E&L magmatic plumbing system hosted in a sinistral-shear transtensional setting (Lightfoot and Evans-Lamswood, 2016). Figure is not to scale.

accretionary wedge mélangé, as well as from sediments and basalts on the subducting oceanic plates. Subduction continued until ~181 Ma, producing the flanking Texas Creek Plutonic Suite (Nelson *et al.*, 2013). The transition from subduction-related to post-collisional magmatism may have been marked by the emplacement of the Nickel Mountain Gabbro Complex, which is approximately the same age as that inferred for the initial closure of the Cache Creek Ocean (Cordey, 2020). During collision with the Cache Creek Terrane, stresses on the northeastern margin of Stikinia caused a shear couple to form across the terrane, resulting in the development of the Eskay Rift as an impactogen at a high angle to the Cache Creek Suture (Nelson *et al.*, 2013) (Fig. 5.14.). Sinistral transtension along the Eskay Rift allowed for the rapid ascent of metasomatized mantle-derived magmas produced by decompression melting (Alldrick *et al.*, 2004; Gagnon *et al.*, 2012; Barresi *et al.*, 2015). These magmas were likely focused into extensional step-overs, which controlled the distribution of magma chambers and conduits, and ultimately, the distribution of Ni-Cu (PGE) sulfide mineralization (Fig. 5.15.). As discussed further below, these structures also played an important role in controlling the distribution of VMS mineralization within the rift.

5.3.3. Comparisons with Other Magmatic Ni-Cu (PGE) Deposits and Implications for Prospectivity in Former Back-arc and Transtensional Settings

The E&L magmatic sulfide deposit shares many similar characteristics with other Ni-Cu-(PGE) deposits in convergent margin and post-collisional settings (Table 5.2). The E&L deposit is most similar to the Permian Ni-Cu-(PGE) deposits in the Central Asian Orogenic Belt (CAOB) of western China (e.g., Kalatongke, Huangshannan, Huangshandong, Lubei). Like E&L, the deposits of the CAOB are inferred to be associated with post-collisional extension-related

magmatism (Chen *et al.*, 2018). Many of these deposits are associated with or located proximal to translithospheric extensional stepovers within strike-slip fault zones (Li *et al.*, 2019), which create the accommodation space required for magma ascent and localize conduits by way of dilation and traps (Lightfoot and Evans-Lamswood, 2016). This contrasts with the tectonic settings of the Giant Mascot (Manor, 2014) and Aguablanca (Piña *et al.*, 2010) deposits, where magmatism and emplacement are interpreted to have occurred in syn-subduction and syn-collisional transpressional settings, respectively. At Aguablanca, however, injections of melt were controlled by the opening of a tensional fracture between two shear zones, indicating that some degree of extension is still required for emplacement even in transpressional settings (Piña *et al.*, 2010). At the other end of the spectrum, the genesis of the Sally Malay (Savannah) and Nova-Bollinger deposits occurred during the syn-subduction extensional development of back-arc basins during the Halls Creek and Albany-Fraser orogenies, respectively (Maier *et al.*, 2016; Mole *et al.*, 2018). Thus, extensional structures play an important role in the majority of compressional regime Ni-Cu (PGE) deposits and this is where future exploration in these settings should be focused.

Many of the Central Asian Orogenic Belt deposits are also associated with post-subduction decompression melting of a previously metasomatized mantle wedge (Gao and Zhou, 2013; Chen *et al.*, 2018), similar to the hypothesized mechanism for melting and formation of the E&L parent magma. Such a mantle source is consistent with those proposed for Sally Malay, Nova-Bollinger, Aguablanca, and Giant Mascot, although in the case of the latter two, wet melting of the mantle has been implicated as the mechanism of magma generation (Tornos *et al.*, 2006; Manor, 2014; Maier *et al.*, 2016; Mole *et al.*, 2018). Therefore, in compressional tectonic regimes, melting of a metasomatized mantle source could be an important ingredient in the

Table 5.2. Comparison of the E&L deposit with selected Ni-Cu (PGE) deposits hosted in convergent margin and collisional environments.

Deposit	Age (Ma)	Tectonic Setting	Tectonic Location ¹	Magma	Lithology	MgO (%)	Mineralization (minerals) ²	Associated Rocks	Transtension Involved?	References
E&L	~180	Microcontinent/orogenic belt	ST/NAC	Tholeiite	Olivine gabbro, two-pyroxene leucogabbro, norite, wehrlite	?	D, N, S, M (Po, Pn, Ccp, Mt)	Lower-Middle Jurassic Hazelton Group sedimentary strata	Y	This Study
Giant Mascot	93	Convergent margin/orogenic belt	CPC/NAC	Oxidized arc magma	Dunite, peridotite, pyroxenite, hornblende pyroxenite, hornblendite	15-30	D, N, S M (Po, Pn, Ccp, Mt, Cb, Tro)	Upper Triassic Settler Schist	N	Manor, 2014; Manor <i>et al.</i> , 2016
Kalatongke	287	Microcontinent	CAOB	High Si + high Mg basaltic magma mixing	Diorite, norite	6.3-11.5	D, N, S, M (Po, Pn, Ccp, Mt)	Carboniferous Nanmingshu Formation clastic sedimentary strata	Y	Li <i>et al.</i> , 2012; Gao and Zhou, 2013; Lu <i>et al.</i> , 2019
Aguablanca	344	Convergent margin/orogenic belt	OMZ/IM	Tholeiite	Gabbronorite	12	D, S, Bx (Po, Pn, Ccp, Mt, Cb)	Neoproterozoic Serie Negra Formation black shales	Y?	Tornos <i>et al.</i> , 2006; Piña <i>et al.</i> , 2010
Nova Bollinger	~1300	Back-arc basin/orogenic belt	AFO/YC	Tholeiite	Metagabbro, pyroxene-garnet granulite, peridotite	8.8	D, N, S, M, Bx (Po, Pn, Ccp, Py)	Mesoproterozoic Snowys Dam Formation metasedimentary rocks	?	Maier <i>et al.</i> , 2016
Lubei	287	Orogenic belt	CAOB	Calc-alkaline	Lherzolite, hornblende peridotite, gabbro, diorite	11	D, N (Po, Pn, Ccp, Mt, Py)	Lower Carboniferous pyroclastic-clastic rocks	Y	Chen <i>et al.</i> , 2018; Chen <i>et al.</i> , 2019
Huangshannan	283	Along Fault	CAOB	Ni-rich	Lherzolite, websterite, gabbronorite, diorite	8.7-12.4	D, S, M (Po, Pn, Ccp)	Lower Carboniferous Quartz Schist	Y	Zhao <i>et al.</i> , 2016; Lu <i>et al.</i> , 2019
Sally Malay	1844	Back-arc basin/orogenic belt	HCO/LP	High-Al tholeiite	Peridotite, olivine gabbro, troctolite, norite, anorthosite	7.4	D, M (Po, Pn, Ccp)	Paleoproterozoic Tikalara Metamorphics metasedimentary rocks	Y?	Mole <i>et al.</i> , 2018

¹Abbreviations: ST – Stikinia, NAC – North American Cordillera, CPC – Coast Plutonic Complex, CAOB – Central Asian Orogenic Belt, OMZ – Ossa Morena Zone, IM – Iberian Massif, AFO – Albany-Fraser Orogen, YC – Yilgarn Craton, HCO – Halls Creek Orogen, LP – Lamboo Province. ²Abbreviations: D-disseminated sulfide, M-massive sulfide, S-semi-massive sulfide, N-net-textured sulfide, Bx – brecciated sulfide.

recipe of generating a magmatic Ni-Cu-(PGE) deposit. Metasomatized subcontinental lithospheric mantle (SCLM) as a metal source has been proposed for the genesis of magmatic sulfide deposits and for the metallogenic endowment of the upper crust (Fiorentini and Beresford, 2008; Griffin *et al.*, 2013; Holwell *et al.*, 2019). However, given the relatively juvenile tectonic setting of the E&L deposit and the relatively high Ni/Cu of E&L and similar deposits, along with arguments provided by Barnes *et al.* (2016), an SCLM source may not be necessary in the genesis of these deposits. Additional research into the specific mantle conditions required to produce these magmatic Ni-Cu-(PGE) mineralized systems is needed.

Barresi *et al.* (2015) have emphasized the integral role that the geographic variations in structural permeability along the Eskay Rift played in the genesis of VMS deposits. VMS deposits in the Eskay Rift (Anyox, Eskay Creek), located in the southern portion of the rift, likely formed as a result of the presence of these structural permeabilities, which facilitated the emplacement of the high-temperature magmas driving hydrothermal convection (Barresi *et al.*, 2015). These “structural permeabilities” (Barresi *et al.*, 2015) are likely transtensional fault structures, which would favour the development of Ni-Cu-(PGE) deposits by allowing for rapid ascent of high-temperature mantle-derived magmas into a sedimentary basin with abundant black shales. The E&L magmas likely exploited these transtensional structures and thus the potential for other gabbro-hosted magmatic sulfide deposits in the southern Eskay Rift is high, especially in areas surrounded by Upper Hazelton Group sediments. Evidence for high regional prospectivity is further supported by the occurrence of taxitic (i.e., heterogeneous) gabbro intrusions in the vicinity of Mt. Shirley, Melville Peak, and the Cone Glacier. Massive Ni-Cu-(PGE) mineralization has also been found in associated with gabbros intruded into Upper Hazelton Group sediments near Anyox (Carter, 1999). Given the multiple episodes of subduction

(with back-arc extension) and related magmatism in the Canadian Cordillera, other regions could also have the potential for significant Ni-Cu mineralization. Exploration should be focused in regions where significant transtensional structures have been identified, especially where these structures are associated with mafic-hosted VMS deposits, which could indicate regions of high structural permeability.

6. Conclusions

Despite the storied mining history in the Golden Triangle of northern British Columbia, exploration for Ni-Cu-(PGE) deposits in this area, and the Canadian Cordillera as a whole, is still in its relative infancy. Significant work has been conducted to characterize the numerous Ural-Alaskan ultramafic-mafic intrusions in British Columbia and Alaska, however, only a few are associated with low-grade, high-tonnage sulfide mineralization (e.g., Turnagain – Scheel *et al.*, 2005; Nixon *et al.*, 2019) or PGE mineralization (e.g., Tulameen – St. Louis *et al.*, 1986; Nixon *et al.*, 2019). Other known Ni-Cu (PGE) deposits in the Cordillera are rare (e.g., Wellgreen – Barkov *et al.*, 2002) and even rarer are high-grade magmatic massive sulfide deposits (e.g., Giant Mascot – Manor, 2014; E&L – this study).

This study of mineralization within the E&L intrusion utilized petrography, scanning electron microscopy, platinum group mineral chemistry, and the LA-ICP-MS analysis of sulfide minerals for their Pb isotopic compositions to characterize the properties, ore-forming processes, and potential sources of mineralization. The intrusion consists of vari-textured and orbicular olivine gabbro, olivine melagabbro, and minor wehrlite, which host disseminated, net-textured, brecciated, semi-massive, and massive sulfide mineralization with grades of up to 7 wt% Ni and 4 wt% Cu. The pyrrhotite-pentlandite-chalcopyrite-magnetite mineral assemblages are similar to those of other magmatic Ni-Cu (PGE) deposits, with the exception of the unusual sieve-textured magnetite in the semi-net-textured sulfides of the Lower Chamber and pseudo-cuneiform magnetite in the Lower Discovery Zone massive sulfides. These magnetite-related textures are consistent with disequilibrium-induced resorption back into the sulfide melt during cooling. Relatively minor post-crystallization deformation produced fractured magnetite crystals, deformation twinning in pyrrhotite, and the partial remobilization of chalcopyrite into fractures

and secondary minerals. Stratigraphic controls on mineralization assemblages within the Lower Discovery Zone are indicated by increasing magnetite, electrum, and sphalerite contents towards the top of the orebody, increasing IPGE-bearing mineral (i.e., Rh-telluride) content towards the middle of the orebody, and increasing abundance of melonite towards the base of the orebody.

The Pb isotopic compositions of sulfide minerals determined directly in thin section using the LA-ICP-MS method are for the most part within analytical uncertainty. There is, however, some evidence to suggest the progressive influence of crustal signatures with cooling of the sulfide melt as minerals that crystallized at high temperatures from monosulfide solid-solution or mss (pyrrhotite, flame pentlandite) have a relatively unradiogenic isotopic composition compared to minerals that crystallized at lower temperatures from intermediate solid solution or iss (chalcopyrite). The majority of the analyzed sulfides from the E&L deposit have isotopic compositions similar to the average composition of galena from the Iskut-Eskay region, suggesting a significant crustal influence on mineralization. Isotopic mixing models are consistent with derivation of the E&L parent magmas from a mantle source that were contaminated at depth by the Triassic-Jurassic island arc basement of Stikinia. Contamination also occurred at shallower depths by Upper Hazelton Group sedimentary rocks, which are the most likely external sulfur source for sulfide saturation. The modelling also rules out significant influence by the local Devonian plutons associated with the Stikine Assemblage. Many of the E&L deposit sulfide compositions are broadly similar to those of other Triassic-Jurassic deposits in the area, indicating a common source of crustal Pb.

Combined, the trace element geochemistry of whole rocks and Pb isotopic geochemistry of sulfides are consistent with transtension-driven decompression melting of a metasomatized mantle source during development of the Eskay Rift in response to the collision between Stikinia

and the Cache Creek Terrane. A maximum age constraint (180.71 Ma, U-Pb zircon, Nickel Mountain Gabbro Complex – Chamberlain, unpublished data) on mineralization precludes a syn-subduction origin for the E&L intrusion. Incompatible trace element ratios indicate that there is no genetic link between E&L intrusion and Nickel Mountain gabbros, suggesting that E&L intrusion may be associated with the main stage of transtension in the Eskay Rift, rather than with incipient development. Minimum age constraints on mineralization, however, remain unknown. The hypothesized tectonomagmatic setting of the E&L intrusion and deposit is similar to that proposed for Ni-Cu-PGE deposits in the Permian Central Asian Orogenic Belt of the Xinjiang region of China, which suggests that deposits of this type may be more common in collisional settings than previously considered. Therefore, the prospectivity for other Ni-Cu-PGE deposits within the Eskay Rift, and the Cordillera as a whole, remains high. Given the lack of an upper age constraint on mineralization and the hypothesized influence of similar structural permeabilities on the ascent of source magmas, the E&L intrusion may potentially be related to the mafic magmas that drove hydrothermal circulation to form the nearby Anyox and Eskay Creek VMS deposits.

6.1. Recommendations for Future Work

Many aspects of the E&L magmatic sulfide Ni-Cu-(PGE) deposit remain unconstrained. As mentioned above, the deposit critically lacks an upper age constraint on mineralization. Precise U-Pb zircon and baddeleyite dates have only been obtained from Nickel Mountain Gabbro Complex samples, thus the temporal relationship between Nickel Mountain and the E&L intrusion is unclear, although cross-sections (Garibaldi Resources Corporation, 2020) suggest that the latter intruded the former. An intensive geochronological sampling program and study of

the E&L intrusion should be undertaken to adequately constrain the timing of magmatism and mineralization. These geochronological results would also help to answer questions regarding the development stages of transtension in the Eskay Rift and the temporal relation of the deposit to nearby VMS deposits, and would be useful in helping to delineate other prospective intrusions.

Research into the mechanisms of sulfide deformation and the structural controls on the deposit should be conducted to identify the timing, styles, and degree of deformation within the E&L intrusion and deposit. The results of this structural study could prove useful in the identification of drill targets for prospective mineralization and defining the overall scale of the deposit. The identification of the controlling structural permeabilities could also aid in identifying other prospective areas in the Eskay Rift.

Further investigation into the source and petrogenesis of the E&L deposit using radiogenic isotopic geochemistry is also recommended. Sulfides could be analyzed for their Re-Os isotopic systematics, which would provide additional insights into the source of mineralization, the degree of crustal contamination, and the age of mineralization (e.g., Re-Os isochron). Given their relative resistance to alteration and metamorphism and their ability to constrain petrogenetic processes from source melting to crystallization, whole-rock Lu-Hf and Sm-Nd isotopic geochemistry could be applied to the silicate-dominated rocks of the E&L intrusion. Given the widespread evidence for secondary alteration in rocks of the E&L intrusion, the application of the Rb-Sr isotopic system is not advised. For all the above-mentioned radiogenic isotopic approaches, samples from the Nickel Mountain Gabbro Complex should also be analyzed to compare and contrast with results from the E&L intrusion.

Given the importance of transtensional structures in controlling the distribution of intrusion-hosted Ni-Cu-(PGE) mineralization in post-collisional and convergent margin settings,

future research should also be focused on identifying other areas of transtension associated with impactogens and back-arc rifting in the Canadian Cordillera. The complex, multi-accretionary history of this geologic province suggests that the development of the Eskay Rift may not be the only event with conditions that favour the development of this deposit type. Thus, exploration for magmatic Ni-Cu-(PGE) massive sulfide deposits in the Canadian Cordillera should be focused on finding sedimentary-hosted mafic-ultramafic intrusions in former transtensional settings.

Bibliography

- Alldrick, D.J., Brown, D.A., Harakal, J.E., Mortensen, J.K., and Armstrong, R.L., 1987, Alldrick, D. J., Brown, D. A., Harakal, J. E., Mortensen, J. K., and Armstrong, R. L., 1987, Geochronology of the Stewart Mining Camp (104B/1): Geological Fieldwork 1986, British Columbia Ministry of Energy, Mines and Petroleum Resources, v. 1987-1, p. 81-92.
- Alldrick, D. J., Stewart, M. L., Nelson, J. L., and Simpson, K. A., 2004, Tracking the Eskay rift through northern British Columbia - geology and mineral occurrences of the Upper Iskut River area: Geological Fieldwork 2003, British Columbia Ministry of Energy and Mines, v. 2004-1, p. 1-18.
- Arndt, N., Leshner, C. M., and Czamanske, G. K., 2006, Mantle-derived magmas and magmatic Ni-Cu-(PGE) deposits: Economic Geology, 100th Anniversary Volume, p. 5-24.
- Ash, C. H., Fraser, T. M., Blanchflower, J. D., and Thurston, B. G., 1994, Tatogga Lake Project, Northwestern British Columbia (104H/11, 12): Geological Fieldwork 1994, British Columbia Ministry of Energy, Mines, and Petroleum Resources, v. 1994-1, p. 343-358.
- Barkov, A. Y., Laflamme, J. H. G., Cabri, L. J., and Martin, R. F., 2002, Platinum-group minerals from the Wellgreen Ni-Cu-PGE deposit, Yukon, Canada: The Canadian Mineralogist, v. 40, p. 651-669.
- Barnes, S. J., and Mungall, J. E., 2018, Blade-shaped dikes and nickel sulfide deposits: A model for the emplacement of ore-bearing small intrusions: Economic Geology, v. 113, p. 789-798.
- Barnes, S. J., and Robertson, J. C., 2019, Time scales and length scales in magma flow pathways and the origin of magmatic Ni-Cu-PGE ore deposits: Geoscience Frontiers, v. 10, p. 77-87.
- Barnes, S. J., Cruden, A. R., Arndt, N., and Saumur, B. M., 2016, The mineral system approach applied to magmatic Ni-Cu-PGE sulphide deposits: Ore Geology Reviews, v. 76, p. 296-316.
- Barnes, S. J., Mungall, J. E., Le Vaillant, M., Godel, B. M., Holwell, D., Lightfoot, P. C., Leshner, C. M., Krivolutskaya, N., and Wei, B., 2017, Sulfide-silicate textures in magmatic Ni-Cu-PGE sulfide ore deposits: Disseminated and net-textured ores: American Mineralogist, v. 101, p. 629-651.
- Barnes, S. J., Staude, S., Le Vaillant, M., Piña, R., and Lightfoot, P. C., 2018, Sulfide-silicate textures in magmatic Ni-Cu-PGE sulfide ore deposits: Massive, semi-massive and sulfide-matrix breccia ores: Ore Geology Reviews, v. 101, p. 629-651.
- Barnes, S. J., Le Vaillant, M., Godel, B., and Leshner, C. M., 2019, Droplets and bubbles: Solidification of sulphide-rich vapour-saturated orthocumulates in the Norilsk-Talnakh Ni-Cu-PGE ore-bearing intrusions: Journal of Petrology, v. 60, p. 269-300.

- Barresi, T., Nelson, J. A. L., and Dostal, J., 2014, Geochemical constraints on magmatic and metallogenic processes: Iskut river formation, volcanogenic massive sulfide-hosting basalts, NW British Columbia, Canada: *Canadian Journal of Earth Sciences*, v. 52, p. 1–20.
- Bell, R. T., 1978, Uranium in black shales—a review: *Uranium Deposits, Their Mineralogy and Origin*, v. 3, p. 307–329.
- Boutroy, E., Dare, S. A. S., Beaudoin, G., Barnes, S. J., and Lightfoot, P. C., 2014, Magnetite composition in Ni-Cu-PGE deposits worldwide: Application to mineral exploration: *Journal of Geochemical Exploration*, v. 145, p. 64–81.
- Carter, N. C., 1999, Geochemical report on the Alice property: Skeena Mining Division, British Columbia. Report for Angel Jade Mines Ltd. AR#25838.
- Celmer, R., 1988, The distribution of minor elements in nickel matte smelting: National Library of Canada.
- Champion, D. C., and Huston, D. L., 2016, Radiogenic isotopes, ore deposits and metallogenic terranes: Novel approaches based on regional isotopic maps and the mineral systems concept: *Ore Geology Reviews*, v. 76, p. 229–256.
- Chen, B. Y., Yu, J. J., and Liu, S. J., 2018, Source characteristics and tectonic setting of mafic–ultramafic intrusions in North Xinjiang, NW China: Insights from the petrology and geochemistry of the Lubei mafic–ultramafic intrusion: *Lithos*, v. 308–309, p. 329–345.
- Chen, B., Yu, J., Liu, S., and Tian, J., 2019, Formation of the Lubei magmatic Ni–Cu deposit in a post-subduction setting in East Tianshan, North West China: *Ore Geology Reviews*, v. 104, p. 356–372.
- Cherniak, D. J., 2010, Diffusion in carbonates, fluorite, sulfide minerals, and diamond: *Reviews in Mineralogy and Geochemistry*, v. 72, p. 871–897.
- Childe, F., 1996, U-Pb geochronology and Nd and Pb isotope characteristics of the Au-Ag-rich Eskay Creek volcanogenic massive sulfide deposit, British Columbia: *Economic Geology*, v. 91, p. 1209–1224.
- Childe, F. C., 1997, Timing and tectonic setting of volcanogenic massive sulphide deposits in British Columbia: Constraints from U-Pb geochronology, radiogenic isotopes, and geochemistry: Unpublished PhD dissertation, University of British Columbia: 319 p.
- Cho, J. O. Y., 2019, A microanalytical investigation of feldspars in the Skaergaard intrusion, East Greenland: ternary feldspar compositional relations and lead isotopic geochemistry: Unpublished MSc thesis, University of British Columbia: 407 p.
- Colpron, M., Nelson, J. A. L., and Murphy, D. C., 2007, Northern Cordilleran terranes and their interactions through time: *GSA Today*, v. 17, p. 4–10.

- Cordey, F., 2020, Timing of Cache Creek Ocean closure: insights from new Jurassic radiolarian ages in British Columbia and Yukon, and their significance for Canadian Cordillera tectonics: *Canadian Journal of Earth Sciences*, v. 0, p. 1-43.
- Cox, K. G., Bell, J. D., and Pankhurst, R. J., 1979, *The Interpretation of Igneous Rocks*: London, George Allen and Unwin.
- Crowe, S. A., Fryer, B. J., Samson, I. M., and Gagnon, J. E., 2003, Precise isotope ratio determination of common Pb using quadrupole LA-ICP-MS with optimized laser sampling conditions and a robust mixed-gas plasma: *Journal of Analytical Atomic Spectrometry*, v. 18, p. 1331-1338.
- Cutts, J. A., Mcnicoll, V. J., Zagorevski, A., Anderson, R. G., and Martin, K., 2015, U-Pb geochronology of the Hazelton Group in the McTagg anticlinorium, Iskut River area , northwestern British Columbia: *Geological Fieldwork 2014, British Columbia Ministry Of Energy and Mines*, v. 2015–1, p. 87–101.
- Dare, S. A. S., Barnes, S. J., and Prichard, H. M., 2010, The distribution of platinum group elements (PGE) and other chalcophile elements among sulfides from the Creighton Ni-Cu-PGE sulfide deposit, Sudbury, Canada, and the origin of palladium in pentlandite: *Mineralium Deposita*, v. 45, p. 765–793.
- Dare, S. A. S., Barnes, S. J., and Beaudoin, G., 2012, Variation in trace element content of magnetite crystallized from a fractionating sulfide liquid, Sudbury, Canada: Implications for provenance discrimination: *Geochimica et Cosmochimica Acta*, v. 88, p. 27–50.
- Darling, J. R., Storey, C. D., Hawkesworth, C. J., and Lightfoot, P. C., 2012, In-situ Pb isotope analysis of Fe-Ni-Cu sulphides by laser ablation multi-collector ICPMS: New insights into ore formation in the Sudbury impact melt sheet: *Geochimica et Cosmochimica Acta*, v. 99, p. 1–17.
- Dostal, J., Dupuy, C., and Coulon, C., 1976, Rare-earth elements in high-alumina basaltic rocks from Sardinia: *Chemical Geology*, v. 18, p. 251–262.
- Eglington, B., 2018, Application of Pb isotopes for exploration: *Topics in Mineral Sciences*, v. 48, p. 77–98.
- Elliott, T., 2004, Tracers of the slab: *Geophysical Monograph Series*, v. 138, p. 23–45.
- Fiorentini, M. L., and Beresford, S. W., 2008, Role of volatiles and metasomatized subcontinental lithospheric mantle in the genesis of magmatic Ni-Cu-PGE mineralization: Insights from in situ H, Li, B analyses of hydromagmatic phases from the Valmaggia ultramafic pipe, Ivrea-Verbano Zone (NW Italy): *Terra Nova*, v. 20, p. 333–340.

- Fonseca, R. O. C., Campbell, I. H., O'Neill, H. S. C., and Fitzgerald, J. D., 2008, Oxygen solubility and speciation in sulphide-rich mattes: *Geochimica et Cosmochimica Acta*, v. 72, p. 2619–2635.
- Fourny, A., 2018, Radiogenic isotopic systematics of layered intrusions: application to the Mesoproterozoic Kiglapait Intrusion of coastal Labrador, Canada, and to mafic-ultramafic rock reference values: Unpublished PhD dissertation, University of British Columbia, p. 1–389.
- Fourny, A., Scoates, J. S., Weis, D., and Amini, M., 2020, Testing for Pb isotopic differences between minerals in the Kiglapait layered intrusion by LA-ICP-MS: *Chemical Geology*, v. 537, p. 119475.
- Gabrielse, H., Monger, J., Wheeler, J., and Yorath, C., 1991, Tectonic framework, Part A. Morphogeological belts, tectonic assemblages and terranes: Chapter 2 of *Geology of the Canadian Orogen in Canada*, p. 13-58.
- Gagnon, J. F., Barresi, T., Waldron, J. W. F., Nelson, J. L., Poulton, T. P., and Cordey, F., 2012, Stratigraphy of the upper Hazelton group and the Jurassic evolution of the Stikine terrane, British Columbia: *Canadian Journal of Earth Sciences*, v. 49, p. 1027–1052.
- Gao, J. F., and Zhou, M. F., 2013, Magma mixing in the genesis of the Kalatongke dioritic intrusion: Implications for the tectonic switch from subduction to post-collision, Chinese Altay, NW China: *Lithos*, v. 162–163, p. 236–250.
- Garbe-Schönberg, D., and Müller, S., 2014, Nano-particulate pressed powder tablets for LA-ICP-MS: *Journal of Analytical Atomic Spectrometry*, v. 29, p. 990–1000.
- Godwin, B. C. I., Gabites, J. E., and Andrew, A., 1990, Leadtable: a galena lead isotope data base for the Canadian Cordillera, with a guide to its use by explorationists: British Columbia Ministry of Energy, Mines and Petroleum Resources Paper 1988-4, 188 p.
- Greene, A. R., Scoates, J. S., Weis, D., Nixon, G. T., and Kieffer, B., 2009, Melting history and magmatic evolution of basalts and picrites from the accreted Wrangellia oceanic plateau, Vancouver Island, Canada: *Journal of Petrology*, v. 50, p. 467–505.
- Griffin, W. L., Begg, G. C., and O'Reilly, S. Y., 2013, Continental-root control on the genesis of magmatic ore deposits: *Nature Geoscience*, v. 6, p. 905–910.
- Halla, J., 2018, Pb isotopes – A multi-function tool for assessing tectonothermal events and crust-mantle recycling at late Archaean convergent margins: *Lithos*, v. 320–321, p. 207–221.
- Hancock, K. D., 1990, Geology of Nickel Mountain and the E&L nickel-copper prospect (104B/10E): *Geological Fieldwork 1989*, British Columbia Ministry of Energy, Mines, and Petroleum Resources, v. Paper 1990, p. 337–341.

- Hauksdottir, S., Enegren, E.G., and Russell, J.K., 1994, Recent basaltic volcanism in the Iskut-Unuk rivers area, northwestern British Columbia: Geological Survey of Canada Paper, v. 94-1A, p. 57-67.
- Hawkesworth, C.J., Turner, S.P., Mcdermott, F., Peate, D.W., and Van, C.P., 1997, U–Th isotopes in arc magmas: implications for element transfer from the subducted crust: *Science*, v. 276, p. 551–555.
- Holwell, D. A., Fiorentini, M., McDonald, I., Lu, Y., Giuliani, A., Smith, D. J., Keith, M., and Locmelis, M., 2019, A metasomatized lithospheric mantle control on the metallogenic signature of post-subduction magmatism: *Nature Communications*, v. 10, p. 1–10.
- Jackson, M. G., and Dasgupta, R., 2008, Compositions of HIMU, EM1, and EM2 from global trends between radiogenic isotopes and major elements in ocean island basalts: *Earth and Planetary Science Letters*, v. 276, p. 175–186.
- Jochum, K. P., and Enzweiler, J., 2013, Reference materials in geochemical and environmental research, in *Treatise on Geochemistry: Second Edition*: Amsterdam, Elsevier Ltd, p. 43-70.
- King, R. L., Bebout, G. E., Grove, M., Moriguti, T., and Nakamura, E., 2007, Boron and lead isotope signatures of subduction-zone mélangé formation: Hybridization and fractionation along the slab-mantle interface beneath volcanic arcs: *Chemical Geology*, v. 239 (3-4), p. 305-322.
- Kyba, J., and Nelson, J., 2015, Stratigraphic and tectonic framework of the Khyber-Sericite-Pins mineralized trend, lower Iskut River, northwest British Columbia: *Geological Fieldwork 2014*, British Columbia Ministry of Energy and Mines, p. 41–58.
- Langmuir, C. H., Vocke, R. D., Hanson, G. N., and Hart, S. R., 1978, A general mixing equation with applications to Icelandic basalts: *Earth and Planetary Science Letters*, v. 37, p. 380–392.
- Leshner, C.M., 2019a, Geology, genesis and exploration for magmatic Ni-Cu-PGE systems: In: *Geology, Genesis and Exploration for Magmatic and Magmatic-Hydrothermal Ore Deposits: PDAC Short Course*.
- Leshner, C. M., 2019b, Up, down, or sideways: Emplacement of magmatic Fe–Ni–Cu–PGE sulfide melts in large igneous provinces: *Canadian Journal of Earth Sciences*, v. 56, p. 756–773.
- Leshner, C. M., Burnham, O. M., Keays, R. R., Barnes, S. J., and Hulbert, L., 2001, Trace-element geochemistry and petrogenesis of barren and ore-associated komatiites: *Canadian Mineralogist*, v. 39, p. 673–696.
- Li, C., Zhang, M., Fu, P., Qian, Z., Hu, P., and Ripley, E. M., 2012, The Kalatongke magmatic Ni-Cu deposits in the Central Asian Orogenic Belt, NW China: Product of slab window magmatism? *Mineralium Deposita*, v. 47, p. 51–67.

- Lianxing, G., and Vokes, F. M., 1996, Intergrowths of hexagonal and monoclinic pyrrhotites in some sulphide ores from Norway: *Mineralogical Magazine*, v. 60, p. 303–316.
- Lightfoot, P. C., 2016, Nickel sulfide ores and impact melts: Origin of the Sudbury igneous complex: Elsevier, p. 1-680
- Lightfoot, P. C., and Evans-Lamswood, D., 2015, Structural controls on the primary distribution of mafic-ultramafic intrusions containing Ni-Cu-Co-(PGE) sulfide mineralization in the roots of large igneous provinces: *Ore Geology Reviews*, v. 64, p. 354–386.
- Lightfoot, P. C., Stewart, R., Gribbin, G., and Mooney, S. J., 2017, Relative contribution of magmatic and post-magmatic processes in the genesis of the Thompson Mine Ni-Co sulfide ores, Manitoba, Canada: *Ore Geology Reviews*, v. 83, p. 258–286.
- Lightfoot, P. C., Hanson, J.A., Makela, E., Regoci, S., and Muggridge, M., 2019, The E&L Discovery: massive Ni-Cu-Co-precious metal sulfide mineralization from the Eskay Rift: PDAC Investor Presentation.
- Logan, J. M., Drobe, J. R., and McClelland, W. C., 2000, Geology of the Forrest Kerr- Mess Creek area, northwestern British Columbia: 164 p.
- Lu, Y., Leshner, C. M., and Deng, J., 2019, Geochemistry and genesis of magmatic Ni-Cu-(PGE) and PGE-(Cu)-(Ni) deposits in China: *Ore Geology Reviews*, v. 107, p. 863–887.
- Maier, W. D., Smithies, R. H., Spaggiari, C. V., Barnes, S. J., Kirkland, C. L., Yang, S., Lahaye, Y., Kiddie, O., and MacRae, C., 2016, Petrogenesis and Ni-Cu sulphide potential of mafic-ultramafic rocks in the Mesoproterozoic Fraser Zone within the Albany-Fraser Orogen, Western Australia: *Precambrian Research*, v. 281, p. 27–46.
- Manor, M. J., 2014, Convergent margin Ni-Cu-PGE deposits: geology, geochronology, and geochemistry of the Giant Mascot magmatic sulfide deposit, Hope, British Columbia: Unpublished MSc thesis, University of British Columbia: 387 p.
- Manor, M. J., Scoates, J. S., Nixon, G. T., and Ames, D. E., 2016, The Giant Mascot Ni-Cu-PGE deposit, British Columbia: Mineralized conduits in a convergent margin tectonic setting: *Economic Geology*, v. 111, p. 57–87.
- Mansur, E. T., Barnes, S. J., and Duran, C. J., 2019, Textural and compositional evidence for the formation of pentlandite via peritectic reaction: Implications for the distribution of highly siderophile elements: *Geology*, v. 47, p. 351–354.
- Marshall, B., and Gilligan, L. B., 1987, An introduction to remobilization: Information from ore-body geometry and experimental considerations: *Ore Geology Reviews*, v. 2, p. 87–131.
- Mathez, E. A., and Waight, T. E., 2003, Lead isotopic disequilibrium between sulfide and plagioclase in the Bushveld complex and the chemical evolution of large layered intrusions: *Geochimica et Cosmochimica Acta*, v. 67, p. 1875–1888.

- Mole, D. R., Barnes, S. J., Le Vaillant, M., Martin, L. A. J., and Hicks, J., 2018, Timing, geochemistry and tectonic setting of Ni-Cu sulfide-associated intrusions of the Halls Creek Orogen, Western Australia: *Lithos*, v. 314–315, p. 425–446.
- Muggridge, M. G., 2019, Assessment Report for Diamond Drilling and Geophysical Work Performed on the E&L Nickel Mtn Property.
- Mukwakwami, J., Lafrance, B., Leshner, C. M., Tinkham, D. K., Rayner, N. M., and Ames, D. E., 2014, Deformation, metamorphism, and mobilization of Ni-Cu-PGE sulfide ores at Garson Mine, Sudbury: *Mineralium Deposita*, v. 49, p. 175–198.
- Mungall, J. E., 2002, Kinetic controls on the partitioning of trace elements between silicate and sulfide liquids: *Journal of Petrology*, v. 43, p. 749–768.
- Naldrett, A. J., 1969, A portion of the system FE - S - O between 900 and 1080 °c and its application to sulfide ore magmas: *Journal of Petrology*, v. 10, p. 171–201.
- Naldrett, A. J., 1989, Sulphide melts - Crystallisation temperatures, solubilities in silicate melts, and Fe, Ni and Cu partitioning between basaltic magmas and olivine, in Whitney, J. A. and Naldrett, A. J. eds., *Ore Deposition Associated with Magmas: New Mexico Bureau of Mines & Mineral Resources*, p. 5–20.
- Naldrett, A. J., 2004, *Magmatic Sulfide Deposits: New York, Springer Berlin Heidelberg*, 744 p.
- Naldrett, A. J., 2010, From the mantle to the bank: The life of a Ni-Cu-(PGE) sulfide deposit: *South African Journal of Geology*, v. 113, p. 1–32.
- Naldrett, A. J., Singh, J., Krstic, S., and Li, C., 2000, The mineralogy of the Voisey's Bay Ni-Cu-Co deposit, Northern Labrador, Canada: Influence of oxidation state on textures and mineral compositions: *Economic Geology*, v. 95, p. 889–900.
- Nelson, J., 2017, Composite pericratonic basement of west-central Stikinia and its influence on Jurassic magma conduits: Examples from the Terrace-Ecstall and Anyox areas: *Geological Fieldwork 2016, British Columbia Ministry of Energy and Mines*, v. 2017–1, p. 61–82.
- Nelson, J., and Colpron, M., 2007, Tectonics and metallogeny of the British Columbia, Yukon and Alaskan Cordillera, 1.8 Ga to the present: *Mineral Deposits of Canada: A Synthesis of Major Deposit-Types, District Metallogeny, the Evolution of Geological Provinces, and Exploration Methods*, v. 2703, p. 755–791.
- Nelson, J., and Kyba, J., 2014, Structural and stratigraphic control of porphyry and related mineralization in the Treaty Glacier – KSM – Brucejack – Stewart trend of western Stikinia: *Geological Fieldwork 2013, British Columbia Ministry of Energy, Mines, and Petroleum Resources*, v. 2014–1, p. 111–140.

- Nelson, J. L., Colpron, M., and Israel, S., 2013, The Cordillera of British Columbia, Yukon, and Alaska: Tectonics and Metallogeny: Tectonics, Metallogeny, and Discovery-the North American Cordillera and similar accretionary settings, p. 53–109.
- Nelson, J., Waldron, J., van Straaten, B., Zagorevski, A., and Rees, C., 2018, Revised stratigraphy of the Hazelton Group in the Iskut River region, northwestern British Columbia: Geological Fieldwork 2017, British Columbia Ministry of Energy and Mines, v. 2018–1, p. 15–38.
- Nicholson, S. W., and Shirey, S. B., 1990, Midcontinent rift volcanism in the Lake Superior region: Sr, Nd, and Pb isotopic evidence for a mantle plume origin: *Journal of Geophysical Research*, v. 95, p. 10851-10868.
- Nixon, G. T., Hammack, J. L., Ash, C. H., Cabri, L. J., Case, G., Connelly, J. N., Heaman, L. M., Laflamme, J. H. G., Nuttall, C., Paterson, W. P. E., and Wong, R. H., 1997, Magmatic and tectonic setting of Alaskan-type complexes, in *Geology and platinum-group-element mineralization of Alaskan-type ultramafic-mafic complexes in British Columbia: Geological Survey Branch, British Columbia Ministry of Employment and Investment Bulletin 93*, p. 119–126.
- Nixon, G. T., Scheel, J. E., Scoates, J. S., Friedman, R. M., Wall, C. J., Gabites, J., and Jackson-Brown, S. Syn-accretionary multistage assembly of an Early Jurassic Alaskan-type intrusion in the Canadian Cordillera: U–Pb and $^{40}\text{Ar}/^{39}\text{Ar}$ geochronology of the Turnagain ultramafic–mafic intrusive complex, Yukon–Tanana terrane: *Canadian Journal of Earth Sciences*, v. 0, p. 1–26.
- Paton, C., Hellstrom, J., Bence, P., Woodhead, J., and Hergt, J., 2011, Iolite: Freeware for the visualization and processing of mass spectrometric data: *Journal of Analytical Atomic Spectrometry*, v. 26, p. 2508–2518.
- Pearce, J. A., and Peate, D. W., 1995, Tectonic implications of the composition of volcanic arc magmas: *Annual Review of Earth and Planetary Sciences*, v. 23, p. 251–285.
- Pietruszka, A. J., and Neymark, L. A., 2017, Evaluation of laser ablation double-focusing SC-ICPMS for “common” lead isotopic measurements in silicate glasses and minerals: *Journal of Analytical Atomic Spectrometry*, v. 32, p. 1135-1154.
- Piña, R., Romeo, I., Ortega, L., Lunar, R., Capote, R., Gervilla, F., Tejero, R., and Quesada, C., 2010, Origin and emplacement of the Aguablanca magmatic Ni-Cu-(PGE) sulfide deposit, SW Iberia: A multidisciplinary approach: *Bulletin of the Geological Society of America*, v. 122, p. 915–925.
- Prichard, H. M., Hutchinson, D., and Fisher, P. C., 2004, Petrology and crystallization history of multiphase sulfide droplets in a mafic dike from Uruguay: Implications for the origin of Cu-Ni-PGE sulfide deposits: *Economic Geology*, v. 99, p. 365–376.

- Ripley, E. M., 2010, Chapter 24 – A new perspective on exploration for magmatic sulfide-rich Ni- Cu-(PGE) deposits: *Economic Geology Special Publications*, v. 15, p. 437–450.
- Ripley, E. M., and Li, C., 2007, Applications of stable and radiogenic isotopes to magmatic Cu-Ni-PGE Deposits: examples and cautions: *Earth Science Frontiers*, v. 14, p. 124–131.
- Robertson, J. C., Barnes, S. J., and Le Vaillant, M., 2015, Dynamics of magmatic sulphide droplets during transport in silicate melts and implications for magmatic sulphide ore formation: *Journal of Petrology*, v. 56, p. 2445–2472.
- Salters, V. J. M., and Stracke, A., 2004, Composition of the depleted mantle: *Geochemistry, Geophysics, Geosystems*, v. 5, p. 1-27.
- Savard, D., Bouchard-Boivin, B., Barnes, S. J., and Garbe-Schönberg, D., 2018, UQAC-FeS: A new series of base metal sulfide quality control reference material for LA-ICP-MS analysis, in *Proceedings of the 10th International Conference on the Analysis of Geological and Environmental Materials*, Sydney, Australia: p. 8–13.
- Scheel, J. E., Nixon, G. T., and Scoates, J. S., 2005, New Observations on the Geology of the Turnagain Alaskan-Type Ultramafic Intrusive Suite and Associated Ni-Cu-PGE Mineralization, British Columbia: *Geological Fieldwork 2004*, British Columbia Ministry of Energy and Mines, v. 2005–1, p. 167–176.
- Seccombe, P. K., and Barnes, H. L., 1990, Experimental mobility of sulfides along hydrothermal gradients: *Economic Geology*, v. 85, p. 1099–1113.
- Sharp, W.M., 1966, Report on current geological evaluation and proposals for further exploration of the E&L Nickel-Copper deposits near Snippaker Creek, Iskut River District, Liard Mining Division, BC for Silver Standard Mines Ltd. (N.P.L.).
- Sinton, J. M., and Fryer, P., 1987, Mariana Trough lavas from 18°N: Implications for the origin of back arc basin basalts: *Journal of Geophysical Research*, v. 92, p. 12782.
- Souders, A. K., and Sylvester, P. J., 2010, Accuracy and precision of non-matrix-matched calibration for lead isotope ratio measurements of lead-poor minerals by LA-MC-ICPMS: *Journal of Analytical Atomic Spectrometry*, v. 25, p. 975-988.
- Stern, R. J., 2002, Subduction zones: *Reviews of Geophysics*, v. 40, p. 3-1-3–38.
- St. Louis, R. M., Nesbitt, B. E., and Morton, R. D., 1986, Geochemistry of platinum-group elements in the Tulameen ultramafic complex, southern British Columbia: *Economic Geology*, v. 81, p. 961–973.
- Sun, S.-s., and McDonough, W. F., 1989, Chemical and isotopic systematics of oceanic basalts: Implications for mantle composition and processes: *Geological Society Special Publication*, v. 42, p. 313–345.

- Tornos, F., Casquet, C., Galindo, C., Velasco, F., and Canales, A., 2001, A new style of Ni-Cu mineralization related to magmatic breccia pipes in a transpressional magmatic arc, Aguablanca, Spain: *Mineralium Deposita*, v. 36, p. 700–706.
- Tornos, F., Galindo, C., Casquet, C., Rodríguez Pevida, L., Martínez, C., Martínez, E., Velasco, F., and Iriondo, A., 2006, The Aguablanca Ni-(Cu) sulfide deposit, SW Spain: Geologic and geochemical controls and the relationship with a midcrustal layered mafic complex: *Mineralium Deposita*, v. 41, p. 737–769.
- Ver Hoeve, T. J., Scoates, J. S., Wall, C. J., Weis, D., and Amini, M., 2018, Evaluating downhole fractionation corrections in LA-ICP-MS U-Pb zircon geochronology: *Chemical Geology*, v. 483, p. 201–217.
- Weis, D., 2016a, Lead, in White, W. M. ed., *Encyclopedia of Geochemistry*: Springer International Publishing, p. 1–6.
- Weis, D., 2016b, Lead Isotopes, in White, W. M. ed., *Encyclopedia of Geochemistry*: Springer International Publishing, p. 1–5.
- White, W. M., 1993, $^{238}\text{U}/^{204}\text{Pb}$ in MORB and open system evolution of the depleted mantle: *Earth and Planetary Science Letters*, v. 115, p. 211–226.
- White, W. M., Hofmann, A. W., and Puchelt, H., 1987, Isotope geochemistry of Pacific mid-ocean ridge basalt: *Journal of Geophysical Research* v. 92, p. 4881-4893.
- Wooden, J. L., Czamanske, G. K., Bouse, R. M., Likhachev, A. P., Kunilov, V. E., and Lyul'ko, V., 1992, Pb isotope data indicate a complex, mantle origin for the Noril'sk-Talnakh Ores, Siberia: *Economic Geology*, v. 87, p. 1153–1165.
- Workman, R. K., Hart, S. R., Jackson, M., Regelous, M., Farley, K. A., Blusztajn, J., Kurz, M., and Staudigel, H., 2004, Recycled metasomatized lithosphere as the origin of the Enriched Mantle II (EM2) end-member: Evidence from the Samoan Volcanic Chain: *Geochemistry, Geophysics, Geosystems*, v. 5, p. 1–44.
- Yang, S., Qu, W., Tian, Y., Chen, J., Yang, G., and Du, A., 2008, Origin of the inconsistent apparent Re-Os ages of the Jinchuan Ni-Cu sulfide ore deposit, China: Post-segregation diffusion of Os: *Chemical Geology*, v. 247, p. 401–418.
- Yoshiki-Gravelsins, K. S., and Toguri, J. M., 1993, Oxygen and sulfur solubilities in Ni-Fe-S-O melts: *Metallurgical Transactions B*, v. 24, p. 847–856.
- Zartman, R. E., and Haines, S. M., 1988, The plumbotectonic model for Pb isotopic systematics among major terrestrial reservoirs-A case for bi-directional transport: *Geochimica et Cosmochimica Acta*, v. 52, p. 1327-1339.

Zhao, Y., Xue, C., Zhao, X., Yang, Y., Ke, J., Zu, B., and Zhang, G., 2016, Origin of anomalously Ni-rich parental magmas and genesis of the Huangshannan Ni-Cu sulfide deposit, Central Asian Orogenic Belt, Northwestern China: *Ore Geology Reviews*, v. 77, p. 57–71.

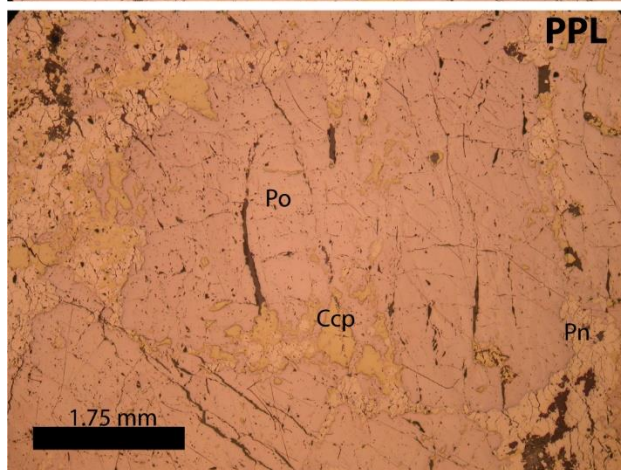
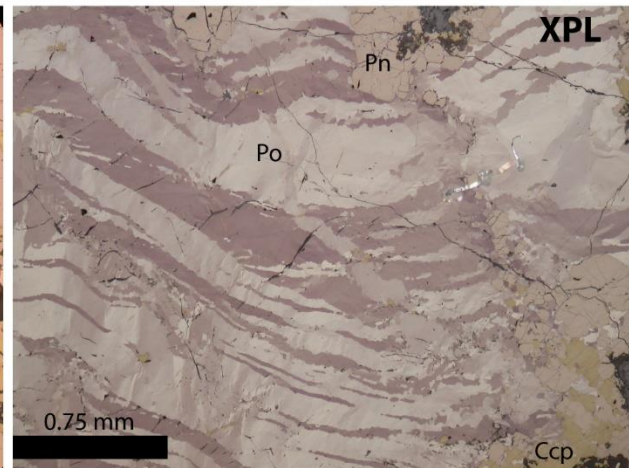
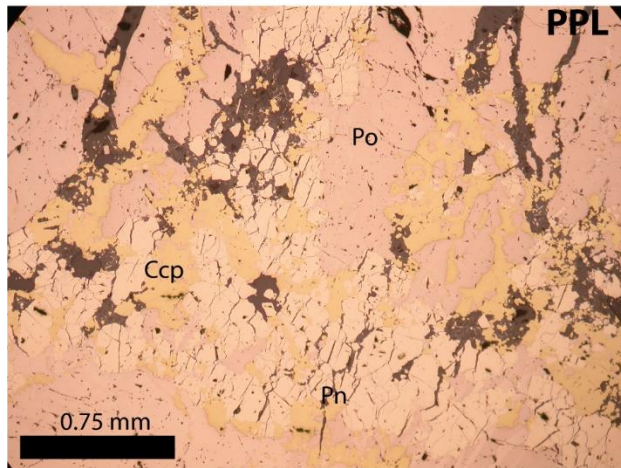
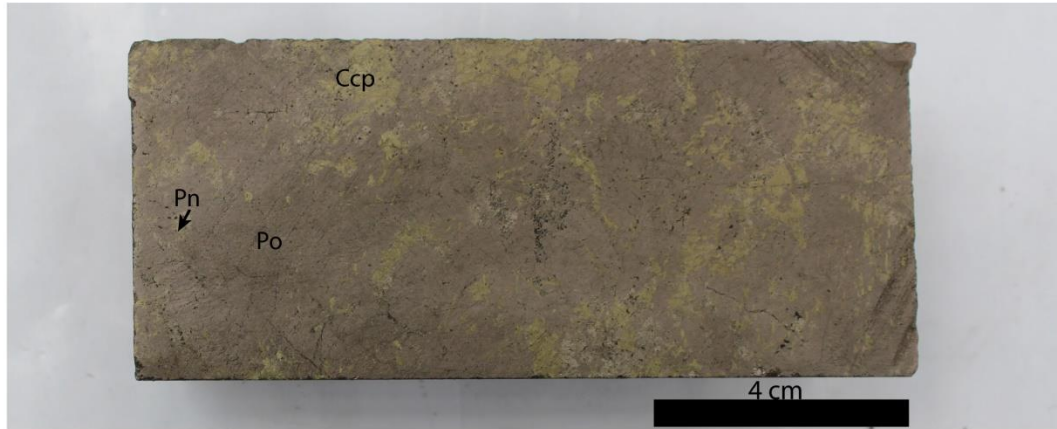
Zindler, A., and Hart, S., 1986, Chemical geodynamics: *Annual Review of Earth and Planetary Sciences*. v. 14, p. 493-571.

Appendix A: Sample Scans, Thin Section Scans, Photomicrographs, and Thin Section Descriptions

19-EV-24-01

(EL-19-24, 188.80-188.85 m)

Lower Discovery Zone



Massive sulfide consisting of:

68% pyrrhotite: <5 mm diameter, anhedral crystals, exhibits "crenulation" monoclinic-hexagonal exsolutions, as well as twinning "veins" that cross-cut the dominant exsolution fabric. Pyrrhotite grains are surrounded by pentlandite and chalcopyrite.

16% granular pentlandite: <4 mm diameter, subhedral-euhedral crystals with little to no violarite alteration.

16% chalcopyrite: <3 mm diameter, anhedral and irregular blebs, veins and fracture infills, generally fringed by pentlandite in larger blebs.

0.5% magnetite: <0.2 mm diameter, subhedral crystals, exhibits strong resorption textures and mainly occurs within chalcopyrite-rich domains.

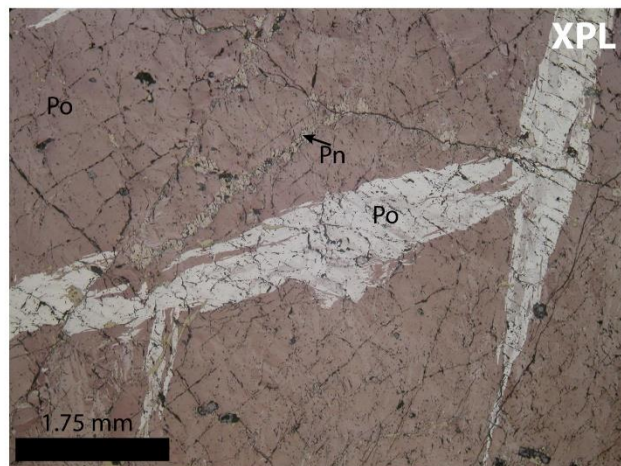
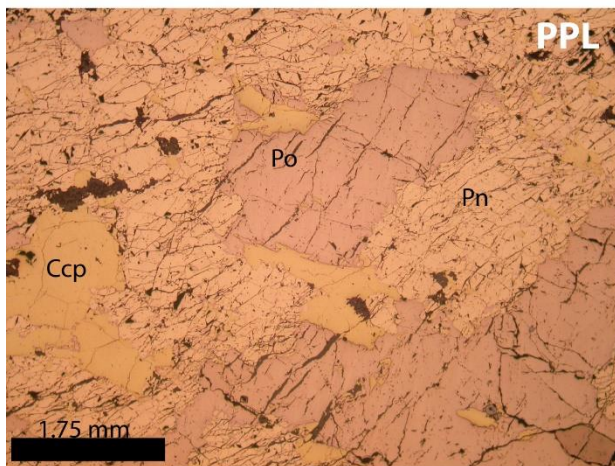
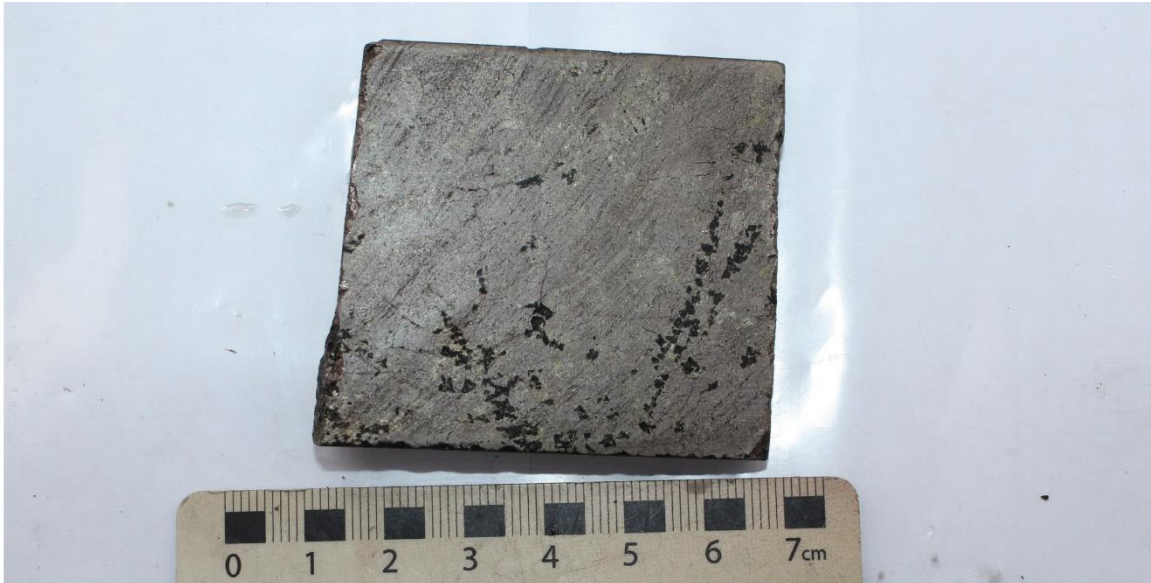
Trace flame pentlandite: <0.1 mm diameter, anhedral exsolution lamellae of pentlandite within pyrrhotite domains.

The coarser grains of pentlandite and blebs of chalcopyrite form loop textures that envelop grains of pyrrhotite.

19-EV-24-02

(EL-19-24, 190.64-190.69 m)

Lower Discovery Zone



Massive sulfide consisting of:

68% pyrrhotite: <5 mm diameter, anhedral crystals, exhibiting a discontinuous "crenulation" monoclinic-hexagonal twinning fabric. Grains are surrounded by pentlandite, chalcopyrite and magnetite.

15% granular pentlandite: <3 mm diameter, subhedral-euhedral granular crystals, ~5 vol% altered to violarite along edges and fractures.

9.5% chalcopyrite: <1 mm diameter, anhedral, forms irregular blebs and veins that comprise loop structure with granular pentlandite, minor infilling of magnetite fractures.

7% magnetite: <3 mm diameter, anhedral-subhedral crystals, exhibiting a low degree of fracturing; found in chalcopyrite- and pentlandite-rich (ISS) zones.

0.5% silicate inclusions: < 0.6 mm diameter.

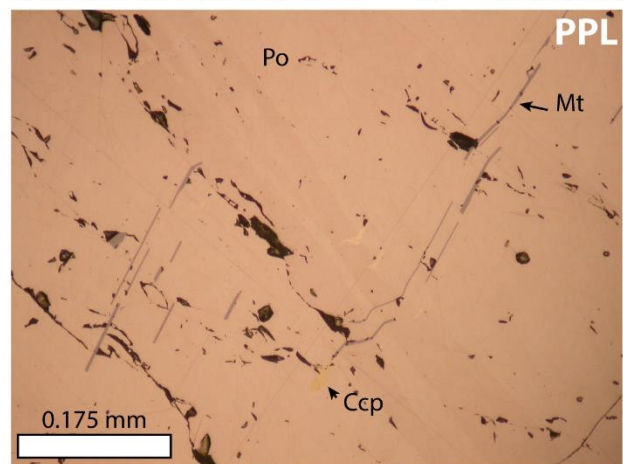
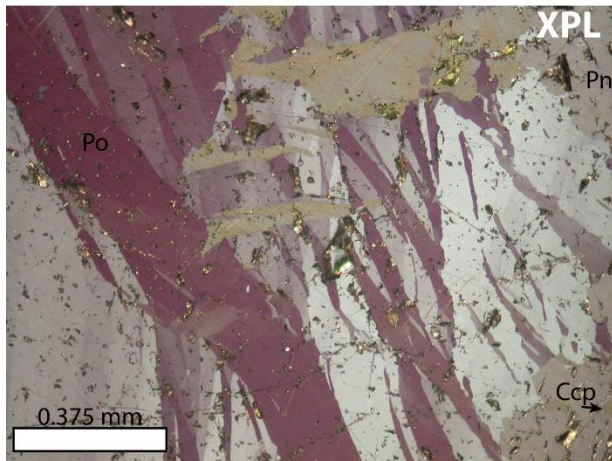
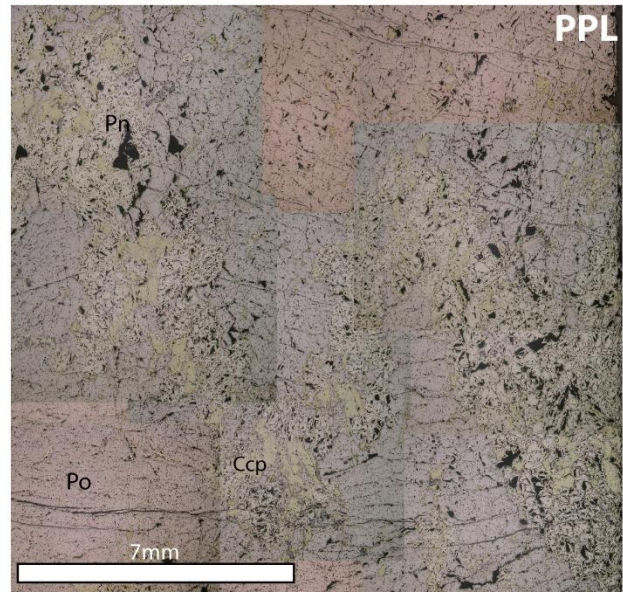
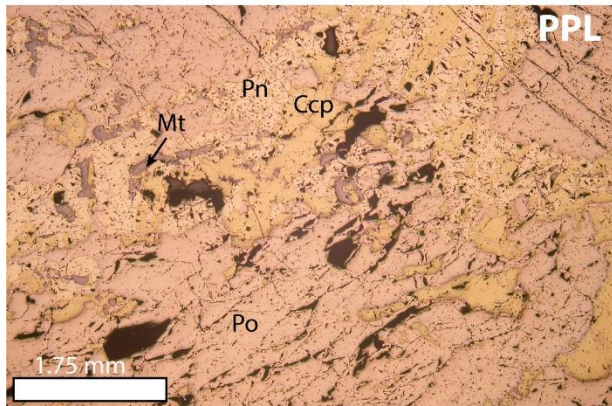
Trace flame pentlandite: < 0.1 mm diameter, anhedral exsolutions within pyrrhotite domains.

Sample exhibits weak loop texture characterized by veins/domains of chalcopyrite and granular pentlandite, enclosing pyrrhotite grains

19-EV-30-01

(EL-19-30, 76.4-76.45 m)

Northeast Zone



Massive sulfide consisting of:

70% pyrrhotite: <5 mm diameter, anhedral crystals, exhibiting moderate deformation twinning and enclosed by folded chalcopyrite and pentlandite loops.

14% granular pentlandite: <2 mm diameter, subhedral-euhedral granular crystals with trace violarite alteration. These pentlandite are less fractured than their Lower Discovery Zone counterparts, forming folded loops with chalcopyrite.

13% chalcopyrite: <2 mm diameter, anhedral irregular blebs and veins, forming folded loop structures with pentlandite.

3% magnetite: <0.35 mm diameter, anhedral-subhedral brittle deformed crystals with little to no resorption; associated with pentlandite and chalcopyrite domains.

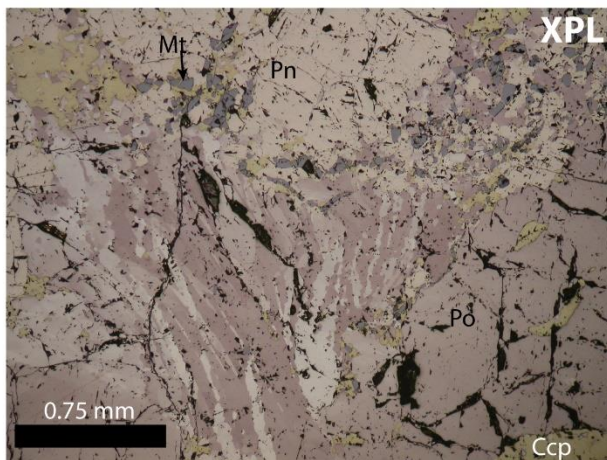
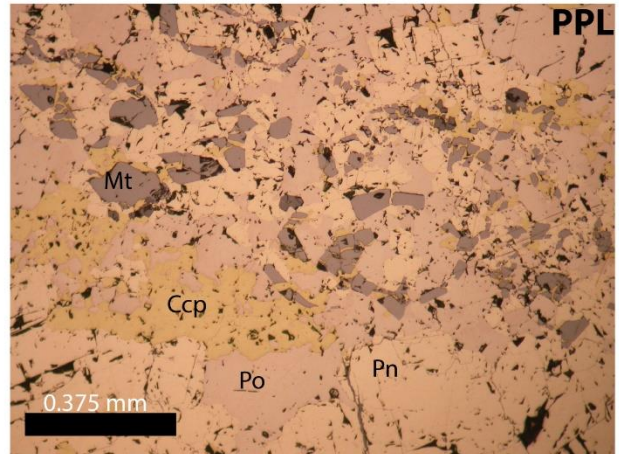
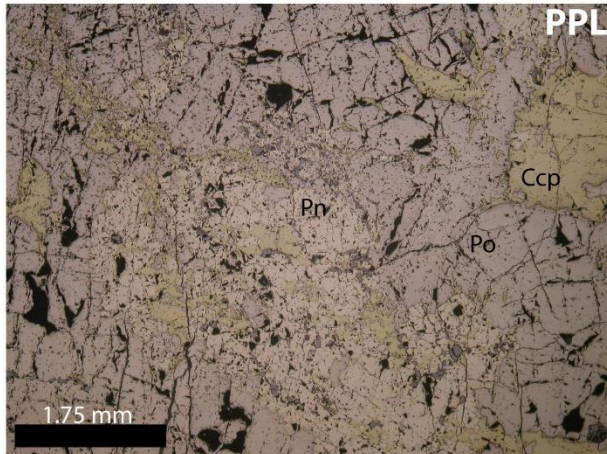
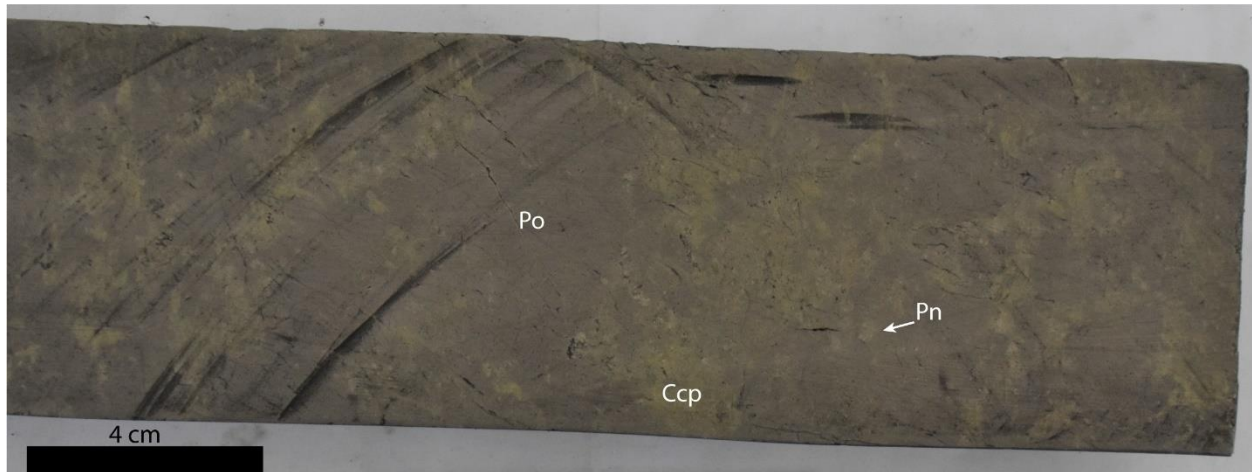
Trace flame pentlandite: <0.2 mm diameter, anhedral flames within pyrrhotite.

The thin section exhibits deformed loop structures, with 3 mm-wide folded loops consisting of granular pentlandite and chalcopyrite.

19-EV-30-02

(EL-19-30, 78.50-78.55 m)

Northeast Zone



Massive sulfide consisting of:

76% pyrrhotite: <5 mm diameter, anhedral crystals, exhibiting moderate deformation and enclosed by folded chalcopyrite and pentlandite.

12% chalcopyrite: <2 mm diameter, anhedral, irregular blebs and veins, occurring with pentlandite. Minor exsolution of chalcopyrite within pyrrhotite is also present.

11% granular pentlandite: <2 mm diameter, subhedral-euhedral granular crystals with trace violarite alteration. Occurs with chalcopyrite.

1% magnetite: <0.4 mm diameter, anhedral-subhedral, brittlely deformed crystals exhibiting little to no resorption, associated with pentlandite and chalcopyrite.

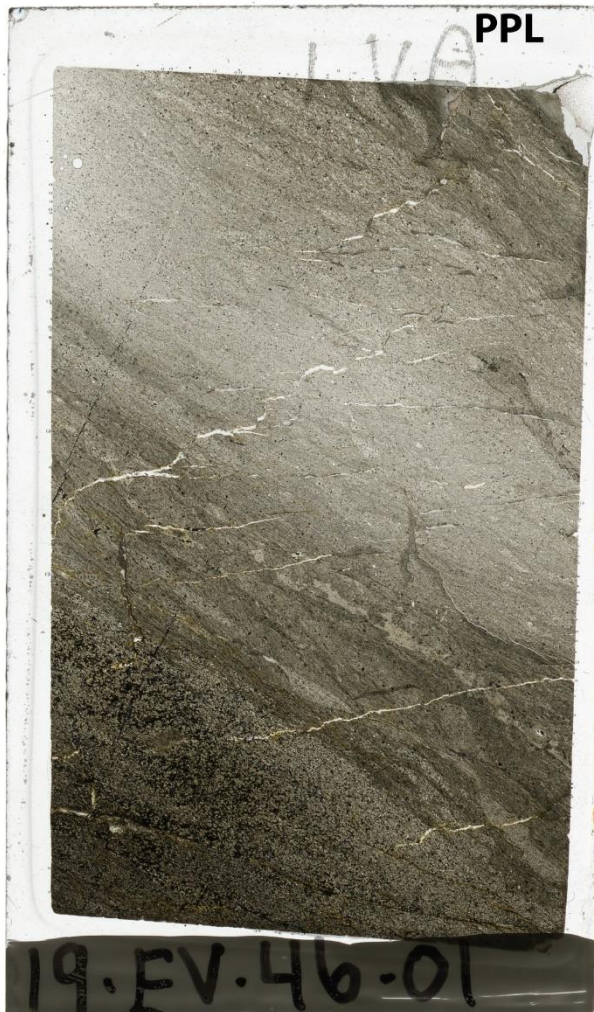
Trace flame pentlandite: < 0.2 mm diameter, anhedral flames within pyrrhotite. Pentlandite flames are most common along pyrrhotite grain boundaries.

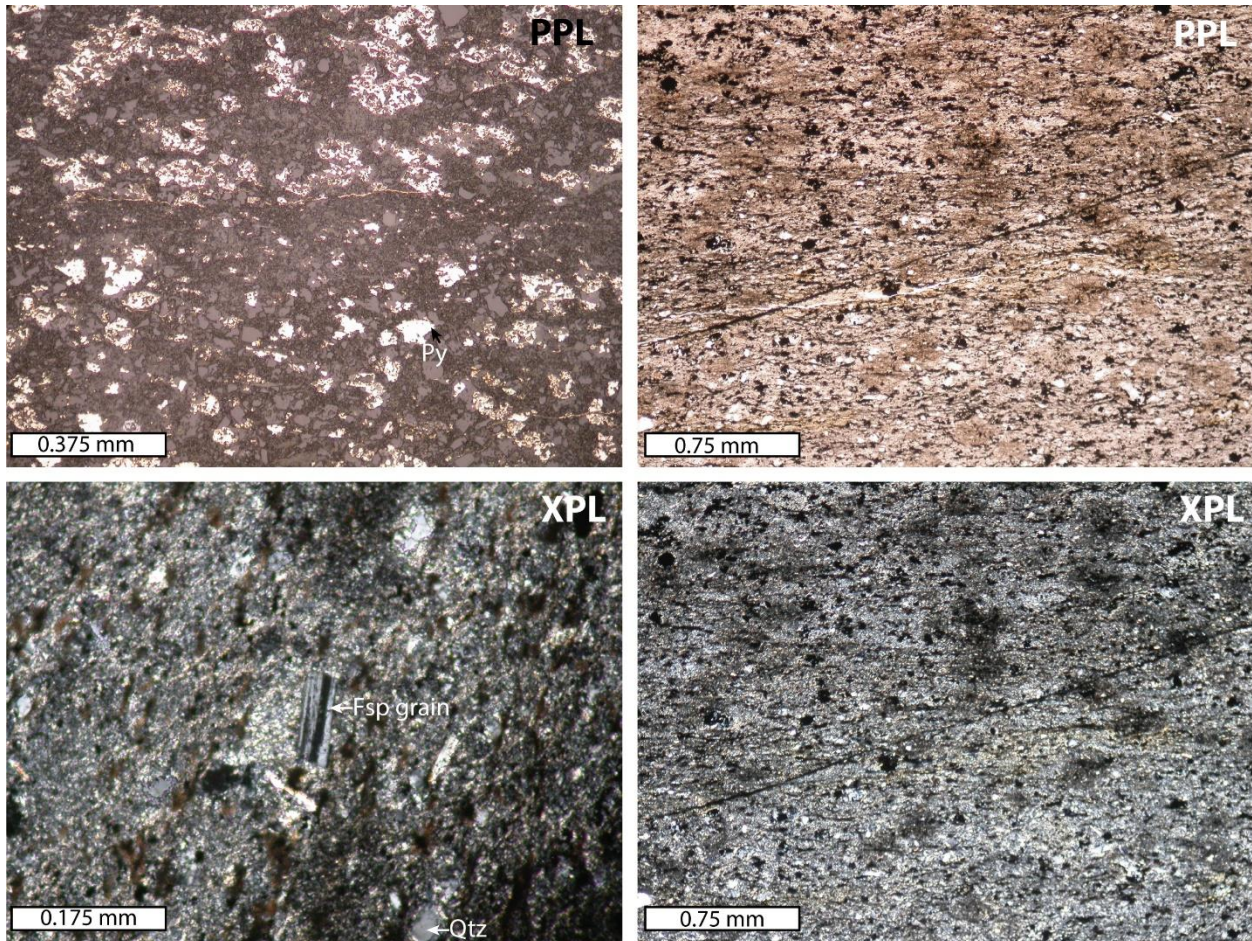
The primary loop texture within this sample has been modified: it appears that many of the pyrrhotite grains have been brittlely fractured and chalcopyrite has infilled these fractures.

19-EV-46-01

(EL-19-46, 230.85-230.90 m)

Hazelton Group





Dark purple grey, medium-bedded pyritic mudstone consisting of:

65% mud-sized particles: green and grey XPL+PPL; green particles are more common on one half of the section. The material is too fine grained to positively identify its composition but is likely consists of clays.

15% fine sand-silt-sized particles: consists predominantly of quartz and feldspar. Particles have rounded shapes, with some feldspar clasts exhibiting polysynthetic twinning.

20% Pyrite: <0.2 mm diameter, subhedral-euhedral, rounded or euhedral cubic-shaped crystals. Most pyrite is likely diagenetic, with the exception of pyrite found within the vein that cross-cuts the sample.

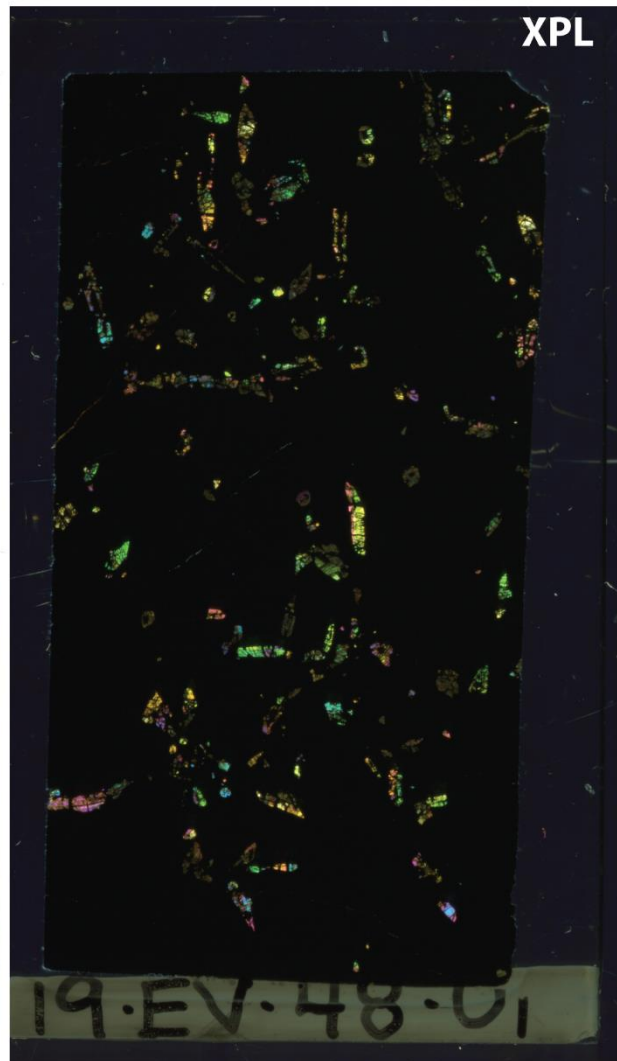
Trace chalcopyrite: locally found within a cross-cutting vein.

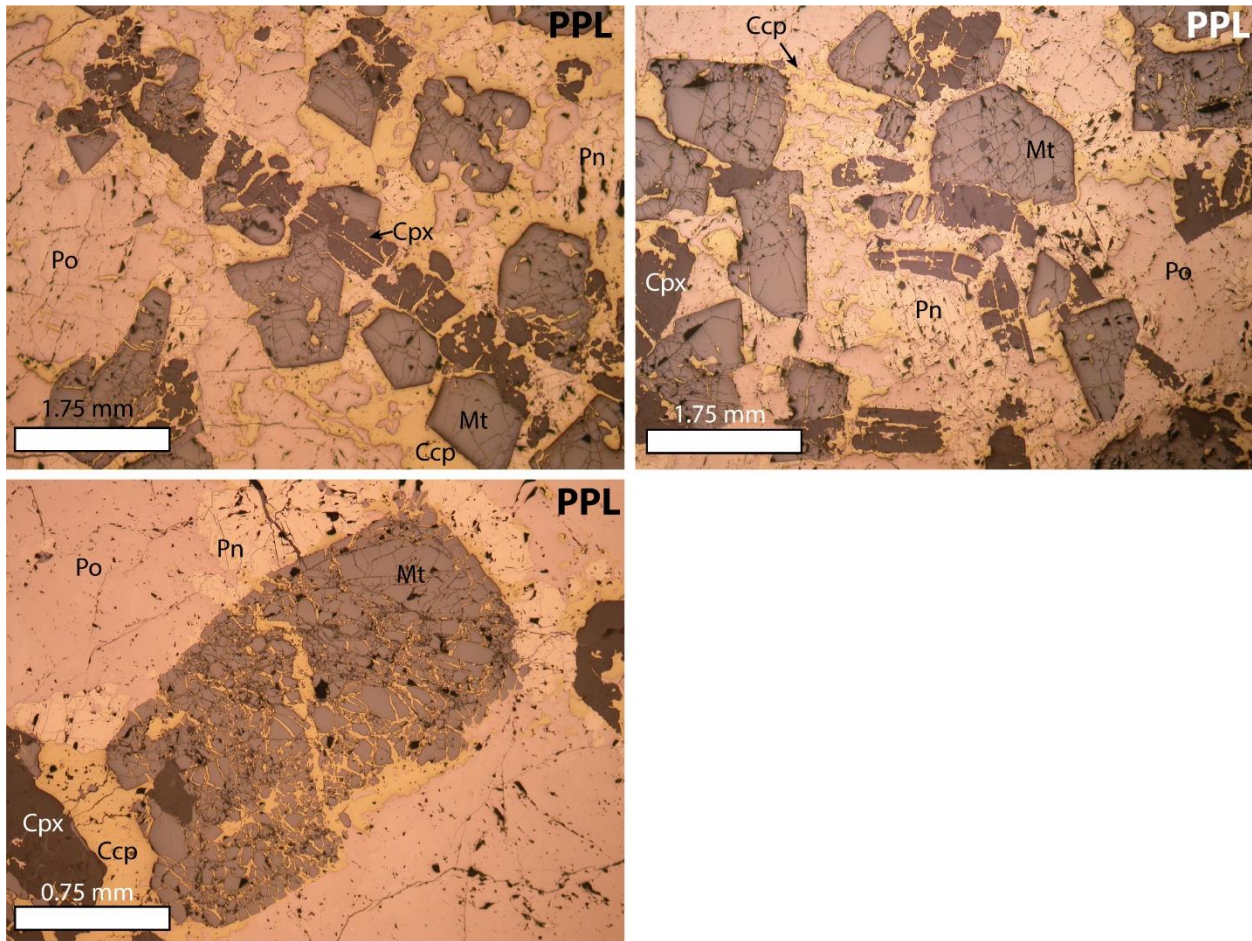
0.05 mm-wide quartz veins with minor hematite, pyrite and chalcopyrite define the alteration within the sample; these veins cross-cut the bedding plane and exhibit a semi-stepped morphology. Sample exhibits a medium-bedded texture, with changes in the modal percentage of pyrite and silt particles defining beds. No macrofossils or microfossils were found.

19-EV-48-01

(EL-19-48, 118.29-118.24 m)

Lower Discovery Zone





Clinopyroxene-bearing semi-massive sulfide consisting of:

48% pyrrhotite: <5 mm diameter, subhedral crystals, exhibiting exsolution of monoclinic and hexagonal pyrrhotite and deformation twinning.

16% magnetite: 0.8-2 mm diameter, subhedral-euhedral crystals, exhibiting resorption textures, strongly associated with chalcopyrite. Some crystals appear shattered, with the fractures infilled by chalcopyrite.

14% chalcopyrite: <2 mm diameter, anhedral, ameboidal blebs and veinlets, associated with pentlandite and magnetite, defining a weak, non-pervasive foliation within the sample.

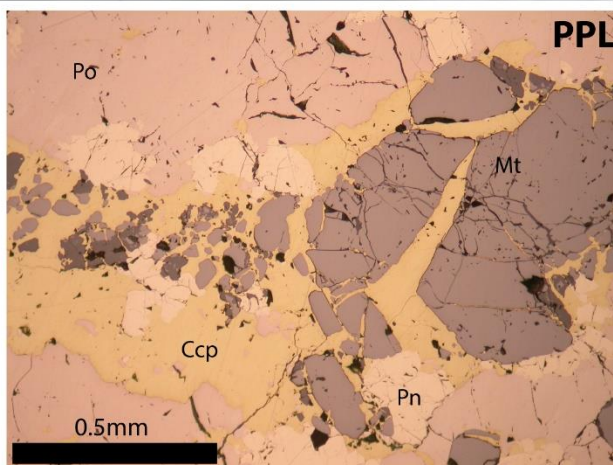
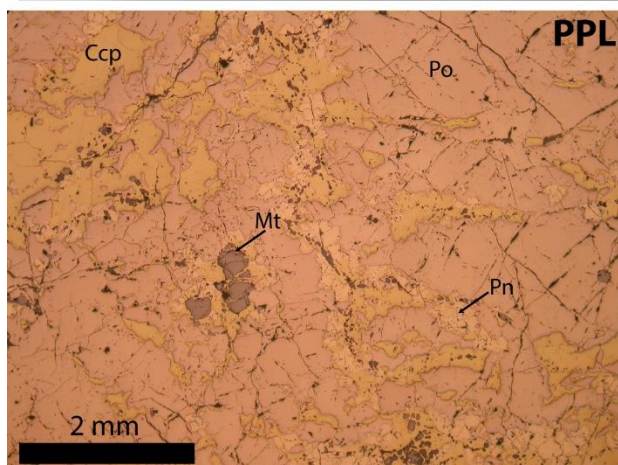
14% clinopyroxene phenocrysts: 1-5 mm diameter, high relief, 3rd order interference XPL, subhedral-euhedral skeletal crystals, locally forming elongated chains.

8% pentlandite: 0.2-3 mm diameter, euhedral crystals with a mostly granular habit. Pentlandite commonly occurs along fringes between chalcopyrite and pyrrhotite, with fractures altered to violarite.

19-EV-48-02

(EL-19-48, 188.77-188.83 m)

Lower Discovery Zone



Massive sulfide consisting of:

70% pyrrhotite: <5 mm diameter, locally fractured, anhedral crystals.

15% chalcopyrite: <2 mm diameter, anhedral, irregular blebs and veins, defining a potential weak foliation. Chalcopyrite infills fractures in magnetite.

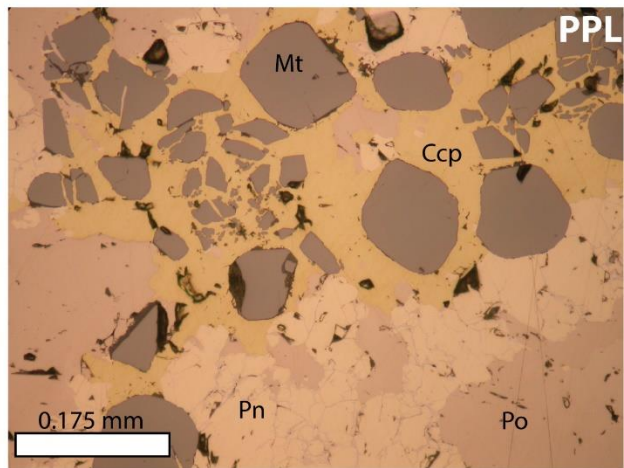
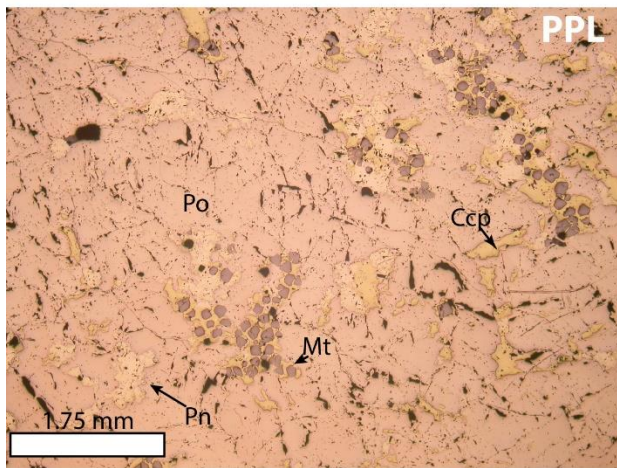
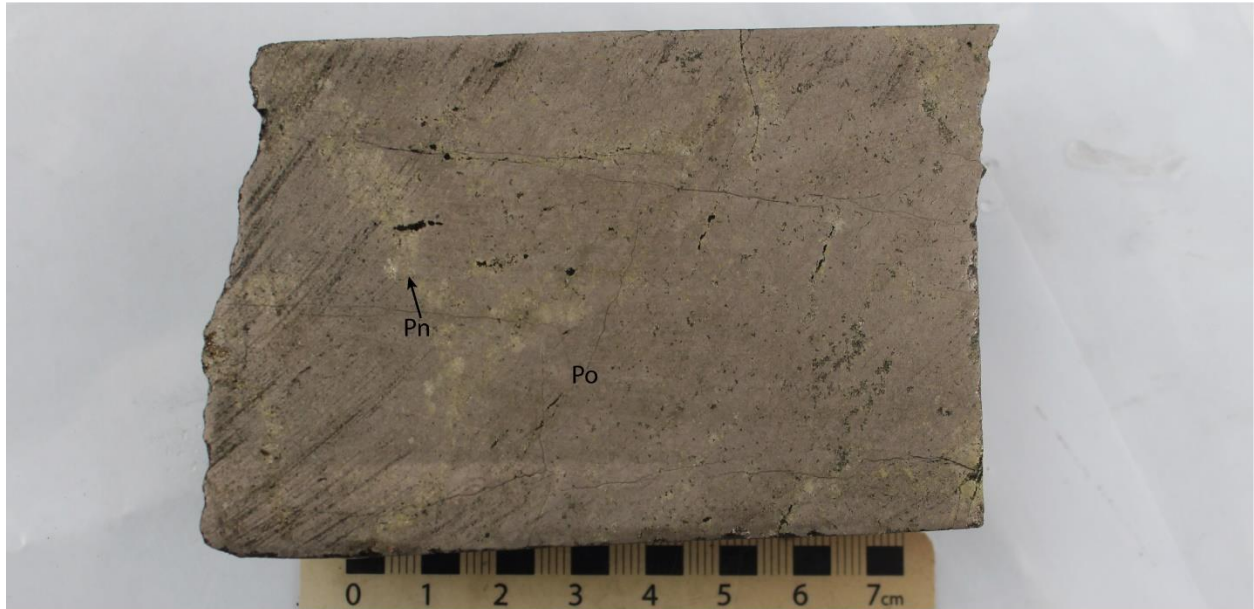
12% granular pentlandite: <3 mm diameter, locally fractured, subhedral-euhedral crystals. Pentlandite is ~10 vol% altered to violarite and commonly occurs with chalcopyrite.

3% magnetite: 1.5 mm diameter, subhedral crystals, exhibiting resorption textures and brittle deformation. Magnetite occurs within chalcopyrite- and pentlandite-rich areas. The smaller crystals are well-rounded, whereas larger crystals are more angular. Some smaller magnetite crystals display an elongate, rod shape.

Trace clinopyroxene phenocrysts: 0.5 mm diameter, euhedral crystals forming skeletal crystal chains.

Trace flame pentlandite: <0.1 mm diameter, anhedral crystals, occurring within pyrrhotite grains due to low temperature MSS exsolution.

The thin section exhibits a weak foliation.



Massive sulfide consisting of:

77% pyrrhotite: <6 mm diameter, anhedral crystals exhibiting monoclinic-hexagonal exsolutions and deformation twinning.

12% granular pentlandite: <2 mm diameter, subhedral-euhedral granular crystals with pronounced fractures, 10% altered to violarite along grain boundaries and fractures.

8% chalcopyrite: <1.5 mm diameter, anhedral blebs and veins occurring in association with granular pentlandite and as infill of fractures within magnetite.

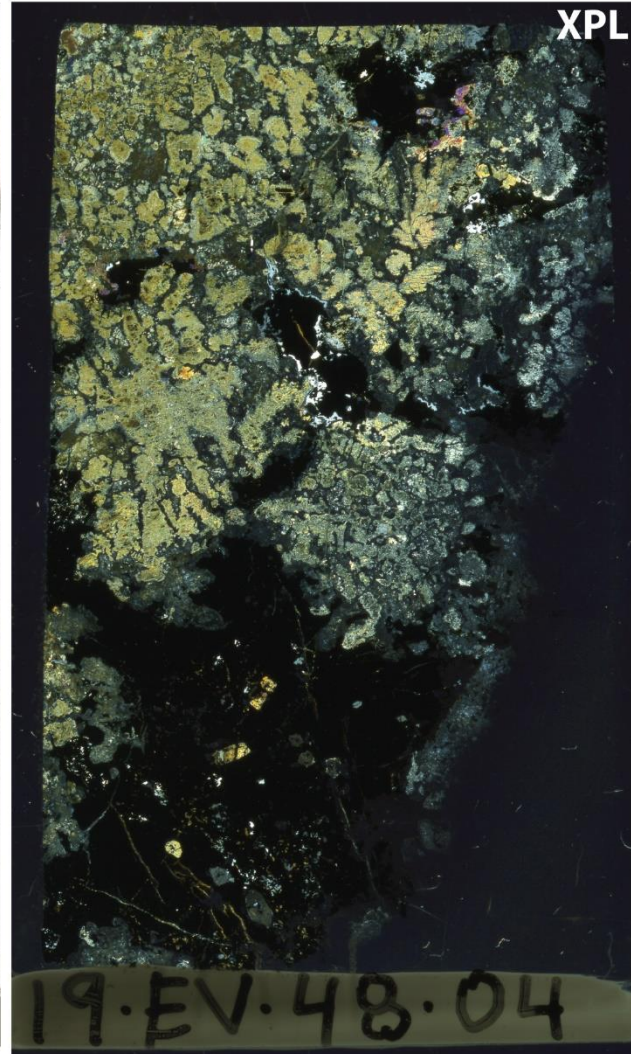
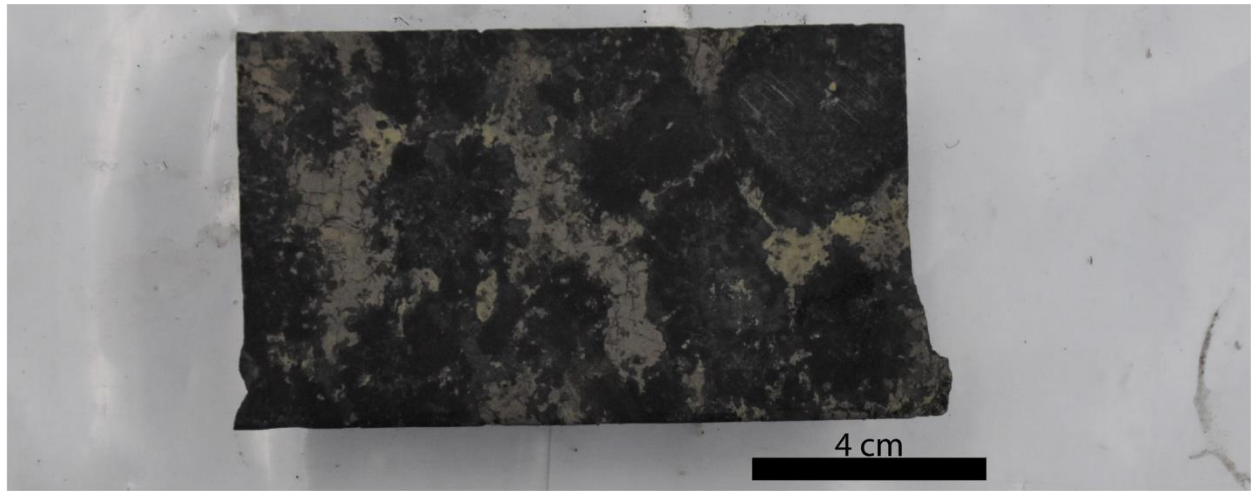
3% magnetite: <0.5 mm diameter, subhedral crystals exhibiting strong resorption textures; found within chalcopyrite and pentlandite domains.

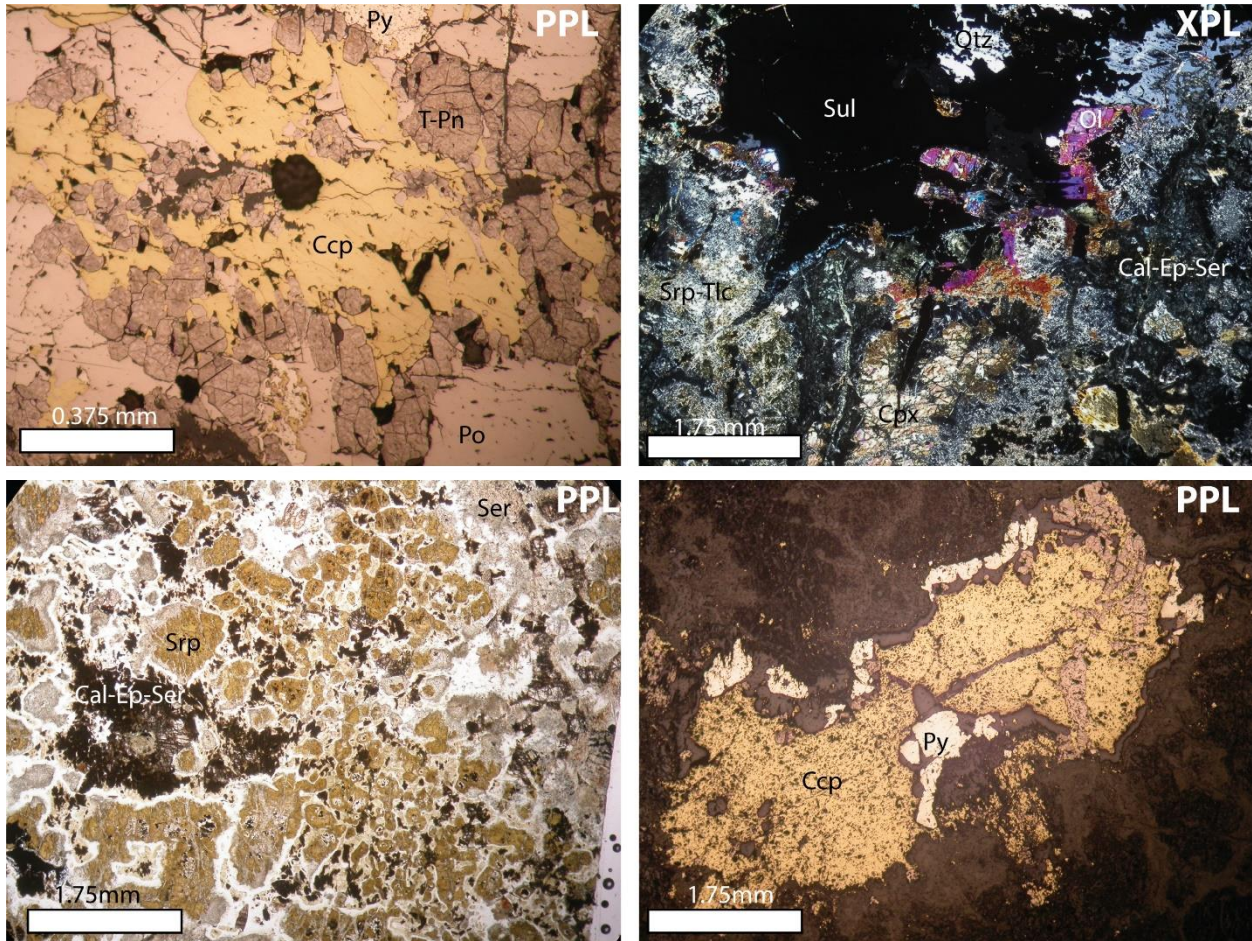
Trace flame pentlandite: <0.05 mm diameter, anhedral flames within pyrrhotite domains.

19-EV-48-04

(EL-19-48, 106.34-106.39 m)

Upper Chamber





Altered orbicular olivine gabbro with globular sulfides consisting of:

19% Olivine: 0.4-1.5 mm diameter, euhedral crystals, 99% altered to serpentine, talc, and magnetite. With the exception of the cores of one or two small crystals, relict crystal shapes are not present.

18% Plagioclase: 0.3-1 mm diameter, anhedral-euhedral laths and blade-shaped crystals, 95% altered to sericite, chlorite, calcite and epidote.

12% Clinopyroxene: 0.5-2 mm diameter, subhedral crystals, 92% altered to sericite and uralite.

The primary texture within this sample is almost completely obliterated, with many former crystals displaying a “shredded” appearance. The primary habits of the crystals are only retained when bounded by sulfides. Only a few crystals of clinopyroxene and olivine escaped are not completely altered and they occur enclosed within sulfides.

The alteration in the sample is characterized by serpentinization, uralitization, oxidation, propylitic and potassic. Pyrite occurs prevalently within strongly altered domains, indicating that it is likely a product of alteration. Quartz also occurs in association with pyrite where sulfide blebs are replaced.

The mineralization within the sample consists of **50% globular sulfides** consisting of 17% chalcopyrite, 19% pyrrhotite, 6% violarite (after pentlandite), and 8% pyrite. Sulfide globules are 1-2 cm in diameter. Chalcopyrite and pyrrhotite are anhedral, whereas pentlandite and some domains of pyrite have well-developed, euhedral crystal structures. Pentlandite is completely altered to violarite.

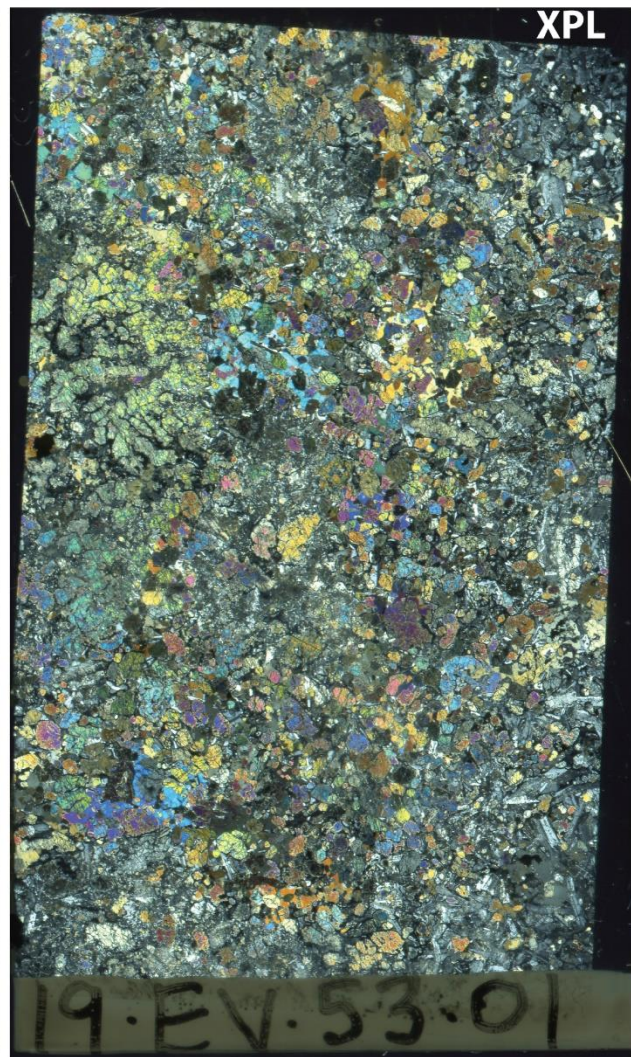
19-EV-53-01

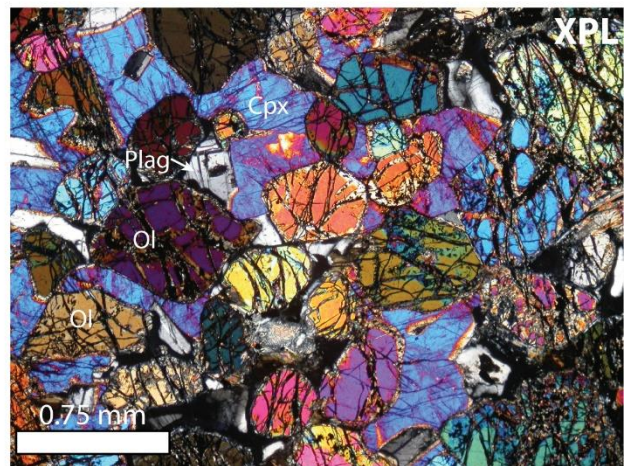
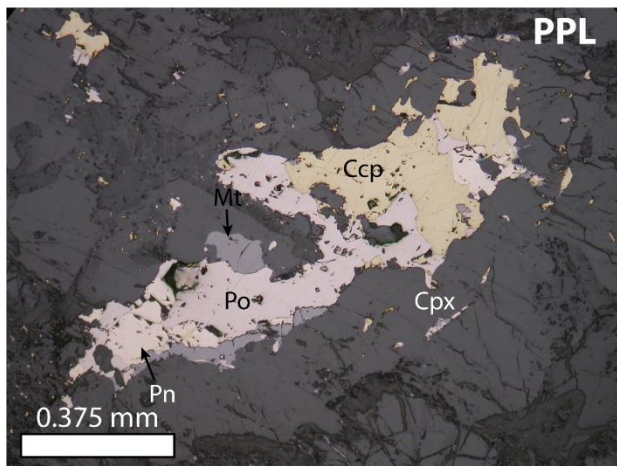
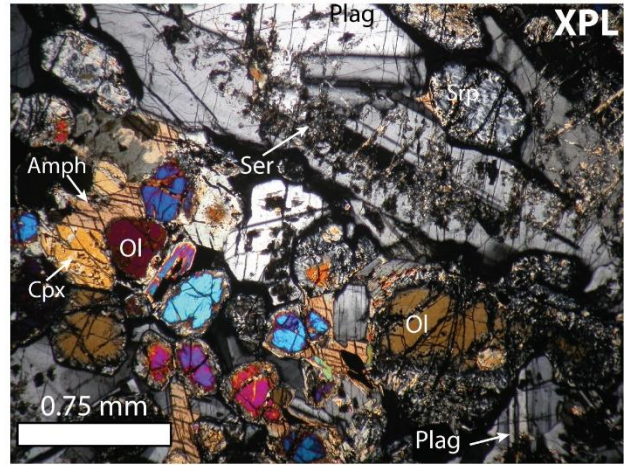
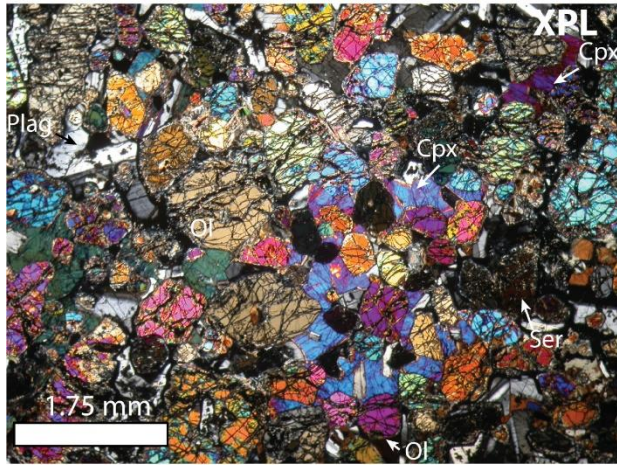
(EL-19-53, 117.42-117.47)

Upper Chamber



4 cm





Medium green grey, medium- to coarse-grained, inequigranular, orbicular-textured olivine gabbro with sparse disseminated sulfides composed of:

38% Olivine: 0.3-4 mm, subhedral-euhedral crystals, locally oikocrystic, but mostly chadacrystic. Olivine is 25-50% altered to serpentine and magnetite, with strong contrasts in the degree of alteration within juxtaposed domains.

36% Plagioclase: 0.3-4 mm, subhedral-euhedral laths and blades, 5-70% altered to sericite, chlorite and biotite. Plagioclase forms the main phase in some domains, located on the edges of the thin section.

23% Clinopyroxene: 0.4-5 mm, anhedral-subhedral crystals with a predominantly oikocrystic/interstitial mode of occurrence. Clinopyroxene is ~4% altered to uralite. Cleavage within crystals is rare and twinning is very sparse.

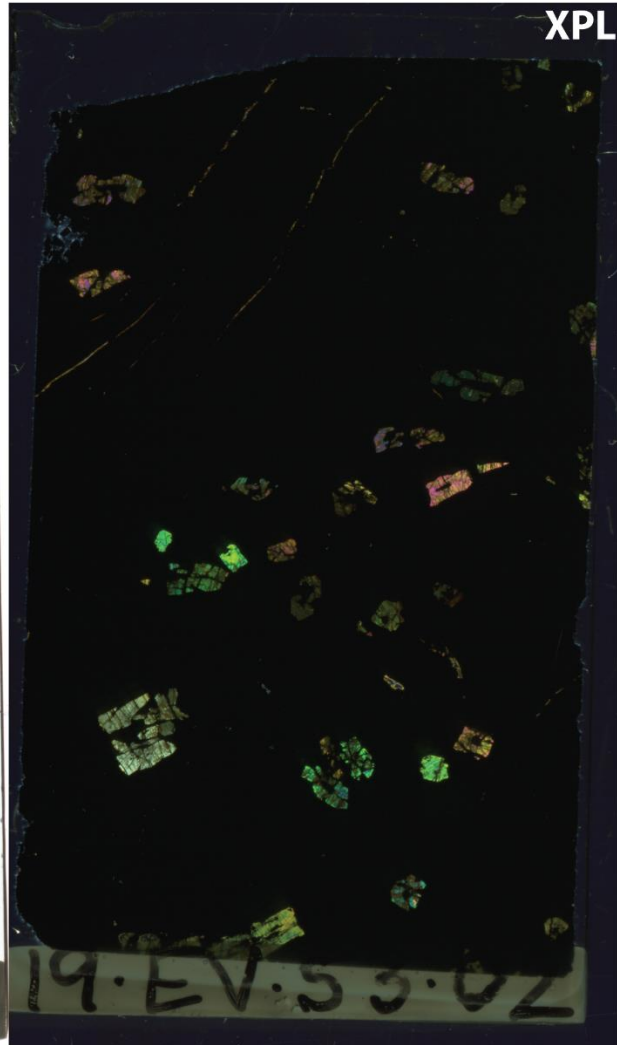
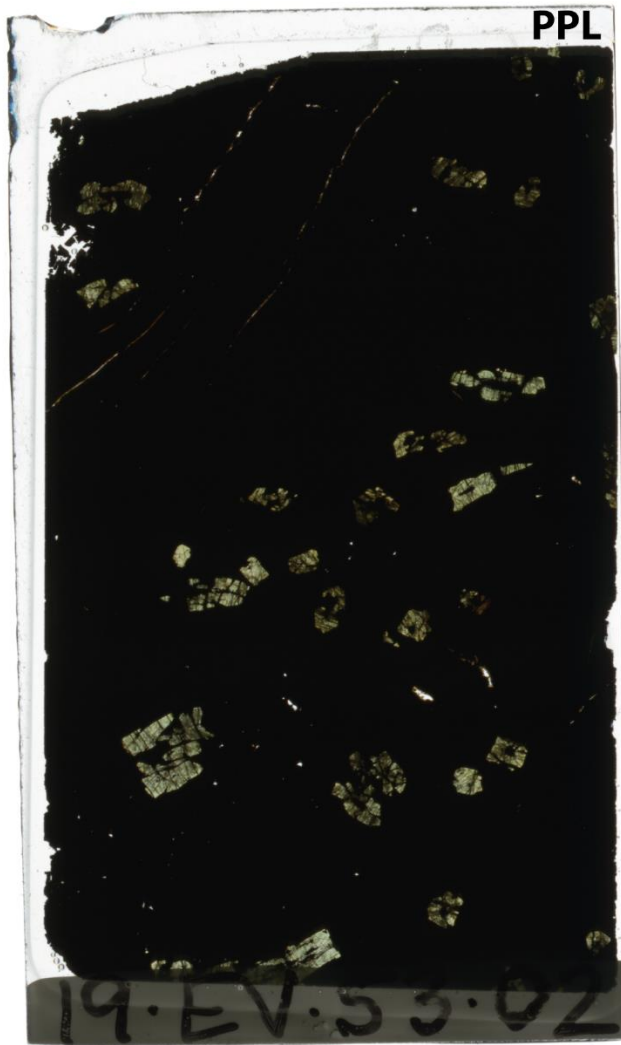
The alteration within the section is highly variable: some areas exhibit nearly unaltered mineralogy, whereas others exhibit nearly complete alteration and obliteration of primary textures. The texture and mineralogy also vary throughout the section: some areas are nearly ultramafic, with an orthocumulate/poikilitic texture of large, branching clinopyroxene oikocrysts enclosing olivine chadacrysts, whereas others exhibit olivine oikocrysts with plagioclase chadacrysts. Some regions are more leucocratic where plagioclase is the main mineral phase.

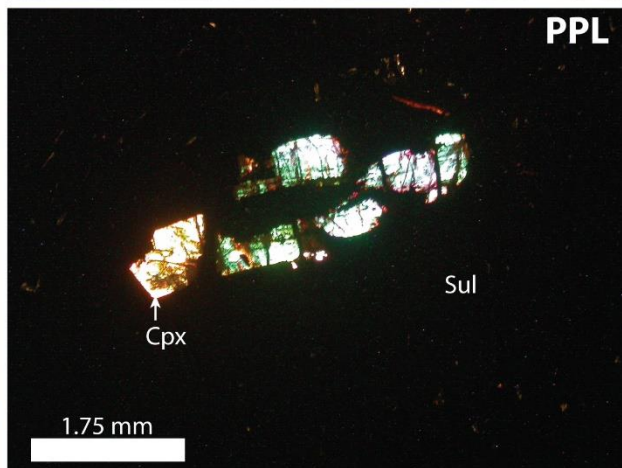
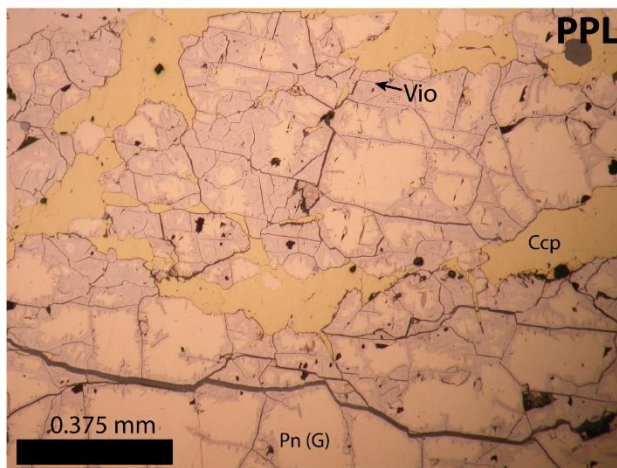
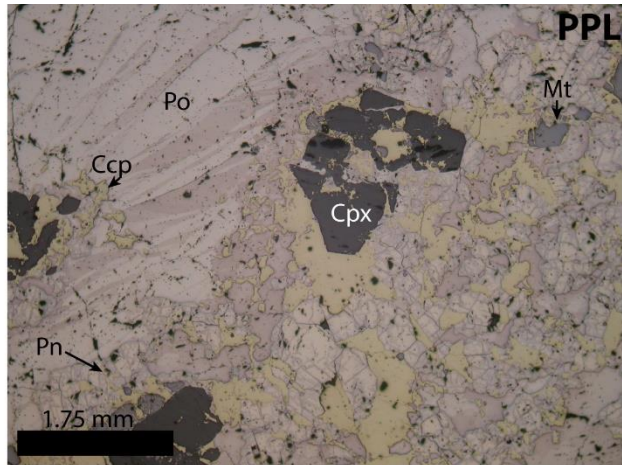
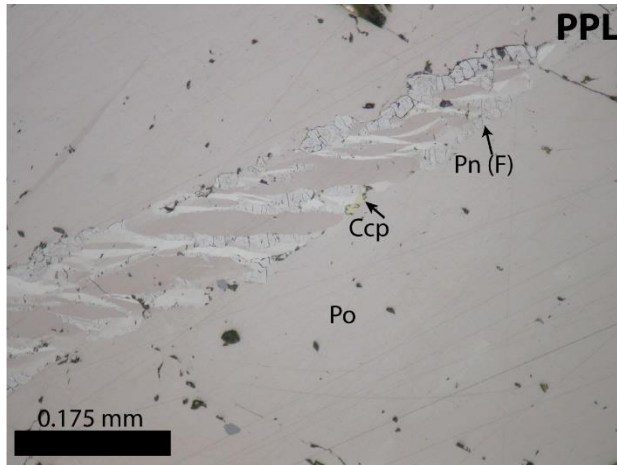
Sparse disseminated sulfide mineralization (0.4%)- 0.01-2 mm diameter interstitial blebs consisting of 0.2% pyrrhotite, 0.15% chalcopyrite, 0.05% pentlandite and trace magnetite.

19-EV-53-02

(EL-19-53, 132.12-132.17 m)

Lower Discovery Zone





Clinopyroxene-bearing massive sulfide consisting of:

60% pyrrhotite: 0.5-5 mm diameter, anhedral grains surrounding pentlandite and chalcopyrite grains. These crystals exhibit monoclinic and hexagonal exsolutions as thin parallel-irregular bands and thicker patches throughout the thin section; the exsolutions in-between pentlandite veins and flames have a “woven” appearance.

17% chalcopyrite: 0.1-3 mm diameter, anhedral, irregular blebs with minor occurrences as veinlets and infill between magnetite, pentlandite, and clinopyroxene fractures.

10.5% granular pentlandite: <2 mm diameter, subhedral-euhedral granular crystals exhibiting a moderate degree of fracturing within grains. Pentlandite is ~15 vol% altered to violarite along grain boundaries and fractures within the grains.

8% clinopyroxene phenocrysts: 1-3 mm diameter, subhedral-euhedral skeletal crystals with high relief and 3rd order interference in XPL. The habit is less skeletal than clinopyroxene in 19-EV-48-01, surrounded by chalcopyrite and pentlandite.

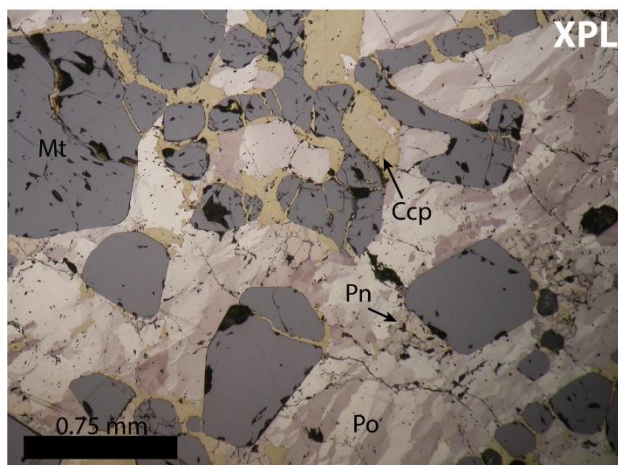
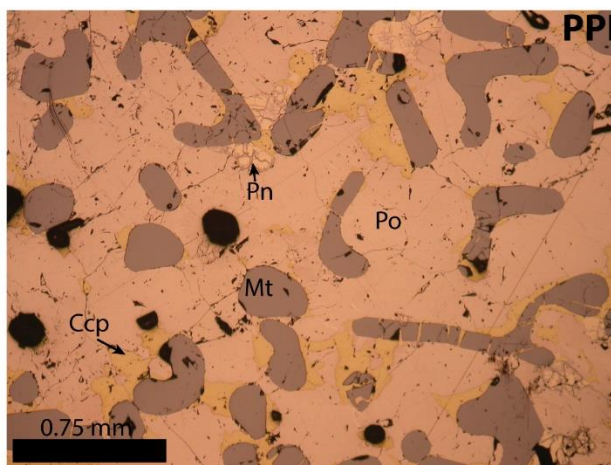
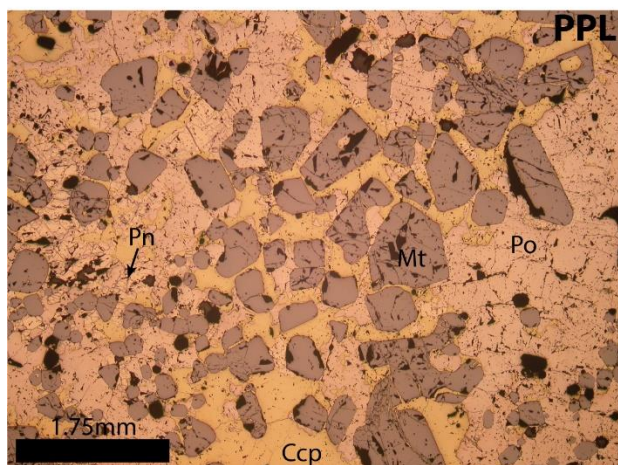
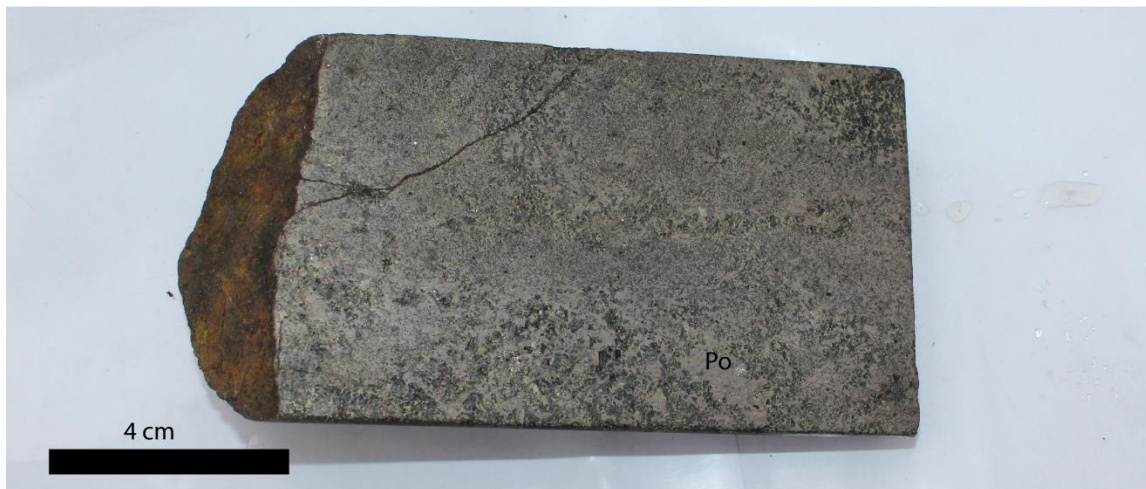
4% magnetite: 0.2-1 mm diameter, anhedral-euhedral crystals exhibiting resorption textures and a moderate association between magnetite and pentlandite- and chalcopyrite-rich zones. Magnetite is less fractured than its counterparts in 19-EV-48-01.

0.5% flame pentlandite <0.02 mm diameter anhedral flame exsolutions within pyrrhotite domains.

19-EV-53-03

(EL-19-53, 133.56-133.61 m)

Lower Discovery Zone



Clinopyroxene-bearing magnetite-rich massive sulfide consisting of:

36% magnetite: <3 mm diameter, subhedral-euhedral “pseudo-cuneiform” crystals displaying brittle deformation fractures. The larger grains are correlated with chalcopyrite-rich domains, whereas smaller

grains are found within pyrrhotite-rich domains. Some grains have shapes akin to the bent triangle morphologies of quartz within cuneiform granite; this is likely the result of resorption.

35% pyrrhotite: <5 mm diameter, anhedral crystals surrounding pentlandite, chalcopyrite and magnetite grains. Some domains display deformation twinning

19% chalcopyrite: <3 mm diameter, anhedral, irregular blebs and veins, with sporadic occurrence as fracture infill within magnetite.

9% granular pentlandite: <2 mm diameter, weakly fractured, subhedral-euhedral granular crystals: ~10 vol% altered to violarite along grain boundaries and within fractures.

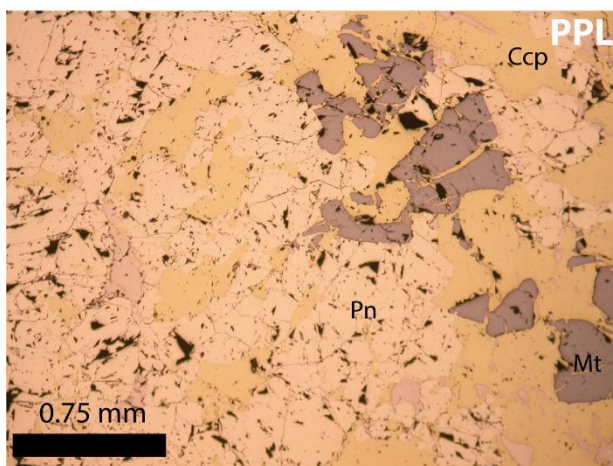
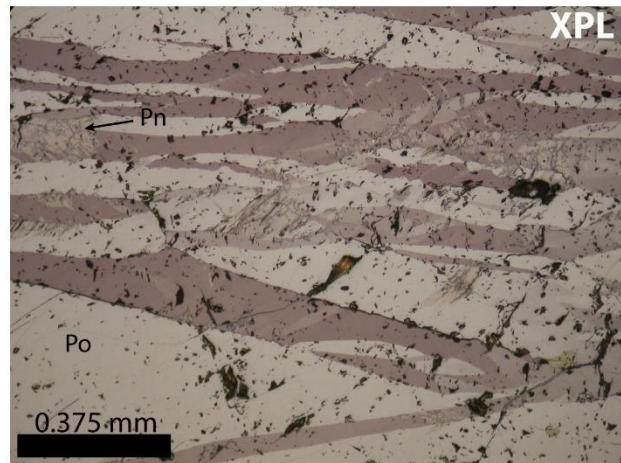
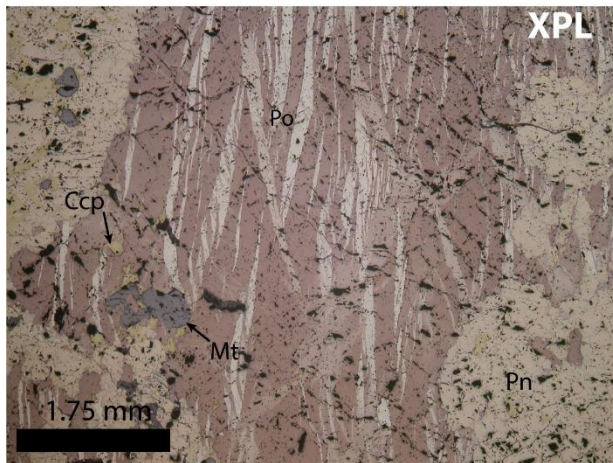
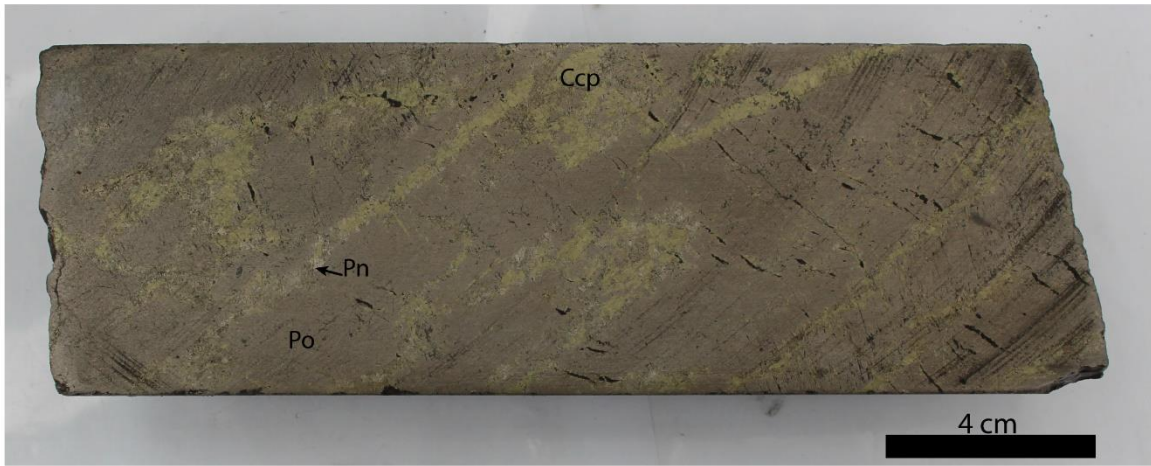
1% clinopyroxene phenocrysts: 1 mm diameter, subhedral-euhedral crystals with high relief and 3rd order interference in XPL.

The sample exhibits a weak loop texture defined by the alignment of chalcopyrite, pentlandite and coarser magnetite grains.

19-EV-53-04

(EL-19-53, 142.85-142.90 m)

Lower Discovery Zone



Massive sulfide consisting of:

36% pyrrhotite: <6 mm diameter, anhedral crystals with unidirectional monoclinic-hexagonal twinning. Most grains are completely enclosed by pentlandite and chalcocopyrite loops. Many areas contain flame pentlandite.

30% granular pentlandite: <4 mm diameter, subhedral-euhedral grains with ~5% violarite alteration. Pentlandite forms loops with chalcopyrite and is less fractured than in most samples.

29% chalcopyrite: <3 mm diameter, anhedral blebs and veins forming loops with pentlandite.

5% magnetite: <1.5 mm diameter, subhedral, brittlely deformed grains with resorption textures. They are found within chalcopyrite- and pentlandite-rich domains and are not enclosed by pyrrhotite.

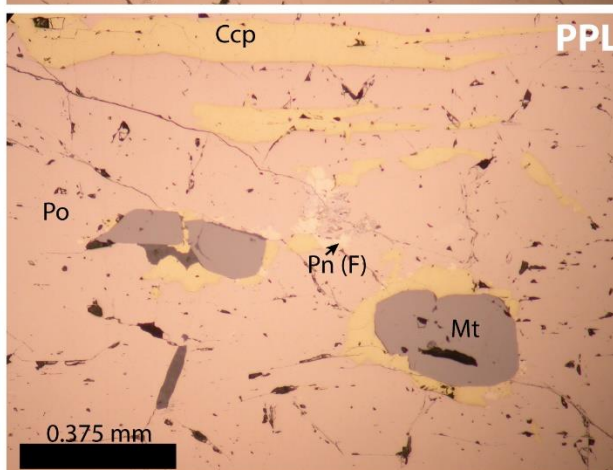
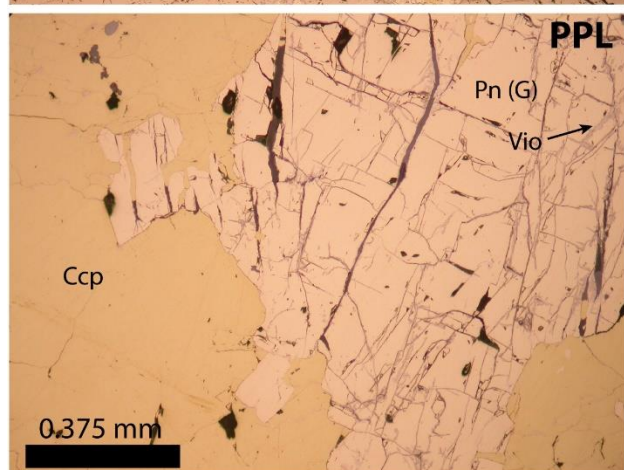
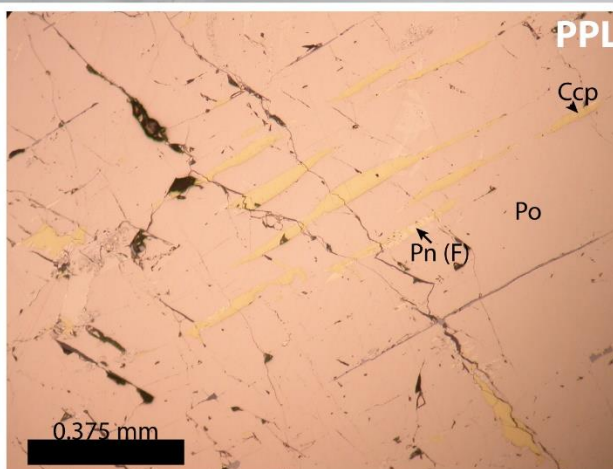
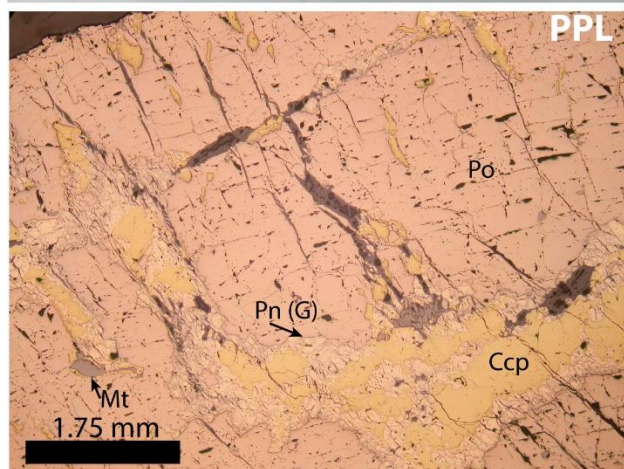
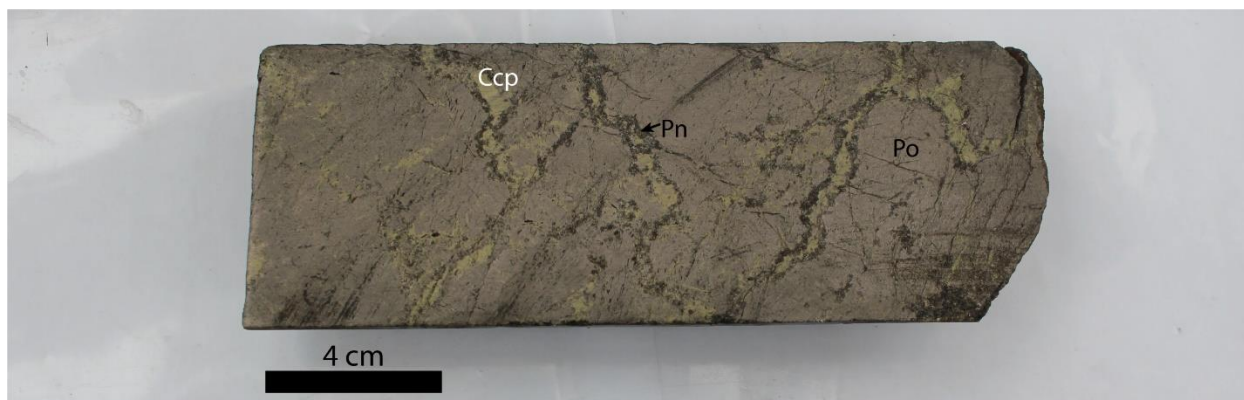
2% flame/vein pentlandite: <0.5 mm long, anhedral exsolutions, arranged parallel to pyrrhotite twinning and ~10 vol% altered to violarite.

The loop texture within the massive sulfide is well-developed, with the long axis of loops parallel to pyrrhotite twinning and flame pentlandite. These loops are approximately 1-2 cm wide and 3-4 cm long and consist of granular pentlandite and chalcopyrite.

19-EV-53-05

(EL-19-53, 144.75-144.80 m)

Lower Discovery Zone



Massive sulfide consisting of:

71% pyrrhotite: <5 mm diameter, anhedral crystals with moderate monoclinic-hexagonal twinning, partially enclosed by chalcopyrite and pentlandite loops.

13% chalcopyrite: <3 mm diameter, irregular blebs and veins, forming dismembered loops with pentlandite.

12% granular pentlandite: <3 mm diameter, subhedral-euhedral fractured crystals with the edges and fractures altered to ~20 vol% violarite; form dismembered loops with chalcopyrite.

2% magnetite: <0.2 mm diameter, brittlely deformed, subhedral crystals, exhibiting resorption textures and enclosed by chalcopyrite and pentlandite.

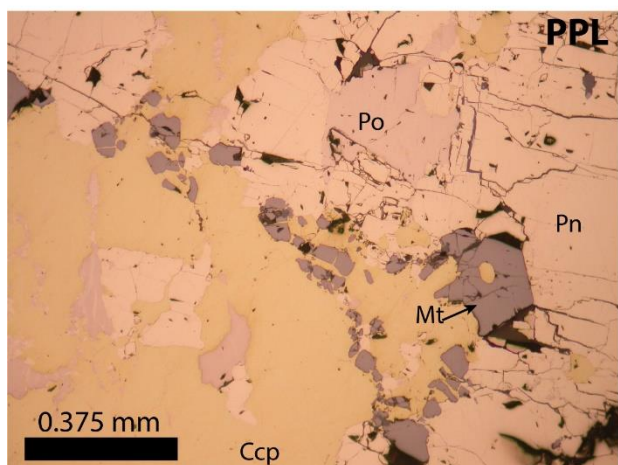
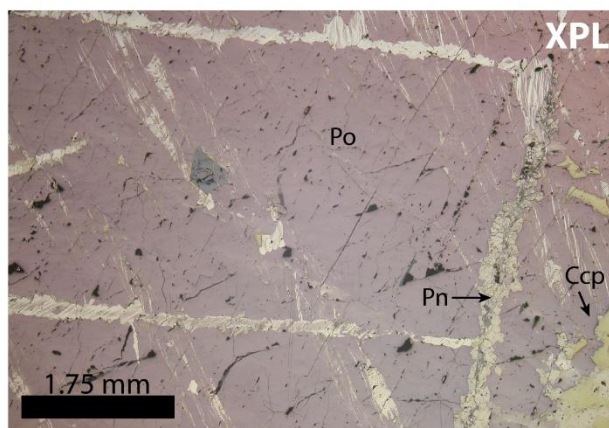
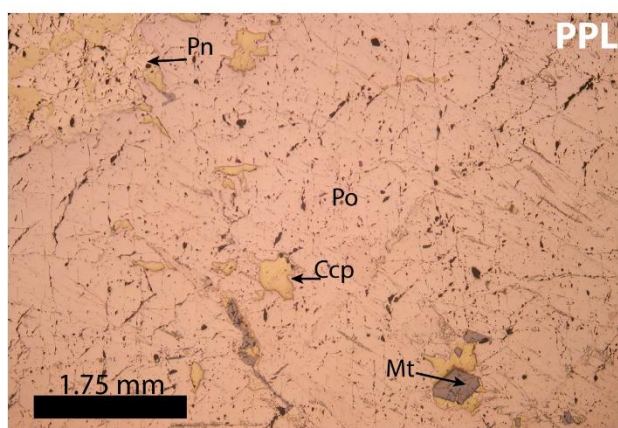
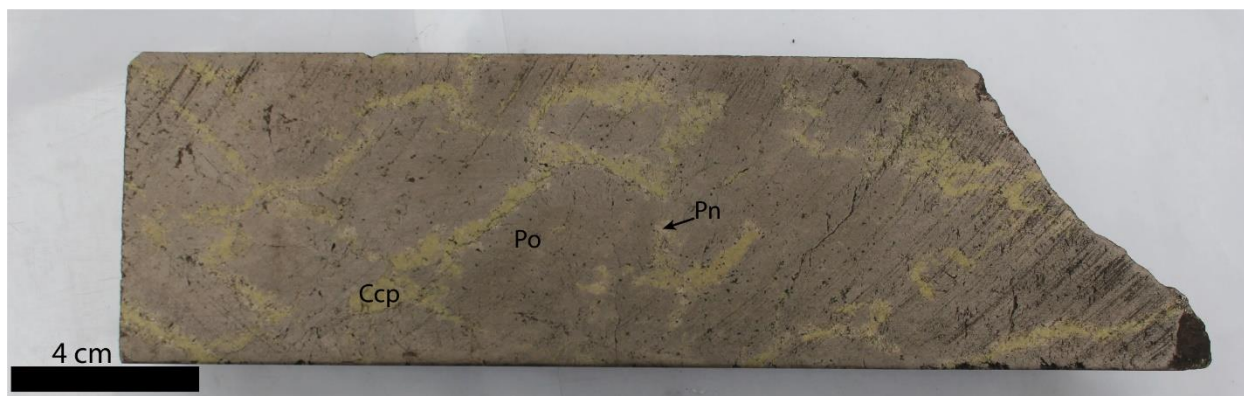
Trace flame pentlandite: <0.1 mm diameter, elongate anhedral exsolutions within pyrrhotite, 70 vol% altered to violarite.

The sample displays a dismembered loop texture defined by the partial enclosure of pyrrhotite by granular pentlandite and chalcopyrite loops.

19-EV-53-06

(EL-19-53, 146.83-146.88 m)

Lower Discovery Zone



Massive sulfide consisting of:

56% pyrrhotite: <6 mm diameter, anhedral crystals with weak monoclinic-hexagonal twinning. Some pyrrhotite lensoids cross-cut the dominant direction of twinning.

26% granular pentlandite: <3.5 mm diameter, subhedral-euhedral, fractured granular crystals, ~10 vol% altered to violarite. The subhedral grains are less altered to violarite than euhedral grains. Granular pentlandite is associated with chalcopyrite and magnetite.

15% chalcopyrite: <2 mm diameter, anhedral irregular blebs, veins and fracture infills, occurring with granular pentlandite and magnetite.

2% flame pentlandite: <0.1 mm wide and <0.7 mm long, anhedral exsolutions within pyrrhotite, forming lineations within the sample. Flame pentlandite is ~20 vol% altered to violarite.

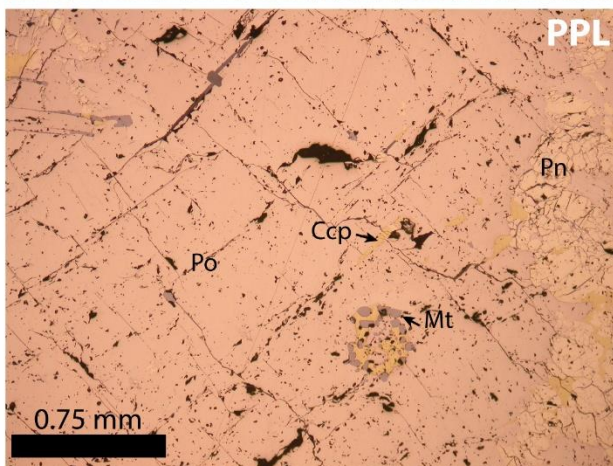
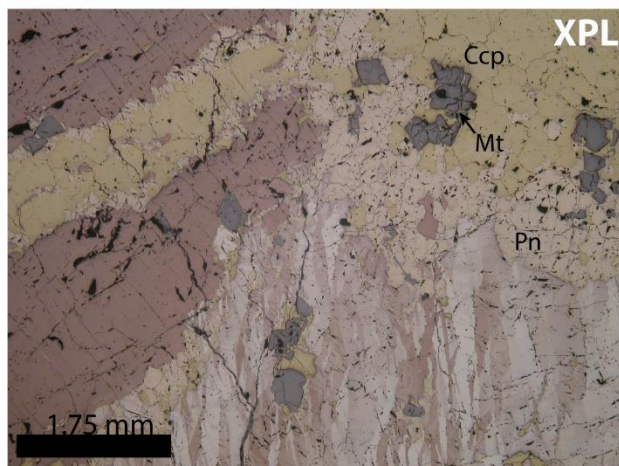
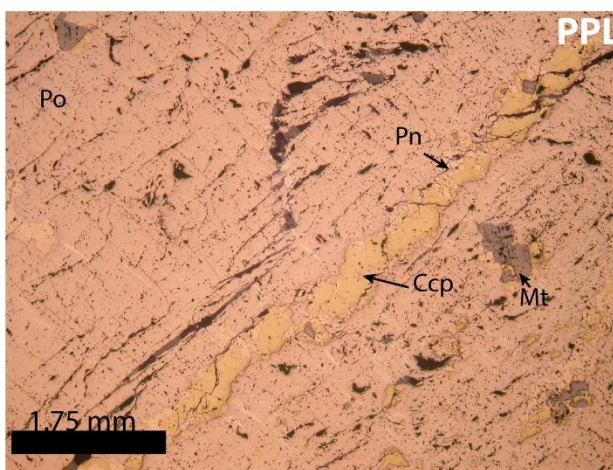
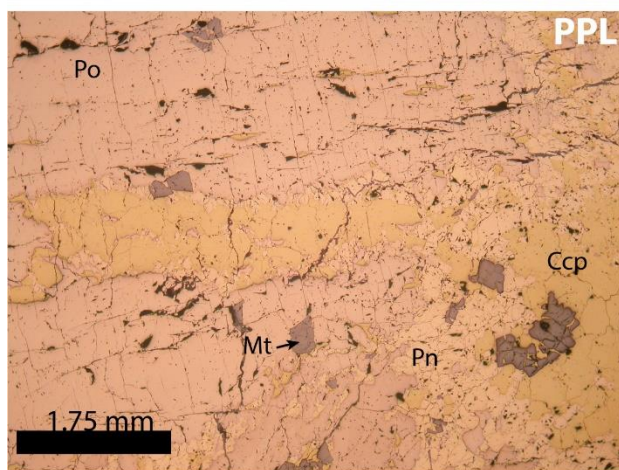
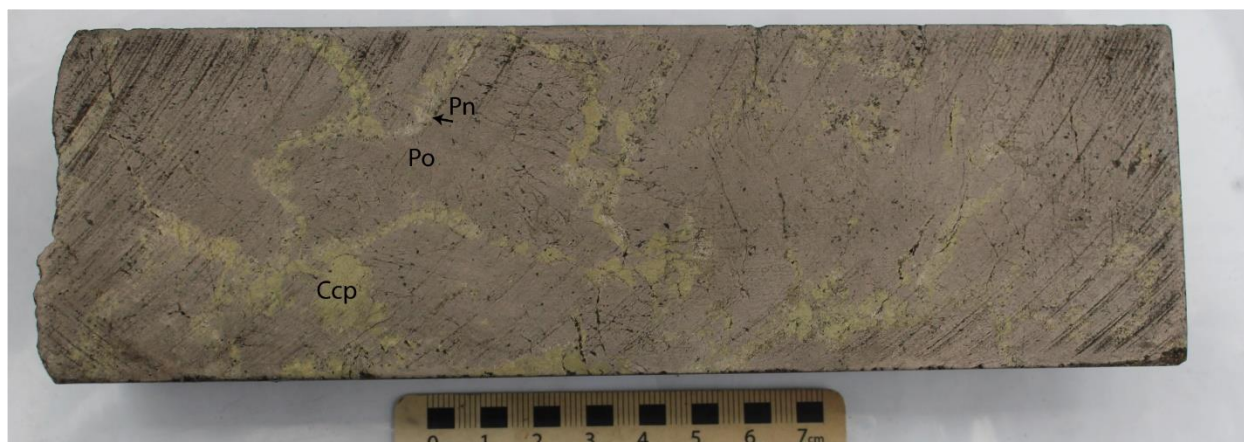
1% magnetite: <0.5 mm diameter, subhedral crystals enclosed by chalcopyrite and pentlandite and exhibiting brittle deformation and resorption textures.

The loop texture within this sample has been cut off by the edge of the thin section.

19-EV-53-07

(EL-19-53, 148.50-148.55 m)

Lower Discovery Zone



Massive sulfide consisting of:

74% pyrrhotite: <6 mm, anhedral crystals, partially enclosed by pentlandite and chalcopyrite; exhibits little to no small-scale twinning - most of it occurs on mm-cm scale at grain boundaries.

13% granular pentlandite: <2 mm, subhedral-euhedral granular crystals, occurring with chalcopyrite and magnetite, 3 vol% altered to violarite, weakly fractured.

12% chalcopyrite: <2 mm, anhedral irregular blebs and veins, occurring with pentlandite. The elongate blebs/veins define the lineations within the sample.

1% magnetite: <0.65 mm, subhedral-euhedral crystals, enclosed by chalcopyrite and pentlandite, with minor brittle deformation and some resorption.

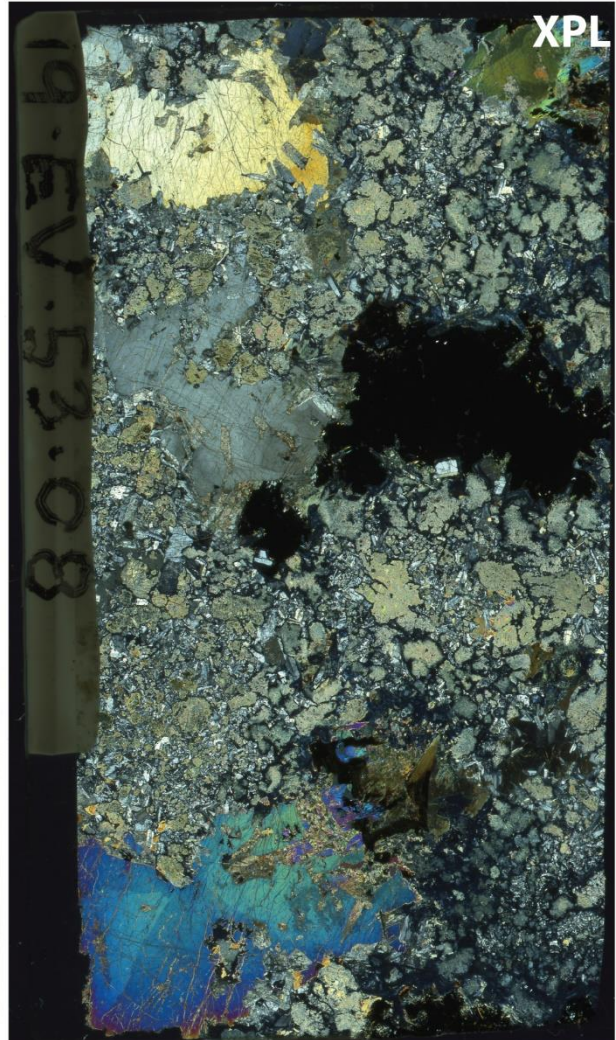
Trace flame pentlandite: 0.1 mm-wide and 0.3 mm-long, anhedral exsolutions, 10 vol% altered to violarite.

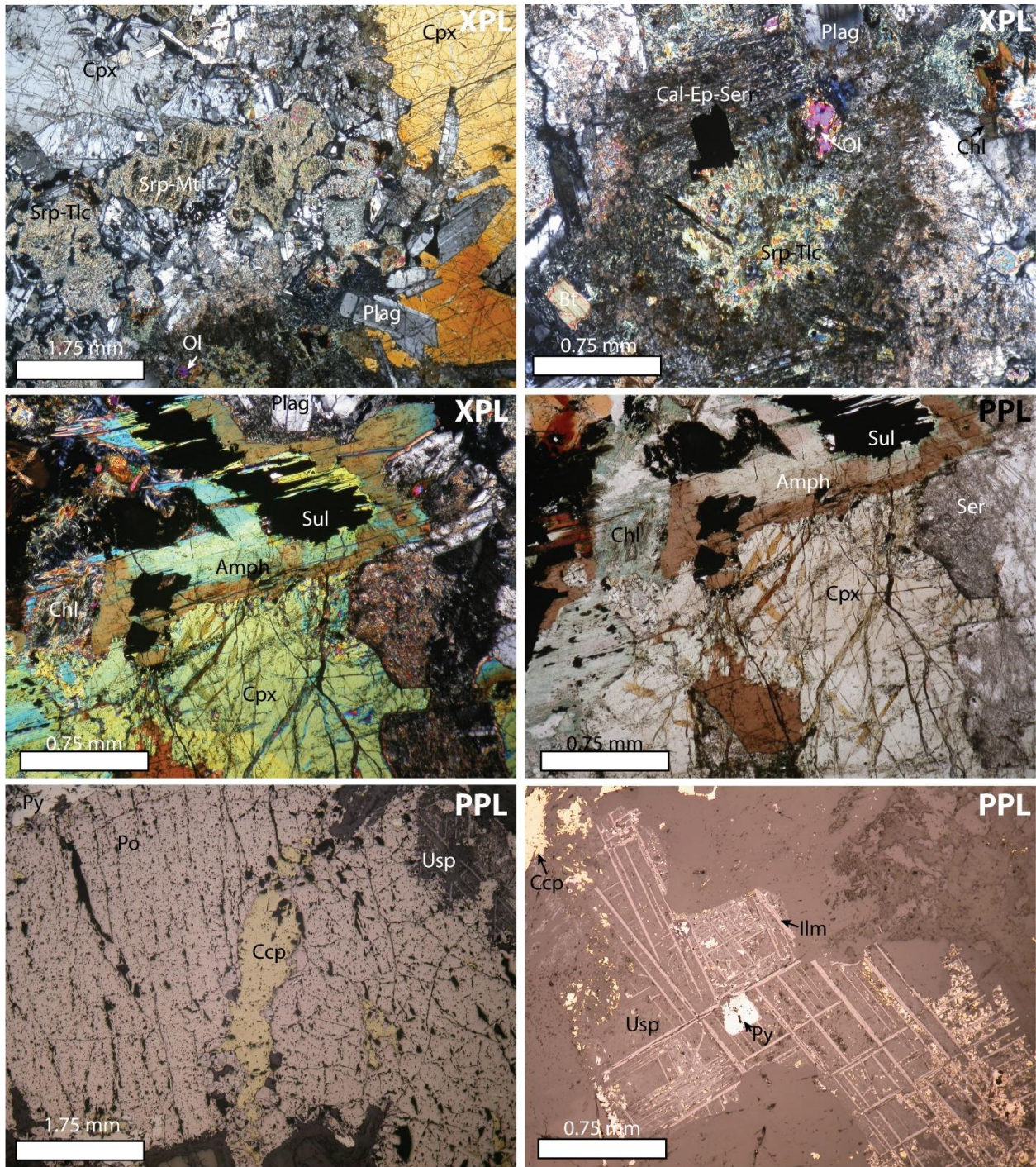
The sample exhibits a deformed loop texture; elongate blebs of chalcopyrite define a lineation.

19-EV-53-08

(EL-19-53, 84.37-84.42 m)

Upper Chamber





Medium green grey, fine- to coarse-grained, inequigranular, orbicular-textured olivine gabbro with blebby sulfides consisting of:

35% plagioclase: 0.08-1 mm diameter, subhedral-euhedral elongate laths, locally forming chadacrysts within large clinopyroxene crystals and plagioclase-rich domains. The crystals are ~50 vol% altered to chlorite and sericite, with the larger crystals appearing to be more susceptible to alteration.

26% olivine: 0.3-2 mm diameter, subhedral, equant crystals, ~90 vol% altered to serpentine, talc, magnetite, and chlorite. Only the cores of some crystals are preserved; this alteration may have affected the mineral habit within the section.

20% clinopyroxene: <13 mm diameter, anhedral-subhedral crystals with an interstitial to locally oikocrystic (enclosing plagioclase chadacrysts) morphology. Clinopyroxene forms very large interstitial crystals along edges of thin section and is 10 vol% altered to uralite, commonly at crystal boundaries. Some larger crystals are also cross-cut by epidote veins.

2.5% titanomagnetite: <3 mm diameter, anhedral crystals displaying ilmenite exsolution lamellae (oxyexsolved). Commonly contain sulfides.

15% blebby sulfides: 2% violarite (after pentlandite) <1mm diameter, euhedral granular crystals

10% pyrrhotite: <4 mm diameter, anhedral crystals occurring within blebs; no monoclinic-hexagonal twinning visible.

1.5% chalcopyrite: <2 mm diameter, anhedral elongate blebs.

1.5% pyrite: <1 mm diameter, anhedral crystals, occurs along edges of blebs, likely an alteration product.

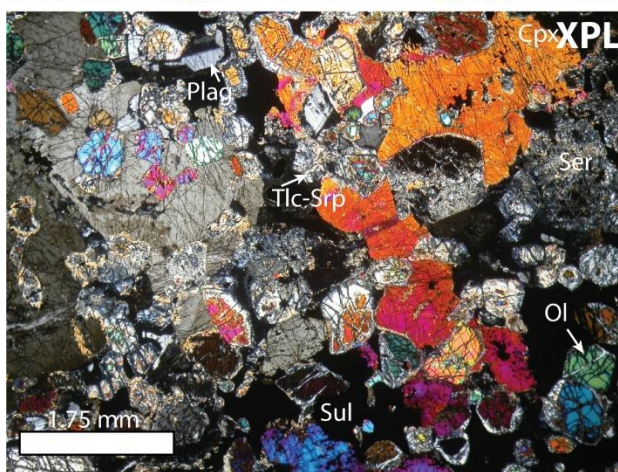
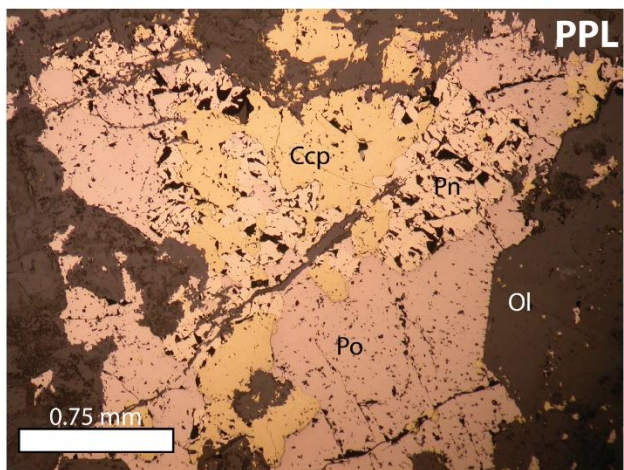
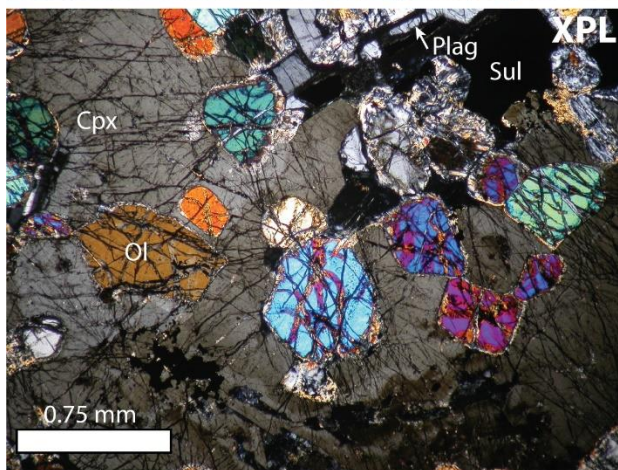
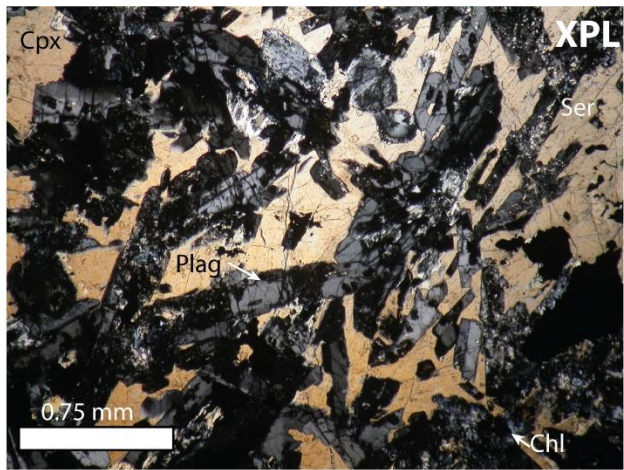
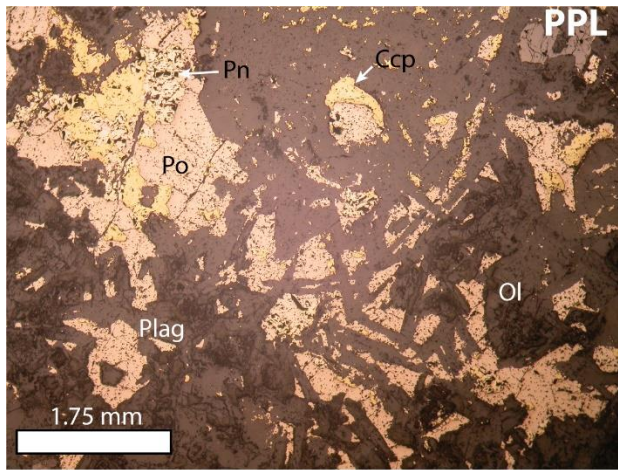
0.5% magnetite: <0.8 mm diameter, anhedral crystals forming an interstitial phase within blebs.

19-EV-54-01

(EL-19-54, 302.23-302.28 m)

Lower Chamber





Dark green grey, medium- to coarse-grained, inequigranular, olivine melagabbro with disseminated sulfides consisting of:

35% clinopyroxene: 0.25-2 mm diameter, anhedral-subhedral crystals with minor uralite alteration, typically forming an interstitial oikocryst phase within the silicate portions of rock, partially or fully enclosing olivine and plagioclase.

34% olivine: 0.3-2 mm diameter, subhedral-euhedral equant crystals, 15-65 vol% altered to serpentine, talc, magnetite, and chlorite. Forms chadacrysts within clinopyroxene oikocrysts

25% plagioclase: 0.2-1.5 mm diameter, anhedral-euhedral crystals, forming an anhedral interstitial phase or subhedral-euhedral laths, variably altered to sericite and chlorite (5-80 vol%). Its relationship with clinopyroxene in some areas defines a locally subophitic texture.

5% Disseminated Sulfides consisting of:

2.25% pyrrhotite: <0.7 mm, anhedral crystals.

1.65% chalcopyrite: <0.5 mm diameter, anhedral blebs within sulfide domains.

1.6% pentlandite: <0.5 mm diameter, subhedral granular crystals with little to no violarite alteration, occurring at the boundary between pyrrhotite and chalcopyrite.

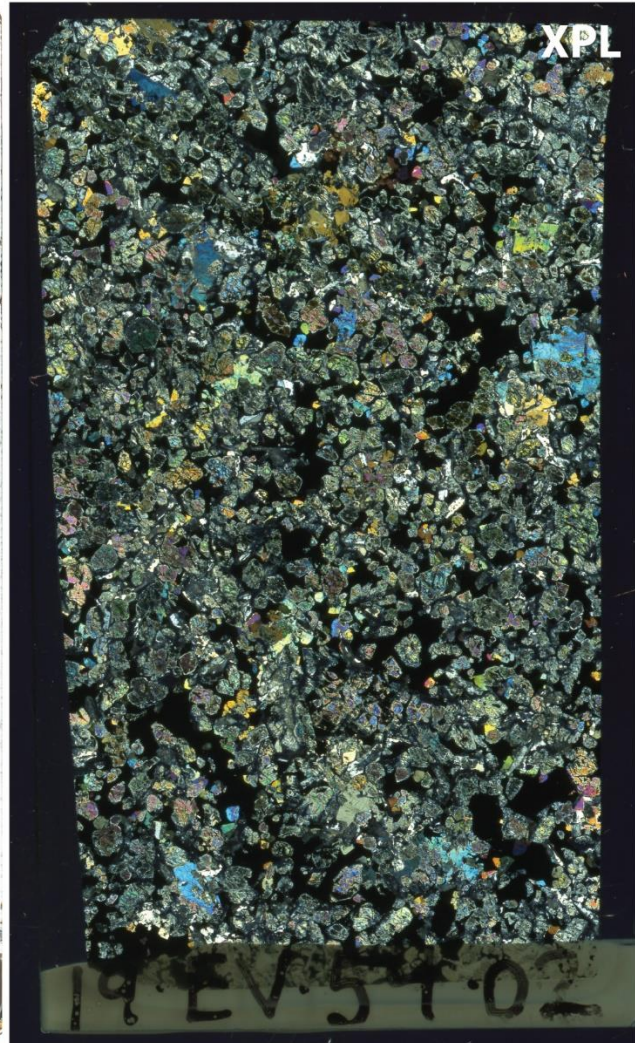
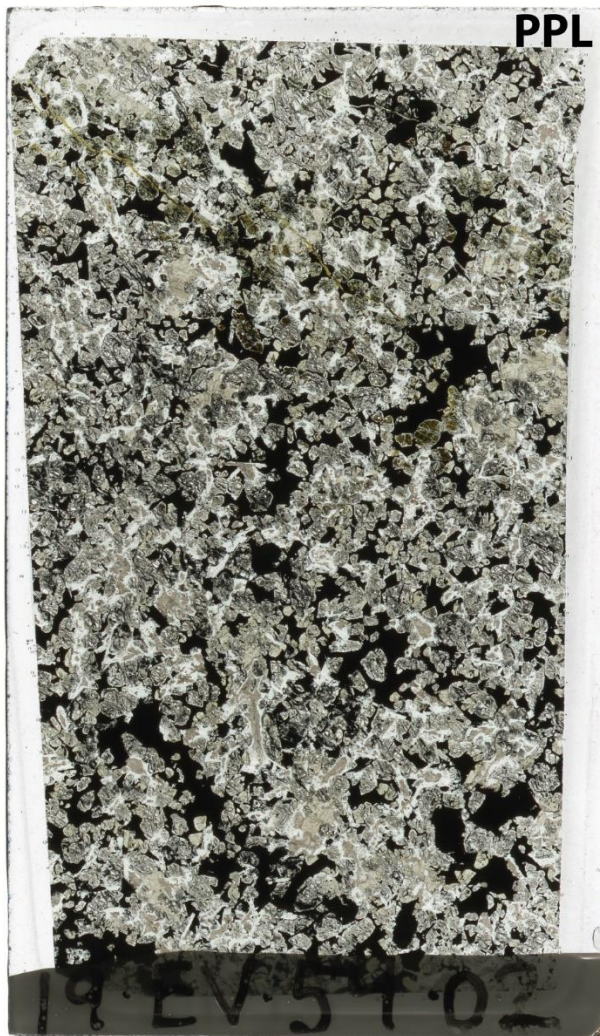
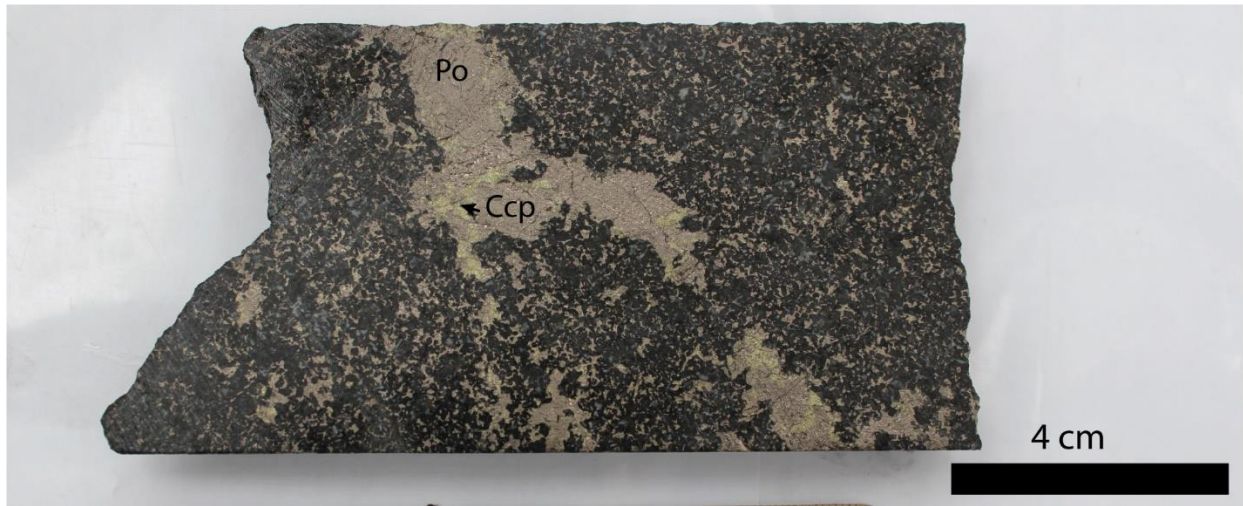
1% primary magnetite: <0.5 mm diameter, subhedral crystals occurring along the edges of sulfide patches.

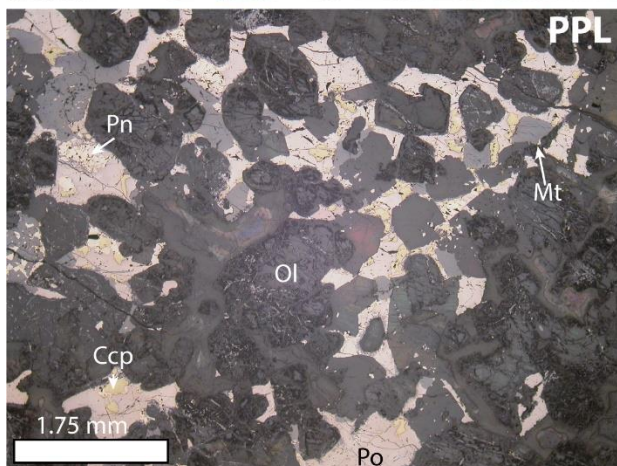
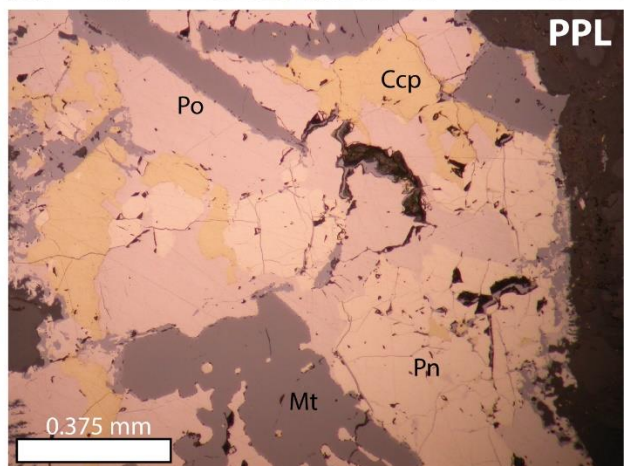
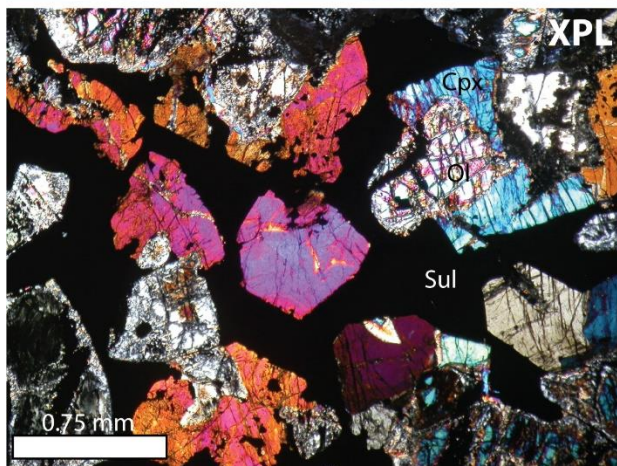
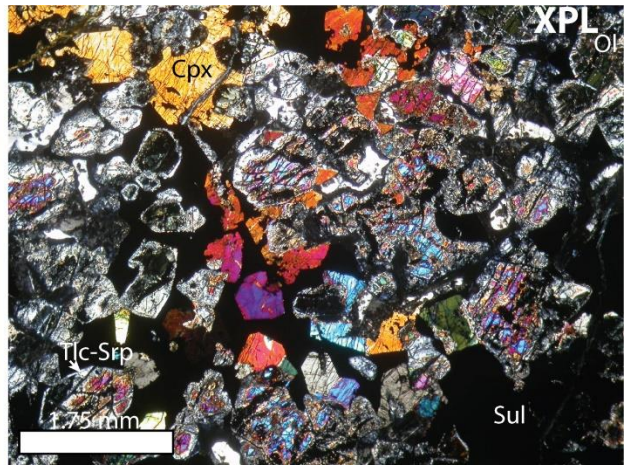
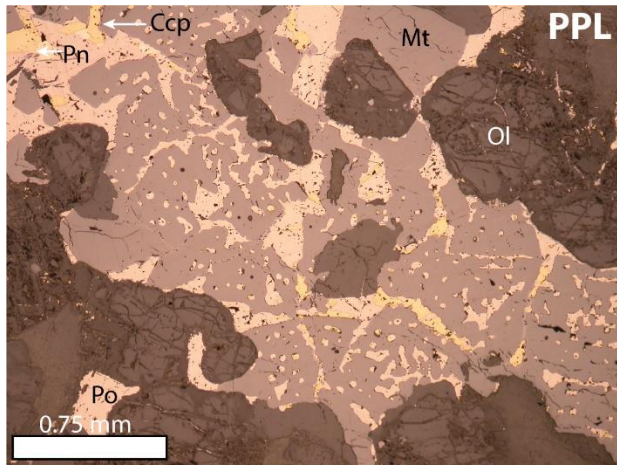
The sample displays a variable texture: a mesocumulate texture is evident in some areas, with olivine chadacrysts and anhedral clinopyroxene oikocrysts with a minor anhedral plagioclase interstitial phase, while other areas could be considered subophitic with euhedral plagioclase chadacrysts and anhedral clinopyroxene oikocrysts. The moderate degree of alteration within the sample appears to be dominated by serpentinization of olivine, sericitization of plagioclase, and uralitization of clinopyroxene. There appears to be an alteration front within the sample, exhibiting a gradational decrease in alteration with increasing distance from the front.

19-EV-54-02

(EL-19-54, 310.19-310.24 m)

Lower Chamber





Dark green grey, medium-grained, inequigranular, hypidiomorphic olivine melagabbro with net-textured sulfides composed of:

39% Olivine: 0.5-2 mm diameter, subhedral-euhedral crystals with visible fractures. Olivine is 40-70 vol% altered to serpentine, talc, magnetite and chlorite and more altered crystals have a greenish tinge in PPL. Olivine locally forms chadacrysts within sulfides and clinopyroxene.

23% Plagioclase: <1.5 mm diameter, euhedral laths and subhedral interstitial crystals, exhibiting polysynthetic twinning and 20-65% altered to sericite and chlorite. The alteration is especially pronounced along the crystal edges.

11% Clinopyroxene: 0.5-3 mm diameter, anhedral-subhedral crystals with an interstitial to locally oikocrystic morphology. Crystals display weak sericite alteration and a weak greenish grey colour with high relief in PPL.

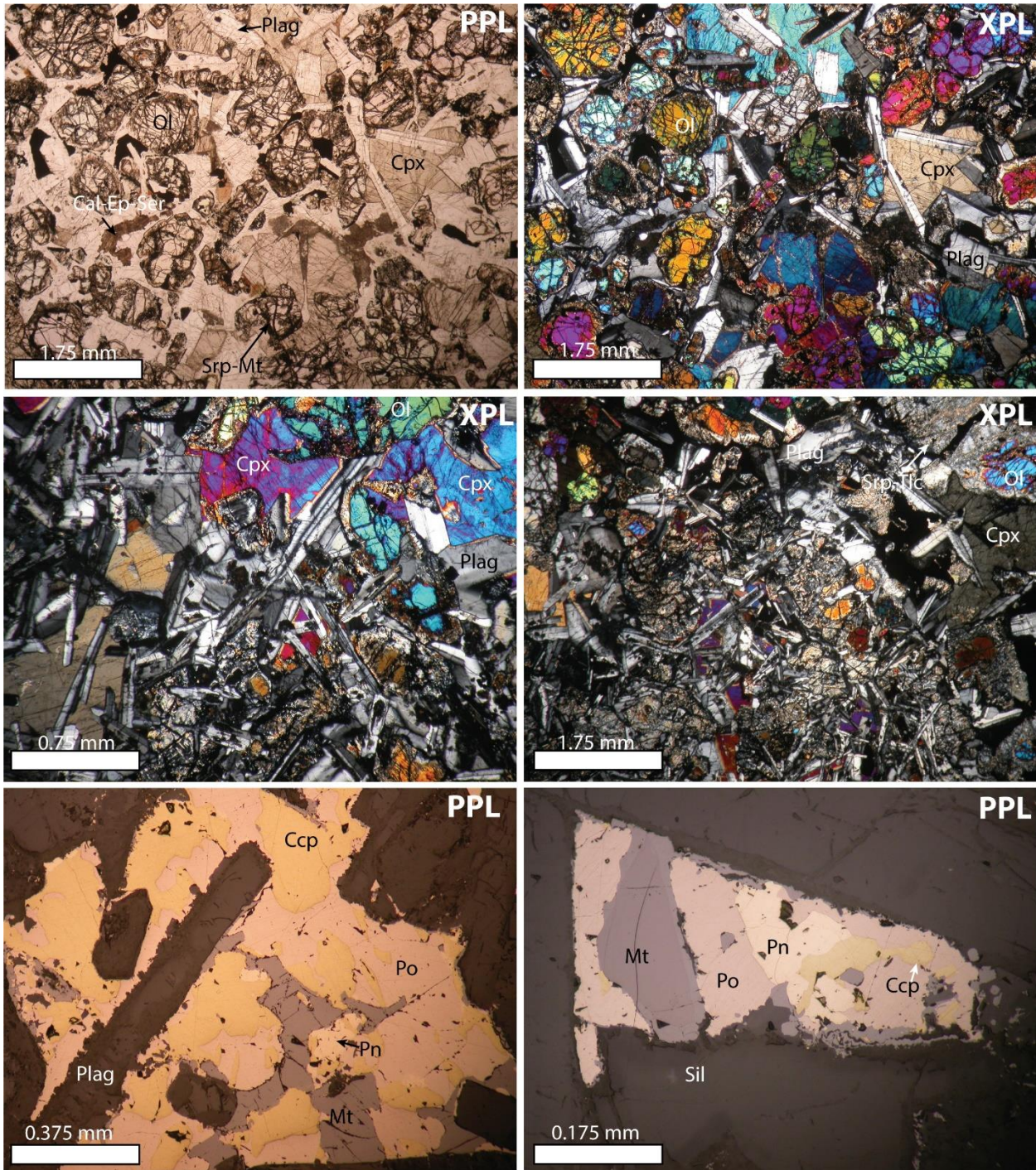
Patchy net textured sulfides consisting of 15% pyrrhotite, 2% chalcopyrite, 6% primary magnetite, and 3% pentlandite. The sulfides locally form an interconnected matrix between olivine crystals. There is no specific pattern to the distribution of chalcopyrite and pentlandite within sulfide matrix and there is a very low degree of violarite alteration within sample. Magnetite also displays a peculiar “sieve” texture, characterized by the “swiss cheese-esque” holes similar to those found in silicate sieve textures. These holes are infilled by sulfides. The sample displays an orthocumulate texture, with a relatively even distribution of minerals and alteration throughout thin section. Minor serpentine veining is also present in some locations.

19-EV-54-03

(EL-19-54, 319.98-320.03 m)

Lower Chamber





Dark green grey, medium-grained, inequigranular, orthocumulate-textured olivine melagabbro with disseminated sulfides consisting of:

44% olivine: 0.3-2 mm diameter, subhedral-euhedral, equant crystals with visible fractures, 20-90 vol% altered to serpentine, magnetite, talc and chlorite. The more altered crystals have a greenish tinge in PPL and the rims are commonly altered to talc and serpentine, but most cores remain intact.

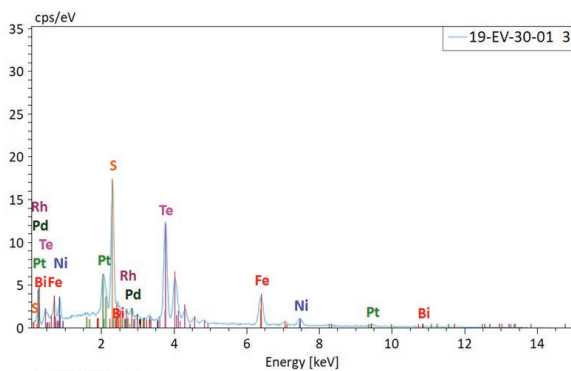
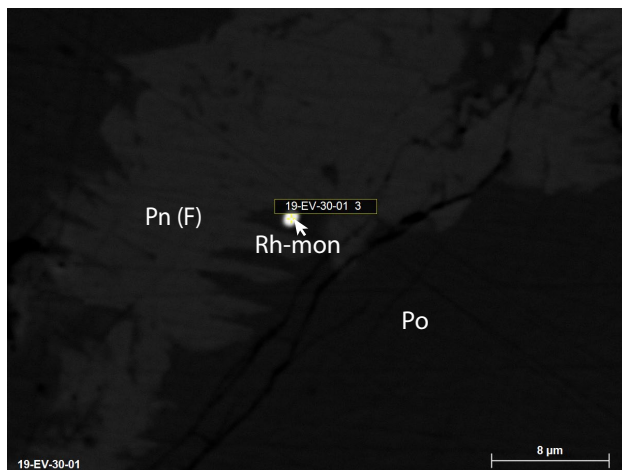
26% plagioclase: 0.1-1 mm diameter, euhedral laths and subhedral interstitial crystals, exhibiting polysynthetic twinning. Plagioclase is 20-90 vol% altered to sericite and chlorite; alteration is especially pronounced along edges of the crystals. In some plagioclase-rich domains, aggregates of euhedral plagioclase crystals take on a stellate texture.

18% clinopyroxene: 0.5-2 mm diameter, anhedral-subhedral crystals with an interstitial to locally oikocrystic morphology. Clinopyroxene is ~5 vol% altered to uralite and exhibits a weak greenish grey colour with high relief in PPL.

Disseminated sulfide consisting of 4% pyrrhotite, 2.5% chalcopyrite, 3% primary magnetite, and 0.5% pentlandite. There is no specific pattern to the distribution of chalcopyrite and pentlandite within the sulfides and there is a very low degree of violarite alteration within sample.

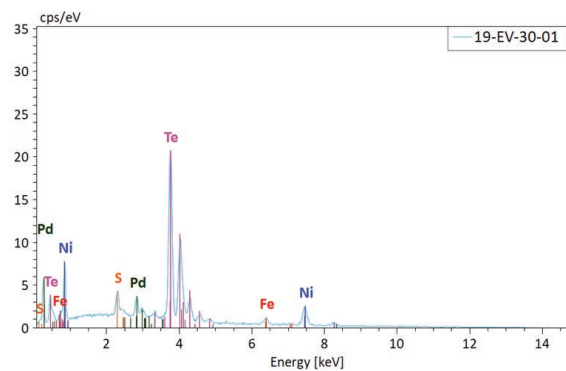
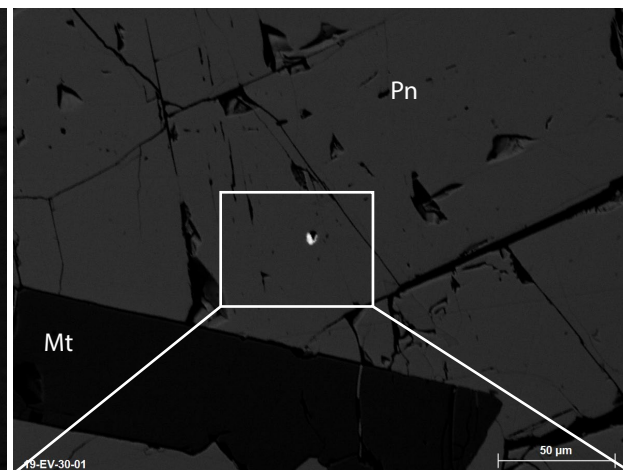
The sample displays an orthocumulate texture.

Appendix B: Backscattered Electron Photomicrographs and EDS Spectra of Select Platinum Group and Trace Minerals



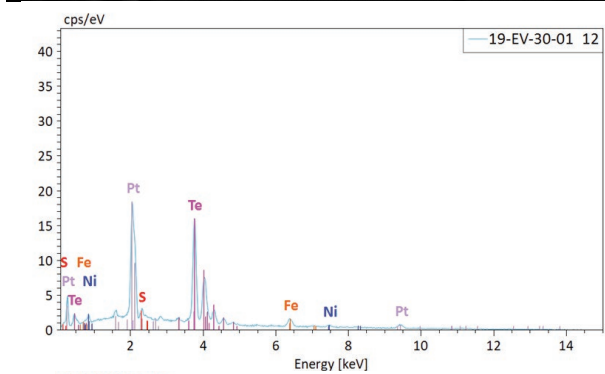
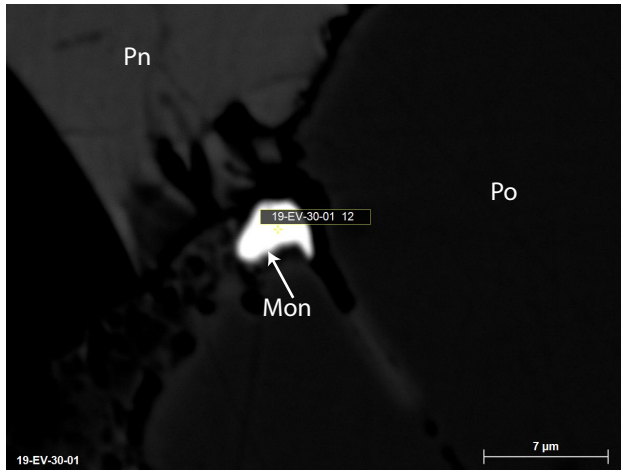
19-EV-30-01 3

Element	At. No.	Netto	Mass [%]	Mass Norm. [%]	Atom [%]	abs. error [%] (1 sigma)	rel. error [%] (1 sigma)
Tellurium	52	23514	39.11	46.43	28.34	1.23	3.15
Iron	26	5129	15.91	18.88	26.33	0.59	3.69
Sulfur	16	14717	9.76	11.59	28.15	0.39	4.00
Platinum	78	6745	8.33	9.89	3.95	0.39	4.66
Nickel	28	1304	6.22	7.38	9.80	0.36	5.74
Bismuth	83	1473	2.02	2.40	0.89	0.18	8.75
Palladium	46	1216	1.48	1.75	1.28	0.14	9.70
Rhodium	45	1174	1.40	1.66	1.26	0.14	9.90
Sum		84.22	100.00	100.00	100.00		



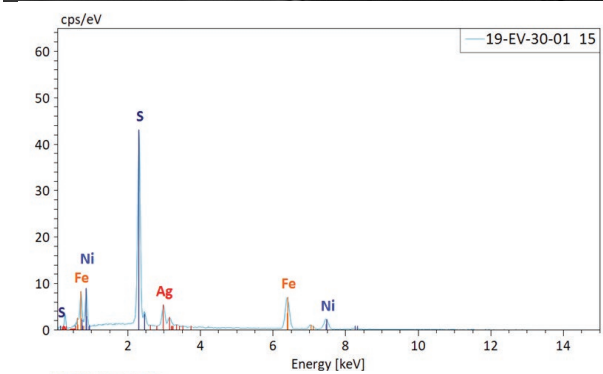
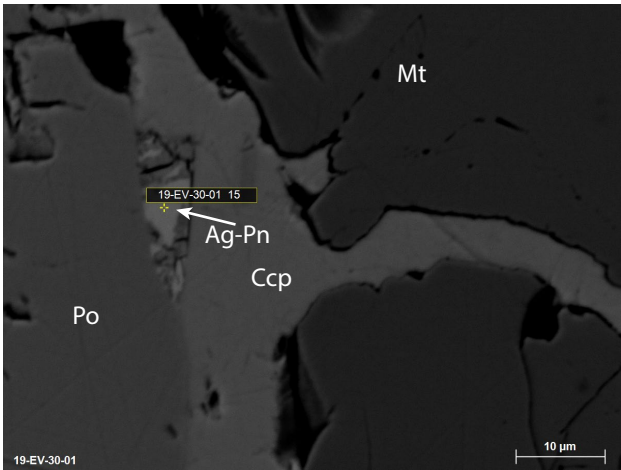
19-EV-30-01 5

Element	At. No.	Netto	Mass [%]	Mass Norm. [%]	Atom [%]	abs. error [%] (1 sigma)	rel. error [%] (1 sigma)
Tellurium	52	40906	64.53	71.98	54.26	1.97	3.06
Nickel	28	3505	15.50	17.29	28.34	0.64	4.10
Palladium	46	3715	4.35	4.86	4.39	0.22	5.04
Iron	26	1073	3.24	3.61	6.22	0.22	6.74
Sulfur	16	2859	2.03	2.26	6.78	0.12	6.02
Sum		89.65	100.00	100.00	100.00		



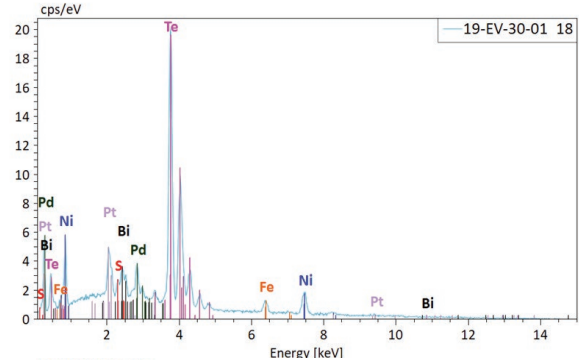
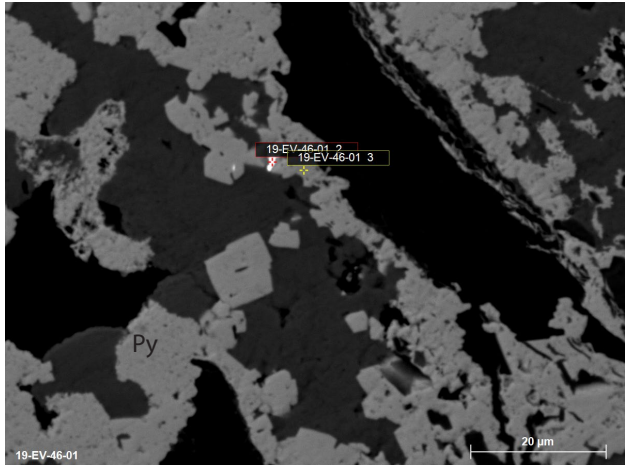
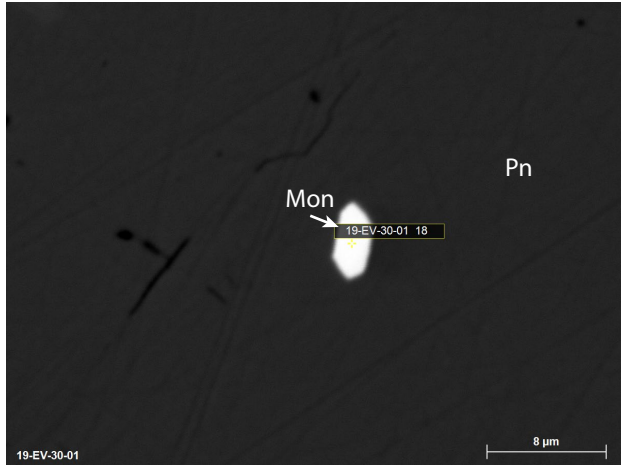
19-EV-30-01 12

Element	At. No.	Netto	Mass [%]	Mass Norm. [%]	Atom [%]	abs. error [%] (1 sigma)	rel. error [%] (1 sigma)
Tellurium	52	29946	49.64	59.32	58.87	1.54	3.11
Platinum	78	22125	26.84	32.08	20.83	1.09	4.05
Iron	26	1758	4.95	5.91	13.41	0.26	5.34
Nickel	28	464	1.73	2.07	4.47	0.20	11.74
Sulfur	16	750	0.51	0.61	2.43	0.08	14.81
Sum			83.67	100.00	100.00		



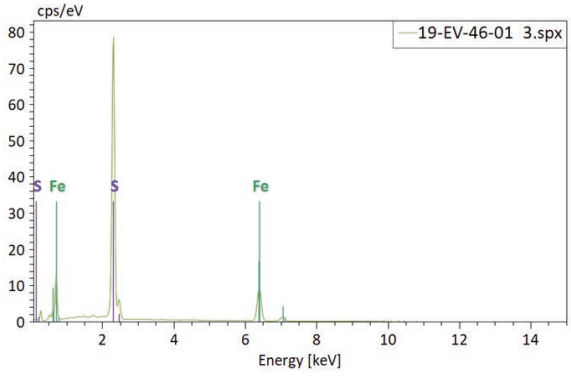
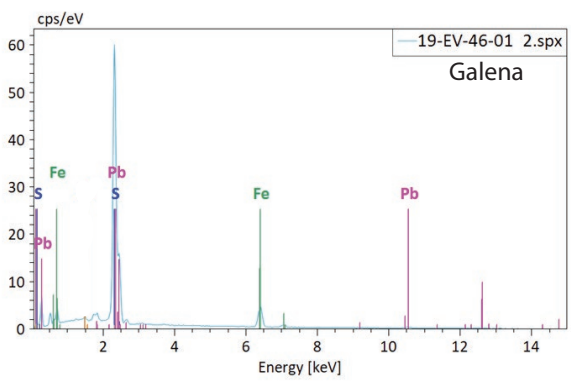
19-EV-30-01 15

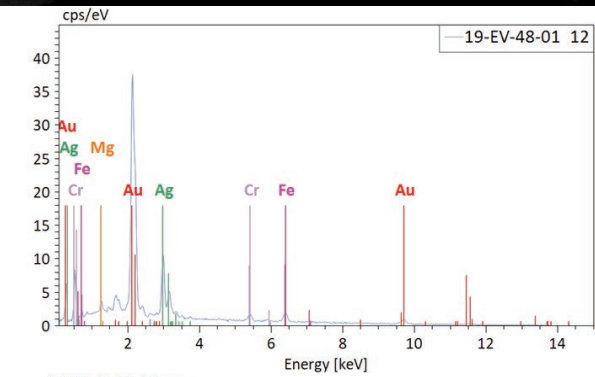
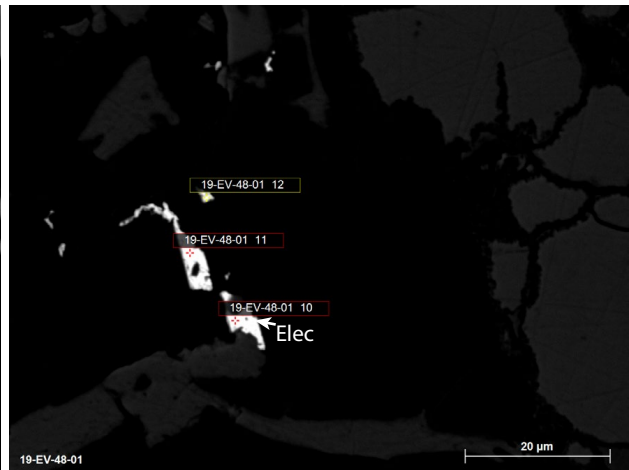
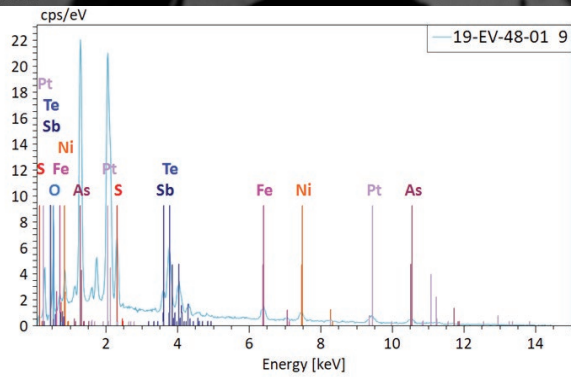
Element	At. No.	Netto	Mass [%]	Mass Norm. [%]	Atom [%]	abs. error [%] (1 sigma)	rel. error [%] (1 sigma)
Iron	26	10255	34.64	39.55	34.60	1.14	3.29
Sulfur	16	38627	24.45	27.91	42.53	0.91	3.70
Nickel	28	3568	18.77	21.43	17.84	0.75	4.00
Silver	47	7244	9.73	11.11	5.03	0.38	3.93
Sum			87.58	100.00	100.00		



19-EV-30-01 18

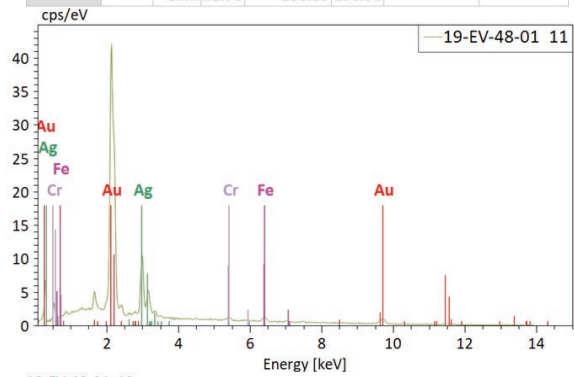
Element	At. No.	Netto	Mass [%]	Mass Norm. [%]	Atom [%]	abs. error [% (1 sigma)]	rel. error [% (1 sigma)]
Tellurium	52	38822	63.56	67.77	57.58	1.95	3.06
Nickel	28	2453	10.77	11.48	21.21	0.49	4.56
Platinum	78	4263	5.77	6.16	3.42	0.30	5.19
Bismuth	83	3270	4.66	4.97	2.58	0.25	5.38
Palladium	46	3833	4.61	4.91	5.00	0.23	4.98
Iron	26	1254	3.74	3.99	7.75	0.23	6.23
Sulfur	16	980	0.68	0.73	2.46	0.08	11.58
Sum			93.79	100.00	100.00		





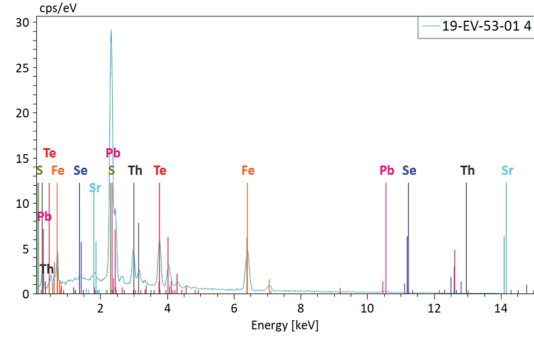
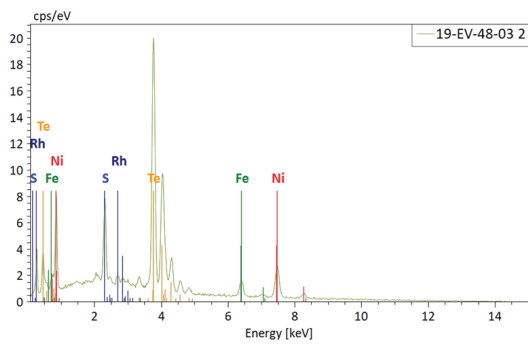
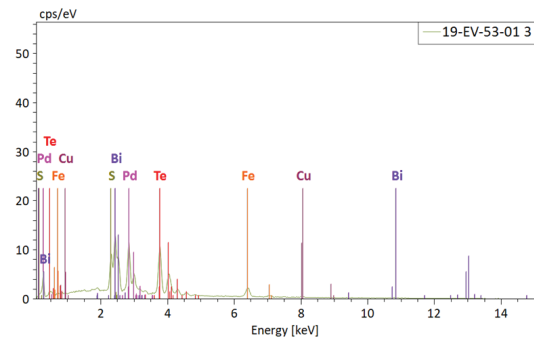
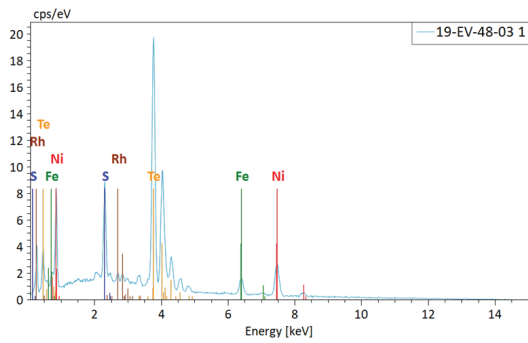
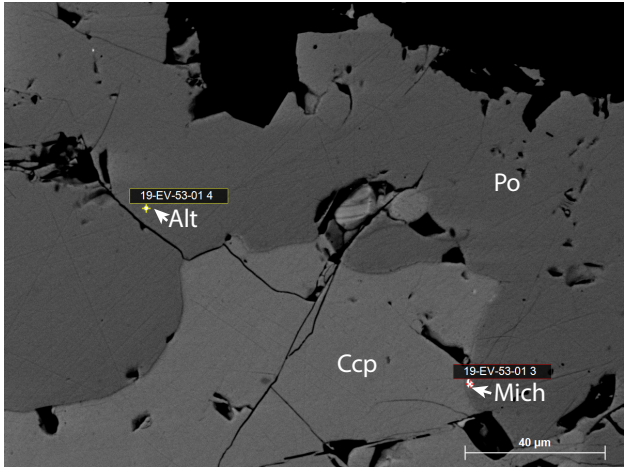
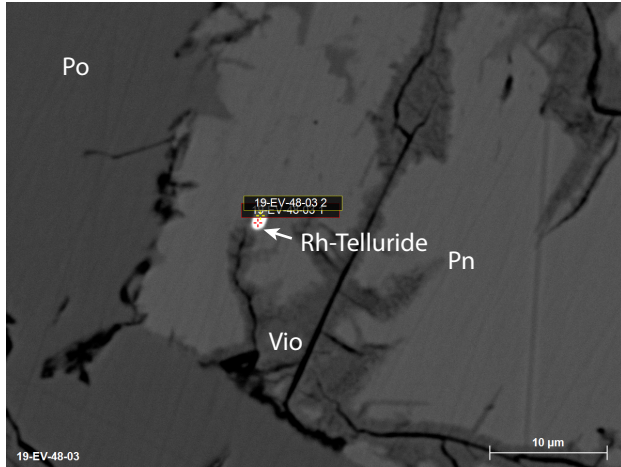
19-EV-48-01 10.spx

Element	At. No.	Netto	Mass [%]	Mass Norm. [%]	Atom [%]	abs. error [%] (1 sigma)	rel. error [%] (1 sigma)
Gold	79	72335	57.45	69.27	52.18	2.19	3.82
Silver	47	21836	22.02	26.56	36.53	0.75	3.42
Iron	26	1314	2.56	3.09	8.21	0.18	7.04
Chromium	24	644	0.90	1.08	3.08	0.12	12.85
Sum		82.93		100.00	100.00		



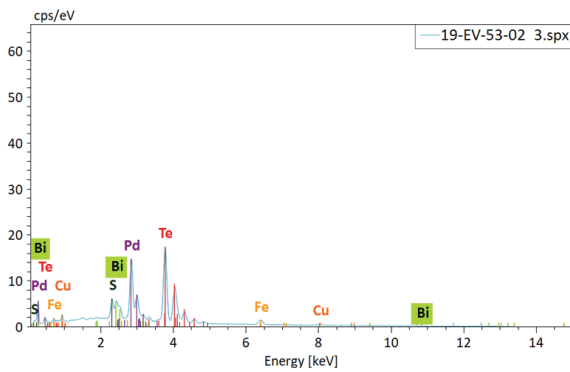
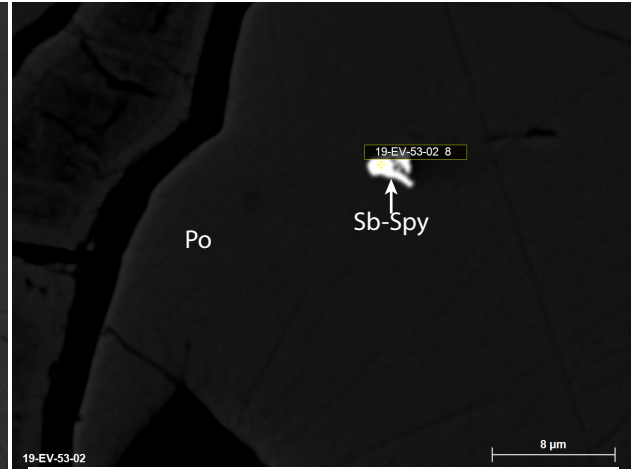
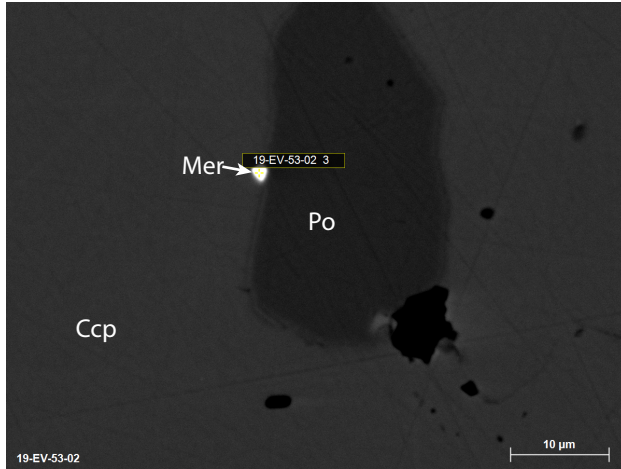
19-EV-48-01 12

Element	At. No.	Netto	Mass [%]	Mass Norm. [%]	Atom [%]	abs. error [%] (1 sigma)	rel. error [%] (1 sigma)
Gold	79	66410	47.37	63.63	41.10	1.82	3.83
Silver	47	20148	18.51	24.86	29.33	0.64	3.46
Iron	26	2739	5.35	7.19	16.37	0.25	4.75
Chromium	24	1785	2.52	3.38	8.28	0.16	6.18
Magnesium	12	1392	0.70	0.94	4.93	0.08	12.03
Sum		74.46		100.00	100.00		



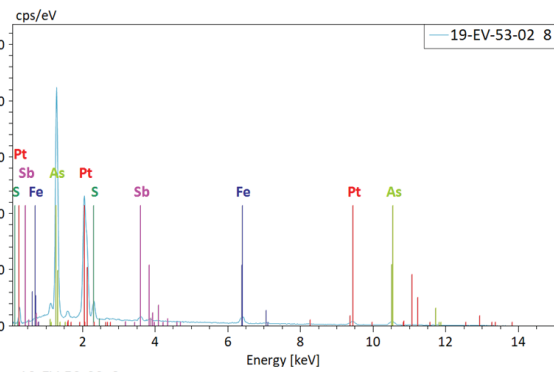
19-EV-48-03 2

Element	At. No.	Netto	Mass [%]	Mass Norm. [%]	Atom [%]	abs. error [% (1 sigma)]	rel. error [% (1 sigma)]
Tellurium	52	69413	60.28	66.59	39.42	1.82	3.02
Nickel	28	7025	17.04	18.82	24.22	0.62	3.67
Carbon	6	1931	2.40	2.65	16.66	0.53	22.08
Sulfur	16	10742	4.07	4.50	10.59	0.18	4.47
Iron	26	3309	5.34	5.90	7.98	0.24	4.49
Rhodium	45	2202	1.39	1.53	1.13	0.11	7.99
		Sum	90.52	100.00	100.00		



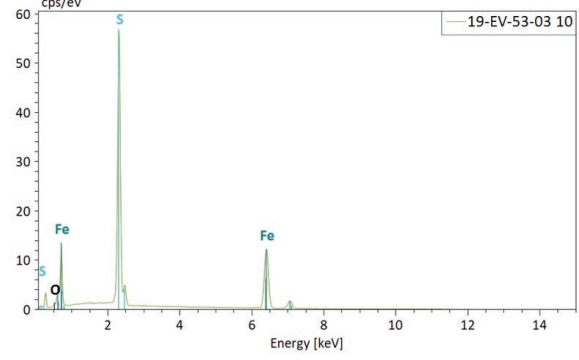
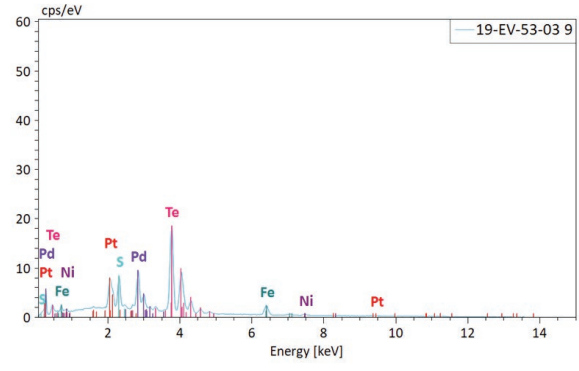
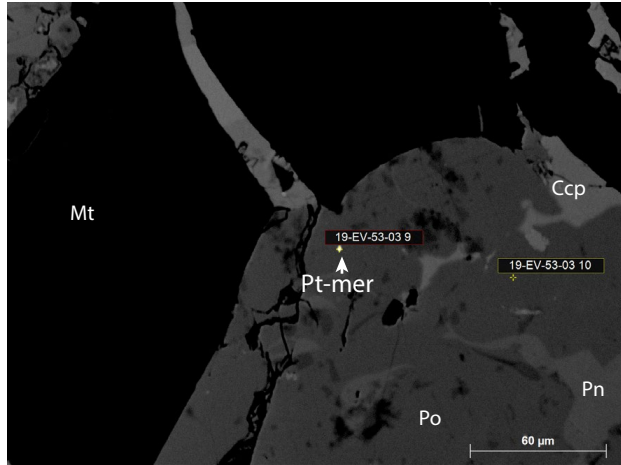
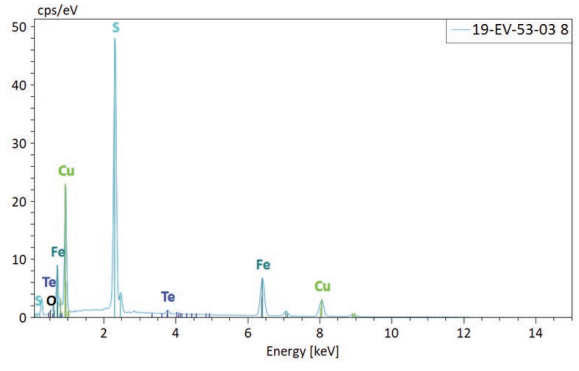
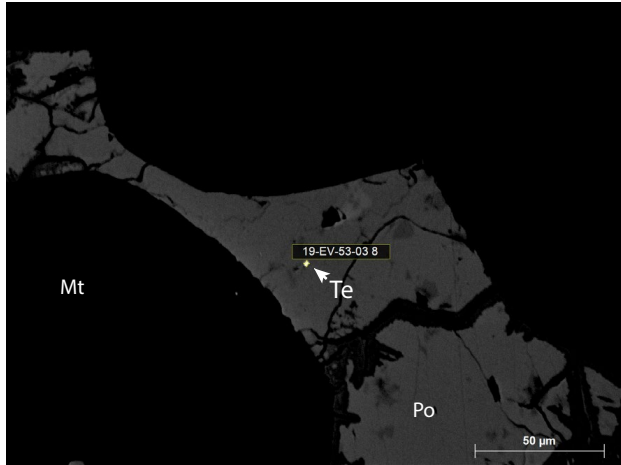
19-EV-53-02 3.spx

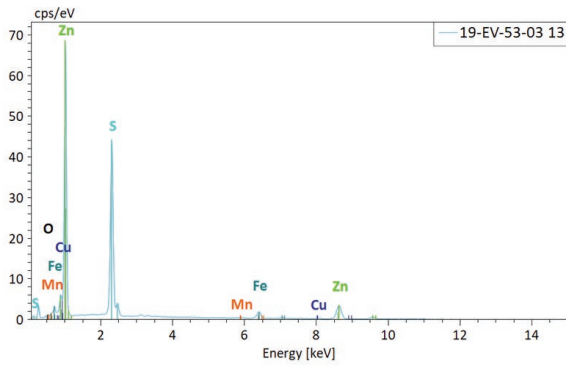
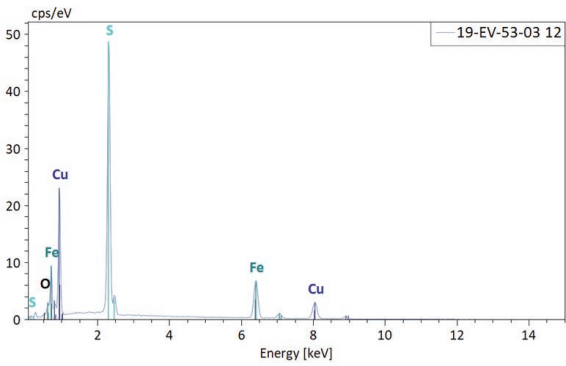
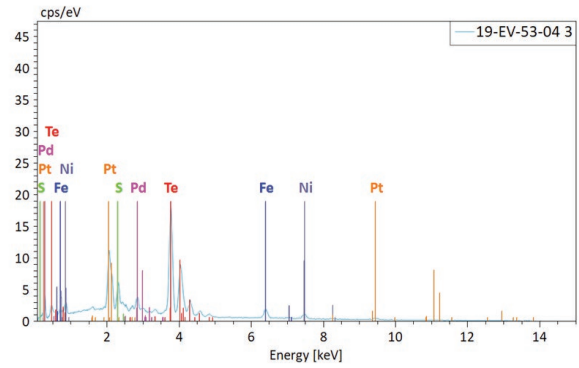
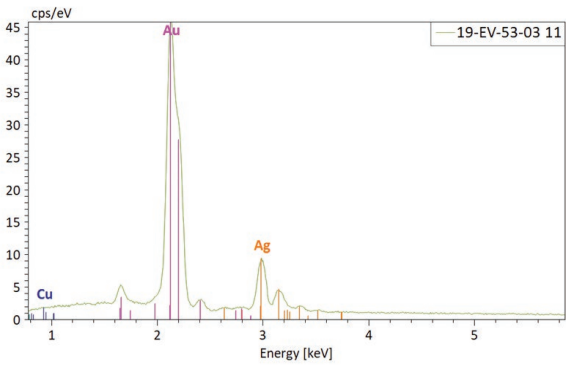
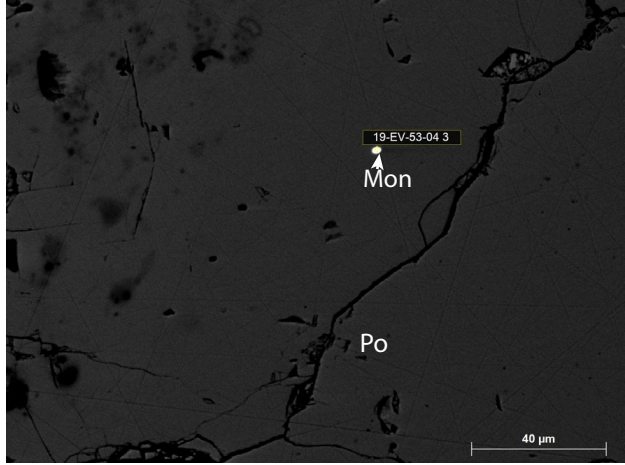
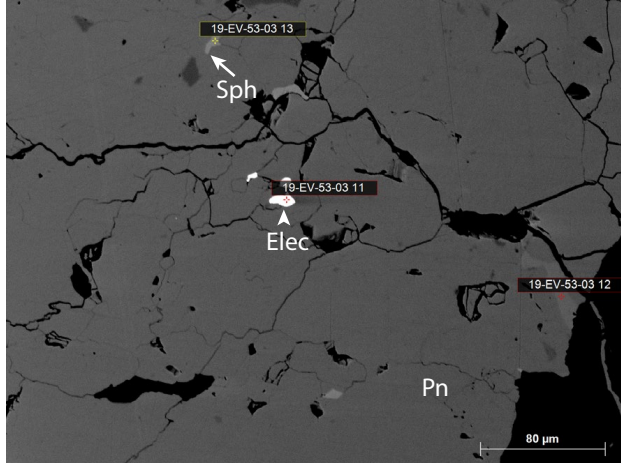
Element	At. No.	Netto	Mass [%]	Mass Norm. [%]	Atom [%]	abs. error [% (1 sigma)]	rel. error [% (1 sigma)]
Tellurium	52	102329	52.40	57.66	48.81	1.58	3.01
Palladium	46	64823	22.59	24.85	25.22	0.76	3.35
Bismuth	83	17462	6.96	7.66	3.96	0.29	4.10
Iron	26	4846	4.32	4.75	9.18	0.19	4.36
Copper	29	1328	2.33	2.57	4.36	0.18	7.73
Sulfur	16	11752	2.28	2.51	8.46	0.11	4.99
		Sum	90.88	100.00	100.00		

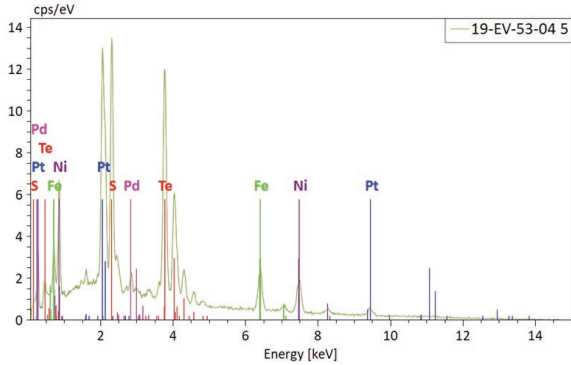
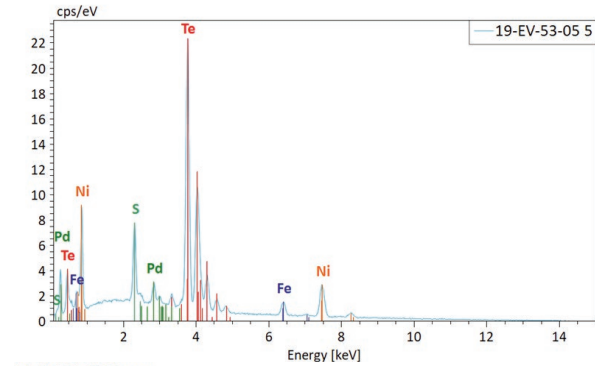
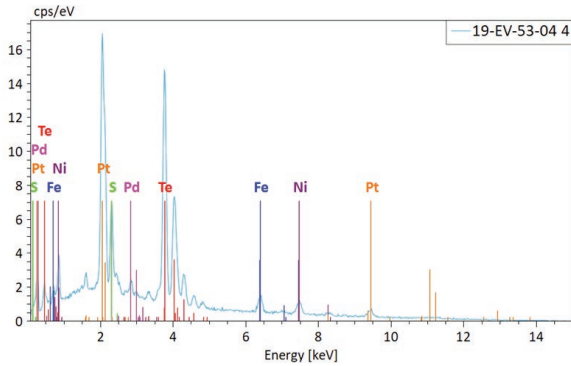
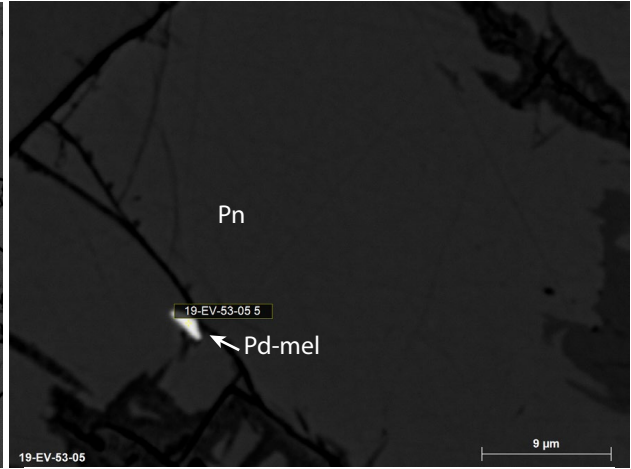
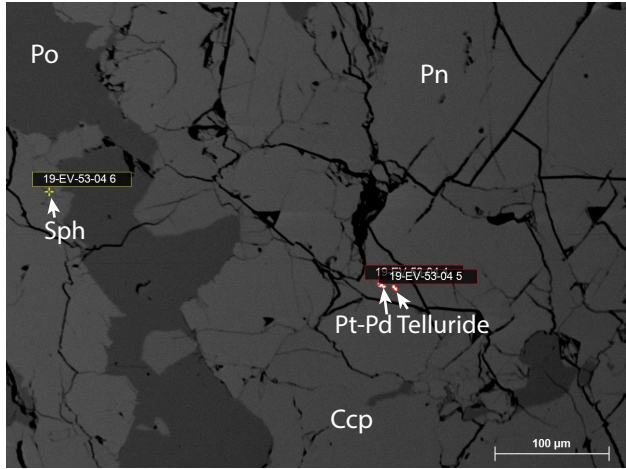


19-EV-53-02 8

Element	At. No.	Netto	Mass [%]	Mass Norm. [%]	Atom [%]	abs. error [% (1 sigma)]	rel. error [% (1 sigma)]
Platinum	78	86774	35.41	47.18	24.05	1.39	3.92
Arsenic	33	102870	29.96	39.93	52.99	1.59	5.32
Iron	26	5642	5.41	7.20	12.83	0.22	4.09
Antimony	51	4475	2.46	3.28	2.68	0.14	5.60
Sulfur	16	7160	1.80	2.40	7.45	0.10	5.58
		Sum	75.04	100.00	100.00		

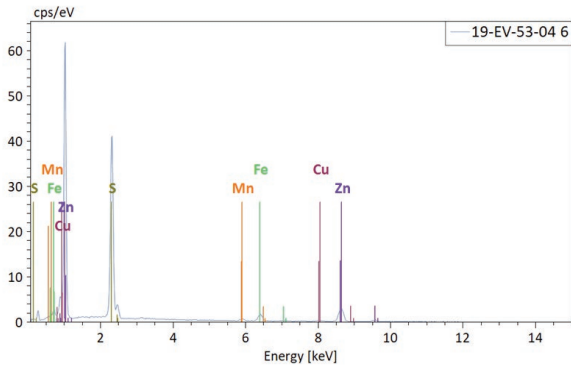


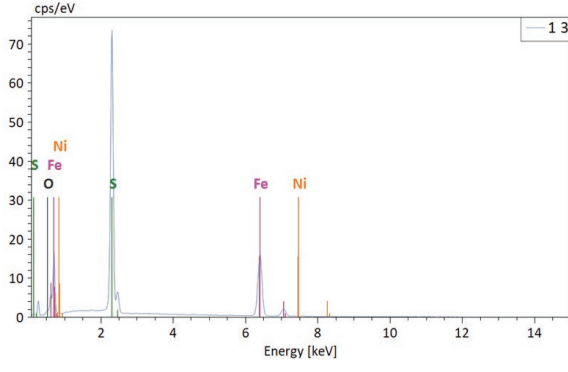
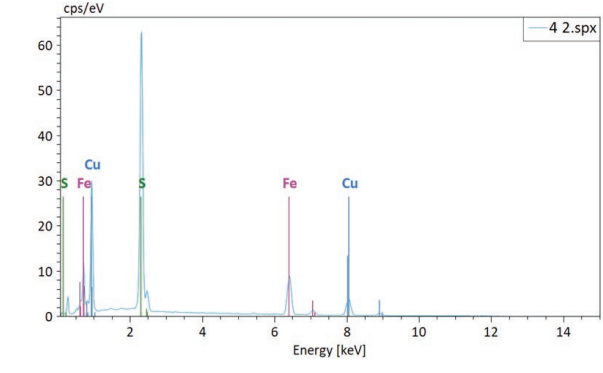
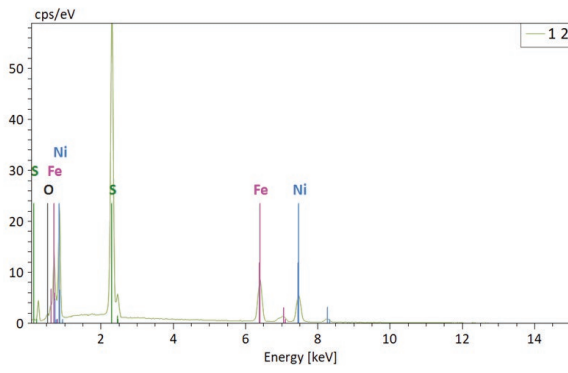
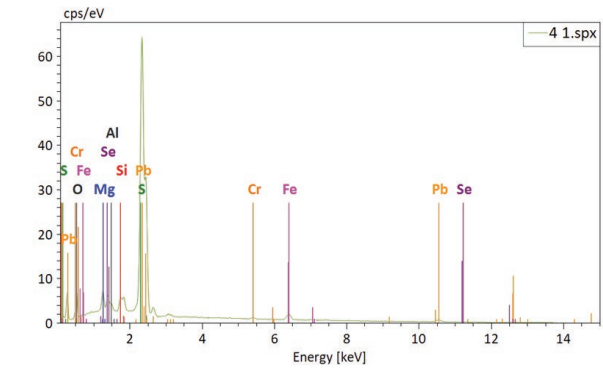
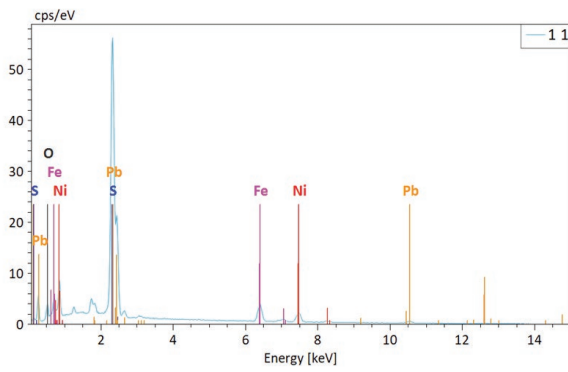
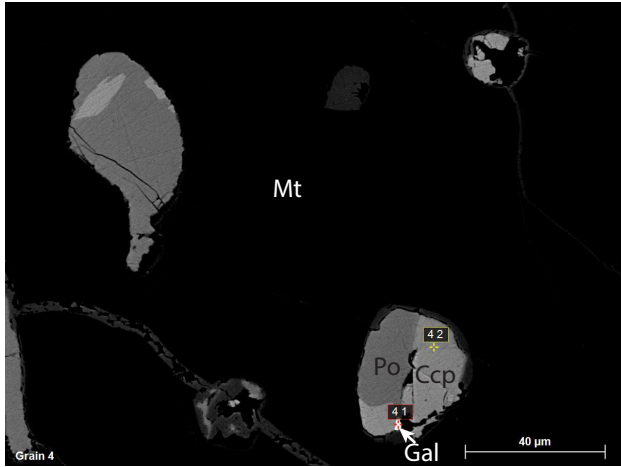
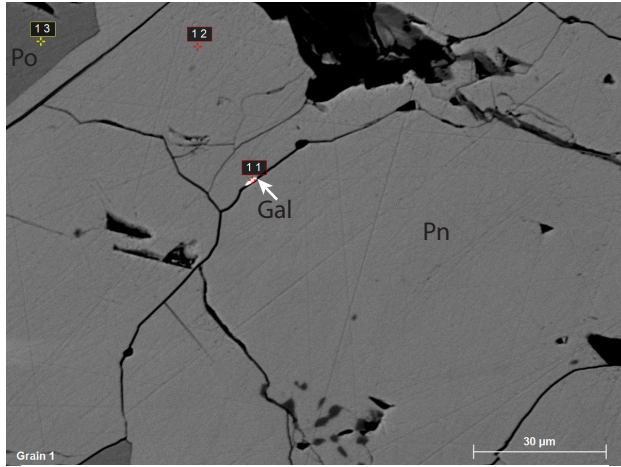


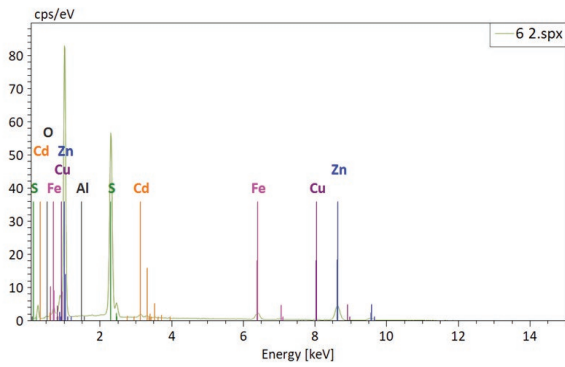
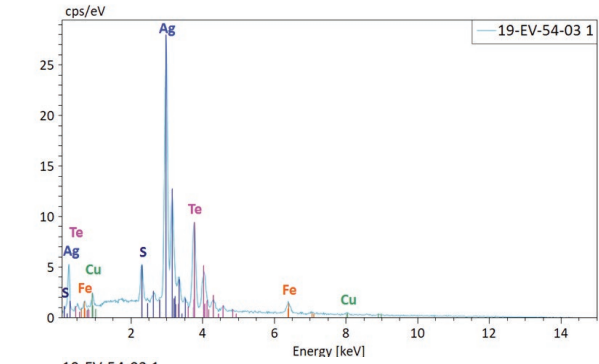
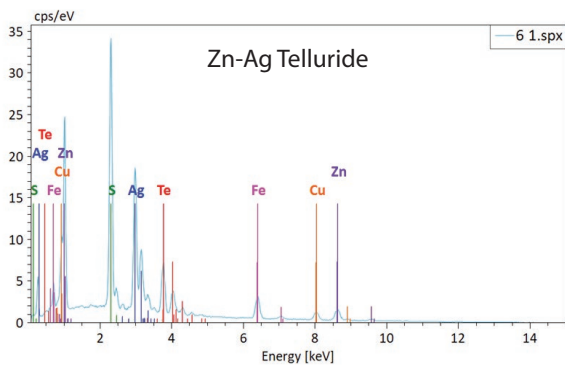
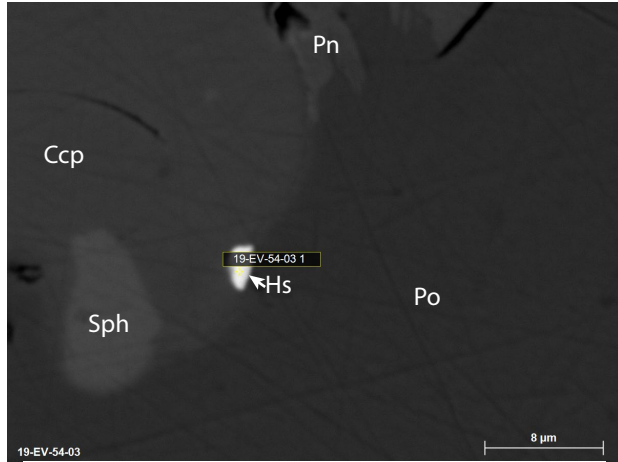
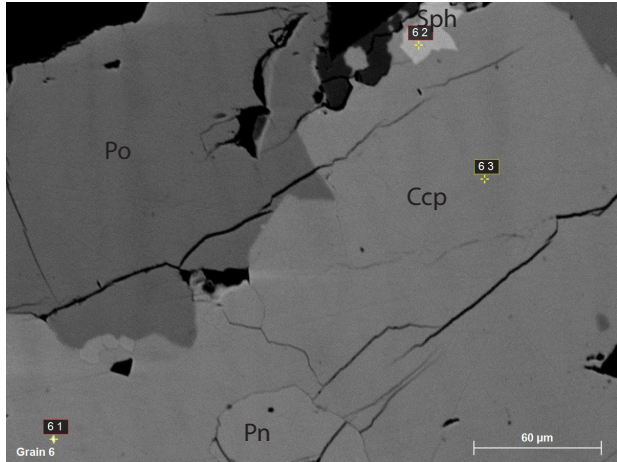


19-EV-53-05 5.spx

Element	At. No.	Netto	Mass [%]	Mass Norm. [%]	Atom [%]	abs. error [%] (1 sigma)	rel. error [%] (1 sigma)
Tellurium	52	130286	62.97	69.36	49.23	1.89	2.99
Nickel	28	12781	17.18	18.93	29.20	0.59	3.46
Iron	26	4862	4.36	4.80	7.79	0.19	4.34
Sulfur	16	17336	3.63	4.00	11.30	0.16	4.43
Palladium	46	7473	2.64	2.91	2.48	0.13	5.00
Sum		90.79		100.00	100.00		

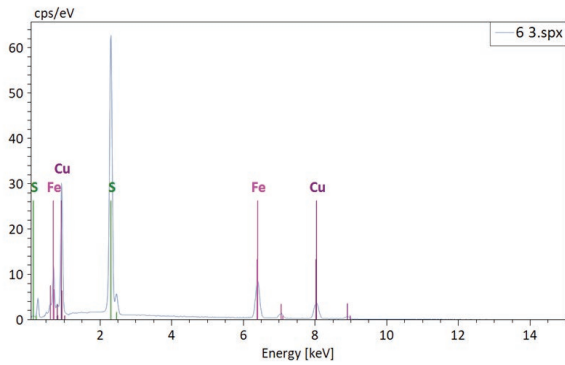


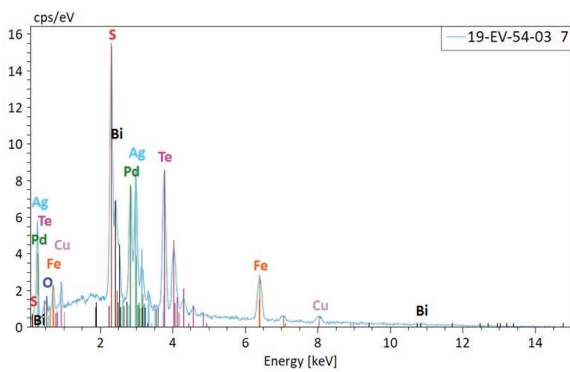
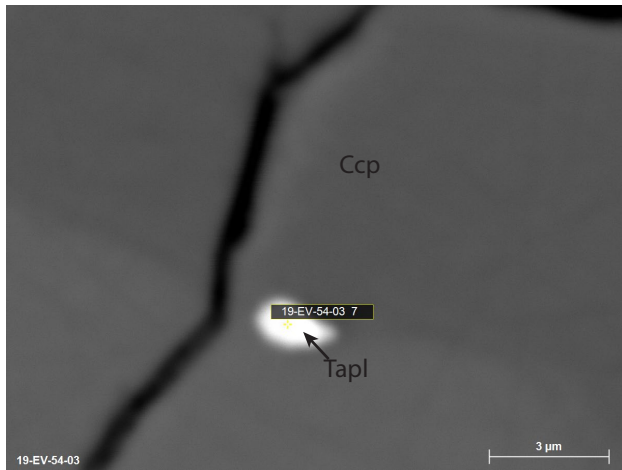




19-EV-54-03 1

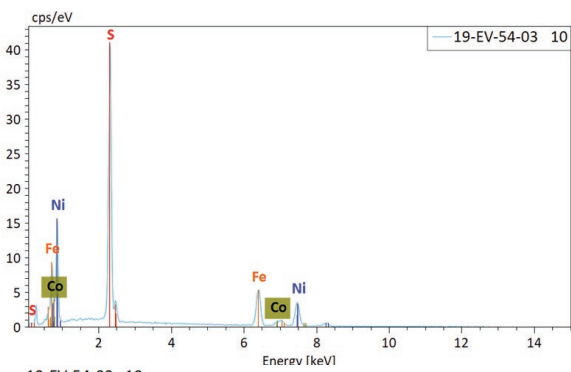
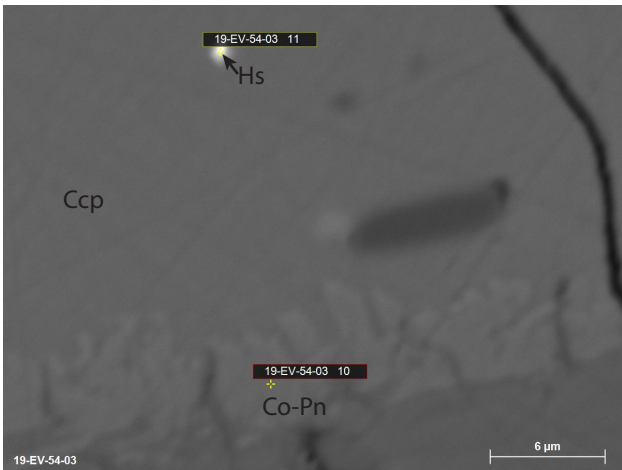
Element	At. No.	Netto	Mass [%]	Mass Norm. [%]	Atom [%]	abs. error [% (1 sigma)]	rel. error [% (1 sigma)]
Silver	47	43109	50.19	55.84	51.95	1.63	3.25
Tellurium	52	16909	30.42	33.85	26.62	0.99	3.25
Iron	26	1593	4.76	5.30	9.52	0.26	5.47
Sulfur	16	3474	2.31	2.57	8.05	0.13	5.66
Copper	29	342	2.19	2.44	3.86	0.28	12.63
Sum		89.88	100.00	100.00			





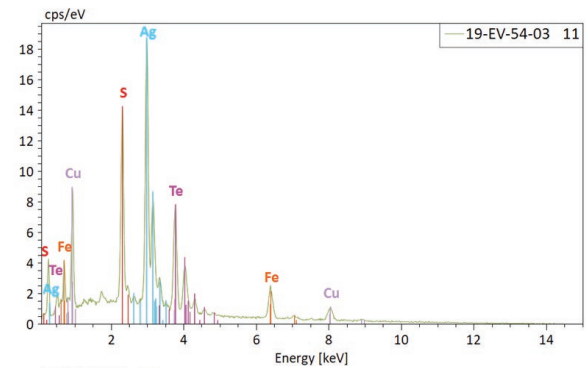
19-EV-54-03 7

Element	At. No.	Netto	Mass [%]	Mass Norm. [%]	Atom [%]	abs. error [% (1 sigma)]	rel. error [% (1 sigma)]
Tellurium	52	16002	26.89	33.62	21.18	0.88	3.26
Palladium	46	10302	11.71	14.65	11.06	0.45	3.82
Iron	26	3710	11.71	14.65	21.08	0.47	3.98
Bismuth	83	7305	8.97	11.22	4.31	0.39	4.32
Silver	47	7222	8.31	10.40	7.75	0.35	4.22
Sulfur	16	13089	7.77	9.72	24.36	0.32	4.09
Copper	29	592	3.97	4.97	6.28	0.34	8.58
Oxygen	8	285	0.63	0.79	3.98	0.31	48.54
Sum			79.98	100.00	100.00		



19-EV-54-03 10

Element	At. No.	Netto	Mass [%]	Mass Norm. [%]	Atom [%]	abs. error [% (1 sigma)]	rel. error [% (1 sigma)]
Nickel	28	11395	30.11	34.51	27.24	1.02	3.40
Iron	26	16723	26.67	30.57	25.36	0.85	3.20
Sulfur	16	77167	26.40	30.26	43.73	0.97	3.66
Cobalt	27	1876	4.07	4.66	3.67	0.22	5.53
Sum			87.25	100.00	100.00		



19-EV-54-03 11

Element	At. No.	Netto	Mass [%]	Mass Norm. [%]	Atom [%]	abs. error [% (1 sigma)]	rel. error [% (1 sigma)]
Silver	47	49886	35.59	40.46	30.12	1.16	3.26
Tellurium	52	24193	26.23	29.82	18.77	0.84	3.20
Iron	26	5315	9.43	10.72	15.42	0.36	3.83
Copper	29	2377	8.43	9.58	12.11	0.41	4.85
Sulfur	16	21224	8.28	9.41	23.58	0.33	3.98
Sum			87.95	100.00	100.00		

Appendix C: Supplementary Information for LA-ICP-MS Analysis of Sulfides

Table C.1. Locations and values for Pb isotopic and trace element analysis of sulfides.

Zone ¹	Sample	Area #	Spot Name	Mineral ²	²⁰⁸ Pb/ ²⁰⁶ Pb	2SE	²⁰⁷ Pb/ ²⁰⁶ Pb	2SE	U (ppm)	Th (ppm)	Pb (ppm)
NEZ	19-EV-30-01	1	EV301Ccp1	Ccp	1.998	0.086	0.816	0.035	<dl	<dl	<dl
		5	EV301Ccp2	Ccp	2.029	0.034	0.822	0.014	<dl	15.8	250.5
NEZ	19-EV-30-02	1	EV301Po2	Po	2.046	0.099	0.867	0.054	<dl	4.7	30.55
		2	EV302Ccp1	Ccp	2.018	0.03	0.83	0.018	<dl	91	520
		4	EV302Ccp2	Ccp	2.055	0.036	0.842	0.016	<dl	<dl	5.415
		1	EV302Pn1	Pn (G)	2.2	0.16	0.857	0.063	<dl	<dl	270.5
		3	EV302Pnf1	Pn (F)	2.054	0.051	0.852	0.023	<dl	<dl	0.6995
HG	19-EV-46-01	1	EV302Po1	Po	1.747	0.085	0.84	0.035	<dl	<dl	<dl
		2	EV46Ccp1	Ccp (S)	2.3	0.21	0.87	0.054	49	150	515
		2	EV46Ccp2	Ccp (S)	2.031	0.071	0.841	0.033	<dl	<dl	534.5
		4	EV46Py1	Py (D)	1.98	0.11	0.811	0.042	<dl	<dl	159
		4	EV46Py2	Py (D)	2.013	0.056	0.829	0.032	<dl	<dl	227
		5	EV46Py3	Py (D)	2.07	0.11	0.84	0.029	<dl	<dl	65.7
		6	EV46Py4	Py (D)	2.036	0.037	0.828	0.018	0.766	1.46	75
LDZ	19-EV-48-01	6	EV46Py5	Py (D)	2.001	0.064	0.816	0.02	15.6	24.4	68.45
		2	Ev481Ccp1	Ccp	2	0.066	0.829	0.034	<dl	<dl	9.585
		5	EV481Ccp2	Ccp	2.047	0.034	0.834	0.018	<dl	<dl	<dl
		4	EV481Pn1	Pn (G)	2.29	0.2	0.911	0.095	<dl	<dl	48.35
		1	EV481Po1	Po	2.05	0.085	0.857	0.036	<dl	<dl	48.75
LDZ	19-EV-48-03	4	Ev481Po2	Po	2.094	0.067	0.876	0.038	<dl	<dl	6.245
		1	EV483Po1	Po	2.22	0.19	0.907	0.086	<dl	<dl	9.3
		5	EV483Po2	Po	2.11	0.11	0.866	0.055	<dl	<dl	34.55
UC	19-EV-48-04	1	EV484Ccp1	Ccp	2.077	0.063	0.851	0.03	<dl	<dl	41.3
		3	EV484Ccp2	Ccp	2.079	0.041	0.839	0.02	<dl	<dl	9.435
		3	EV484Po1	Po	2.119	0.086	0.867	0.032	<dl	<dl	<dl
		4	EV484Py1	Py (S)	2.158	0.063	0.85	0.034	<dl	<dl	<dl
		6	Ev484Py2	Py (S)	2.14	0.24	0.823	0.046	<dl	<dl	7.7
		6	EV484Vio1	Vio	2.071	0.045	0.838	0.018	<dl	<dl	11.8
UC	19-EV-53-01	6	EV484Vio2	Vio	2.084	0.047	0.848	0.021	<dl	<dl	11.75
		4	EV531Ccp2	Ccp	2.012	0.072	0.819	0.035	<dl	<dl	<dl
		1	EV531Pn1	Pn	2.2	0.22	0.865	0.069	<dl	<dl	<dl
		2	EV531Pn2	Pn	2.34	0.2	0.93	0.1	<dl	<dl	38.55
		1	EV531Po1	Po	2.037	0.084	0.823	0.048	<dl	<dl	4.4
LDZ	19-EV-53-02	4	EV531Po2	Po	1.95	0.14	0.843	0.077	<dl	<dl	3.995
		1	EV532Ccp1	Ccp	2.04	0.021	0.833	0.011	<dl	<dl	21.55
		3	EV532Ccp2	Ccp	2.053	0.04	0.843	0.02	<dl	<dl	<dl
		2	EV532Pn1	Pn (G)	2.09	0.11	0.837	0.042	<dl	<dl	4.555
		1	EV532Po1	Po	2.032	0.064	0.84	0.023	<dl	<dl	<dl
LDZ	19-EV-53-03	2	EV532Po2	Po	2.07	0.072	0.845	0.028	<dl	<dl	22.55
		1	EV533Ccp1	Ccp	2.049	0.055	0.846	0.025	<dl	<dl	16.535

Zone ¹	Sample	Area #	Spot Name	Mineral ²	²⁰⁸ Pb/ ²⁰⁶ Pb	2SE	²⁰⁷ Pb/ ²⁰⁶ Pb	2SE	U (ppm)	Th (ppm)	Pb (ppm)
		5	EV533Ccp2	Ccp	2.037	0.05	0.817	0.021	<dl	<dl	1.57
		1	EV533Po1	Po	2.15	0.15	0.866	0.071	<dl	<dl	25.4
		4	EV533Po2	Po	2.037	0.029	0.841	0.013	<dl	<dl	7.24
LDZ	19-EV-53-04	2	EV534Ccp1	Ccp	2.045	0.023	0.8257	0.009	<dl	<dl	12.8
		5	EV534Ccp2	Ccp	2.047	0.025	0.828	0.012	<dl	34	249.5
		5	EV534Pn2	Pn (G)	2.04	0.11	0.837	0.044	<dl	<dl	3.345
		1	EV534Pnf1	Pn (F)	2.11	0.047	0.866	0.032	<dl	<dl	0.951
		4	EV534Pnf2	Pn (F)	2.066	0.057	0.832	0.028	<dl	<dl	<dl
		1	EV534Po1	Po	2.08	0.12	0.876	0.072	<dl	<dl	4.755
		4	EV534Po3	Po	2.12	0.13	0.804	0.067	<dl	<dl	6.6
		4	EV534Po4	Po	2.089	0.065	0.86	0.03	<dl	<dl	0.3715
LDZ	19-EV-53-05	1	EV535Ccp1	Ccp	2.05	0.039	0.84	0.021	<dl	<dl	14.185
		4	EV535Ccp2	Ccp	2.02	0.056	0.805	0.021	<dl	<dl	19.4
		5	EV535Ccp3	Ccp	2.04	0.039	0.842	0.018	<dl	<dl	14.45
		4	EV535Pnf1	Pn (F)	2.053	0.024	0.834	0.012	<dl	<dl	4.48
		3	EV535Po1	Po	1.98	0.1	0.826	0.049	<dl	<dl	4.515
		4	EV535Po2	Po	2.13	0.14	0.878	0.073	<dl	<dl	0.78
LDZ	19-EV-53-06	3	EV536Ccp1	Ccp	2.045	0.033	0.829	0.013	<dl	<dl	48.35
		4	EV536Ccp2	Ccp	2.059	0.033	0.823	0.017	<dl	<dl	3.285
		2	EV536Pn1	Pn (G)	1.96	0.15	0.794	0.068	<dl	<dl	2.6
		3	EV536Pn2	Pn (G)	2.023	0.05	0.843	0.026	<dl	<dl	0.4115
		1	EV536Pnf1	Pn (F)	2.12	0.11	0.835	0.046	<dl	<dl	26.45
		1	EV536Po1	Po	2.05	0.1	0.81	0.059	<dl	<dl	0.3905
		4	EV536Po2	Po	2.062	0.06	0.854	0.028	<dl	<dl	0.389
		4	EV536Po3	Po	2.035	0.078	0.824	0.034	<dl	<dl	4.1
LDZ	19-EV-53-07	1	EV537Ccp1	Ccp	2.058	0.036	0.821	0.015	<dl	<dl	0.995
		3	EV537Ccp2	Ccp	2.033	0.023	0.835	0.014	<dl	<dl	0.4635
		2	EV537Pn1	Pn (G)	2.073	0.069	0.809	0.022	<dl	<dl	1.22
		3	EV537Pn2	Pn (G)	2.2	0.11	0.877	0.049	<dl	<dl	4.04
		1	EV537Pnf1	Pn (F)	2.068	0.064	0.81	0.026	<dl	<dl	2.545
		1	EV537Po1	Po	2.18	0.15	0.886	0.073	<dl	<dl	0.4725
		3	EV537Po2	Po	2.2	0.14	0.884	0.066	<dl	<dl	0.452
LC	19-EV-54-02	4	EV542Ccp1	Ccp	2.042	0.029	0.823	0.015	<dl	<dl	229
		3	EV542Ccp2	Ccp	2.056	0.05	0.844	0.025	<dl	<dl	42.2
		3	EV542Pn2	Pn	2.042	0.06	0.844	0.023	<dl	117	625
		3	EV542Po2	Po	2.1	0.11	0.873	0.045	16	67	263
LC	19-EV-54-03	5	EV543Ccp1	Ccp	2.052	0.095	0.802	0.031	<dl	57	235.5
		4	EV543Ccp2	Ccp	2.069	0.044	0.821	0.019	<dl	<dl	<dl
		2	EV543Pn1	Pn	2.163	0.09	0.822	0.033	<dl	<dl	15.8
		3	EV543Pn2	Pn	2.057	0.042	0.82	0.017	<dl	<dl	4.365
		2	EV543Po1	Po	2.053	0.071	0.825	0.033	<dl	<dl	<dl
		3	EV543Po2	Po	2.073	0.053	0.835	0.022	<dl	<dl	<dl

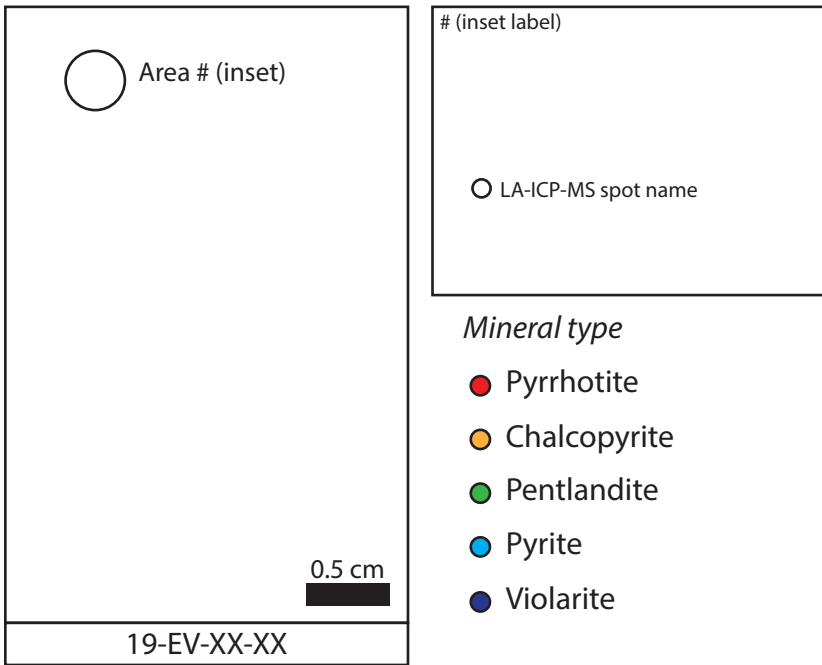
All reported values are measured ratios. 2SE is 2×standard error for each analysis. <dl denotes below detection limit.

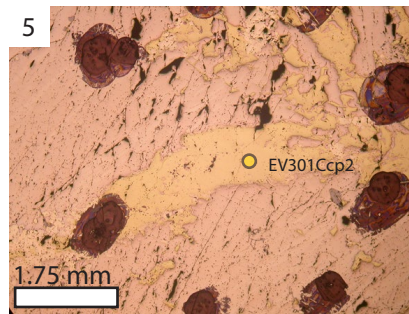
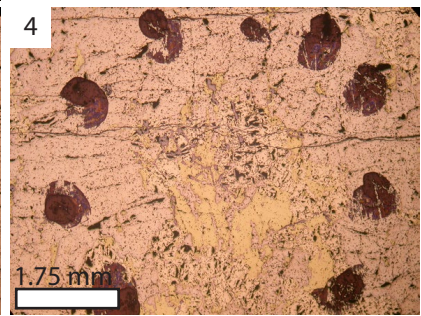
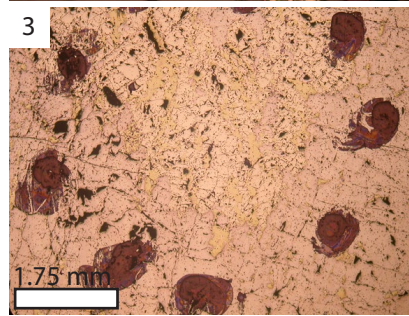
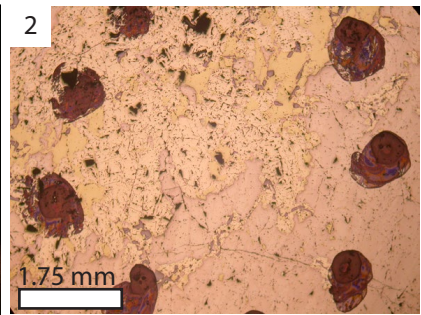
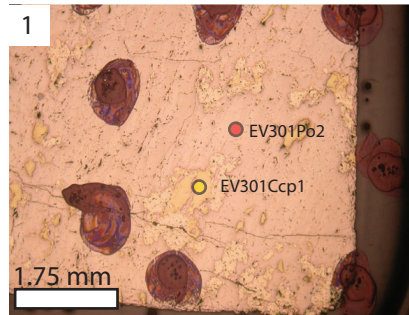
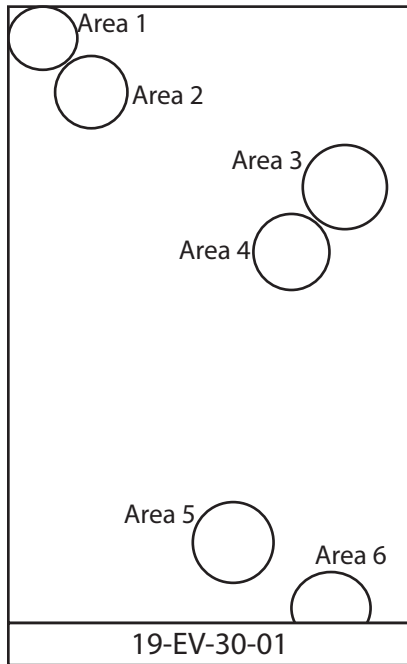
¹Abbreviations: HG – Hazelton Group, LDZ – Lower Discovery Zone, LC – Lower Chamber, NEZ – Northeast

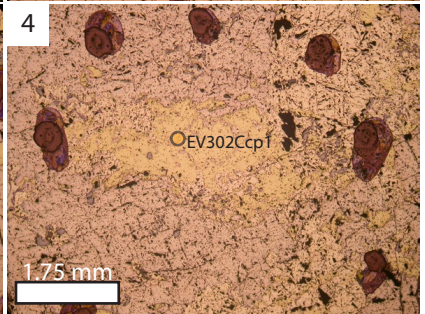
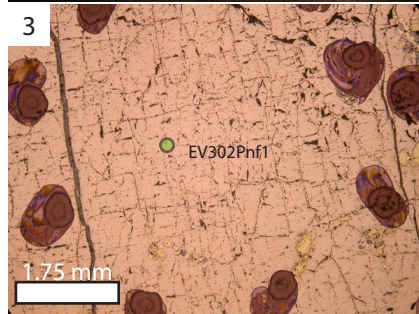
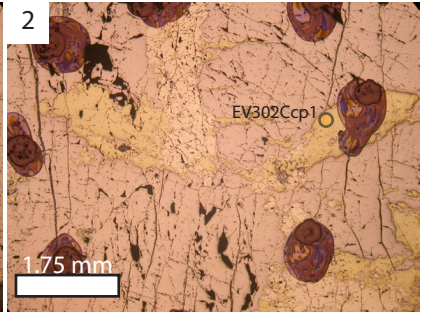
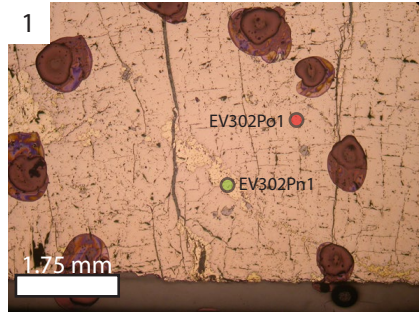
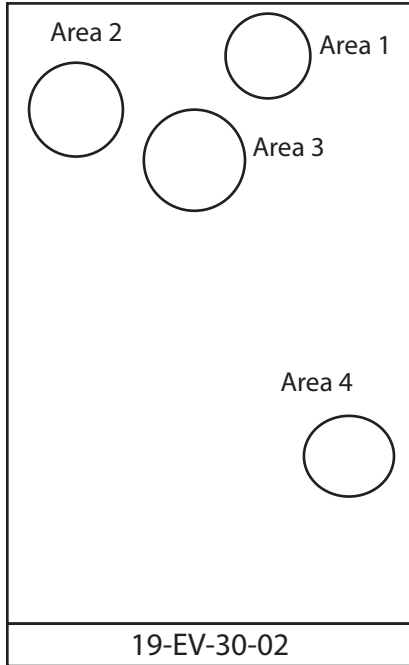
Zone, UC – Upper Chamber. ²Abbreviations: (S) – denotes secondary mineralization, Ccp – chalcopyrite, Pn (G) – granular pentlandite, Pn – pentlandite, Pn (F) – flame pentlandite, Po – pyrrhotite, Py – diagenetic pyrite (unless denoted with (S)), Vio – Violarite.

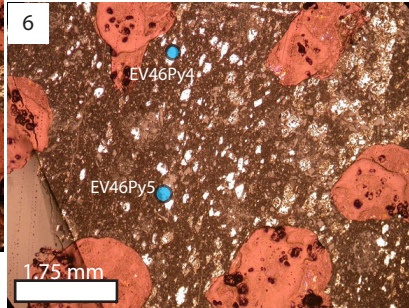
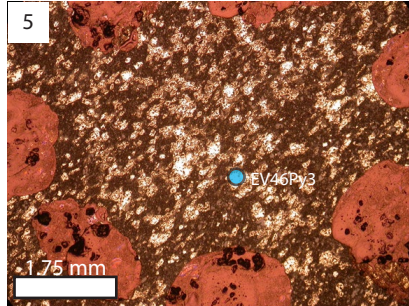
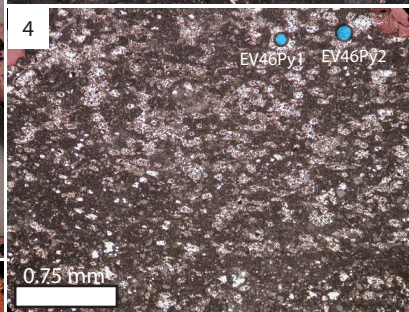
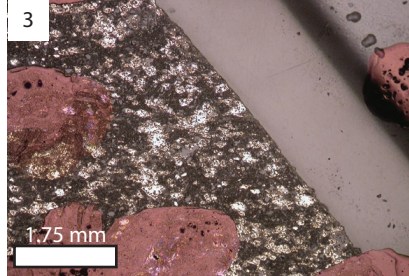
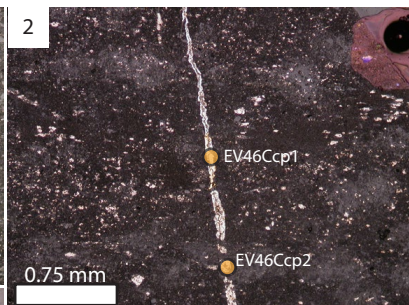
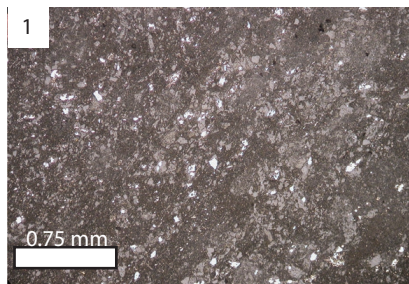
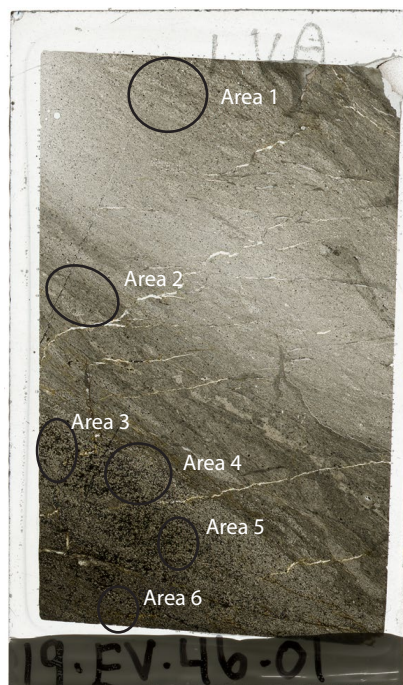
C.2. Spot locations for LA-ICP-MS analyses.

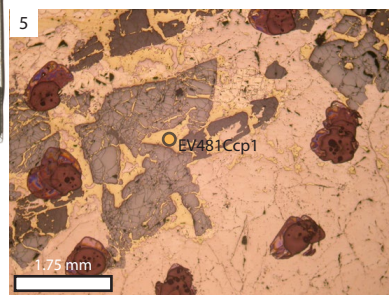
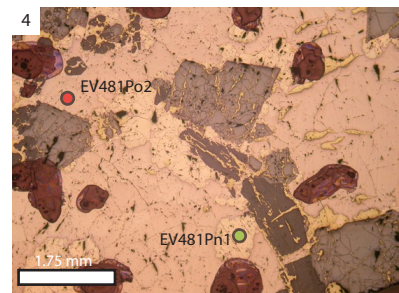
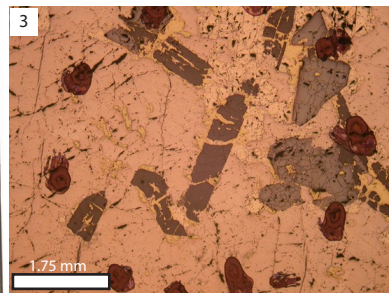
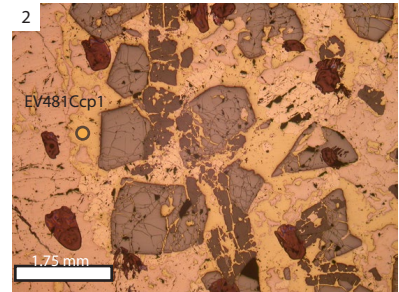
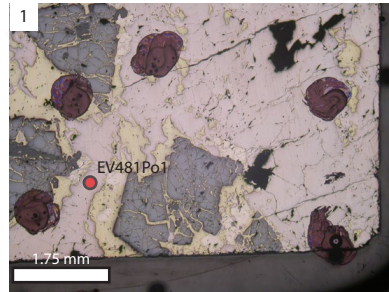
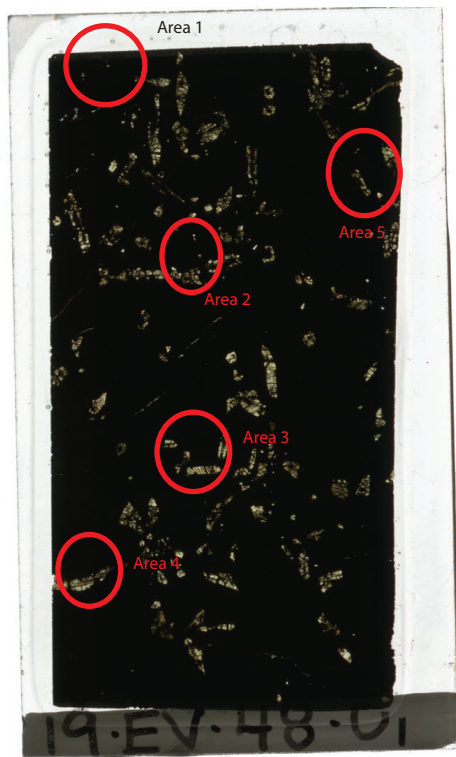
Index Page: samples are described using the following format

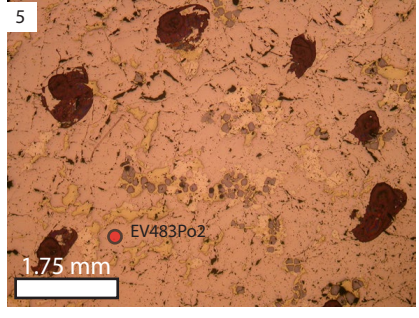
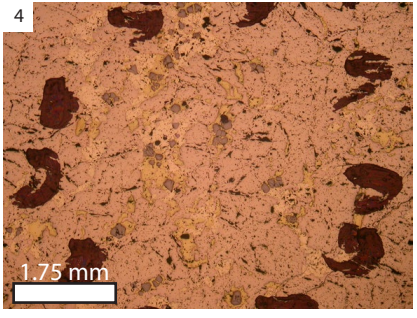
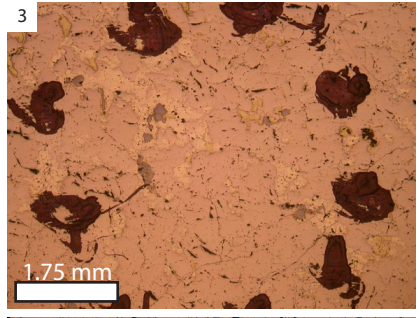
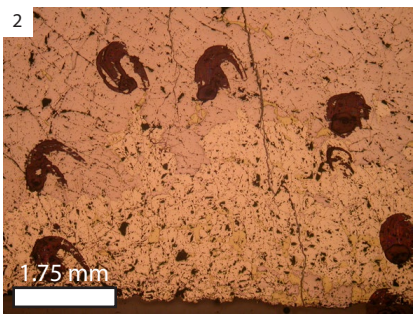
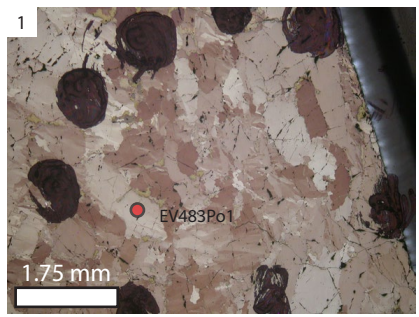
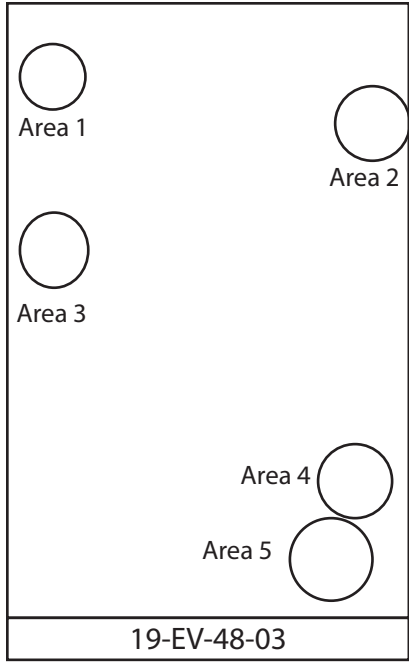


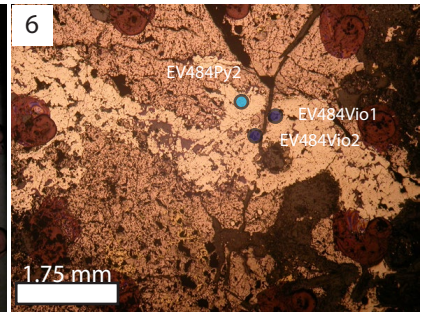
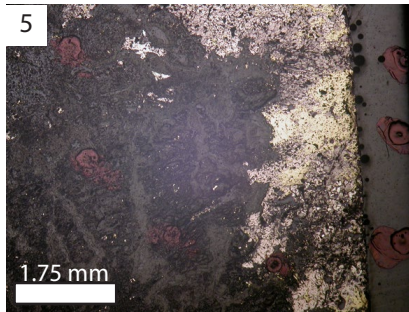
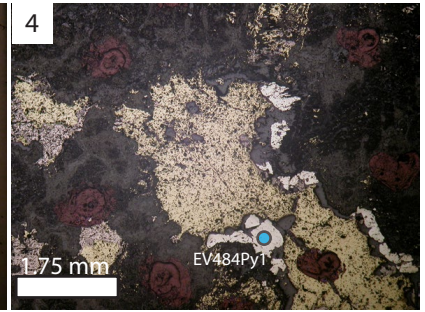
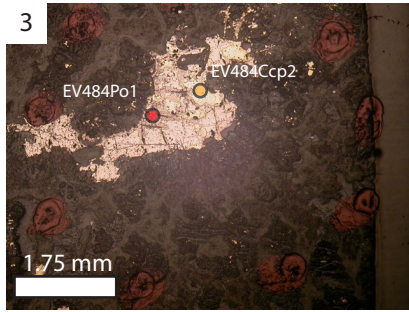
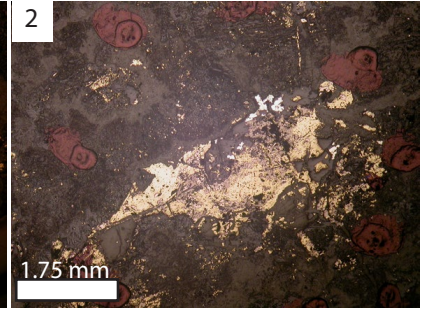
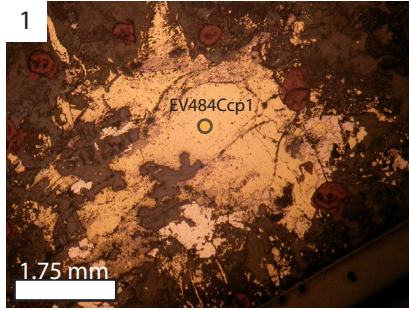
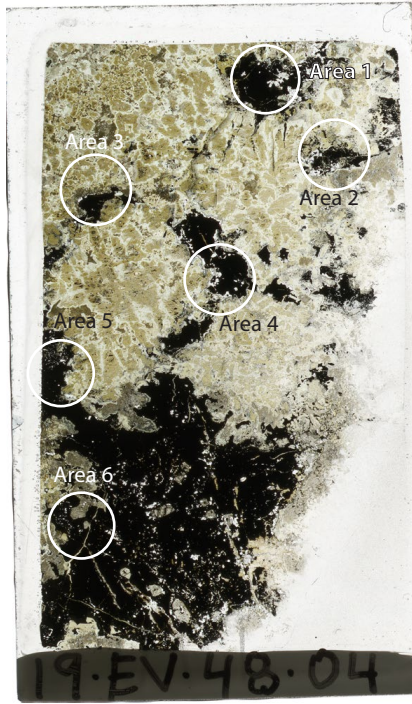


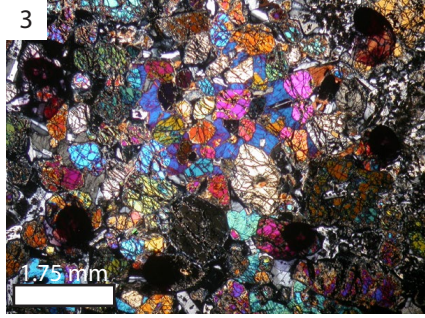
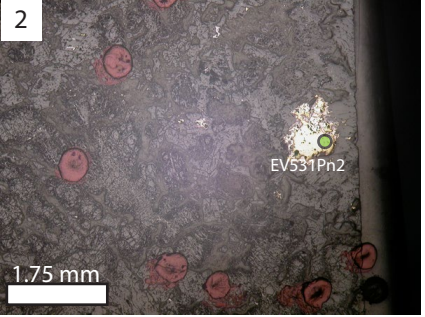
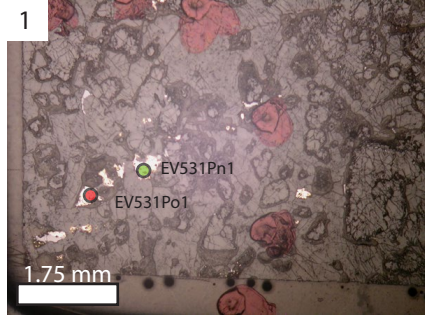


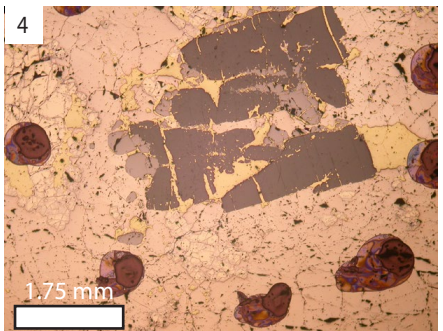
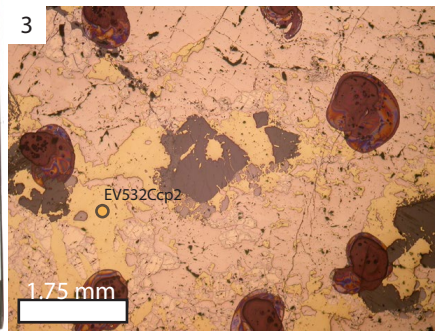
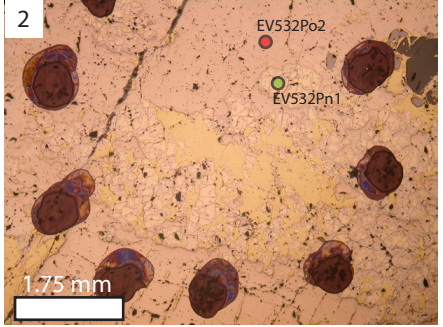
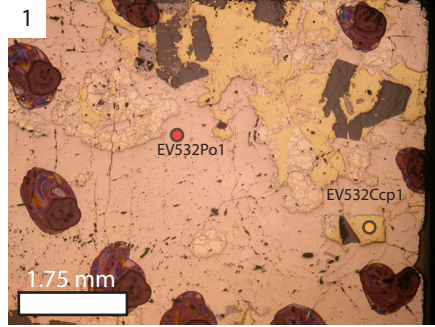
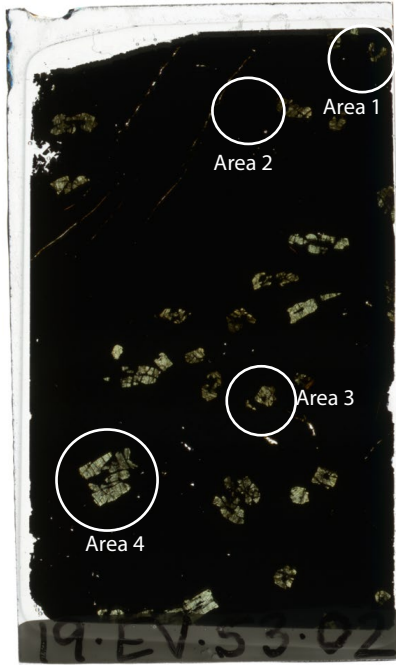


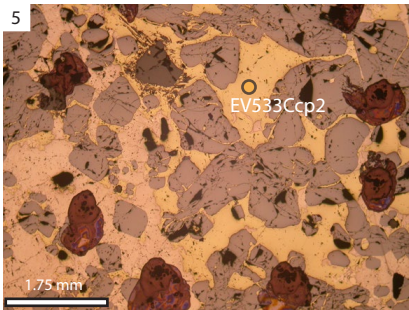
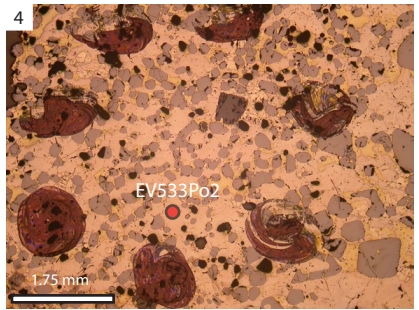
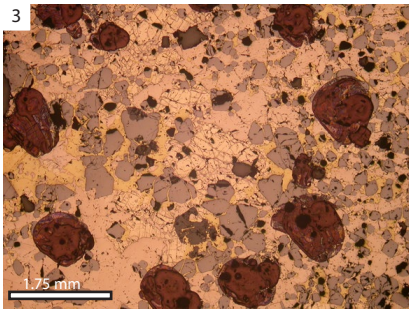
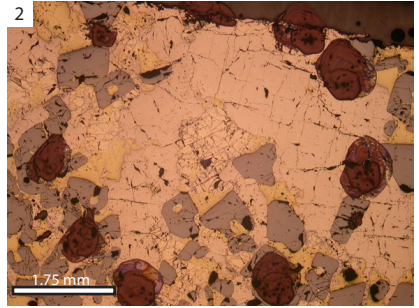
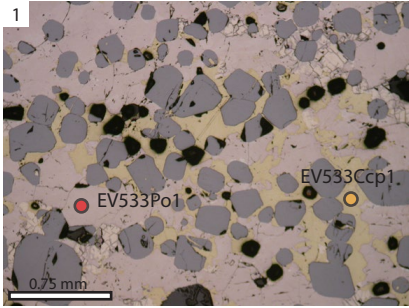
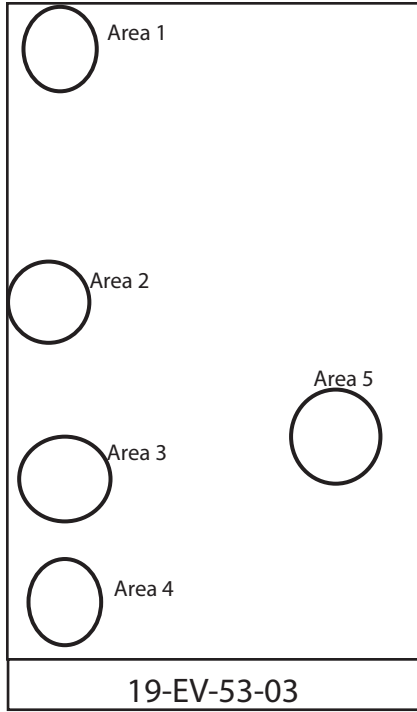


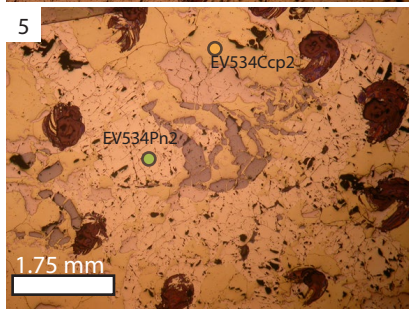
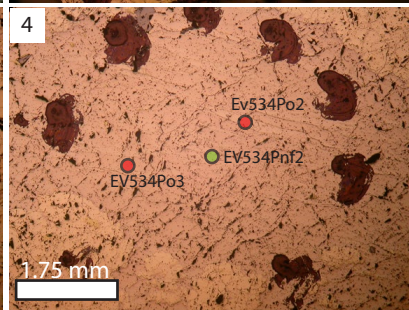
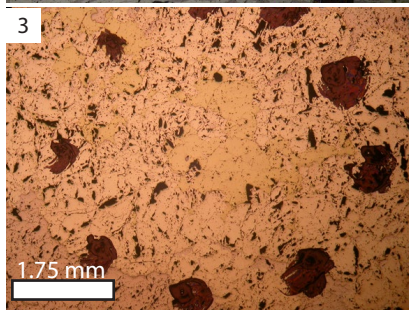
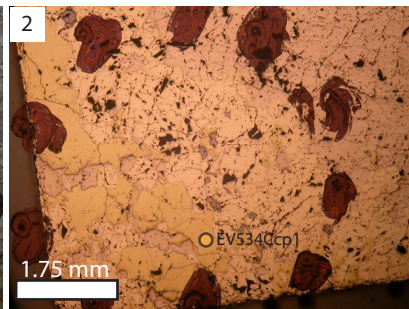
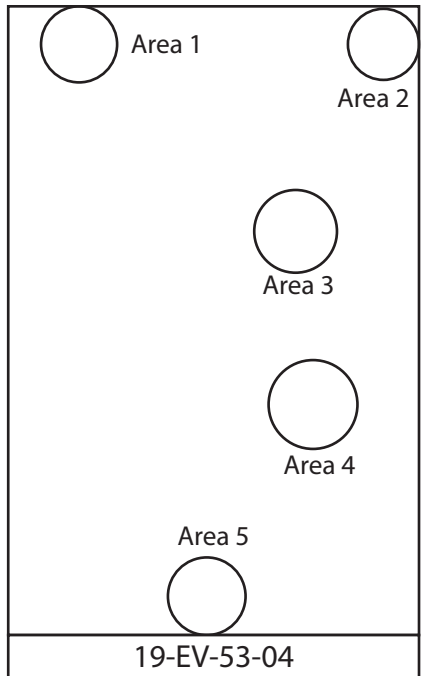


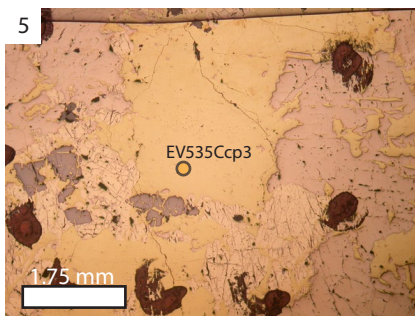
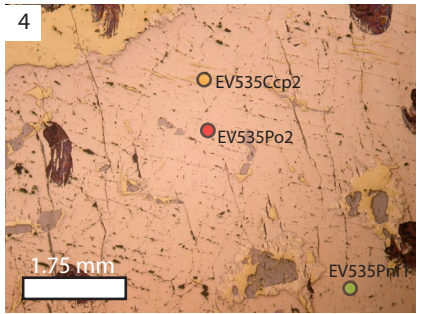
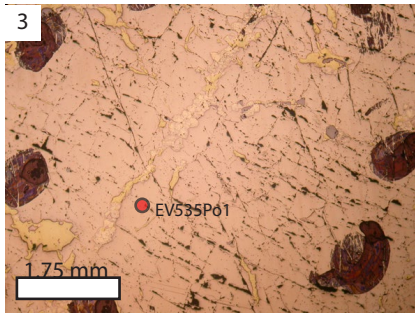
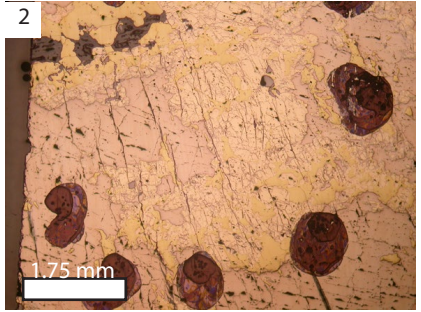
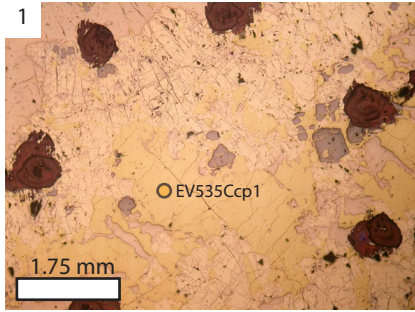
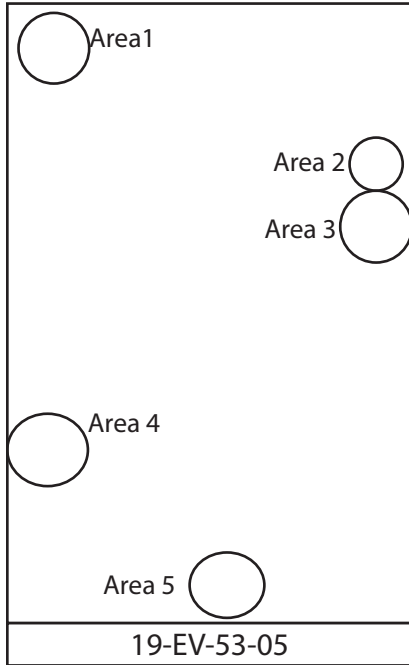


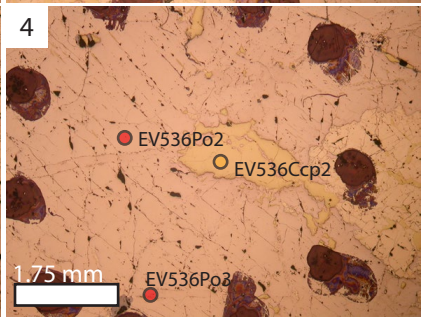
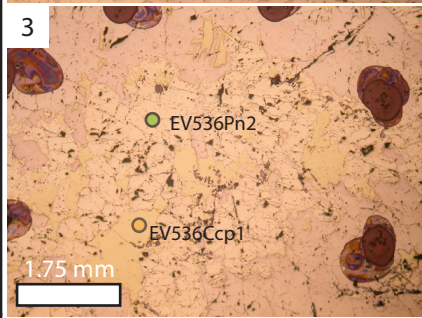
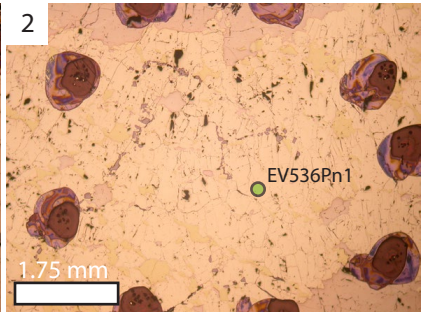
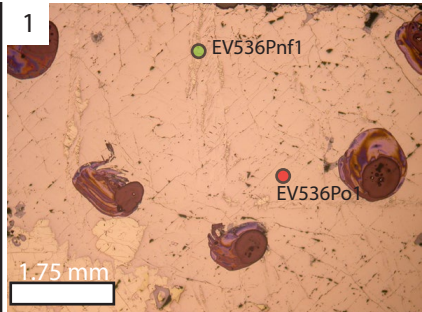
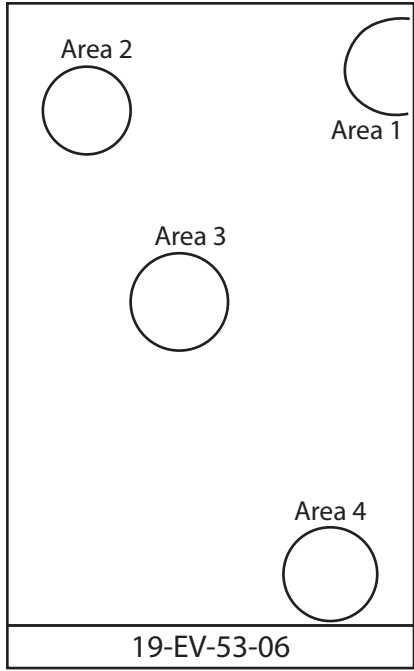


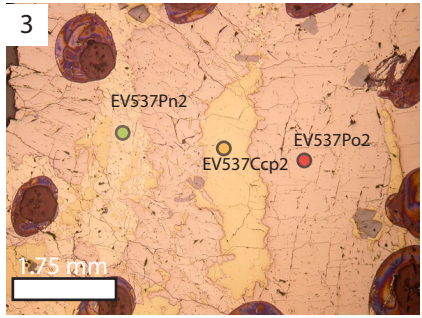
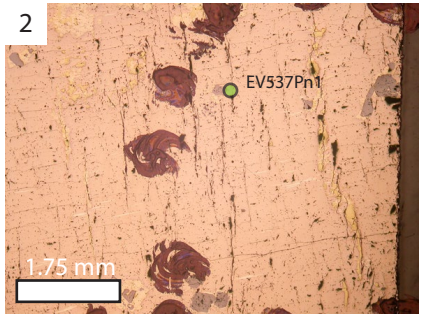
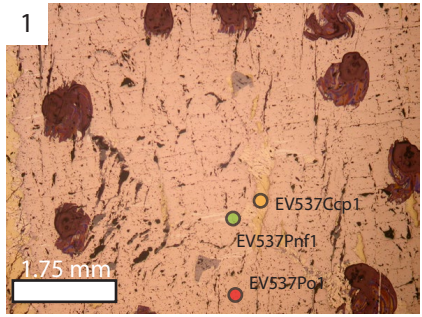
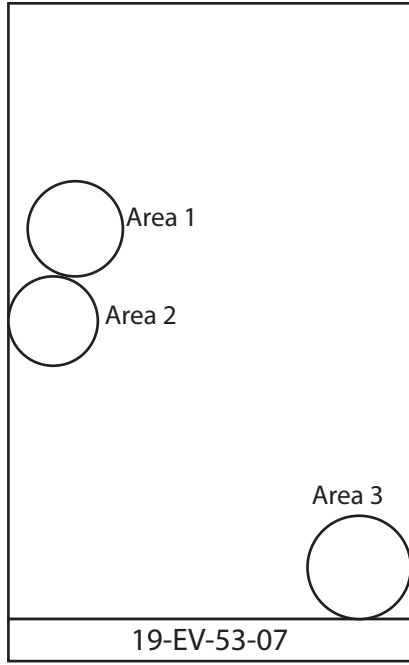


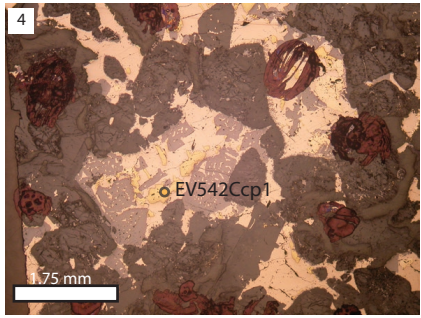
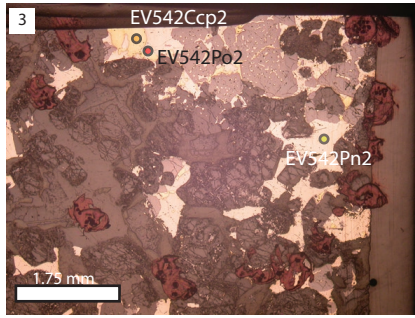
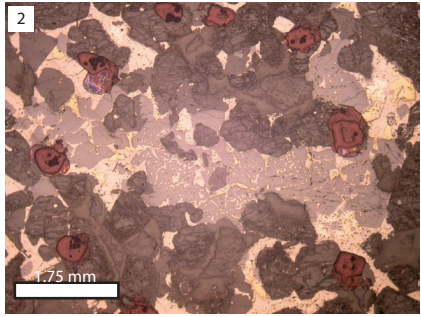
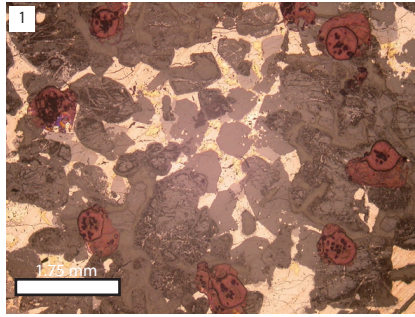
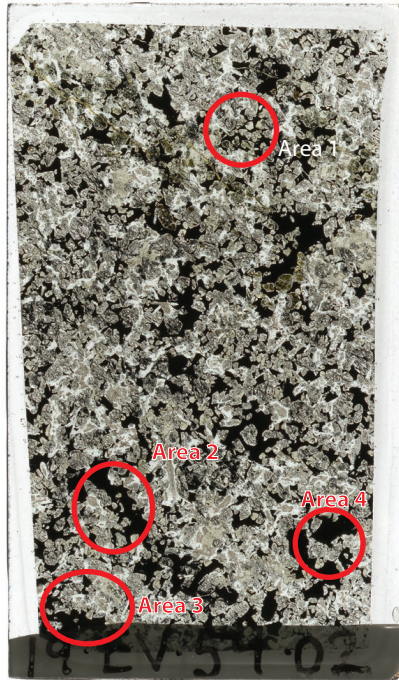












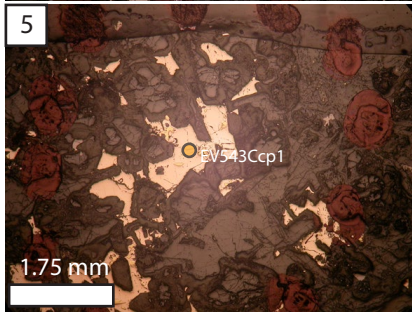
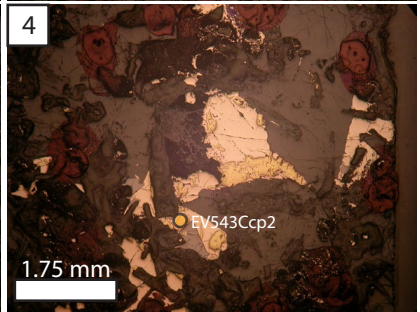
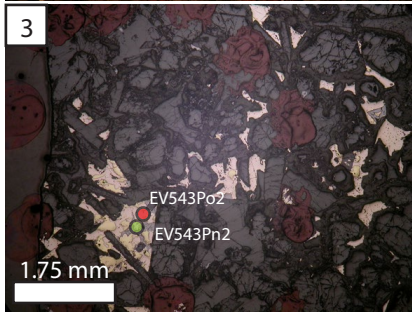
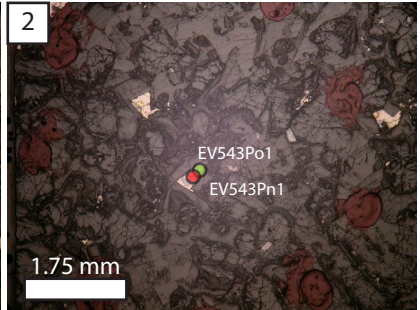
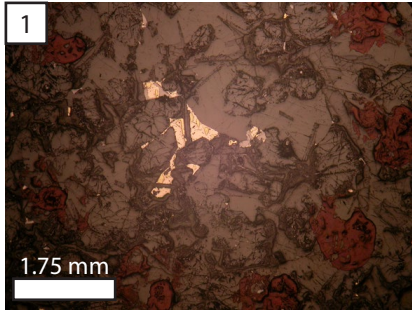
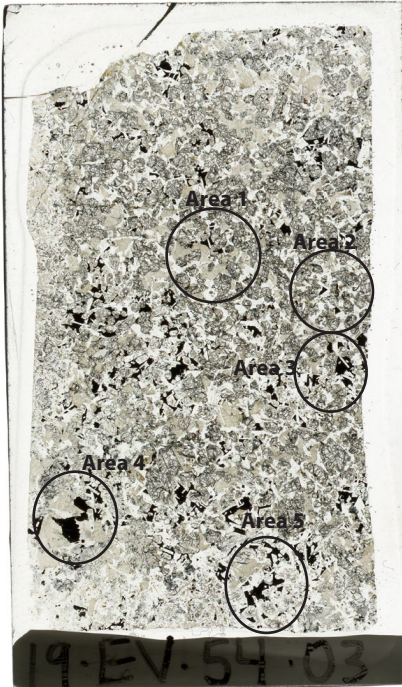


Table C.3. Measured Pb isotopic compositions of NIST SRM 610.

Sequence	Spot	$^{208}\text{Pb}/^{206}\text{Pb}$	2SE	$^{207}\text{Pb}/^{206}\text{Pb}$	2SE	Pb (ppm)
19-EV-48-01	G_NIST610_1	2.1682	0.0041	0.9094	0.0019	422.4
	G_NIST610_2	2.1683	0.0056	0.9098	0.0025	429.7
	G_NIST610_3	2.1655	0.006	0.9093	0.0024	429
	G_NIST610_4	2.1708	0.0045	0.9129	0.003	420.8
	G_NIST610_5	2.1664	0.0057	0.9085	0.0023	427.15
19-EV-54-02	G_NIST610_1	2.168	0.0058	0.9108	0.0024	421.45
	G_NIST610_2	2.1686	0.0059	0.9072	0.0026	429.75
	G_NIST610_3	2.1689	0.0059	0.9104	0.0027	429.05
	G_NIST610_4	2.1675	0.0051	0.9095	0.0027	427.95
	G_NIST610_5	2.1691	0.0078	0.9101	0.0026	423.1
19-EV-53-01	G_NIST610_1	2.1683	0.0066	0.91	0.003	424.55
	G_NIST610_2	2.1699	0.0065	0.9099	0.0026	425
	G_NIST610_3	2.1705	0.0064	0.9092	0.0031	425.45
	G_NIST610_4	2.1629	0.0055	0.9079	0.0026	432.65
	G_NIST610_5	2.1724	0.0069	0.9112	0.0027	421.85
19-EV-48-04	G_NIST610_1	2.1655	0.0054	0.9087	0.0026	418.85
	G_NIST610_2	2.1685	0.0059	0.9116	0.003	432.45
	G_NIST610_3	2.1722	0.0058	0.9102	0.0027	427.25
	G_NIST610_4	2.1653	0.0061	0.909	0.0025	427.85
	G_NIST610_5	2.1685	0.0066	0.9098	0.0029	421.9
19-EV-54-03	G_NIST610_1	2.1692	0.0055	0.9113	0.0025	420.35
	G_NIST610_2	2.168	0.0051	0.9095	0.0023	427.95
	G_NIST610_3	2.1677	0.0061	0.9082	0.0024	432.45
	G_NIST610_4	2.1669	0.0055	0.9071	0.0033	426.55
	G_NIST610_5	2.1691	0.005	0.9116	0.0027	421.75
19-EV-48-01	G_NIST610_1	2.1668	0.0068	0.9095	0.0029	425.95
	G_NIST610_2	2.1707	0.0074	0.909	0.0031	428.85
	G_NIST610_3	2.169	0.0066	0.9102	0.0027	426.05
	G_NIST610_4	2.1677	0.0055	0.91	0.0029	418.45
	G_NIST610_5	2.1681	0.0057	0.9093	0.0027	430.55
19-EV-48-03	G_NIST610_1	2.1666	0.0065	0.9108	0.0032	422.05
	G_NIST610_2	2.1702	0.0051	0.9095	0.0023	430.35
	G_NIST610_3	2.1658	0.0046	0.9098	0.0023	425.55
	G_NIST610_4	2.1664	0.0054	0.908	0.0022	427.15
	G_NIST610_5	2.1702	0.0065	0.9108	0.0033	424
19-EV-53-02	G_NIST610_1	2.1666	0.0065	0.9087	0.0034	422.1
	G_NIST610_2	2.1669	0.0066	0.9104	0.0028	431.4
	G_NIST610_3	2.1707	0.0063	0.91	0.0032	428.1
	G_NIST610_4	2.1679	0.0057	0.909	0.0027	425.05
	G_NIST610_5	2.1664	0.0061	0.9095	0.0026	424.45
19-EV-53-03	G_NIST610_1	2.1672	0.0051	0.9098	0.0027	421.35

Sequence	Spot	$^{208}\text{Pb}/^{206}\text{Pb}$	2SE	$^{207}\text{Pb}/^{206}\text{Pb}$	2SE	Pb (ppm)
	G_NIST610_2	2.1733	0.0054	0.9099	0.0027	434.3
	G_NIST610_3	2.1642	0.0055	0.9092	0.0024	424.45
	G_NIST610_4	2.167	0.0053	0.9101	0.0023	426.15
	G_NIST610_5	2.17	0.0062	0.9096	0.0029	423.85
19-EV-53-04	G_NIST610_1	2.1676	0.0065	0.908	0.0033	425.6
	G_NIST610_2	2.1683	0.0056	0.9116	0.002	430.7
	G_NIST610_3	2.1673	0.0067	0.9069	0.0026	419.1
	G_NIST610_4	2.1686	0.0061	0.9106	0.0027	431
	G_NIST610_5	2.1673	0.0067	0.9097	0.0032	425.2
19-EV-53-05	G_NIST610_1	2.17	0.006	0.9092	0.0027	425.6
	G_NIST610_2	2.1669	0.0056	0.9106	0.0024	428.7
	G_NIST610_3	2.167	0.0057	0.9086	0.0028	422.45
	G_NIST610_4	2.1676	0.0051	0.91	0.0024	428.25
	G_NIST610_5	2.1689	0.0056	0.9095	0.0025	425.4
19-EV-53-06	G_NIST610_1	2.1678	0.0059	0.91	0.0029	427.35
	G_NIST610_2	2.1686	0.0058	0.9082	0.0026	424.85
	G_NIST610_3	2.1704	0.0063	0.9105	0.0027	428.65
	G_NIST610_4	2.1662	0.0056	0.91	0.0025	421.15
	G_NIST610_5	2.1685	0.0046	0.9097	0.0025	428.8
19-EV-53-07	G_NIST610_1	2.1684	0.0057	0.91	0.0025	423.85
	G_NIST610_2	2.167	0.0051	0.9089	0.0026	425.75
	G_NIST610_3	2.1689	0.0057	0.9094	0.0025	429.35
	G_NIST610_4	2.167	0.0059	0.9109	0.0027	426.9
	G_NIST610_5	2.1693	0.0071	0.909	0.0032	423.95
19-EV-30-01	G_NIST610_1	2.1654	0.0059	0.9145	0.0028	421.1
	G_NIST610_2	2.1647	0.0067	0.9097	0.0029	431.85
	G_NIST610_3	2.1662	0.0062	0.9059	0.0026	426.5
	G_NIST610_4	2.1673	0.0067	0.908	0.0028	428.2
	G_NIST610_5	2.173	0.0072	0.9065	0.0031	422.7
19-EV-30-02	G_NIST610_1	2.1708	0.0064	0.9104	0.0026	423
	G_NIST610_3	2.1718	0.0065	0.9067	0.0029	427.35
	G_NIST610_4	2.1664	0.0056	0.9102	0.0026	428.05
	G_NIST610_5	2.1683	0.0055	0.9104	0.0029	423.45

Table C.4. Measured Pb isotopic compositions of NIST SRM 612 normalized to NIST SRM 610.

Sequence	Spot	$^{208}\text{Pb}/^{206}\text{Pb}$	2SE	$^{207}\text{Pb}/^{206}\text{Pb}$	2SE	Pb (ppm)
19-EV-46-01	G_NIST612_1	2.153	0.012	0.9029	0.007	42.2
	G_NIST612_2	2.172	0.011	0.909	0.0065	42.85
	G_NIST612_3	2.164	0.012	0.907	0.0063	42.15
	G_NIST612_4	2.149	0.014	0.9063	0.0059	43.3
	G_NIST612_5	2.156	0.012	0.9045	0.0059	43.45

Sequence	Spot	$^{208}\text{Pb}/^{206}\text{Pb}$	2SE	$^{207}\text{Pb}/^{206}\text{Pb}$	2SE	Pb (ppm)
19-EV-54-02	G_NIST612_1	2.164	0.011	0.9067	0.0057	40.1
	G_NIST612_2	2.154	0.011	0.8991	0.0069	41.7
	G_NIST612_3	2.167	0.016	0.9144	0.0068	42.8
	G_NIST612_4	2.166	0.017	0.9107	0.0081	42.2
	G_NIST612_5	2.165	0.015	0.9061	0.007	40.595
19-EV-53-01	G_NIST612_1	2.162	0.013	0.9059	0.0059	39.18
	G_NIST612_2	2.168	0.013	0.9053	0.0067	43.1
	G_NIST612_3	2.162	0.013	0.9081	0.0065	42.45
	G_NIST612_4	2.177	0.014	0.9103	0.0064	43.9
	G_NIST612_5	2.164	0.013	0.9067	0.0067	40.25
19-EV-48-04	G_NIST612_1	2.168	0.012	0.9158	0.0059	40.2
	G_NIST612_2	2.164	0.012	0.9105	0.0066	41.55
	G_NIST612_3	2.157	0.014	0.9071	0.0053	42.25
	G_NIST612_4	2.166	0.014	0.9094	0.0084	42.2
	G_NIST612_5	2.154	0.012	0.9077	0.0062	43
19-EV-54-03	G_NIST612_1	2.15	0.012	0.9068	0.0063	42.55
	G_NIST612_2	2.156	0.017	0.9045	0.0084	40.95
	G_NIST612_3	2.155	0.013	0.9079	0.0063	44.6
	G_NIST612_4	2.166	0.012	0.9079	0.0056	43.15
	G_NIST612_5	2.179	0.014	0.9101	0.0069	43.5
19-EV-48-01	G_NIST612_1	2.145	0.014	0.9056	0.0056	41.55
	G_NIST612_2	2.162	0.016	0.91	0.0075	41.1
	G_NIST612_3	2.172	0.014	0.9129	0.0071	42.55
	G_NIST612_4	2.161	0.012	0.9102	0.0061	38.85
	G_NIST612_5	2.167	0.015	0.9053	0.0074	62.5
19-EV-48-03	G_NIST612_1	2.163	0.013	0.9054	0.0059	39.45
	G_NIST612_2	2.172	0.014	0.9125	0.0071	42.55
	G_NIST612_3	2.167	0.015	0.9076	0.0065	42.55
	G_NIST612_4	2.16	0.012	0.9057	0.0055	41.4
	G_NIST612_5	2.167	0.013	0.9086	0.0063	41.55
19-EV-53-02	G_NIST612_1	2.17	0.014	0.9115	0.0076	41.1
	G_NIST612_2	2.174	0.014	0.9075	0.0071	42.3
	G_NIST612_3	2.175	0.015	0.9087	0.0071	43.25
	G_NIST612_4	2.161	0.014	0.9084	0.0072	42.2
	G_NIST612_5	2.159	0.015	0.9096	0.0074	41
19-EV-53-03	G_NIST612_1	2.162	0.013	0.909	0.0054	41.75
	G_NIST612_2	2.154	0.027	0.908	0.013	34.25
	G_NIST612_3	2.161	0.014	0.9088	0.0067	41.8
	G_NIST612_4	2.172	0.013	0.9052	0.0063	40.85
	G_NIST612_5	2.163	0.013	0.9065	0.007	39.5
19-EV-53-04	G_NIST612_1	2.16	0.014	0.9047	0.0066	40.8
	G_NIST612_2	2.167	0.013	0.9117	0.0071	40.35
	G_NIST612_3	2.161	0.011	0.9084	0.0065	44.25

Sequence	Spot	$^{208}\text{Pb}/^{206}\text{Pb}$	2SE	$^{207}\text{Pb}/^{206}\text{Pb}$	2SE	Pb (ppm)
19-EV-53-05	G_NIST612_4	2.161	0.012	0.9041	0.0064	42.05
	G_NIST612_5	2.163	0.015	0.901	0.0056	41.5
	G_NIST612_1	2.174	0.011	0.9148	0.0071	44.95
	G_NIST612_2	2.16	0.011	0.9077	0.0062	44.55
	G_NIST612_3	2.152	0.014	0.9028	0.0053	43.8
19-EV-53-06	G_NIST612_4	2.162	0.013	0.9061	0.0073	42.05
	G_NIST612_5	2.162	0.014	0.908	0.0073	44.9
	G_NIST612_1	2.164	0.014	0.9067	0.0074	41.95
	G_NIST612_2	2.169	0.015	0.9081	0.0074	41
	G_NIST612_3	2.174	0.013	0.9103	0.0052	42.05
19-EV-53-07	G_NIST612_4	2.17	0.014	0.9089	0.007	42.4
	G_NIST612_5	2.174	0.012	0.908	0.0059	41.45
	G_NIST612_1	2.154	0.016	0.9081	0.0058	39.3
	G_NIST612_2	2.159	0.014	0.8999	0.0066	42.05
	G_NIST612_3	2.157	0.014	0.911	0.0065	41.45
19-EV-30-01	G_NIST612_4	2.164	0.012	0.9059	0.0053	43.2
	G_NIST612_5	2.165	0.015	0.9079	0.0065	38.5
	G_NIST612_1	2.16	0.014	0.9044	0.007	42.65
	G_NIST612_2	2.168	0.015	0.9103	0.0076	43.3
	G_NIST612_3	2.178	0.014	0.9113	0.0062	42.3
19-EV-30-02	G_NIST612_4	2.155	0.019	0.911	0.013	36.45
	G_NIST612_5	2.163	0.014	0.9048	0.0061	38.85
	G_NIST612_1	2.13	0.012	0.908	0.0065	40.65
	G_NIST612_3	2.145	0.011	0.9063	0.0068	40.2
	G_NIST612_4	2.173	0.022	0.915	0.012	35
	G_NIST612_5	2.168	0.012	0.9057	0.0052	40.55

Table C.5. Measured Pb isotopic compositions of BCR2-G normalized to NIST SRM 610.

Sequence	Spot	$^{208}\text{Pb}/^{206}\text{Pb}$	2SE	$^{207}\text{Pb}/^{206}\text{Pb}$	2SE	Pb (ppm)
19-EV-46-01	G_BCR2G_1	2.055	0.022	0.832	0.012	10.365
	G_BCR2G_2	2.07	0.023	0.839	0.011	10.73
	G_BCR2G_3	2.061	0.031	0.835	0.014	11.09
	G_BCR2G_4	2.045	0.026	0.835	0.013	10.575
	G_BCR2G_5	2.055	0.027	0.826	0.011	10.45
19-EV-54-02	G_BCR2G_1	2.08	0.033	0.843	0.012	10.515
	G_BCR2G_2	2.057	0.024	0.819	0.012	10.65
	G_BCR2G_3	2.072	0.031	0.839	0.015	10.915
	G_BCR2G_4	2.075	0.023	0.838	0.013	10.83
	G_BCR2G_5	2.062	0.033	0.833	0.015	10.495
19-EV-53-01	G_BCR2G_1	2.068	0.023	0.833	0.011	10.535
	G_BCR2G_2	2.065	0.025	0.832	0.011	10.72
	G_BCR2G_3	2.077	0.027	0.826	0.012	11.185

Sequence	Spot	$^{208}\text{Pb}/^{206}\text{Pb}$	2SE	$^{207}\text{Pb}/^{206}\text{Pb}$	2SE	Pb (ppm)
	G_BCR2G_4	2.063	0.024	0.832	0.013	10.655
	G_BCR2G_5	2.048	0.029	0.839	0.013	10.45
19-EV-48-04	G_BCR2G_1	2.052	0.032	0.838	0.018	10.7
	G_BCR2G_2	2.084	0.035	0.843	0.013	10.29
	G_BCR2G_3	2.083	0.028	0.85	0.014	10.235
	G_BCR2G_4	2.067	0.029	0.839	0.015	10.405
	G_BCR2G_5	2.066	0.03	0.825	0.018	9.92
19-EV-54-03	G_BCR2G_1	2.066	0.023	0.83	0.012	10.415
	G_BCR2G_2	2.052	0.031	0.812	0.013	10.69
	G_BCR2G_3	2.042	0.028	0.828	0.015	10.86
	G_BCR2G_4	2.063	0.04	0.821	0.016	10.74
	G_BCR2G_5	2.038	0.033	0.821	0.014	10.55
19-EV-48-01	G_BCR2G_1	2.068	0.03	0.832	0.015	10.22
	G_BCR2G_2	2.069	0.031	0.835	0.014	10.355
	G_BCR2G_3	2.068	0.033	0.836	0.017	10.315
	G_BCR2G_4	2.024	0.028	0.825	0.013	10.13
	G_BCR2G_5	2.072	0.036	0.835	0.016	10.12
19-EV-48-03	G_BCR2G_1	2.083	0.035	0.833	0.014	10.23
	G_BCR2G_2	2.085	0.031	0.839	0.012	10.39
	G_BCR2G_3	2.078	0.034	0.855	0.015	10.28
	G_BCR2G_4	2.076	0.032	0.835	0.014	10.065
	G_BCR2G_5	2.091	0.033	0.841	0.013	10.47
19-EV-53-02	G_BCR2G_1	2.057	0.028	0.843	0.016	10.265
	G_BCR2G_2	2.016	0.03	0.808	0.013	10.355
	G_BCR2G_3	2.043	0.035	0.837	0.015	10.425
	G_BCR2G_4	2.066	0.033	0.827	0.017	10.225
	G_BCR2G_5	2.069	0.029	0.839	0.014	10.135
19-EV-53-03	G_BCR2G_1	2.075	0.026	0.826	0.016	10.33
	G_BCR2G_2	2.09	0.029	0.843	0.014	10.24
	G_BCR2G_3	2.088	0.04	0.831	0.016	10.325
	G_BCR2G_4	2.072	0.033	0.842	0.017	10.355
	G_BCR2G_5	2.066	0.028	0.835	0.014	10.105
19-EV-53-04	G_BCR2G_1	2.065	0.027	0.841	0.01	10.385
	G_BCR2G_2	2.064	0.027	0.823	0.011	10.15
	G_BCR2G_3	2.065	0.027	0.83	0.012	10.89
	G_BCR2G_4	2.064	0.03	0.837	0.016	10.315
	G_BCR2G_5	2.042	0.032	0.823	0.015	10.26
19-EV-53-05	G_BCR2G_1	2.102	0.028	0.842	0.014	10.065
	G_BCR2G_2	2.055	0.026	0.83	0.014	10.34
	G_BCR2G_3	2.062	0.024	0.84	0.012	10.845
	G_BCR2G_4	2.058	0.031	0.835	0.013	10.99
	G_BCR2G_5	2.079	0.028	0.831	0.012	10.45
19-EV-53-06	G_BCR2G_1	2.078	0.028	0.837	0.014	10.09

Sequence	Spot	$^{208}\text{Pb}/^{206}\text{Pb}$	2SE	$^{207}\text{Pb}/^{206}\text{Pb}$	2SE	Pb (ppm)
19-EV-53-07	G_BCR2G_2	2.07	0.032	0.833	0.014	10.4
	G_BCR2G_3	2.055	0.037	0.842	0.015	10.15
	G_BCR2G_4	2.088	0.026	0.833	0.014	10.305
	G_BCR2G_5	2.071	0.03	0.83	0.015	10.465
	G_BCR2G_1	2.069	0.03	0.835	0.011	10.13
19-EV-30-01	G_BCR2G_2	2.06	0.031	0.829	0.016	10.1
	G_BCR2G_3	2.097	0.025	0.841	0.014	10.14
	G_BCR2G_4	2.056	0.03	0.817	0.015	10.165
	G_BCR2G_5	2.071	0.036	0.824	0.016	10.245
	G_BCR2G_1	2.055	0.03	0.832	0.014	10.535
19-EV-30-02	G_BCR2G_2	2.072	0.035	0.831	0.014	10.77
	G_BCR2G_3	2.066	0.031	0.823	0.017	10.455
	G_BCR2G_4	2.075	0.033	0.845	0.016	10.405
	G_BCR2G_5	2.093	0.033	0.84	0.015	10.28
	G_BCR2G_1	2.11	0.03	0.837	0.016	10.215
	G_BCR2G_3	2.058	0.034	0.829	0.014	10.235
	G_BCR2G_4	2.078	0.028	0.845	0.014	10.035
	G_BCR2G_5	2.071	0.027	0.832	0.013	10.415

Table C.6. Measured Pb isotopic compositions of MASS-1 normalized to NIST SRM 610.

Sequence	Spot	$^{208}\text{Pb}/^{206}\text{Pb}$	2SE	$^{207}\text{Pb}/^{206}\text{Pb}$	2SE	Pb (ppm)
18-EV-46-01	P_MASS_1_1	2.017	0.016	0.8258	0.006	2184
	P_MASS_1_2	2.041	0.011	0.8263	0.0058	2492.5
	P_MASS_1_3	2.042	0.011	0.8241	0.0041	2089.5
	P_MASS_1_4	2.049	0.01	0.8291	0.0042	2625
	P_MASS_1_5	2.04	0.012	0.826	0.0052	2408.5
19-EV-54-02	P_MASS_1_1	1.939	0.047	0.838	0.02	1835
	P_MASS_1_2	2.053	0.0077	0.8282	0.0031	2375
	P_MASS_1_3	2.0523	0.0096	0.829	0.0045	2284.5
	P_MASS_1_4	2.043	0.0086	0.8276	0.0036	2100
	P_MASS_1_5	2.0385	0.0099	0.8232	0.004	1480.5
19-EV-53-01	P_MASS_1_1	1.965	0.077	0.831	0.051	1800
	P_MASS_1_2	2.0487	0.0064	0.8281	0.0031	2385.5
	P_MASS_1_3	2.0475	0.0081	0.8261	0.0028	2400
	P_MASS_1_4	2.0526	0.0065	0.8269	0.0033	2279
	P_MASS_1_5	2.0568	0.0064	0.8314	0.0024	2600
19-EV-48-04	P_MASS_1_1	2.0543	0.0076	0.8305	0.0031	2284
	P_MASS_1_2	2.0441	0.0078	0.8259	0.0041	2425.5
	P_MASS_1_3	2.045	0.0099	0.8242	0.0038	1960.5
	P_MASS_1_4	2.0581	0.0067	0.8302	0.0032	2091
	P_MASS_1_5	2.0346	0.0098	0.8224	0.0061	1819.5
19-EV-54-03	P_MASS_1_1	2.0482	0.0077	0.827	0.0035	2285.5

Sequence	Spot	²⁰⁸ Pb/ ²⁰⁶ Pb	2SE	²⁰⁷ Pb/ ²⁰⁶ Pb	2SE	Pb (ppm)
	P_MASS_1_2	2.0439	0.0083	0.8266	0.004	1294.5
	P_MASS_1_3	2.038	0.023	0.827	0.011	1376.5
	P_MASS_1_4	2.049	0.011	0.826	0.0042	2195
	P_MASS_1_5	2.0549	0.0058	0.8304	0.0027	2206
19-EV-48-01	P_MASS_1_1	2.0535	0.0079	0.8277	0.0039	2239.5
	P_MASS_1_2	2.0444	0.0082	0.8285	0.0049	2239
	P_MASS_1_3	2.0549	0.0086	0.8278	0.0031	2509
	P_MASS_1_4	2.0614	0.0063	0.8321	0.0039	3305
	P_MASS_1_5	2.0477	0.008	0.8293	0.0033	1599.5
19-EV-48-03	P_MASS_1_1	2.043	0.0087	0.83	0.0047	2273
	P_MASS_1_2	2.055	0.011	0.8289	0.0038	2075.5
	P_MASS_1_3	2.0525	0.0063	0.8249	0.0028	3205
	P_MASS_1_4	2.053	0.0079	0.8249	0.0041	1355
	P_MASS_1_5	2.045	0.025	0.838	0.015	1857.5
19-EV-53-02	P_MASS_1_1	2.0566	0.0095	0.8292	0.0038	2178
	P_MASS_1_2	2.0473	0.0076	0.8234	0.0032	2326.5
	P_MASS_1_3	2.0618	0.0082	0.8276	0.0036	1633
	P_MASS_1_4	2.021	0.016	0.8265	0.007	2353.5
	P_MASS_1_5	2.0502	0.0092	0.826	0.004	1650
19-EV-53-03	P_MASS_1_1	2.029	0.012	0.8287	0.0058	1996
	P_MASS_1_2	2.0398	0.0066	0.8283	0.0028	2475
	P_MASS_1_3	2.0494	0.0093	0.8269	0.0033	2275
	P_MASS_1_4	2.0432	0.0082	0.8279	0.0028	2131.5
	P_MASS_1_5	2.038	0.012	0.8262	0.0051	2715
19-EV-53-04	P_MASS_1_1	2.042	0.013	0.823	0.0055	2195.5
	P_MASS_1_2	2.044	0.0083	0.8244	0.0038	3535
	P_MASS_1_3	2.0544	0.0076	0.827	0.0035	2012
	P_MASS_1_4	1.89	0.12	0.871	0.067	84.35
	P_MASS_1_5	2.0526	0.0079	0.8273	0.0032	2245.5
19-EV-53-05	P_MASS_1_1	2.0563	0.0062	0.8266	0.0032	2061.5
	P_MASS_1_2	2.0545	0.0048	0.8285	0.0026	2510
	P_MASS_1_3	2.0515	0.0086	0.8251	0.0033	3040
	P_MASS_1_4	2.0489	0.0082	0.8249	0.0035	2503
	P_MASS_1_5	2.04	0.01	0.8276	0.0051	2207
19-EV-53-06	P_MASS_1_1	2.0572	0.0078	0.828	0.0038	1312.5
	P_MASS_1_2	2.055	0.0088	0.8304	0.0038	2195
	P_MASS_1_3	2.001	0.038	0.828	0.032	1060
	P_MASS_1_4	2.0544	0.0062	0.8249	0.0028	1858.5
	P_MASS_1_5	2.0542	0.0077	0.8294	0.0035	2465
19-EV-53-07	P_MASS_1_1	2.0519	0.0093	0.8273	0.0044	2145
	P_MASS_1_2	2.0484	0.0081	0.8292	0.0044	3365
	P_MASS_1_3	2.039	0.022	0.834	0.014	1903.5
	P_MASS_1_4	2.0505	0.0077	0.8261	0.0037	2285.5

Sequence	Spot	$^{208}\text{Pb}/^{206}\text{Pb}$	2SE	$^{207}\text{Pb}/^{206}\text{Pb}$	2SE	Pb (ppm)
19-EV-30-01	P_MASS_1_5	2.046	0.011	0.8263	0.0051	1597.5
	P_MASS_1_1	2.0496	0.0098	0.8305	0.0055	1876.5
	P_MASS_1_2	2.028	0.017	0.8321	0.0084	1930
	P_MASS_1_3	2.0525	0.007	0.8258	0.0031	2633.5
	P_MASS_1_4	2.0529	0.0092	0.8259	0.0054	1703.5
19-EV-30-02	P_MASS_1_5	2.05	0.013	0.8361	0.007	1498
	P_MASS_1_1	2.114	0.012	0.8279	0.0036	1412
	P_MASS_1_3	2.0295	0.0074	0.8254	0.0032	2520
	P_MASS_1_4	2.0544	0.0073	0.8251	0.0036	2416
	P_MASS_1_5	2.051	0.026	0.824	0.01	1206

Table C.7. Measured Pb isotopic compositions of FeS-1 normalized to NIST SRM 610.

Sequence	Spot	$^{208}\text{Pb}/^{206}\text{Pb}$	2SE	$^{207}\text{Pb}/^{206}\text{Pb}$	2SE	Pb (ppm)
19-EV-46-01	P_FeS_1_1	2.167	0.015	0.9208	0.0064	92.25
	P_FeS_1_2	2.1718	0.0086	0.9239	0.0044	95.35
	P_FeS_1_3	2.1693	0.0086	0.9228	0.0039	95.5
	P_FeS_1_4	2.1702	0.0086	0.9252	0.0039	86.75
	P_FeS_1_5	2.169	0.013	0.9241	0.0057	96.95
19-EV-54-02	P_FeS_1_1	2.1667	0.0099	0.9236	0.0045	86.25
	P_FeS_1_2	2.167	0.011	0.9238	0.0042	87.35
	P_FeS_1_3	2.18	0.016	0.923	0.0063	103.05
	P_FeS_1_4	2.182	0.021	0.934	0.01	103.2
	P_FeS_1_5	2.139	0.02	0.895	0.014	120.5
19-EV-53-01	P_FeS_1_1	2.1699	0.0071	0.9201	0.0039	91.85
	P_FeS_1_2	2.1644	0.0098	0.9213	0.0043	92.6
	P_FeS_1_3	2.158	0.011	0.9157	0.0056	91.15
	P_FeS_1_4	2.1737	0.0092	0.928	0.0044	91.55
	P_FeS_1_5	2.162	0.018	0.9205	0.0079	86.4
19-EV-48-04	P_FeS_1_1	2.1674	0.0084	0.923	0.0044	83
	P_FeS_1_2	2.1666	0.0082	0.9214	0.0031	82.2
	P_FeS_1_3	2.1756	0.009	0.9221	0.0046	88.85
	P_FeS_1_4	2.1617	0.0099	0.9188	0.0046	85.6
	P_FeS_1_5	2.171	0.01	0.9254	0.0052	91.25
19-EV-54-03	P_FeS_1_1	2.155	0.011	0.9146	0.0044	79.45
	P_FeS_1_2	2.182	0.012	0.9278	0.0061	91.45
	P_FeS_1_3	2.1666	0.0083	0.9228	0.0048	90.7
	P_FeS_1_4	2.147	0.013	0.9149	0.0057	87.6
	P_FeS_1_5	2.172	0.023	0.923	0.011	88.3
19-EV-48-01	P_FeS_1_1	2.156	0.011	0.9215	0.0047	85.1
	P_FeS_1_2	2.1812	0.0096	0.9273	0.0045	88.3
	P_FeS_1_3	2.155	0.013	0.9158	0.0053	83.95
	P_FeS_1_4	2.1668	0.0095	0.9225	0.0042	78.9

Sequence	Spot	$^{208}\text{Pb}/^{206}\text{Pb}$	2SE	$^{207}\text{Pb}/^{206}\text{Pb}$	2SE	Pb (ppm)
19-EV-48-03	P_FeS_1_5	2.168	0.012	0.9247	0.0049	82.65
	P_FeS_1_1	2.169	0.011	0.9242	0.0047	80.2
	P_FeS_1_2	2.168	0.01	0.9212	0.0052	87.7
	P_FeS_1_3	2.171	0.01	0.9227	0.0051	87.15
	P_FeS_1_4	2.156	0.011	0.915	0.0042	82.55
19-EV-53-02	P_FeS_1_5	2.165	0.011	0.9204	0.0045	77.1
	P_FeS_1_1	2.159	0.012	0.9165	0.0049	85.4
	P_FeS_1_2	2.16	0.011	0.9197	0.0054	87.3
	P_FeS_1_3	2.161	0.025	0.921	0.012	84.45
	P_FeS_1_4	2.191	0.011	0.9314	0.006	96.35
19-EV-53-03	P_FeS_1_5	2.163	0.012	0.9213	0.0058	87
	P_FeS_1_1	2.164	0.01	0.924	0.0045	86.35
	P_FeS_1_2	2.177	0.011	0.9289	0.0055	88.8
	P_FeS_1_3	2.147	0.023	0.914	0.01	87.6
	P_FeS_1_4	2.1783	0.0098	0.9241	0.0043	84.5
19-EV-53-04	P_FeS_1_5	2.1788	0.0096	0.9231	0.0048	90.05
	P_FeS_1_1	2.1738	0.0099	0.9221	0.0042	83.45
	P_FeS_1_2	2.1787	0.0097	0.9269	0.0039	87.05
	P_FeS_1_3	2.1685	0.009	0.9172	0.0046	85.35
	P_FeS_1_4	2.164	0.012	0.9178	0.0061	81.05
19-EV-53-05	P_FeS_1_5	2.1748	0.0078	0.9211	0.0036	82.5
	P_FeS_1_1	2.162	0.022	0.9194	0.0079	84.1
	P_FeS_1_2	2.164	0.0082	0.9191	0.0042	82.35
	P_FeS_1_3	2.16	0.011	0.9175	0.0049	90.7
	P_FeS_1_4	2.1586	0.0089	0.919	0.0037	85.9
19-EV-53-06	P_FeS_1_5	2.138	0.029	0.909	0.011	85.7
	P_FeS_1_1	2.1621	0.0094	0.9177	0.0047	81.7
	P_FeS_1_2	2.165	0.011	0.9172	0.0068	79.95
	P_FeS_1_3	2.1658	0.0084	0.9209	0.0038	83.6
	P_FeS_1_4	2.167	0.01	0.9174	0.004	83.05
19-EV-53-07	P_FeS_1_5	2.1835	0.0081	0.9243	0.0043	85.6
	P_FeS_1_1	2.158	0.01	0.9172	0.0044	83.95
	P_FeS_1_2	2.1738	0.009	0.9291	0.0045	87.85
	P_FeS_1_3	2.167	0.011	0.9223	0.0052	85.55
	P_FeS_1_4	2.1716	0.0092	0.9198	0.004	84.6
19-EV-30-01	P_FeS_1_5	2.183	0.011	0.9324	0.0057	92
	P_FeS_1_1	2.1752	0.0071	0.9253	0.0038	87.35
	P_FeS_1_2	2.1733	0.0071	0.9212	0.0035	83.65
	P_FeS_1_3	2.1648	0.0083	0.9187	0.0037	84
	P_FeS_1_4	2.1731	0.0078	0.9166	0.0041	82
19-EV-30-02	P_FeS_1_5	2.172	0.011	0.9214	0.0056	87.65
	P_FeS_1_1	2.295	0.019	0.938	0.011	113
	P_FeS_1_3	2.1528	0.0094	0.9226	0.0046	85.05

Sequence	Spot	$^{208}\text{Pb}/^{206}\text{Pb}$	2SE	$^{207}\text{Pb}/^{206}\text{Pb}$	2SE	Pb (ppm)
	P_FeS_1_4	2.18	0.01	0.924	0.0046	83.45
	P_FeS_1_5	2.177	0.01	0.9208	0.0046	85.35